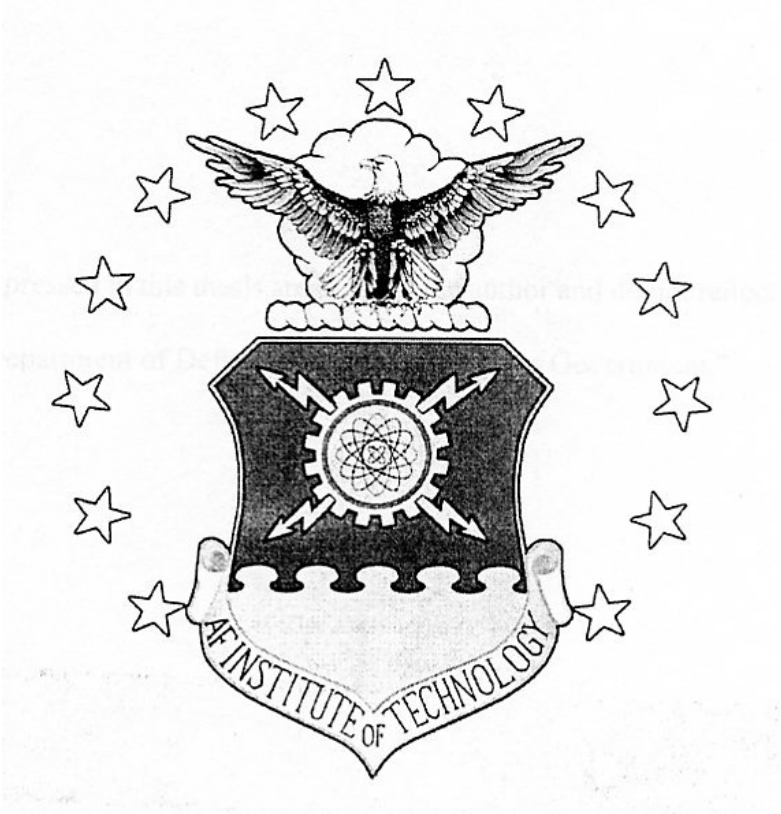

EFFECTS OF VARIABLE CONTACT LOAD ON FRETTING FATIGUE BEHAVIOR OF SHOT-PEENED AND UN-PEENED TITANIUM ALLOY

THESIS

Chia-hwa Lee, Captain, Taiwan Army

AFIT/GAE/ENY/04-D01

DEPARTMENT OF THE AIR FORCE
AIR UNIVERSITY

AIR FORCE INSTITUTE OF TECHNOLOGY

Wright-Patterson Air Force Base, Ohio

AFIT/GAE/ENY/04-D01

EFFECTS OF VARIABLE CONTACT LOAD ON FRETTING FATIGUE BEHAVIOR OF SHOT-PEENED AND UN-PEENED TITANIUM ALLOY

THESIS

Presented to the Faculty

Department of Aeronautics and Astronautics

Graduate School of Engineering and Management

Air Force Institute of Technology

Air University

Air Education and Training Command

In Partial Fulfillment of the Requirements for the

Degree of Master of Science in Aeronautical Engineering

Chia-hwa Lee

Captain, Taiwan Army

December 2004

AFIT/GAE/ENY/04-D01

EFFECTS OF VARIABLE CONTACT LOAD ON FRETTING FATIGUE BEHAVIOR OF SHOT-PEENED AND UN-PEENED TITANIUM ALLOY

Chia-hwa Lee, BS
Captain, Taiwan Army

Approved:

/signed/	11/24/04
Shankar Mall (Chairman)	date
/signed/	11/30/04
Vinod K. Jain (Member)	date
/signed/	11/24/04
Theodore Nicholas (Member)	date

Abstract

Fretting fatigue occurs between two components in contact under relative motion and reduces fatigue life when compared with plain fatigue. Shot-peening, on the other hand, is the most commonly used cold working process to improve material fatigue resistance in aeronautical industries. Nearly all work accomplished to date has assumed a constant contact load while investigating fretting fatigue. The primary goal of this study was to explore fretting fatigue behavior under constant and variable contact load configurations using both shot-peened and un-peened specimens made up of Ti-6Al-4V alloy. Contact loads were applied with four frequencies, and they were 0 Hz, 2.5 Hz, 10 Hz, and 30 Hz. Applied axial loads were also manipulated to produce tension-tension and tension-compression test conditions on the specimens at the frequency of 10 Hz. Cracks were always found to initiate near the trailing edge for all tests. The crack initiated on the contact surface of un-peened specimens and within the interior of shot-peened specimens. Finite element analysis was performed by a commercially available software, ABAQUS, to obtain contact region state variables such as stress, strain, and displacement which were computed for the development of fretting fatigue parameters. Fatigue parameters, such as the stress range, effective stress, and modified shear stress range (MSSR), were analyzed for their applicability on fretting fatigue life prediction. No strong correlation between contact load conditions and fretting fatigue mechanisms was found, and shot-peening improved fretting fatigue life despite contact load conditions. Also, the MSSR parameter was effective in fretting fatigue predictions under constant and variable contact load conditions in terms of fatigue life, crack initiation location and orientation.

Acknowledgments

I would like to express my sincere appreciation to my thesis advisor Dr. Mall for his guidance and teaching throughout this thesis project.

I would also like to thank Dr. Hyukjae Lee, USAF Captain Andrew j. Jutte, and USAF Captain Lewis C. Lietch who gave me all the technical supports needed for conducting this project.

In addition, I would like to thank my academic advisor Dr. King for his helps on leading me to accomplish all the academic eligibility requirements from AFIT for my graduation.

Finally, I would like to express my gratitude to CCIT of Taiwan's DoD who believed in me and gave me a chance and honor to complete my Master of Science degree in Aeronautical Engineering in AFIT, USA.

Chia-hwa Lee

Table of Contents

Page

Page

List of Figures

Figure Page

Page

Page

List of Tables

Table Page

List of Symbols

a	contact half-width
$a_{analytical}$	contact half-width carried out from analytical solution
$a_{Exp,\ max}$	maximum contact half-width measured from experiments
$a_{FEA,\ max}$	contact half-width at maximum load conditions from FEA
$a_{FEA,\ step1}$	contact half-width at Step 1 from FEA
$a_{Ruiz,\ max}$	contact half-width at maximum load conditions from Ruiz program
A	a specimen's cross section area
b	a specimen's half thickness
c	stick zone boundary
d	specimen thickness
E	modulus of elasticity
f	coefficient of friction
f_{FEA}	coefficient of friction used in FEA
FEA	finite element analysis
h	depth of penetration
L	specimen overall length
MSSR	modified shear stress range fatigue predictive parameter
N_f	numbers of fatigue cycles to break a specimen into two pieces
N_i	numbers of fatigue cycles to crack initiation
p	contact pressure distribution in the contact zone
P	applied contact loads
P_0	maximum contact pressure or Hertzian Peak Pressure

P_{Freq}	frequency of the applied contact loads
P_{max}	maximum applied contact loads
P_{min}	minimum applied contact loads
q	surface shear stress distribution
Q	tangential loads
Q_{max}	maximum tangential loads
Q_{min}	minimum tangential loads
r	fretting pad radius
R	stress ratio
R_1	radius of fretting pad
R_2	radius of fretting specimens
R_σ	stress ratio of axial stress
SEM	scanning electronic microscopy
S_{xx} or σ_{xx}	normal stress along x-direction
S_{xy} or σ_{xy}	shear stress on x-y plane
S_{yy} or σ_{yy}	normal stress along y-direction
u	displacement
w	specimen width
Y_0	the depth within a specimen where residual stress is zero
ε_a	total strain amplitude
ν	Poisson's ratio
θ	direction of stress in a material, observed angle of orientation
$\Delta\sigma$	axial stress range

$\Delta\tau$	shear stress range
σ	normal stresses at a given point with a specific orientation
$\sigma_{1,2}$	principal normal stresses
σ_{axial}	applied axial stress
$\sigma_c(y)$	residual compressive stress along y-direction
σ_{eff}	effective axial stress
$\sigma_t(y)$	residual tensile stress along y-direction
σ_{Freq}	frequency of the applied axial stress
σ_{max}	maximum applied axial stress
σ_{min}	minimum applied axial stress
σ_N	bulk axial stress
σ_{xx} or S_{xx}	normal stress along x-direction
$(\sigma_{xx})_{axial}$	x-direction normal stress contributed from axial load
$(\sigma_{xx})_{contact}$	x-direction normal stress contributed from contact load
$(\sigma_{xx})_{tangential}$	x-direction normal stress contributed from tangential load
σ_{xy} or S_{xy}	shear stress on x-y plane
$\sigma_x(z1)$	true stress before a layer was removed
σ_{yy} or S_{yy}	normal stress along y-direction
τ	shear stress at a given point with a specific orientation
τ_{max}	maximum shear stress at a given point

EFFECTS OF VARIABLE CONTACT LOAD ON FRETTING FATIGUE BEHAVIOR OF SHOT-PEENED AND UN-PEENED TITANIUM ALLOY

I. Introduction

1.1. Fretting Fatigue

Fretting fatigue research is the study of fatigue phenomenon under contact mechanism. For fretting fatigue, the material damage accrual is caused by localized relative motion between the components under vibratory loads and results in premature crack initiation and failure, causing fatigue life reduction. The United States Air Force is interested in this issue because it has been encountered on certain important structures, such as turbine engine parts. Fretting fatigue usually occurs at the interface of components such as the turbine engine disk slot and blade attachment (Figure 1) and reduces the service life of components. In order to compensate the life-debit effect caused from fretting fatigue, over-conservative design adjustments are made to ensure that the safety factor of mechanical parts is at an acceptable level during their service life. However, these adjustments reduce operation performance of mechanical components and increase maintenance expenses as well. Fretting fatigue phenomenon investigation can provide a better understanding on the crack initiation mechanism and hence suggest potential scenarios that will be able to decrease maintenance cost and enhance operating efficiency for future design. A succession of extensive studies associated with fretting

fatigue have conducted by several researches to investigate the crack initiation mechanism as well as to formulate fatigue predictive parameters in an attempt to optimize the operational performance which are elaborated in Chapter II.

1.2. Shot-peening

Shot-peening is the most commonly used cold working process that involves bombarding the material surface with small, hard steel balls. This procedure causes bi-axial yielding, introducing residual compressive stress and grain distortion near the shot-peened surface accompanied by compensatory tensile stress within the interior. It is this residual compressive stress that plays a critical role in crack initiation, and crack propagation retardation under fretting fatigue condition [1]. Due to the beneficial effects introduced by shot-peening residual compressive stress near the contact surface, cracks initiated at depths between 180~250 μm instead of at the contact surface for shot-peened specimens used in this study. Moreover, fatigue life for shot-peened specimens was extended when compared with that for un-peened specimens. This leads us to point out that shot-peening can improve fatigue life, enhancing operation performance by the introduction of compressive residual stress. However, it should be mentioned that surface residual stress is only beneficial when subsequent yielding effect doesn't occur from operational applied loads in service as this may remove the compressive residual stress or even change it to a harmful tensile stress.

1.3. Purpose and Objectives

Fretting fatigue reduces fatigue life when compared with plain fatigue, inducing extensive operating cost from inspection and maintenance in a component service life. In order to reduce these expenses and improve the operating performance, comprehensive

studies are needed to analyze different variables, such as shot-peening process, fretting pad geometry, axial load frequency, elevated temperature, and environment corrosion which are addressed in Chapter II. However, most of previous studies were accomplished under constant contact load condition, and only little effort has been devoted to investigate the effect from variable contact loads under fretting fatigue condition. In reality, mechanic components of a turbine engine, such as the turbine engine disk slot and blade attachment, are operated under complicated vibratory load environment and experience both variable axial and contact loads simultaneously. A better understanding of how variable contact loads affect the fretting fatigue behavior can help engineers to better account for its effects, and, therefore, more investigations focusing on the variable contact load effects are imperative.

The primary purpose of this study is to investigate the fretting fatigue behavior under constant and variable contact loads for both shot-peened and un-peened Ti-6Al-4V alloy. In this study, four different frequencies were chosen for contact load (P), and they were 0 Hz, 2.5 Hz, 10 Hz, and 30 Hz. The higher bound of contact load was 4448 N while 2224 N was the lower bound. Although the mean stress and stress ratio for the applied axial loads were varied for each test to produce tension-tension as well as tension-compression stress conditions on the specimens, the frequency of the axial loads was fixed as 10 Hz throughout this study. A cylindrical-end shape with 50.8 mm radius was chosen as the fretting pad geometry. In addition, experiments were conducted with both shot-peened and un-peened specimens so that comprehensive comparisons could be made based on contact load conditions and the specimen surface treatment. It should be mentioned that shot-peening process introduces residual compressive stress on the shot-

peened surface and creates tensile stresses within the interior of shot-peened specimens. Moreover, it has been reported that the residual stress is subject to relaxation during fretting fatigue cycles. Original residual stress along with stress relaxation phenomenon modifies contact stress profiles and causes different operating performance in fretting fatigue life.

The emphasis of this study was laid down on the correlation between variable contact load conditions and fretting fatigue mechanisms in terms of fatigue life, crack initiation location, and crack initiation orientation. Fretting fatigue mechanisms under variable contact loads were also compared with those from constant contact load tests. In addition, effects of shot-peening process were also investigated under constant and variable contact load conditions. Shot-peening induced residual stress was determined with different stress relaxation rates to investigate fatigue predictive parameters such as the stress range, effective stress, and modified shear stress range for their effectiveness in predicting fretting fatigue behavior in terms of fatigue life, crack initiation location, and crack initiation orientation.

1.4. Methodology

Due to the complexity introduced by real component geometry and load bearing condition of turbine engines, replicating the exact configuration as a turbine engine will make studies complex, time consuming, and expensive. Therefore, a simplified cylinder-on-flat model (Figure 2) was adopted as the experimental setup in this study for the sake of investigating fretting fatigue behavior. A bi-axial servo-hydraulic machine was used to apply desired load conditions and record experimental results. The fatigue life diagrams, i.e. S-N curves were developed to investigate the effect introduced by variable contact

loads. Optical and scanning electron microscopy (SEM) was performed to examine the fracture surface, contact half-width, crack initiation location, crack initiation orientation, and so forth. Finite element analysis (FEA) was conducted to compute local fretting variables such as stress, strain, and displacement. The X-ray diffraction technique was applied to measure the shot-peening induced residual stress, which accompanied with stress relaxation was superimposed into FEA stress solutions for the development of fatigue predictive parameters. The stress evolution, stress concentration, contact half-width, and other variables were also analyzed under constant and variable contact loads at different load steps. In addition, several fatigue predictive parameters, such as the stress range, effective stress, and modified shear stress range were evaluated for their effectiveness on fretting fatigue predictions in terms of fatigue life, crack initiation location, and crack initiation orientation.

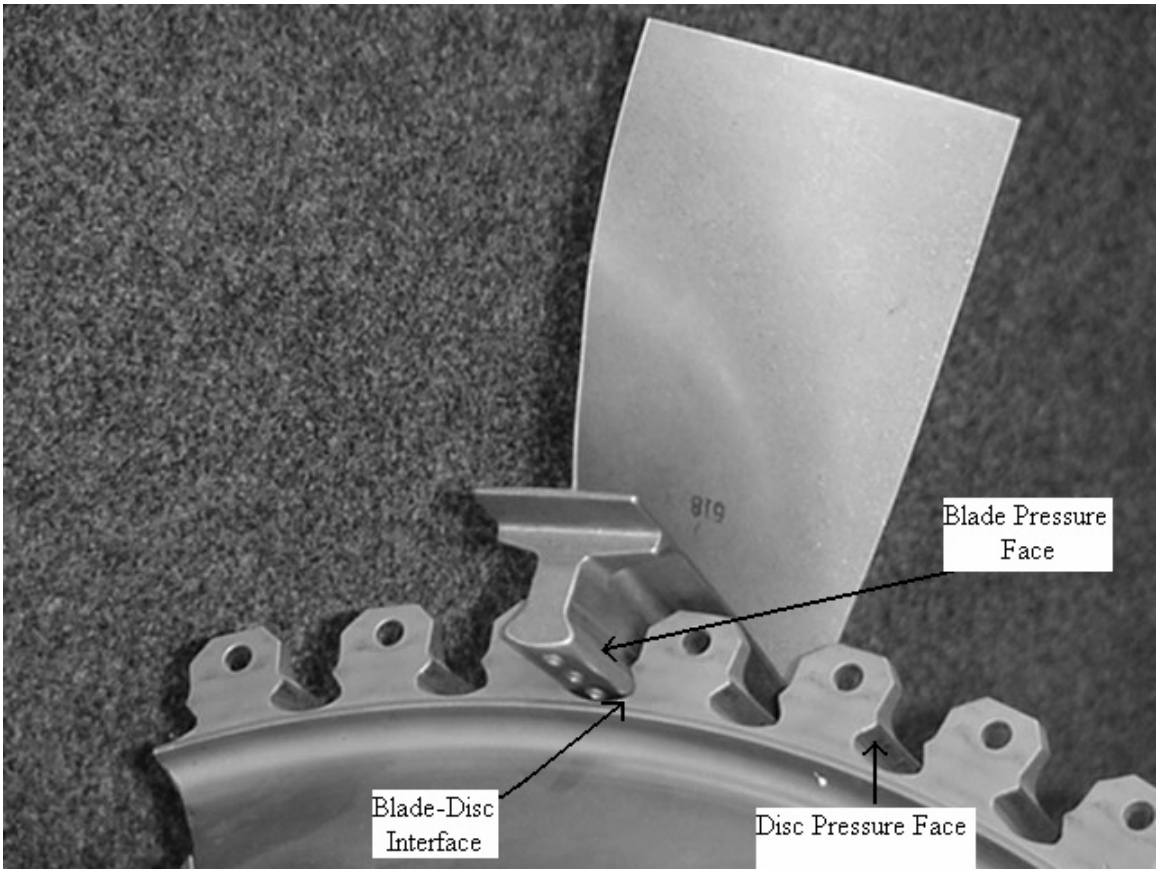

Figure 1. Blade/Disc Dovetail Joint in Turbine Engine.

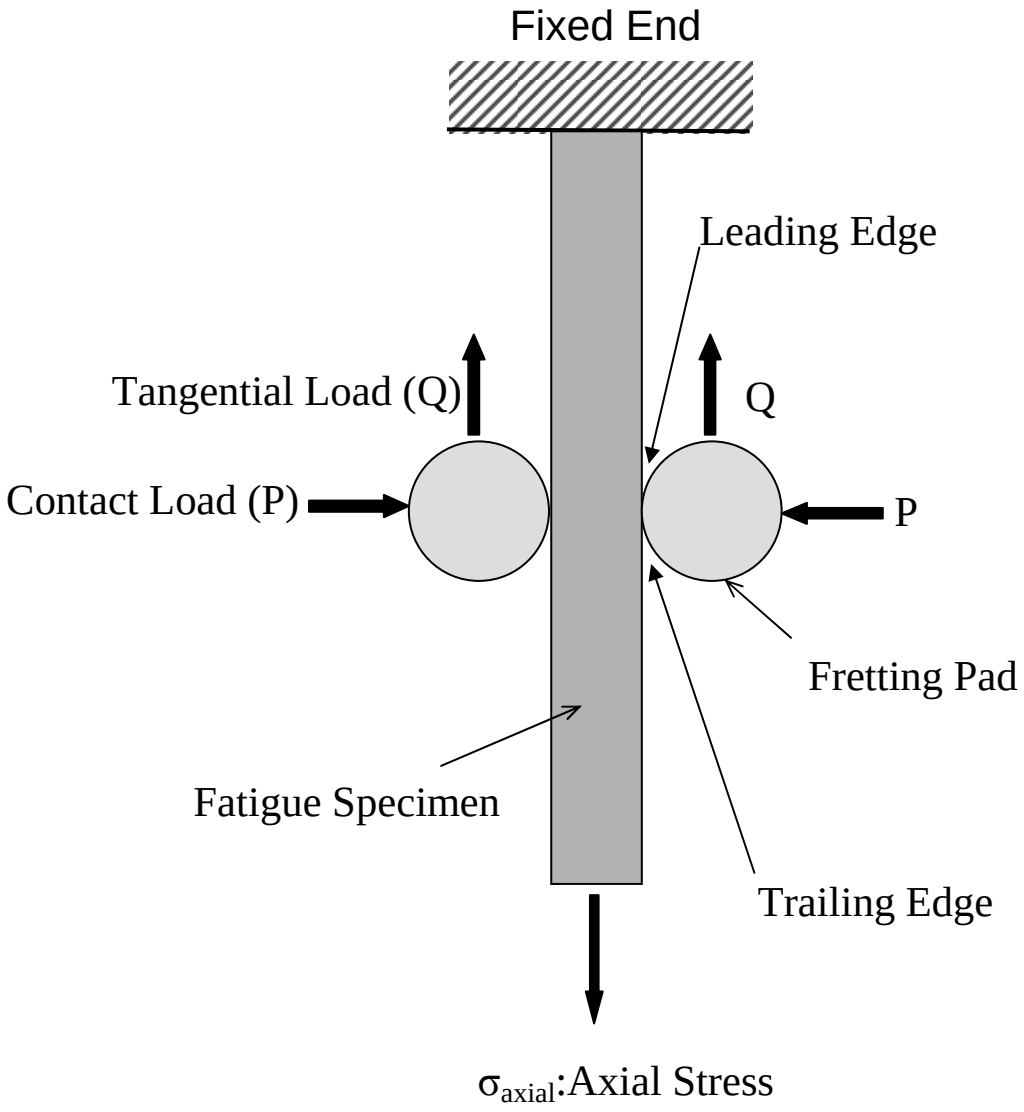

Figure 2: Simplified Fretting Fatigue Configuration

II. Background

Due to the significance of fretting fatigue, an extensive number of studies have been conducted for the sake of better understanding fretting fatigue mechanisms. This chapter addresses contact mechanics and the associated analytical solutions in terms of contact width, Hertzian peak pressure, and so forth. Effects from shot-peening process are also presented. Fretting fatigue contributing factors, such as the coefficient of friction, fretting pad geometry, axial load frequency, contact pressure, elevated temperature, and environment corrosion are discussed as well. Investigations on fatigue parameters are also looked into and summarized in this chapter.

2.1. Contact Mechanics

In this study, a cylindrical-end body in contact with a flat body setup is adopted as the fretting fatigue configuration. Contact mechanics and analytical solutions associated with this configuration are discussed in detail in this section. A diagram of two bodies in contact under fretting fatigue loads is shown in Figure 3. Here, A represents the cross sectional area of the fretting specimen, σ_{axial} represents the applied axial stress, P is the applied contact load, Q is the reacted tangential load, d is the thickness of a specimen, b indicates half thickness of a specimen, and a represents the contact half width. The constant radius of fretting pads in the cross sectional plane is r, and the radius of the fretting fatigue specimen is infinite in the cross sectional plane, that is, a flat surface of specimens is used in this study. For analytical solutions, an assumption was made at the beginning that these two contact bodies have infinite boundaries, and analytical equations were formulated based on the displacement relationships of the two contact bodies.

Assume that given points in the contact zone are displaced in the y-direction by $v_1(x)$-$v_2(x)$ and invoke the displacement relationship developed by Hills and Nowell [1,4]; we obtained the relationships in the contact region:

$$\frac{1}{A^*}\frac{\delta h(x)}{\delta x} = \frac{1}{\pi}\int \frac{p(\xi)}{x-\xi}\,d\xi - \beta q(x) \tag{1}$$

where $h(x)=v_1(x)-v_2(x)$ is the amount of overlap that will occur if the contacting bodies could penetrate each other freely, p is the pressure in the contact zone and q is the surface shear stress. The other parameters of equation (1) are:

$$A^* = 2\{\frac{1-\nu_1^2}{E_1} - \frac{1-\nu_2^2}{E_2}\} \tag{2}$$

$$\beta = \frac{1}{2A^*}\{\frac{1-2\nu_1}{E_1} - \frac{1-2\nu_2}{E_2}\} \tag{3}$$

where E is modulus of elasticity and ν is Poisson's ratio for the contact bodies, respectively.

If one assumes the tangential displacement to be defined by $g(x) = u_1(x)-u_2(x)$, a similar equation can be formulated as follows:

$$\frac{1}{A^*}\frac{\delta g(x)}{\delta x} = \frac{1}{\pi}\int \frac{q(\xi)}{x-\xi}\,d\xi - \beta p(x) \tag{4}$$

In this study, since the contact bodies are made of the same material, hence $\beta=0$, and equations (1) and (4) can be further simplified.

When fretting bodies are brought into contact with each other by applying a contact load, the displacement of adjoining points on the contact surface within the stick zone will be the same. Furthermore, a pressure distribution p(x,y) will be introduced by the contact load. The solution of the pressure distribution from the contact load is usually

termed Hertz solution. In order to solve the pressure distribution, two primary assumptions are made. First, the radii of both bodies are large in comparison to the contact dimension. Second, the contacting bodies have infinite boundaries. The infinite boundary assumption is commonly referred to as the half space assumption. A half space exists if one half of the specimen thickness (b= d/2) matches the requirement b/a > 10. Fellows et al. [5] found the violation of the infinite half space assumption will introduce significant deviation into analytical solutions when compared to solutions from finite element analysis.

If one idealizes the profile of contact surfaces as a parabola, a weight function can then be achieved as:

$$w(x) = \sqrt{a^2 - x^2} \tag{5}$$

where a is the contact half-width. Solving equations (4) and (5) yields:

$$p(x) = -\frac{k}{a}\sqrt{a^2 - x^2} \tag{6}$$

where k is termed the radius of curvature, $k=1/R_1+1/R_2$, where R_1 and R_2 are the radii of fretting pad and specimen, respectively. Equilibrium in the contact surface between the applied contact load and the pressure distribution can then be defined as

$$P = -\int_{-a}^{a} P(\xi)d\xi = \frac{\pi k a^2}{2A^*} \tag{7}$$

From equations (6) and (7), one can write with the following:

$$p(x) = -P_0\sqrt{1-(\frac{x}{a})^2} \tag{8}$$

where P_0 is maximum pressure (Hertzian Peak Pressure) defined as:

$$p_0 = \frac{2P}{\pi a} \tag{9}$$

Contact half-width, a, can be found from equation (7) as follows:

$$a^2 = \frac{2PA^*}{\pi k} \tag{10}$$

In this study, since the fretting specimen has a flat surface ($R_1=\infty$), equation (10) can be simplified as:

$$a = \sqrt{\frac{8PR_1}{\pi}\frac{1-\nu^2}{E}} \tag{11}$$

The axial stress resulting from the applied contact load P can be expressed in Cartesian coordinates as:

$$(\sigma_{xx})_{contact} = -p_0\{\frac{\sqrt{a^2-x^2}}{a}\} \tag{12}$$

As shown in Figure 4, after applying a contact load (P) and the accompanying tangential load (Q), there will be a stick zone in the middle portion of the contact surface and slip zones at both sides. The portion between –c and c defines stick zones whereas the portions between –a and -c as well as c and a present the slip zones. The stick zone is a portion where the adjoining contact points of the fretting bodies, the specimen and the pad, move together. On the other hand, the adjoining contact points can move freely with each other within the slip zones. The stick zone in fretting fatigue configuration is determined simplistically by the contact geometry, contact pressure and coefficient of friction. The formation of the stick zone leads to an amplification of remotely applied stresses in the vicinity of contact surface and premature crack initiation.

Shear stress distribution along the contact surface can be expressed as:

$$q(x) = \frac{C}{\sqrt{a^2 - x^2}} \tag{13}$$

where C=Q/π, Q is the total shear stress along the contact length which is obtained by integrating the shear stress distribution as:

$$Q = \frac{fp_0\pi}{2a}(a^2 - c^2) \tag{14}$$

where f is the coefficient of friction, and the stick zone size is described as:

$$\frac{c}{a} = \sqrt{1 - |\frac{Q}{fP}|} \tag{15}$$

The stress distribution cased by the tangential load in the X-direction is found as:

$$(\sigma_{xx})_{\tan gential} = 2fp_0 - \frac{2}{\pi}\int_{-a}^{a}\frac{q'(x)}{x+a}dx \tag{16}$$

where

$$q'(x) = -\frac{fp_0 c}{a}\sqrt{1 - (\frac{x-e}{c})^2} \tag{17}$$

and

$$e = \frac{\sigma a}{4fp_0} \tag{18}$$

$$\sigma = \frac{E\varepsilon_{xx}}{1-\nu^2} \tag{19}$$

where ε_{xx} is the corresponding strain induced by the axial tensile stress (σ_{axial}) under plane strain.

Total axial stress along the contact surface between the fretting specimen and the fretting pad can then be expressed as:

$$\sigma_{xx} = (\sigma_{xx})\text{contact} + (\sigma_{xx})\text{tangential} + (\sigma_{xx})\text{axial} \tag{20}$$

Chan and Lee [6] wrote a FORTRAN program named “Ruiz program” to calculate the numerical solutions required by analytical analyses for variables such as Hertzian Peak Pressure in Equation (9), contact half-width in Equation (11), σ_{xx} in Equation (20), and so forth. These solutions from both analytical equations and Ruiz program are computed to verify the finite element model used in this study in Chapter IV and to compare with experimental results in Chapter VI.

2.2. Typical Fretting Fatigue Configuration

For the sake of enhancing comprehension and understanding in fretting fatigue phenomenon, previous studies have developed and adopted a general and simplified test scheme as described in Figure 5 to isolate controlling variables and simplify analysis. In this general fretting fatigue configuration, fretting specimen and pads are presented as two mechanical components in contact with each other. Axial stress, σ_{axial}, is typically applied by a hydraulic test machine at one end of a specimen that is normally gripped at the other end. The applied axial load can be controlled to produce fatigue loads with different frequency, waveform, magnitude, and stress ratio to simulate the load conditions in demand. Simultaneously, the fretting pads are pressed against the specimen by a contact load, P, in the direction perpendicular to an applied axial load. The geometry of pads may vary in radii and shape for achieving the desired effect. In addition, contact loads can also be imposed under different combinations of magnitude, frequency, and waveform. Fretting fatigue contributing variables can be controlled by using specimens and pads made up of identical or dissimilar materials under laboratory or elevated test temperature, and so forth.

When applying axial loads and contact loads, a tangential load, also known as shear load (Q), is induced along the contact surface. This tangential load makes pads and specimens move relative to each other in a partial slip condition instead of gross slippage. The tangential load is determined as half of the difference between the applied axial load and the load measured at the gripped end of specimens. Fretting fatigue creates a contact region along the contact surface of a pad and specimen. Customarily, the edge of the contact region near the fixed end is called leading edge, and the edge of the contact region near the applied axial loads is defined as trailing edge. Contact half-width, a, incorporates both stick-zone (c) and partial slip zones, and the center of contact width is defined as the origin of x-direction. A similar fretting fatigue configuration, cylindrical-end pads in contact with a flat specimen, was used in this study, and the detailed experiment setup is elaborated in Chapter III.

2.3. Shot-peening Surface Treatment

2.3.1. Introduction to Shot-peening

Fretting fatigue can damage microstructure on the highly stressed contact surface by introducing plastic deformation, work hardening, and ageing effect and, therefore, impairs material fatigue resistance, reducing fatigue life. On the other hand, surface treatment such as shot-peening is widely known to improve material strength under fatigue conditions and is commonly used in aeronautical industries.

Shot-peening process uses high velocity spherical projectiles, called shot, such as iron, glass, or ceramic beads to bombard material surface, creating plastically deformed surface layer constrained by un-deformed interior underneath as seen in Figure 6. By this mean, shot-peening introduces a biaxial residual stress profile on the peened material,

which is compressive near the peened surface and tensile far away the peened surface as presented in Figure 7. Besides, Shot-peening changes the surface roughness, grain size, and work hardening on the peened surface.

It is the shot-peening induced compressive stress that plays a critical role in crack initiation/propagation retardation mechanism under plain and fretting fatigue conditions. This residual compressive stress can not only close pre-exist crack tip at the early stage of fatigue life but can also reduce crack propagation rate by compensating detrimental tensile stress applied by global loads [7]. However, it must be noticed that too severe of a compressive residual stress may result in a very brittle material, which is highly sensitive in the presence of a notch, and turn beneficial into detrimental effects during fatigue life. In order to optimize shot-peening induced fatigue strength, shot-peening controlling parameters should be manipulated carefully including shot-peening media, shot velocity or pressure, angle of impingement, shot hardness and shape, intensity and percentage of surface coverage.

In this study, both shot-peened and un-peened specimens were used to investigate fretting fatigue behavior under constant and variable contact load effects. Also, shot-peening induced residual stress was superimposed into results from finite element analysis in order to evaluate the effectiveness of fatigue predictive parameters to be discussed in Chapter III, V, and IV.

2.3.2. Shot-peening Intensity and Surface Coverage

As mentioned in the previous section, shot-peening uses shots to strike a material surface, which acts like a tiny peening hammer punching into a material surface. The impact creates local material yielding on the struck surface constrained by the elastic

substance underneath. The local yielding introduces compressive stress on the surface balanced by tensile stress within the interior material.

Under fatigue conditions, material fatigue strength is highly susceptible to the depth of residual compressive stress as well as residual stress gradient induced by shot-peening. In order to optimize the beneficial effect from shot-peening, shot-peening parameters must be controlled carefully. Martinez [**2**] conducted a survey to investigate the effects on residual stress contributed from two control parameters, shot-peening intensity and surface coverage, to be discussed in the remainder of this section.

The shot-peening intensity, known as Almen intensity, is a measurement of shot-peening stream energy and is directly related to the induced residual stress magnification and distribution. Using larger beads and/or increasing shot velocity of shot stream can increase Almen intensity. On the other hand, surface coverage is defined as the ratio of a shot-peened surface area to the whole specimen surface area. Due to the fact that residual compressive stress does not exist in the un-peened portion of specimen surface, crack initiation and stress corrosion can not be retarded in un-peened area, and thus complete (100 %) coverage of shot-peened surface is crucial for improving specimen fatigue resistance [2]. Mattson et al [8] investigated the relation between surface coverage and fatigue life and found that once 100% saturation coverage was achieved, further projection didn't have significance in fatigue life determination.

Martinez [2] investigated fretting fatigue behavior under shot-peening specification 4, 7, and 10 Almen intensity with 100% or 400% surface coverage. She showed the residual stress on a peened surface was not significantly different under different Almen and surface coverage. Nevertheless, underneath the peened surface, a

significant difference up to 600 MPa in the residual stress profile was observed. Moreover, the greater the peening intensity the greater compressive depth and magnitude were for specimens under different Almen intensity with 100% coverage. Additionally, increasing surface coverage from 100% to 400%, while keeping the same Almen intensity, didn't provide significant deviation in residual stress distribution. It was also shown that the crack initiation location occurred on the peened surface under 4A and 7A, but in the interior under 10A due to the greater residual tensile stress magnitude induced by a 10A shot-peening process. In this study, all shot-peened specimens were peened under 7 Almen intensity with 100% surface coverage to investigate the effects of variable contact loads under fretting fatigue configuration.

2.3.3. Determination of Residual Stress

Shot-peening process introduces residual compressive stress near the peened surface, and compensatory residual tensile stress is formed at the same time within the interior of the peened specimen in order to keep the requirement of equilibrium.

The standard and primary technique for residual stress determination in the last decades is X-ray diffraction. This technique determines residual stress by measuring residual stress-induced inter-planar (strain) changes. Adopting this approach, material must be removed in layers until desired depths are reached in order to measure the needed residual stress on these new exposed surfaces. However, layer removal changes the original residual stress remaining in the material underneath and, hence, introduces variation into measurement accuracy. In order to account for the deviation induced by layer removal, Sikarsie [2] developed a formula, which works well with shallow depth removal in a flat plate geometry, to compensate the undesirable effect expressed as:

$$\sigma_x(z_1) = \sigma_{xobs}(z_1) + 2\int_{z1}^{H} \frac{\sigma_{xobs}(z)}{z}\,dz - 6z_1\int_{z1}^{H} \frac{\sigma_{xobs(z)}}{z^2}\,dz \tag{21}$$

where H is the original thickness of the plate, z_1 is the depth from the lower surface to the uncovered depth of interest, $\sigma_x(z_1)$ is the true stress before a layer was removed, and $\sigma_{xobs}(z_1)$ represents the measured stress value at that depth. The correction in stress at z_1 is the difference between the true and measured value.

As mentioned above, X-ray diffraction technique requires removing layers from specimens being measured in order to obtain the residual stress far away from the peened surface, hence introducing deviation in measurement results. Additionally, Equation (21) is most effective on the correction for layer removal in the vicinity of a peened surface. In order to estimate and rebuild residual stress profile away from the peened surface, Namjoshi et al. [9] proposed using an alternative numerical approach to depict residual stress profile as follows:

$$\int_0^{Y_0} \sigma_c(y)dy = \int_{Y_0}^{d/2} \sigma_t(y)dy \tag{22}$$

$$\left(\frac{d\sigma_c}{dy}\right)_{-Y_0} = \left(\frac{d\sigma_t}{dy}\right)_{-Y_0} \tag{23}$$

$$[\sigma_t(y)]_{y=d/2} = 0 \tag{24}$$

$$[\sigma_t(y)]_{y=Y_0} = 0 \tag{25}$$

where $\sigma_c(y)$, $\sigma_t(y)$ are the compressive and tensile residual stresses in the specimen as a function of depth y, respectively. Y-axis is defined as the transverse direction along the thickness of the specimen, Y_0 is the depth at which the residual compressive stress is zero,

and d is the thickness of the specimen. The resulting residual tensile stress profile can then be expressed as:

$$\sigma_t(y) = \frac{pq(M+r)}{(M+r)^2 + p^2} - s; \qquad d/2 > y > Y_0 \tag{26}$$

where $M=y-Y_0$, and p, q, r, s are all constants that must be determined by solving equations (22)~(25) simultaneously while adopting this numerical approach.

Previous studies [2,13] found that shot-peening process produced spatially, directionally homogeneous stress distribution on the peened surfaces. In addition, induced residual stress tensors, σ_{xx} and σ_{yy}, are assumed biaxial, and shear stress τ_{xy} is assumed to be negligible. Previous studies [1,2,9] also showed that even specimens were shot-peened under the same specification, 7Almen with 100% surface coverage, the variation of residual stress on the peened surfaces could be observed varying from -575 to -793 MPa, and this variation reduced to a relatively smaller scale at a depth higher than 76 μm. Determining residual stress profiles are critical for analyses of shot-peened specimens under fretting fatigue phenomenon because these profiles must be superimposed into stress profiles induced by applied loads to evaluate the effectiveness of critical plane based fatigue predictive parameters to be discussed in Section 2.5.

2.3.4. Residual Stress Relaxation Behavior

Under cyclic loading conditions, residual stress has been reported to be subject to relaxation. This relaxation effect reduced the improvement on material fatigue strength under fretting fatigue conditions [2,3,13]. Hauk et al. [14] addressed that residual stress can relax under the effects of alternating stress as well as thermal energy. Namjoshi et al. [9] found stress relaxation under plain fatigue conditions was as much as 80 percent, and

it occurred more rapidly under fretting fatigue conditions. Martinez et al [2,13] used specimens peened with specification of 7A±1 under 100 % surface coverage to investigate the contribution of fretting fatigue on residual stress relaxation behavior. It was shown that before a specimen failed due to fretting fatigue cycles, residual stress profile became non-uniform and anisotropic within a fretting scar on the contact surface. Moreover, stress relaxation increased with the increase of fretting fatigue cycles until a specimen failed. After failure occurred, almost 100% relaxation on residual stress was measured within the contact surface, accompanied with 0 % relaxation far away from the contact region. As a fretting region was approached, residual stress was observed under some degree of relaxation on the contact surface. Lee et al. [3,15] showed that, under fretting fatigue at laboratory temperature, the same percentage of stress relaxation was measured to occur from the contact surface throughout different depths of peened specimens.

Other researches [1,3,9,16] found that residual stress relaxation due to fretting fatigue cycles affected fatigue life and crack initiation location significantly. Larger relaxation caused more fatigue life reduction and might shift crack initiation location from a contact surface to the interior of specimens. In this study, equations (22) to (26) were used to determine residual stress profiles for peened specimens. The effects on fretting fatigue behavior as well as fatigue predictive parameters from different residual stress relaxation rate are discussed in Chapter V and IV.

2.3.5. Shot-peening Effect on Fretting Fatigue Life

Previous studies [1,2,3,9,13] showed that due to the introduction of residual compressive stress induced by shot-peening process in the substrate specimens, both

plain and fretting fatigue strength under laboratory environment was improved for shot-peened Ti-6Al-4V specimens when compared with un-peened ones. In addition, these studies also found that crack initiation locations for shot-peened specimens may occur either on the contact surface or far away from contact surface at a depth of 200-300 microns. These initiation sites were close to the location where maximum tensile residual stress existed, depending on factors among the residual stress profile gradient, the depth of compressive residual stress, microstructure crack on the contact surface, and specimen thickness. In order to get the most beneficial effects from residual compressive stresses, the depth of the compressive regime must be greater than the depth where cracks may initiate such that pre-existing crack tips could be closed, and crack initiation as well as propagation can be retarded. In other words, a method that is able to produce a residual stress with a smaller gradient and deeper residual compressive stress profile will provide a better contribution on improving fretting fatigue strength for shot-peened specimens.

Martinez et al. [2,16] found that increasing peeing intensity from 4 Almen to 10 Almen under 100% surface coverage increased fretting fatigue life dramatically for Ti-6Al-4V specimens. On the other hand, increasing surface coverage from 100% to 400%, while keeping the same Almen intensity, didn’t provide further improvement in fatigue life. That is, further projection didn’t have significant contribution once 100% saturation coverage is achieved. It was also shown that fretting fatigue life was significantly affected by the depth and magnitude of residual compressive stress.

Another benefit from the shot-peening process is helping specimens against the detrimental effects from environment corrosion; Allen [17] showed that under seawater corrosive conditions, shot-peened Ti-6Al-4V specimens were more resistant to stress

corrosion than un-peened specimens in both high and low cycle fatigue regime. On the other hand, when comparing fretting fatigue strength for shot-peened specimens, seawater corrosion reduced fatigue life as compared to dry conditions.

2.4. Fretting Fatigue Contributing Factors

2.4.1.Coefficient of Friction

The coefficient of friction on a contact interface is generally dependent on the applied contact loading conditions. There must be also 5,000 to 10,000 fretting fatigue cycles applied before a stabilized coefficient of friction could be measured. Afterwards, a predetermined contact load was first decided and then imposed onto the specimen by fretting pads. A monotonically increasing axial load was applied slowly to one end of the specimen, while the other end was keeping free, until gross slip between a specimen and pads eventually occurred. At the same time, the resulting tangential load was monitored and recorded continuously. The static coefficient of friction could then be determined by the following formula:

$$f = Q/P \tag{27}$$

where f is the static coefficient of friction, Q is the tangential load, and P is the applied contact load. The experimental stabilized static coefficient of friction was determined to be ranging among 0.37~0.46 [18] for un-peened Ti-6Al-4V specimens and 0.33~0.46 for shot-peened Ti-6Al-4V specimens [1,9]. It can be seen from these measurements that the shot-peening process didn’t alter the stabilized coefficient of friction significantly.

Hills et al. [19] postulated that the coefficient of friction may vary in magnitude based on the dynamic ratio Q/P during fretting fatigue cycles. Based on this assumption, varying coefficients of friction are needed for fretting fatigue analysis. On the other hand,

previous studies [20,21] also showed that comparing the effects induced by coefficients of friction, a variation from 0.45 to 0.7 (66% increase) in friction only caused relatively small variation on fretting fatigue variables such as 20% increase in strain range. This observation infers a practical simplification in analysis to assert the coefficient of friction as a constant, and this constant friction assumption is adopted in this study as one of the FEA input variables to be discussed in Chapter IV and VI.

Namjoshi [22] showed that for coefficients of friction changing from 0.5 to 0.8, MSSR always predicted crack orientation at about ±45˚ for a cylindrical-end pad configuration, as observed from experimental counterparts. Moreover, increasing coefficients of friction didn't affect crack initiation location prediction from MSSR parameter. It was also shown that increasing coefficients of friction from 0.5 to 0.8 (60% increase), only about 32% increase in MSSR was observed under cylindrical-end pad geometry, and average 12% increase in MSSR under flat-end pad geometry. In this study, a constant coefficient of friction, 0.5, was assigned as the material property for all tests except for these cases where $(Q/P) < 0.5$ was violated from experimental results. The friction coefficients used in this study for FEA were listed in Table 5, Chapter VI, and effects from varying coefficients of friction on contact half-width, stress distribution, and MSSR parameter are discussed in Chapter VI.

2.4.2. Contact Pad Geometry

Namjoshi [22,23,50] investigated fretting fatigue mechanism with un-peened Ti-6Al-4V specimens under influence of different contact pad geometry. These studies used cylindrical-end pad geometry with three different radii as well as two different flat-end-with-radius-edge pad geometry and showed fretting fatigue life was significantly reduced

as fretting fatigue life was compared to plain fatigue life despite pad geometry. Strong dependence between fretting fatigue life and pad geometry was also found. Increasing applied normal pressure on fretting pads decreased fretting fatigue life at a given applied axial stress. Crack initiation location was found at the contact surface near the trailing edge with orientation at about either -45˚ or +45˚ under variation of ±15˚ from the direction perpendicular to the applied axial load. In addition, there was no significant correlation between pad geometry/load conditions and crack initiation location/orientation.

2.4.3. Axial Load Frequency and Contact Pressure

Iyer et al. [18] showed that for un-peened Ti-6Al-4V specimens under fretting fatigue conditions, increasing axial load frequency from 1 Hz to 200 Hz, while keeping contact loads at a constant value of 1338 N, reduced the fretting fatigue life. Also, increasing constant contact loads from 1338 N to 3567 N reduced fretting fatigue life for tests conducted under 1 Hz axial loads. However, increasing constant contact loads from 1338 N to 3567 N with 200 Hz axial loads didn't cause apparent variation in fatigue life. In this study, a clear dominate stick zone and a narrow slip zone with little debris was observed at a larger contact load, 3567 N, while wear/ plastic deformation across the entire contact region was found in cases under a lower contact load, 1335 N. The crack initiation location was found near the trailing edge in all tests on the contact surface.

In another previous study [21], finite element analysis was conducted in an attempt to explain the life reduction phenomenon with increasing contact pressure. It was reported that fretting fatigue loading results in an amplified stress range in the vicinity of contact region due to the local build-up of compressive stresses upon loading and

unloading. Furthermore, the decrease of fretting fatigue life with increasing contact pressure can be related to the increase in the local stress range amplification along, without any regard to the increase in the local shear stress or slip amplitude.

Jutte [25] conducted fretting fatigue test using un-peened Ti-6Al-4V specimens under both unidirectional shear and bi-directional shear configuration with 20 Hz axial load. He found that fatigue life was reduced for tests with increasing contact loads under unidirectional shear tests. Additionally, fretting fatigue life with variable contact loads was observed less than fatigue life for tests with equivalent higher or lower constant contact loads under unidirectional shear tests. Nevertheless, it was also noticed that the fatigue life reduction due to increasing constant and variable contact loads was much less significant under bi-directional shear tests as compared to unidirectional shear cases. Fatigue life reduction was observed less distinguishable for tests with variable contact loads at higher magnitude under bi-directional shear tests. In Jutte's study, crack initiation location was found near the trailing edge on contact surface, and crack initiation orientation was about -50˚.

2.4.4. Elevated temperature

Lee et al. [3,15] investigated shot-peened Ti-6Al-4V specimens under influence of temperature at 25˚C, 100˚C, and 260˚ C. It was shown that shot-peening increased fretting fatigue life under room temperature in comparison with un-peened specimens, but no significant improvement was observed at 260˚C. That is, no beneficial effect from shot-peening was observed at 260˚. For un-peened specimens, on the other hand, there was no effect on fretting fatigue life from rising temperature up to 260˚. For all the tests, multiple-crack initiation pattern was observed, and cracks always initiated at the trailing

edge on the contact surface. In their study, most of the scar surface was basically covered by debris/oxides, and no noticeable effect on changing the coefficient of friction was observed.

Stress relaxation phenomenon a little bit away from the contact region was observed for all specimens that failed at 25˚C, 100˚C and 260˚C. In addition, higher temperature as well as longer exposure time induced larger stress relaxation. For specimens tested at 25˚C, approximately 31% residual stress relaxation was observed a little bit away from the contact region, and 62% relaxation was measured for specimens under fretting tests at 260˚C. In addition, stress relaxation in the interior of specimens was determined using X-ray diffraction to be almost the same with relaxation rate measured on the surface for both 25˚C and 260˚C conditions. Lee postulated that approximately 30% of residual stress occurred due to the fretting mechanistic mechanism at 25˚C, and an additional 30% relaxation was due to exposing shot-peened specimens to elevated temperature. Furthermore, stress relaxation due to elevated temperature and fretting loads could be treated as independent processes, and total stress relaxation could be linearly superimposed from fretting mechanistic effect and elevated temperature effect, respectively. In these studies, contact loads were found to have a relatively less effect on stress relaxation mechanism when compared to elevated temperature and applied axial stress.

Previous research [3] also showed that microscopic damage on contact surface and residual stress relaxation caused cracks initiated on the contact surface instead of within the interior of specimens. However, it should be mentioned that in addition to residual stress relaxation, the thickness of specimens and shot-peening intensity are other

important factors to determine a crack initiation location because the residual stress profile and gradient are highly affected by these factors. Under thin specimens or higher shot-peeing intensity, due to the higher residual tensile stress profile and gradient within the specimen, crack initiation location might be shifted from the contact surface into the interior of a peened specimen as seen from previous studies [2,9] .

2.4.5. Environment Corrosion

Due to the synthesized co-ordination introduced by mechanical and chemical actions on disrupt surface films, fretting components in a corrosive environment, compared to laboratory dry conditions, was subjected to exposing the underlying metal to corrosive agents and, therefore, are greatly influenced on crack initiation and propagation results. It is known that when components are subjected to fretting fatigue conditions, the surface oxide film is damaged and material corrosive resistance is reduced. As a result, the fatigue resistance strength of substrate titanium alloy is degraded, and the alloy becomes more susceptible to the attacks from both fretting mechanistic mechanisms and environmental corrosion.

When fretting fatigue occurs in a corrosive environment, electrochemical reactions occur to accelerate crack propagation. Hydrogen, at least partially, is considered to be responsible for increasing propagation of the crack tip. On the other hand, a material's susceptibility to hydrogen induced cracking is mainly dependent on its microstructure. Waterhouse and Dutta [10] found fretting fatigue life under 1% NaCl solution corrosion will be reduced at higher alternating stresses but improved at lower stress regime when compared to tests under dry conditions. Wharton and Waterhouse [11] then made a hypothesis trying to explain this phenomenon; that is, at higher stresses,

environment corrosion increases crack propagation, resulting in a reduced fatigue life, but the protective corrosive debris which remained on the fretting contact surface under lower stresses can retard crack initiation and improve fatigue life. Hoeppner et al. [12] conducted fretting fatigue tests for Ti-6Al-4V alloy in laboratory air, distilled water, and 3.5% NaCl solution. A greater reduction on fatigue life in 3.5% NaCl solution than in distilled water or air was found.

Lietch [29] conducted environment corrosive fretting fatigue tests using un-peened Ti-6Al-4V specimens with synthesized sea water. Lietch found that, for un-peened specimens under dry and seawater conditions, seawater corrosion fretting fatigue life is reduced under low cycle fatigue but improved under high cycle fatigue which was consistent to the hypothesis mentioned above [11]. He also showed that fretting crack initiated at the trailing edge on the contact surface among his tests. From his experimental and FEA results, applied stress range and MSSR could be conservatively used to predict seawater corrosion fretting fatigue life from dry fatigue life data under the high cycle fatigue regime for un-peened Ti-6Al-4V specimens. Later on, Allen [17] conducted seawater corrosion fretting fatigue tests using shot-peened Ti-6Al-4V specimens and showed crack initiated near the trailing edge on the contact surface just as observed from un-peened specimens mentioned above. In addition, he also found that in both high and low cycle fatigue regime using shot-peened specimens, seawater corrosion fretting fatigue life was reduced when compared to fretting fatigue life under dry conditions.

2.5. Fatigue Parameters

In plain fatigue, crack initiation models and predictive parameters are developed on the basis of stress or strain history of the plain fatigue configuration. These techniques

can be extended to fretting fatigue data. Recent attention has been drawn to the use of multiaxial fatigue parameters such as a critical plane approach to describe fretting fatigue behavior. Critical plane fatigue parameters were generated based on the maximum damage plane which is formulated during the fatigue.

The fatigue life of mechanic components under fretting fatigue conditions has been demonstrated to be significantly reduced as compared to fatigue life under plain fatigue conditions [1,20,25]. Fretting fatigue is a condition associated with high cycle fatigue (HCF), where a large fraction of fatigue life is spent in crack nucleation and growth to a detectable size while only a very small fraction of life is spent in the crack propagation from detectable size to a critical size. Therefore, unlike using damage tolerant approach for predicting fatigue life under low cycle fatigue regime, an alternative approach is needed to predict HCF crack initiation behavior.

2.5.1. Plain Fatigue Techniques

Coffin [30] and Manson [31] showed that in low cycle fatigue regime, the relationship of fatigue life can be expressed as follows:

$$\left(\frac{\Delta\varepsilon}{2}\right)_p = \varepsilon_f^{'}(2N_f)^{c'} \tag{28}$$

where $(\Delta\varepsilon/2)_p$ is the plastic strain amplitude, ε_f' is the fatigue ductility coefficient, N_f is the number of strain reversals to failure (1/2 cycle =1 reversal) and c' is the fatigue ductility exponent.

Basquin [32] also proposed that stress vs. fatigue life relationship can be correlated as follows:

$$\left(\frac{\Delta\varepsilon}{2}\right)_e = \frac{\sigma_f'}{E}(2N_f)^{b'} \tag{29}$$

where $(\Delta\varepsilon/2)_e$ is the elastic strain amplitude, σ_f' is the fatigue strength coefficient, E is modulus of elasticity, N_f is the number of strain reversals to failure (1/2 cycle =1 reversal) and b' is the fatigue strength exponent.

The strain life equation can then be obtained by combining equations (28) and (29) as follows [20]:

$$\varepsilon_a = \frac{\sigma_f'}{E}(2N_i)^{b'} + \varepsilon_f'(2N_i)^{c'}$$

where ε_a is total strain amplitude, N_i is the cycles to crack initiation. It must be noted that the strain life equation only applies under constant strain ratio conditions but does not hold for different strain ratios.

The Walker shift formula [33] which can be used to collapse data from different strain ratios onto a single curve can be written as:

$$\varepsilon_{\max,R_\varepsilon} = \varepsilon_{\max}(1-R_\varepsilon)^m \tag{30}$$

where $\varepsilon_{max,R\varepsilon}$ represents the maximum strain corrected for the strain ratio, ε_{max} is the maximum strain, R_ε is the strain ratio ($R_\varepsilon=\varepsilon_{min}/\varepsilon_{max}$), and m is the material fitting parameter that was chosen to collapse plain fatigue crack initiation data at different strain ratios. Lykins [20] showed this parameter could predict number to cycles to crack initiation and crack initiation location along a contact surface very well, but not for crack initiation orientation prediction.

Socie [34] showed that maximum principal strain could be used as a fatigue parameter for multiaxial plain fatigue loading as follows:

$$\varepsilon_{1,R1} = \varepsilon 1,_{\max} (1 - R_1)^m \quad (31)$$

where $\varepsilon_{1,R1}$ is maximum principal strain, $\varepsilon_{1,max}$ is maximum principal strain, and R_1 is principal strain ratio. Lykins [20] found this parameter was not in good agreement with the number of cycles to crack initiation and initial crack orientation from experimental results. Nishioka and Hirokawa [35,36] showed Equation (31) could be used as a fatigue parameter for crack initiation location prediction.

2.5.2. Stress Range and Effective Stress

The reality of fretting fatigue conditions is under effect from local interfacial mechanistic parameters such as peak contact pressure, local cyclic bulk stress, local cyclic shear stress, slip amplitude, and contact semi-width [37]. However, predictive parameters based on global boundary conditions, i.e. contact load, tangential load, and nominal (far field) stresses are still favored in some fields because global boundary conditions are more readily controlled in experiments and are the most obvious variables in a practical situation. Consequently, predictive models relating global mechanistic variables are most desirable in terms of applicability, and two such parameters, stress range and effective stress, are discussed in the remainder of this section.

Stress range for applied axial load can be described as:

$$\Delta\sigma = \sigma_{\max} - \sigma_{\min} \quad (32)$$

Equation (32) doesn't include the effect from mean stress or stress ratio, which were well documented in fatigue literature to be relevant to fatigue strength. Namjoshi et al. [9] proposed an alternative method using effective stress to account for the effects from stress ratio as well as residual stress as follows:

$$\sigma_{eff} = (\sigma_{\max} + \sigma_{residual}^{tensile})(1 - \frac{\sigma_{\min} + \sigma_{residual}^{tensile}}{\sigma_{\max} + \sigma_{residual}^{tensile}})^{m} \quad (33)$$

where σ_{eff} is the effective stress taking into account the effect from stress ratio and residual stress, and m was found to be 0.45 by Lykins [20]. Equation (33) takes the stress ratio and mean stress effects into account when compared to Equation (32). In addition, this equation can also incorporate residual stress induced by shot-peening procedure into consideration.

When evaluating effectiveness of Equation (33) for un-peened Ti-6Al-4V specimens in fatigue life prediction under fretting fatigue conditions, Mall et al. [41,50] found this equation could only collapse fretting fatigue life data into a single curve well under specific pad geometries. Andrew [25] showed Equation (33) was able to collapse fretting fatigue life into a single curve under constant and variable contact load conditions. Also, Lee et al. [3] noticed Equation (33) worked well in fretting fatigue life prediction under elevated temperature up to 260˚ C. Under synthesized seawater corrosion, Lietch [29] found Equation (33) was able to correlate fatigue life with effective stress.

When the effectiveness of the same equation, Equation (33), was evaluated in terms of σ_{effc}-N_f curve for shot-peened Ti-6Al-4V specimens under fretting fatigue conditions, Yeksel [1] found this equation is effective in fatigue life prediction for tests conducted under applied axial loads using 5 Hz, 10 Hz and 200 Hz frequencies. Namjoshi et al. [9] found that when induced residual stress was taken into account, Equation (33) was in good agreement with fatigue life between plain and fretting fatigue conditions using shot-peened specimens. Under elevated temperature, Lee et al. [3] showed effective stress was able to predict fatigue life at 25˚C and 260˚C, respectively. Additionally, Allen

[17] noticed that when effective stress was applied, fatigue life data could be plotted within a narrow scatter.

Another phenomenon observed by Namjoshi [9] was that when residual stress was considered into the stress profiles of shot-peened specimens under fretting fatigue condition, the fatigue life from shot-peened specimens matched that from un-peened specimens under plain fatigue very well. It indicated that shot-peening eliminated the life reduction effect induced by fretting fatigue to some extent.

Although Equation (32) and (33) worked well in correlating fatigue life with global load conditions under certain circumstance, it should be noted that these equations only provide a simplistic nature on a mechanic basis. In other words, they do not include the stress concentration effect occurring at the trailing edge of contact region and multiaxial loading conditions induced by fretting fatigue. This explains why critical plane-based predictive parameters, as to be described in the subsequent sections, formulated on local stress distribution are needed.

2.5.3. Critical Plane Based Fatigue Approach

Maximum or minimum in-plane principal stresses acting at a specific point can be expressed as:

$$\sigma_{1,2} = \frac{\sigma_{xx} - \sigma_{yy}}{2} \pm \sqrt{(\frac{\sigma_{xx} - \sigma_{yy}}{2})^2 + \tau_{xy}^2} \tag{34}$$

$$\tau_{\max} = \sqrt{(\frac{\sigma_{xx} - \sigma_{yy}}{2})^2 + \tau_{xy}^2} \tag{35}$$

where σ_1 and σ_2 are principal normal stresses, and the planes on which they act are called principal planes. σ_{xx}, σ_{yy}, τ_{xy} are stress components at a local point. τ_{max} is the maximum

shear stress at a given point, and it always acts on a plane with 45^o from the orientation of principal planes.

Additionally, the critical plane is defined as the plane where a fatigue parameter has its maximum value. In order to evaluate critical plane-based fatigue parameters, local normal and shear stresses are computed as follows

$$\sigma = \frac{\sigma_{xx} + \sigma_{yy}}{2} + \frac{\sigma_{xx} - \sigma_{yy}}{2} \cos(2\theta) + \tau_{xy} \cos(2\theta) \tag{36}$$

$$\tau = -\frac{\sigma_{xx} - \sigma_{yy}}{2} \sin(2\theta) + \tau_{xy} \cos(2\theta) \tag{37}$$

where θ is evaluated from -90^o to $+90^o$. A good critical plane fatigue parameter formulated from Equations (36) and (37) should be able to predict fatigue life, crack initiation location, and crack initiation orientation. These aforementioned requirements will be adopted to examine the validity of fatigue parameters to be discussed in subsequent sections.

2.5.4. Smith-Watson-Topper Parameter (SWT)

Smith-Watson-Toper [38] proposed a fatigue parameter as follows

$$SWT = \frac{\left(\sigma_f^{'}\right)^2}{E} * \left(2N_i\right)^{2b'} + \sigma_f^{'} \varepsilon_f^{'} \left(2N_i\right)^{b'+c'} \tag{38}$$

where $\sigma_f^{'}$ is fatigue strength coefficient, b_f' is fatigue strength exponent, ε_f'is fatigue ductility coefficient, c' is fatigue ductility exponent, E is the elasticity modulus, and N_i is cycles to crack initiation. This equation is widely known as Smith-Watson-Topper (SWT) parameter.

Szolwinski and Farris [39] made modifications to SWT parameter using critical plane approach as follows:

$$SWT = \sigma_{\max} \varepsilon_a \quad or \quad \max(\sigma_{\max} \varepsilon_a) \tag{39}$$

where σ_{max} is the stress normal to a critical plane, and ε_a is the normal strain amplitude to a critical plane. This parameter asserts crack initiation occurs on the plane where the product of σ_{max} and ε_a is maximal. Using the computed local stress and strain from finite element analysis of the fretting fatigue experiments, this parameter was calculated at all planes ranging from $-90^o \leq \theta \leq +90^o$, which provided this parameter's maximum value.

Previous studies [39,40,41,50] found SWT parameter, for un-peened specimens, was effective in predicting the number of cycles to crack initiation and crack initiation location with strong dependence on pad geometry. However, it didn't provide good agreement with crack initiation orientation. In addition, Neu et al. [40] also found that maximum shear strain amplitude did not coincide with crack initiation location under fretting fatigue conditions for un-peened specimens as it showed under plain fatigue tests. For shot-peened specimens, Yeksel et al. [1] found this parameter was effective in crack initiation location prediction but failed in predicting either fatigue life or crack initiation orientation.

2.5.5. Shear Stress Range Parameter (SSR)

SSR parameter considers only maximum and minimum shear stress on the critical plane. To compute this parameter, the shear stress was calculated at all points along all planes ranging from $-90^o \leq \theta \leq 90^o$ from the state of stress (σ_{xx}, σ_{yy}, τ_{xy}) computed from FEA by applying the following equation:

$$\tau = -\frac{\sigma_{xx} - \sigma_{yy}}{2} \sin 2\theta + \tau_{xy} \cos 2\theta \tag{40}$$

Then SSR, $\Delta\tau = \tau_{max} - \tau_{min}$ was computed at all planes and at all points in the contact region, where $\tau_{max} - \tau_{min}$ are shear stresses due to the applied maximum and minimum axial load, respectively. Since the mean stress or stress ratio also affect fretting fatigue behavior, this effect on the critical plane was accounted by incorporating a technique proposed by Walker [42]. Thus SSR parameter is expressed as:

$$(SSR = \Delta\tau_{crit}) = \tau_{\max}(1 - R_{\tau})^{m} \tag{41}$$

where τ_{max} and R_{τ} are the maximum shear stress and the shear stress ratio (τ_{min} / τ_{max}) at the critical plane, respectively, and m is a fitting parameter determined as 0.45 from a previous study [43].

Mall et al. [41,50] showed SSR, for un-peened specimens with different pad geometry, was useful in conjunction fretting fatigue life with plain fatigue life. In addition, this parameter can also correlate crack initiation location and orientation with experimental observations very well. On the other hand, for shot-peened specimens, Yeksel et al. [1] showed that under fretting fatigue conditions, this parameter is only effective in crack initiation orientation prediction but failed in predicting both fatigue life and crack initiation location.

2.5.6. Findley Parameter (FP)

The crack initiation mechanism in multiaxial loading fatigue conditions should be influenced by both normal and shear stresses. Since SSR only accounts for the effect from shear stress, another multiaxial fatigue parameter involved the effect from normal stress on a critical plane in addition to shear stress amplitude can be found in Findley's study [44] as follows

$$FP = \tau_a + k\sigma_{\max} \tag{42}$$

where k is an influence factor determined to be 0.35 from plain fatigue data [50], and τ_a is stress amplitude defined as $\tau_a = (\tau_{max} - \tau_{min})/2$. FP was calculated at all planes ranging from $-90^o \leq \theta \leq +90^o$ from computed stresses and strains obtained from finite element analysis. These calculations provided the critical plane , where this parameter is the maximum.

Mall et al. [41,50] found that for un-peened specimens with different geometry pads under fretting fatigue conditions, FP could predict crack initiation location well but was not able to predict fretting fatigue life from plain fatigue data. In addition, the predicted crack orientations were different from experimental observations. For shot-peened specimens under fretting fatigue conditions, Yeksel et al. [1] found this parameter was most effective in crack initiation location prediction but failed to predict fatigue life and crack initiation orientation.

2.5.7. Modified Shear Stress Range Parameter (MSSR)

MSSR parameter is formed by combing maximum normal stress, which generally aids in opening the crack surface, on a critical plane of maximum SSR into the original SSR as follows

$$MSSR = A\Delta\tau_{crit}^{B} + C\sigma_{\max}^{D} \tag{43}$$

where $\Delta\tau_{crit}$ is same as Equation (41), and σ_{max} is the maximum normal stress on the critical plane of the SSR parameter. A, B, C, D are fitting constants determined by curve fitting approach. These constants are determined empirically as A=0.75, B=0.5, C=0.75, and D =0.5 [50]. MSSR was calculated at all planes ranging from $-90^o \leq \theta \leq +90^o$ from computed stresses and strains obtained from finite element analysis. These calculations provided the critical plane, where this parameter is the maximum.

Previous studies [1,41,50] showed that MSSR was the only critical plane-based parameter eligible in predicting fatigue life, crack initiation location, and crack initiation orientation along with their experimental counterparts for both shot-peened and un-peened Ti-6Al-4V specimens with little dependency on pad geometry under fretting fatigue conditions. Therefore, MSSR parameter was determined to be an appropriate fatigue predictive parameter while investigating crack initiation behavior of both shot-peened and un-peened Ti-6Al-4V under fretting fatigue phenomenon.

Namjoshi et al. [22] showed MSSR was able to satisfactorily characterized fretting crack initiation orientation and location independent of contact geometry for two values of coefficient of friction, 0.5 and 0.8. Additionally, increasing coefficients of friction from 0.5 to 0.8 (60% increase) only caused an average 32% increase in MSSR parameter under cylindrical-end pad geometry. Nevertheless, MSSR satisfactorily predicted fatigue life for a given coefficient of friction, respectively. Lietch [29] found MSSR could be used in fretting fatigue life prediction for un-peened Ti-6Al-4V specimens under synthetic seawater corrosion. Lee et al. [3] observed that MSSR was effective in fretting fatigue life prediction for shot-peened specimens under elevated temperature from 25˚C up to 260˚C when residual stress was imposed with stress relaxation phenomenon. Sabelkin et al. [16] showed that MSSR could predict fretting fatigue life as well as crack initiation location in agreement with experimental counterparts for specimens shot-peened under 4A, 7A, and 10A specification with 100% surface coverage.

In this study, MSSR was adopted as the fatigue parameter to be investigated in fretting fatigue behavior prediction. Further details as to how this parameter was applied in the present research as well as the analysis results are elaborated in Chapter V and VI.

2.5.8. Alternate MSSR

Jutte [25] mentioned in his study an alternative form of Equation (43) expressed as follow:

$$MSSR = A\Delta\tau_{crit}^{B} + C\left|\sigma_{\max} - \sigma_{\min}\right|^{D} \tag{44}$$

where the absolute difference between maximum and minimum normal stress , $|\sigma_{max} - \sigma_{min}|$, at a point along with the critical plane is used as an alternative term rather than the original term, σ_{max}. He also used this formula to evaluate MSSR-N_f relations on his study and showed this alternative parameter was able to collapse well for fatigue life data under constant contact loads, accompanied with larger scatter for cases under variable contact loads. Based on his study, this alternative form infers a potential application for future analysis.

2.6. Summary of Fretting Fatigue Mechanisms

2.6.1. Fretting Fatigue Life

For un-peened specimens, previous studies [9,45,46,47] have shown that fatigue life was reduced under fretting fatigue conditions when compared to plain fatigue. Strong dependence of fatigue life on geometry was also reported [22,23,50]. Iyer et al. [18,21] found that increasing contact loads from 1338 N to 3567 N reduced fatigue life under 1 Hz axial load frequency, but no significant effect was observed under 200 Hz axial load frequency. In addition, Jutte [25] applied 20 Hz axial load frequency in his fretting fatigue tests and recorded a fatigue life reduction under unidirectional shear test

configuration. However, this reduction was relatively smaller under bi-directional shear tests. For elevated temperatures from 25˚C up to 260˚C, no significance on fretting fatigue life was observed [3]. Lietch [29] investigated environmental corrosion using synthetic seawater and reported that fretting fatigue life was reduced under LCF conditions but improved under HCF load configuration due to the protective debris formed on a contact region.

For shot-peened specimens, previous researches [1,2,3,17,41] found that shot-peening improved fretting fatigue life as compared to un-peened specimens under the same fatigue conditions. In addition, Martinez [2] observed that once 100% saturation surface coverage was shot-peened, further surface coverage from 100% to 400% didn't have significance on specimen fatigue resistance. However, when shot-peening intensity increased from 4A to 10A while keeping 100% surface coverage, specimen fatigue strength was increased. Under elevated temperature, fretting fatigue strength was impaired for fretting specimens under higher temperatures [3]. Also, Allen [17] found similar beneficial effect from shot-peening process under seawater corrosion fretting fatigue configuration.

2.6.2. Crack initiation Mechanism

For un-peened specimens under fretting fatigue conditions, previous studies [20, 23,25,29,41,50] showed that the main or primary crack, which caused failure in all specimens, always initiated near the trailing edge on a contact surface. Some small secondary cracks, which did not grow enough to cause specimen failures, could also be observed. The experimentally observed primary crack initiation angle were either -45^{o} or $+45^{o}$ from a direction perpendicular to the axial loading direction with a variation of $\pm 15^{o}$

and were independent on pad geometry and load conditions. It should also be noted that because maximum shear stress range can occur on two planes, one in the positive quadrant and the other in the negative quadrant with orthogonality to each other. Thus, for each state of stress there are always two critical shear stress planes that have equal possibility for crack orientation. Nevertheless, local microstructure property variation may cause one to be more preferred than another.

Crack initiation observation showed that fretting crack initiated and propagated in intergranular/transgranular manners; that is, grain boundaries were not the preferred location or direction for crack initiation and propagation under fretting fatigue conditions. Furthermore, fretting crack initiation and propagation behavior is independent of the fretting pad geometry and fretting load conditions.

Previous researchers [1,9] also found that, for shot-peened specimens with crack initiation location at the contact surface, fretting crack initiation and propagation behavior presented a similar pattern to that observed from un-peened specimens. The primary crack initiation angle were also either -45^{o} or $+45^{o}$ from a direction perpendicular to the axial load direction with a variation of $\pm 15^{o}$, and crack initiated near the trailing edge. However, even though the primary crack always occurred near the trailing edge of a contact region, the depths for crack initiation could vary from the contact surface to some depth within the specimen, where residual tensile stress exists. That is, the onset sites of crack initiation were susceptible to the specimen thickness, residual stress gradient, and shot-peening intensity [1,2,3,9,15]. From the investigations of fatigue parameters in Section 2.5, the fretting fatigue crack mechanism in titanium alloy is dominated by the combination of shear and normal stress on the critical plane.

2.7. Summary

The review of fretting fatigue literature can be summarized in the following. Fretting fatigue occurs between two contact components under relative motion and reduces fatigue life when compared with plain fatigue. Shot-peening, on the other hand, improves material fatigue strength. In order to better understand fretting fatigue mechanisms, analytical solutions have been developed and comprehensive researches have been conducted to analyze different contributing variables, such as shot-peening process, the coefficient of friction, fretting pad geometry, axial load frequency, elevated temperature, and environment corrosion. Predictive parameters using both plain fatigue technique and critical plane-based approach were also investigated for the effectiveness in fretting fatigue mechanism predictions. However, most of the previous studies were accomplished using constant contact load with alternating axial stress configuration. So far, only little effort has been devoted on the investigation of effects from variable contact loads. However, in a real turbine engine application, components are subjected to both vibratory axial and contact stresses during operation. For the sake of better understanding the fretting fatigue phenomenon in a real application, the primary object of this study was to investigate fretting fatigue behavior under constant and variable contact load conditions using both shot-peened and un-peened specimens made up of Ti-6Al-4V alloy.

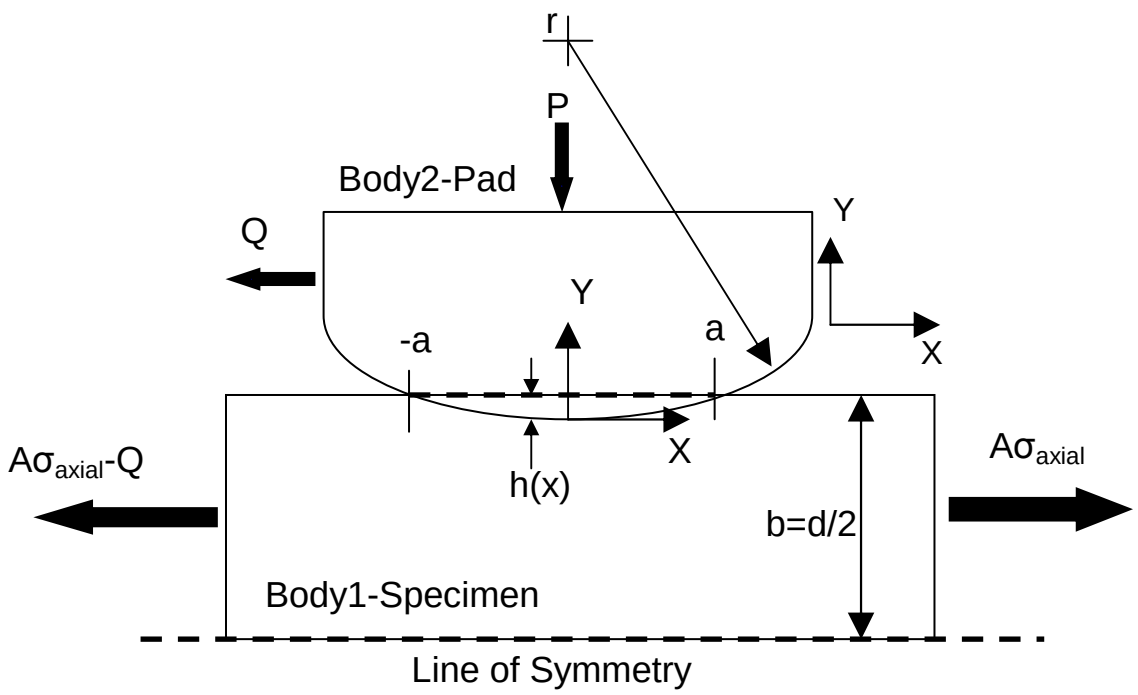

Figure 3. Free Body Diagram of Two Bodies under Fretting Fatigue Loads

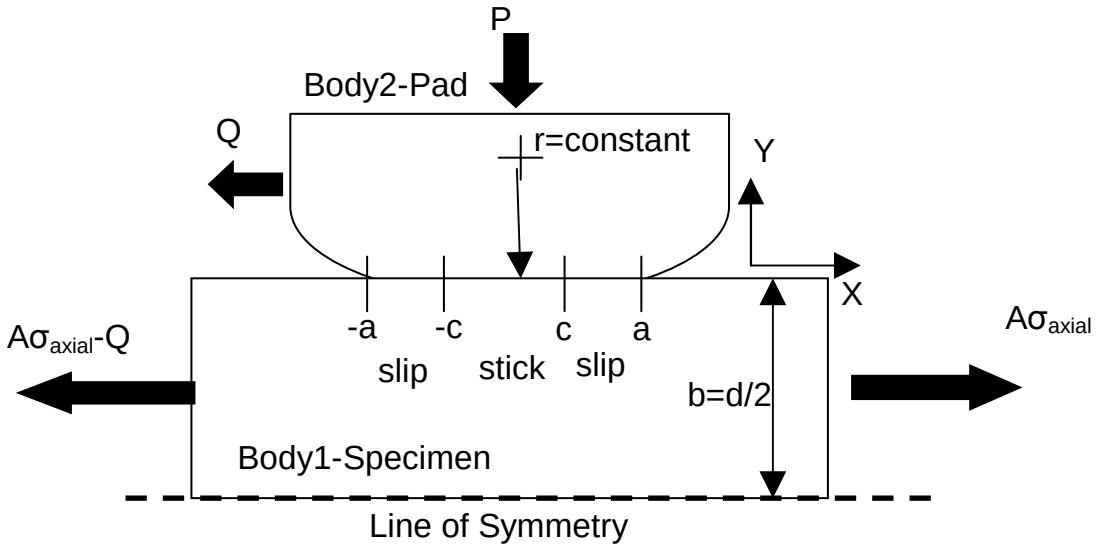

Figure 4. Partial Slip Condition for Deformed Bodies

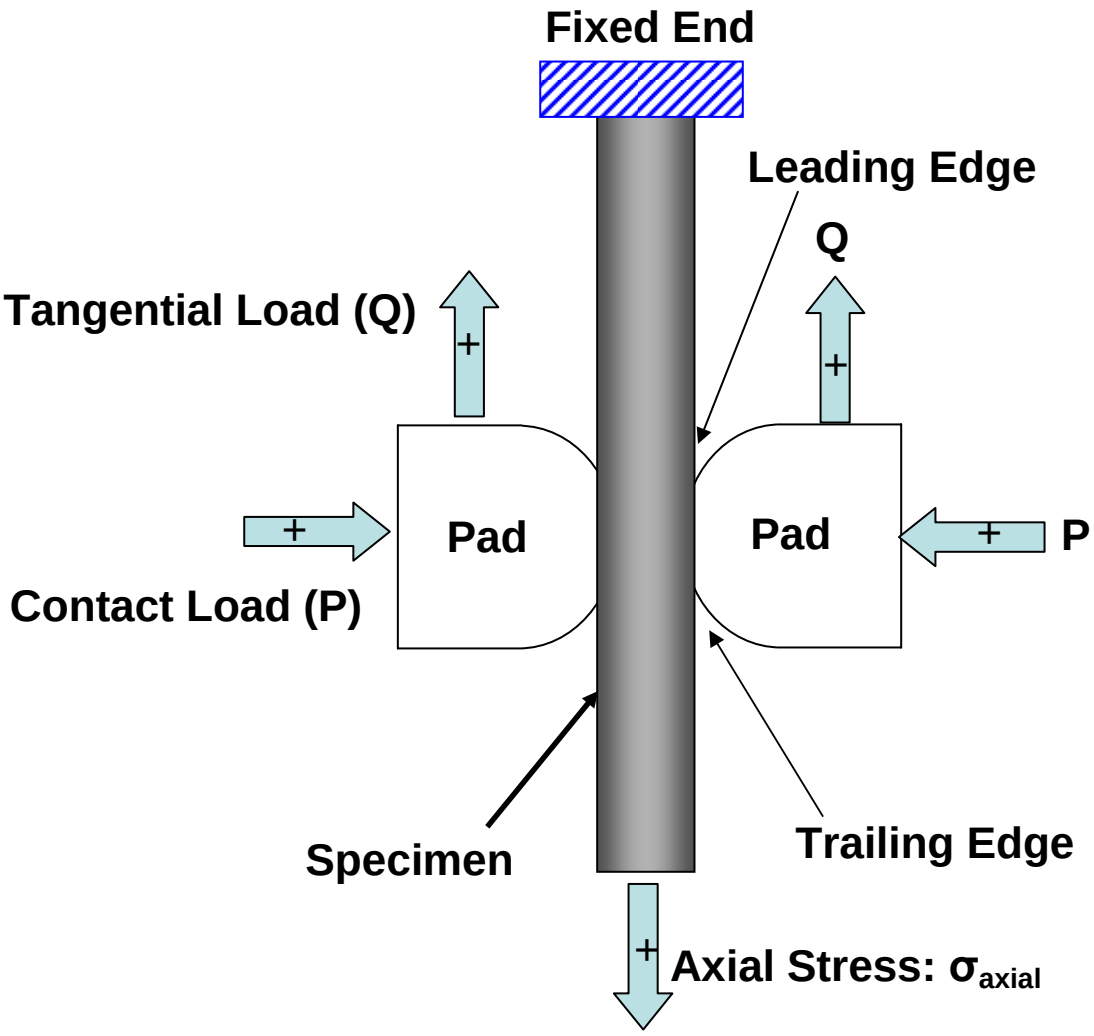

Figure 5. Typical Fretting Fatigue Configuration

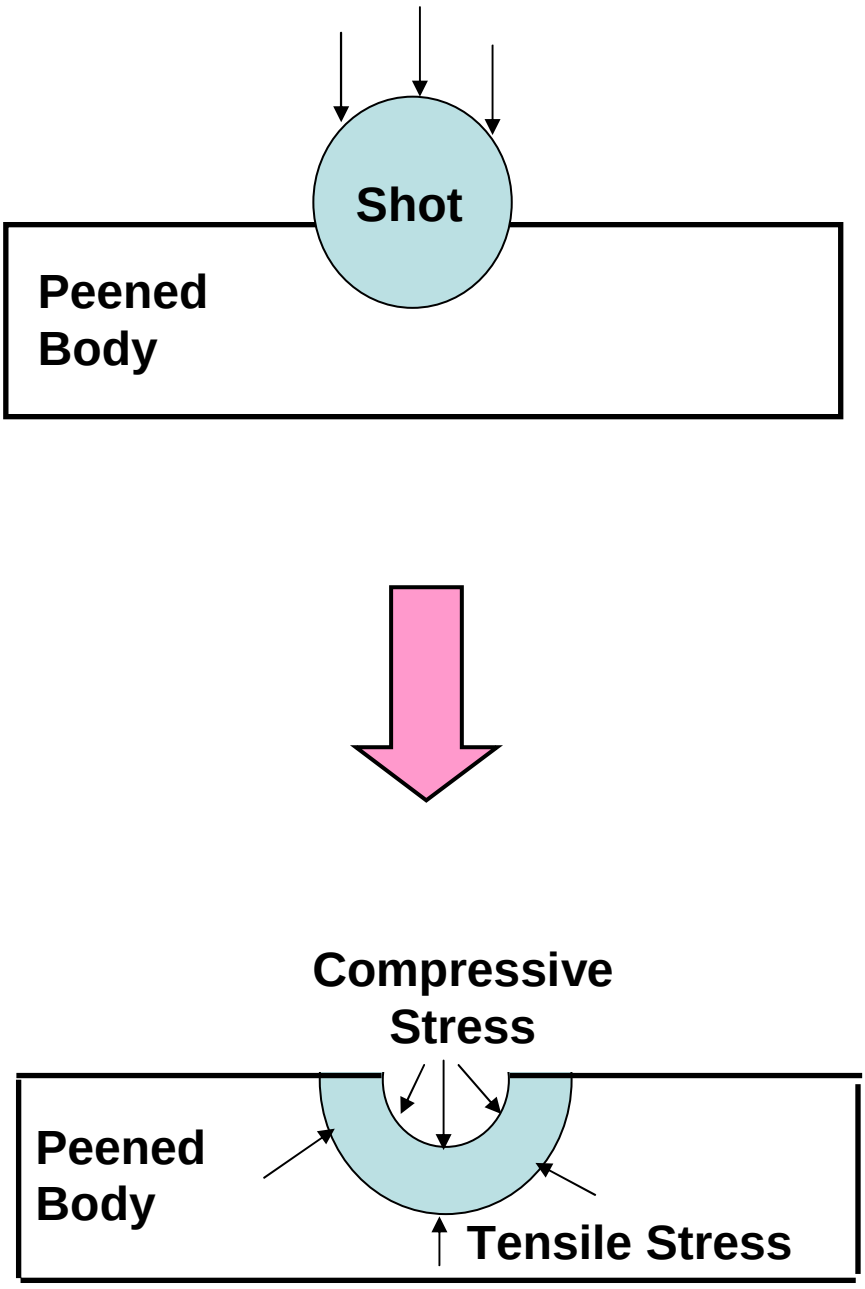

Figure 6. Schematics of Shot-peening Process

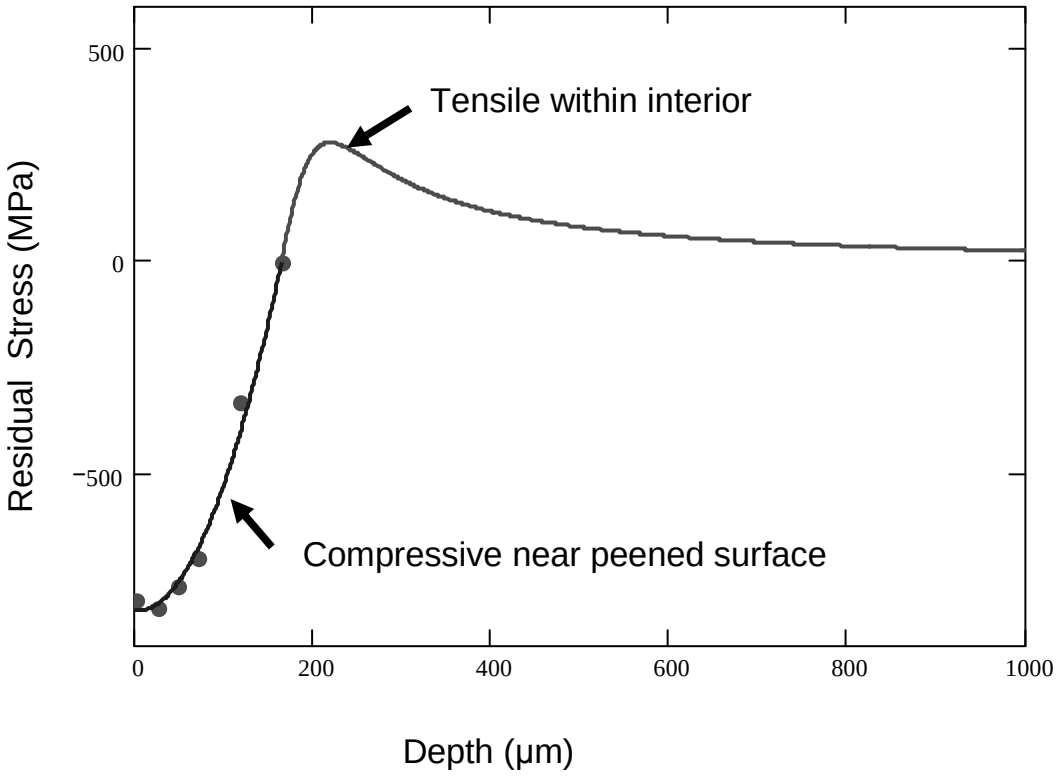

Figure 7. Typical Residual Stress Profile Induced by Shot-peening ($\sigma_{xx}=\sigma_{yy}$, $\tau_{xy}=0$)

III. Experimental Configuration

This chapter documents the experimental configuration used in this study to investigate the effects of constant and variable contact loads on the fretting fatigue behavior using Ti-6Al-4V specimens. Experimental test details such as test apparatus, specimen and pad geometry, material property, load determination, and test procedure are covered in this chapter.

3.1. Test Apparatus

The experimental setup in this study incorporated a bi-axial servo-hydraulic test machine at room temperature in the laboratory atmosphere. A photograph showing the complete test machine is presented in Figure 8. This test machine, as demonstrated in Figure 9 and 10, consisted of a rigid steel horizontal fixture frame, a 100kN lower axial servo-hydraulic actuator, and one 5kN contact load servo-hydraulic actuator to which a tappet shaft assembly was affixed. These two actuators were controlled by MTS 793.10 Multi-Purpose Test Software (MPT), one built-in function of MTS Model 793.00 system software. MPT allows users to vary the magnitude, frequency, waveform, and phase lag for both the axial loads and contact loads at the same time. Total three load cells were installed into this machine at different positions, the upper axial servo-hydraulic train, lower axial servo-hydraulic train as well as right hand side of fixture frame to sense load conditions. Two sets of holding blocks were designed to keep a pair of fretting pads in a precise alignment and prevent pads from moving freely. The left hand side holding block was affixed to the tappet shaft of the contact load actuator assembly, and the right hand side holding block was attached to the contact load cell which was mounted onto the

fixture frame. Each fretting pad was contained within one set of holding blocks individually. The contact load was applied by the contact load actuator to the fretting pad, and the contact load cell, which was attached to the fixture frame, was used to sense the applied contact loads and produce feedback signals for compensating contact load deviations occurring during biaxial-load test conditions.

3.2. Specimen and Pad Geometry

The dimensions of the dog-bone specimens are illustrated in Figure 11. For shot peened specimens, the thickness (2b) of the gauge section is 4.826 mm, and width (w) is 6.35 mm, accompanied with gauge cross sectional area (A) 30.6451 mm^2 and overall length (L) 200.32 mm. Un-peened specimens, on the other hand, have 3.81 mm thickness in the gauge section, and the width is 6.35 mm, with 24.1935 mm^2 gauge cross section area and 228.6 mm overall length.

The geometry of the fretting pads is also displayed in Figure 11. These cylindrical-end pads have an equivalent radius (r) of 50.8 mm at one end with flat-end at the other side. The thickness of pads is 9.525 mm, and width is 9.525 mm.

3.3. Material Property

Both the substrate specimens and the pads used in this study were made up of the forged titanium alloy, Ti-6Al-4V, for this alloy is commonly used to fabricate turbine engine disks and blades. The alloy was preheated and solution treated at 935˚C for 105 minutes, cooled in air, then vacuum annealed at 705˚C for 2 hours, and cooled again in argon. The resulting micro structure showed 60 % by volume of α (HCP) phase (platelets) and 40 % by volume of β (BCC) phase (matrix). The measured grain size was about 10

μm. The material had a modulus of elasticity of 126 GPa, yield strength of 930 MPa, Poisson's ratio of 0.3, and Brinell hardness number of 302.

Dog-bone specimens were machined by the wire electrical discharged method. In addition, the shot-peened specimens were shot-peened per SAE Aerospace Material Specification (AMS) 2432 standard, using computer controlled equipment with 7 Almen intensity. The process was accomplished with ASR 110 cast steel shot with 100% surface coverage on the gauge section.

Residual stress on the surface for the shot-peened specimen was measured via X-ray diffraction technique before fretting fatigue cycles were applied, and the value was determined as about -800 MPa which is similar to Martinez's observation for 7A100 Ti-6Al-4V specimens [2]. Therefore, the residual stress profile measured from Martinez's study for 7A100 shot-peened specimens was adopted as one of the input variables for finite element analysis (FEA) and Modified Shear Stress Range (MSSR) parameter calculation in this study.

The static coefficient of friction listed in Table 1 was measured before applying fretting fatigue cycles, using contact loads at different levels of magnitude. In comparison with previous studies, the static coefficient of friction in this study for shot-peened specimens was similar to that from Yuksel's finding [1]. Table 1 also shows that the difference in coefficients of friction between shot-peened and un-peened specimens is not significant. Moreover, previous studies have shown that varying coefficients of friction only produced relatively small effects on fretting fatigue variables as mentioned in Section 2.4.1. From previous studies, the experimentally stabilized static coefficient of friction was determined to be 0.37~0.46 for un-peened Ti-6Al-4V specimens [18] and

0.33~0.46 for shot-peened Ti-6Al-4V specimens [1,9]. It is clear that shot-peening process didn't alter coefficients of friction significantly. Based on the aforementioned discussion, an assumption suggesting a constant value for coefficient of friction, which was adopted in this study, seems to be rational under fretting fatigue configuration. A constant value of 0.5 was designated as the static coefficient of friction for all tests except for those cases where Q/P measured from experimental results exceeded 0.5. For these exceptions, a maximum value of Q/P from experimental records was assigned instead. The effects on FEA stress profiles and the MSSR parameter from varying coefficients of friction are discussed in Section 6.2.

3.4. Determination of Applied Load

The main goal of this study is to investigate the effects of variable contact loads on the fretting fatigue behavior. The applied load conditions used in this study are illustrated in Figure 12 and tabulated in Table 2. For all tests in this study, the axial stress, σ_{axial}, was applied at a frequency of 10 Hz with varying magnitudes to produce tension-tension and tension-compression axial stress conditions. The frequencies of contact loads were varied as 0 Hz, 2.5 Hz, 10 Hz, and 30 Hz. The maximum contact load in each test was always applied as the first step to prevent gross slip condition, followed by maximum σ_{axial} as the second step. After maximum normal and axial loads were applied at Step 2, subsequent load steps were then applied as a sinusoidal function, using peak/valley load and frequency documented in Table 2 until specimens broke into two pieces.

3.5. Test Procedure

One pair of fretting pads was mounted individually into the holding blocks that were affixed to a fixture frame. The pads were aligned to ensure the contact surfaces of pads were orthogonal to specimen and perpendicular to the applied axial load. Afterwards, specimens were then taken out from hydraulic machine, and a warm-up procedure programmed in MPT was executed to warm up the test machine for at least 30 minutes. This warm-up procedure was programmed using force control for the contact load actuator and displacement control for the axial load actuator. Next, a test specimen was mounted and clamped into test machine by the upper and the lower grips. Contact loads were then applied with an increment of 200 N/s until a predetermined maximum value listed in Table 2 was reached. Axial loads followed as Step 2 at an increment of 500 N/s until a maximum load tabulated in Table 2 was met. After Step 2, the applied loads were then imposed using a sinusoidal function with maximum/minimum load and frequency recorded in Table 2 until specimens broke into two pieces. Four different frequencies were chosen for contact load, and they were 0 Hz, 2.5 Hz, 10 Hz, and 30 Hz. The higher bound of contact load was 4448 N while 2224 N was the lower bound. Although the mean stress and stress ratio for the applied axial loads were varied for each test to produce tension-tension as well as tension-compression stress conditions on the specimens, the frequency of the axial loads was fixed at 10 Hz throughout this study. A graphical explanation for the applied load conditions is demonstrated in Figure 12.

During the tests, peak-valley compensator (PVC) was activated for both contact and axial loads to reduce variation between command and feedback signals sensed by the test machine. The induced tangential load was determined by half of the difference between the lower axial load and upper axial load after tests were executed for 10,000

fretting fatigue cycles. Axial loads, contact loads, and tangential loads were monitored and recorded continuously during tests until an experiment was ended due to specimen failure. After a specimen failed, the fretting fatigue cycles were recorded as its fretting fatigue life. These aforementioned fretting variables were then used as the load inputs for FEA modeling and MSSR prediction to be discussed in latter chapters.

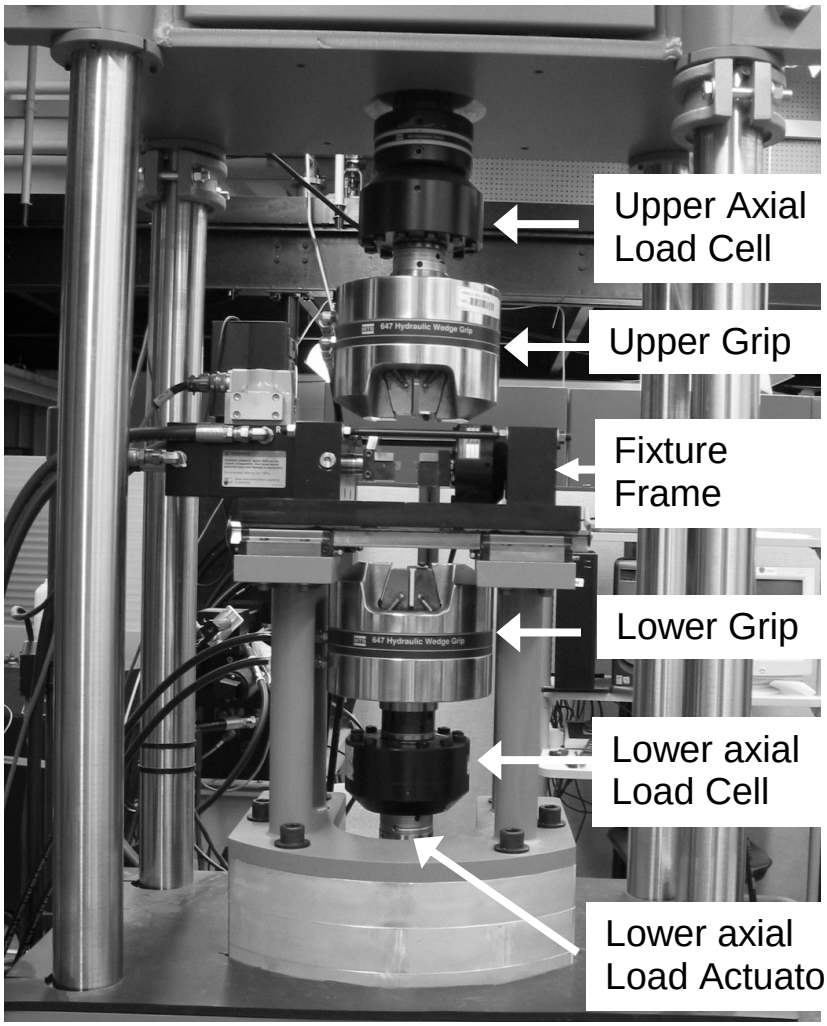

Figure 8. Bi-axial Servo-Hydraulic Material Test Machine

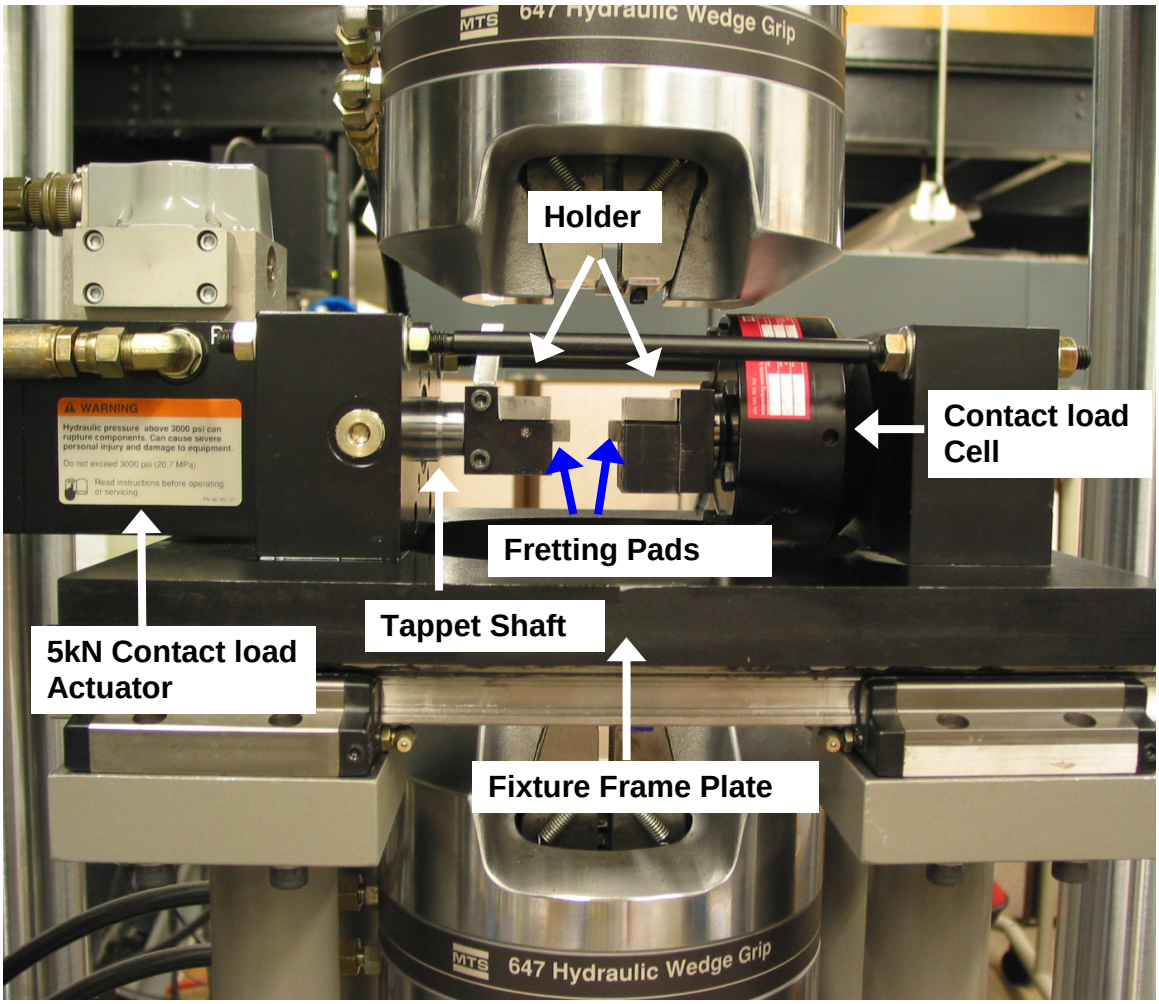

Figure 9. Fretting Fatigue Fixture Details

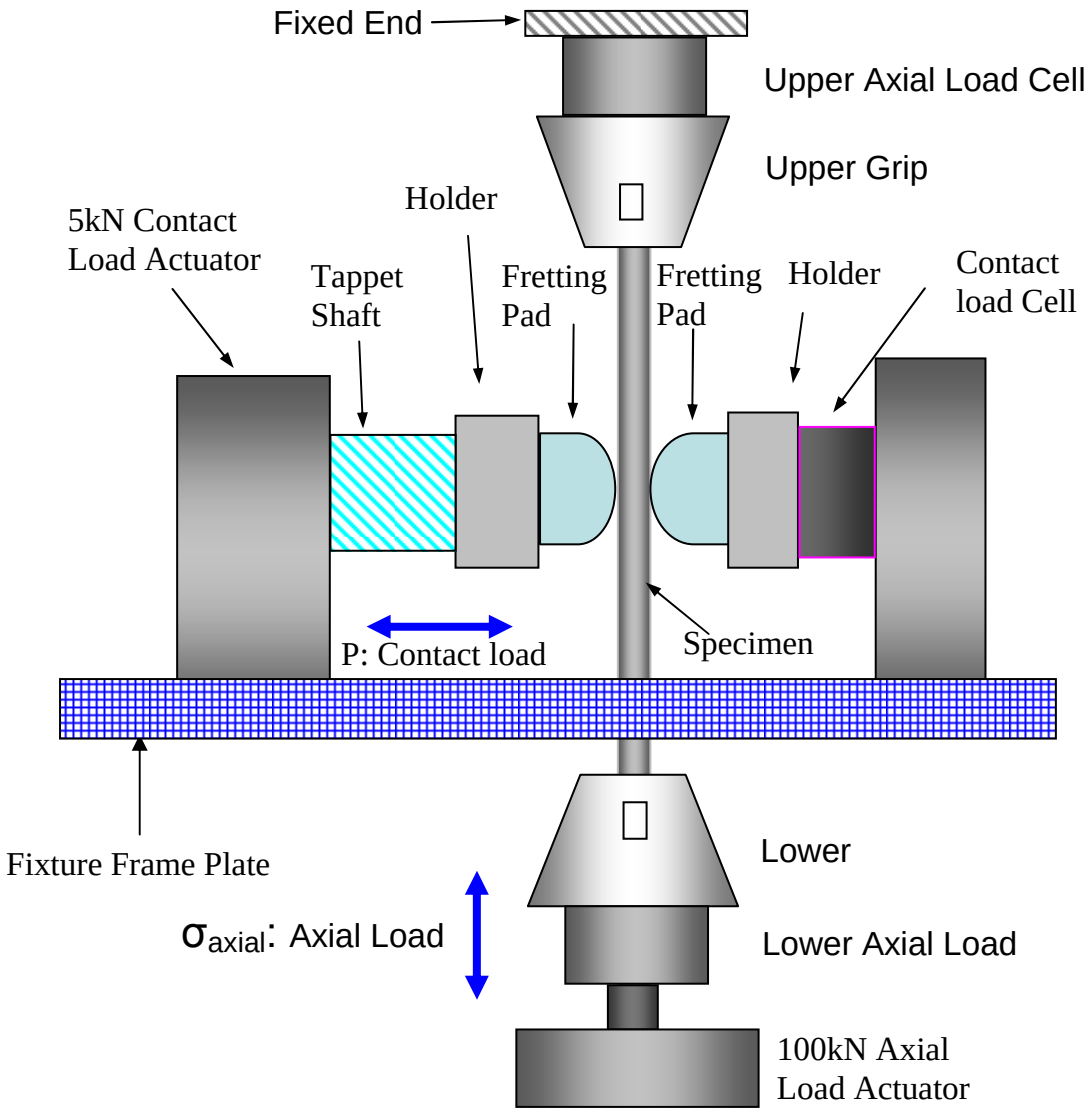

Figure 10. Schematic of Biaxial Fretting Fatigue Set-up Configuration

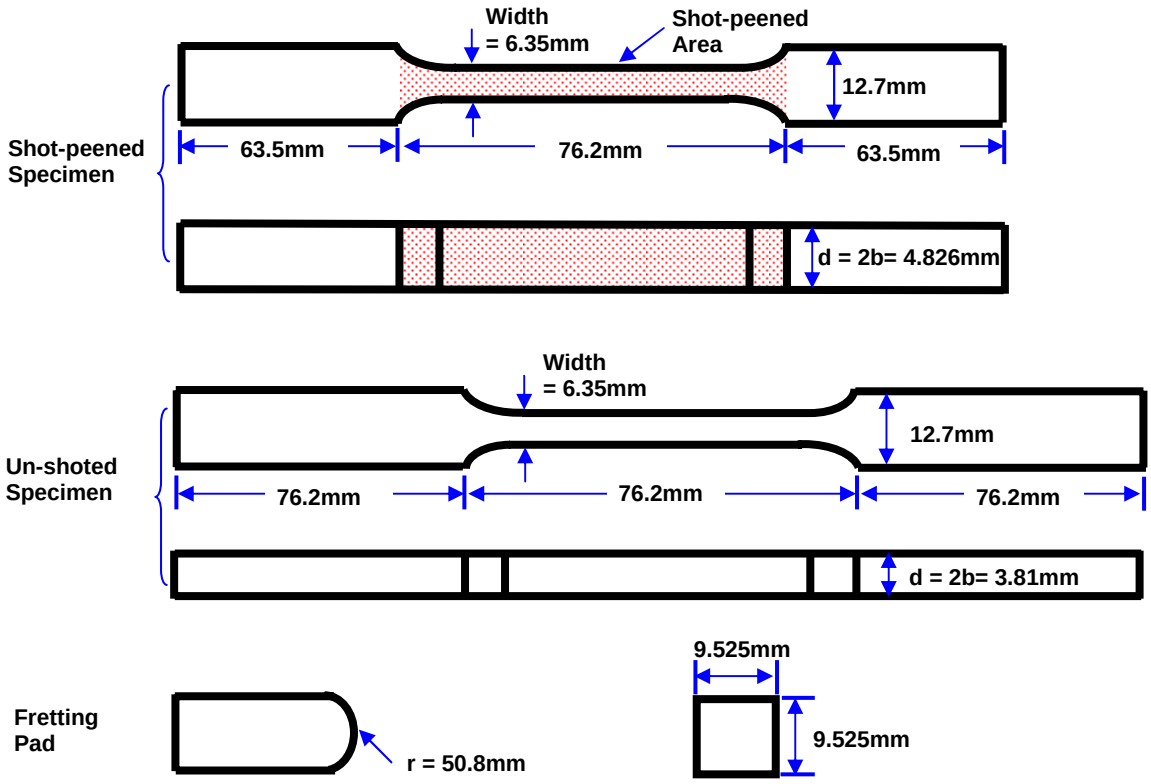

Figure 11. Specimen and Pad Geometry

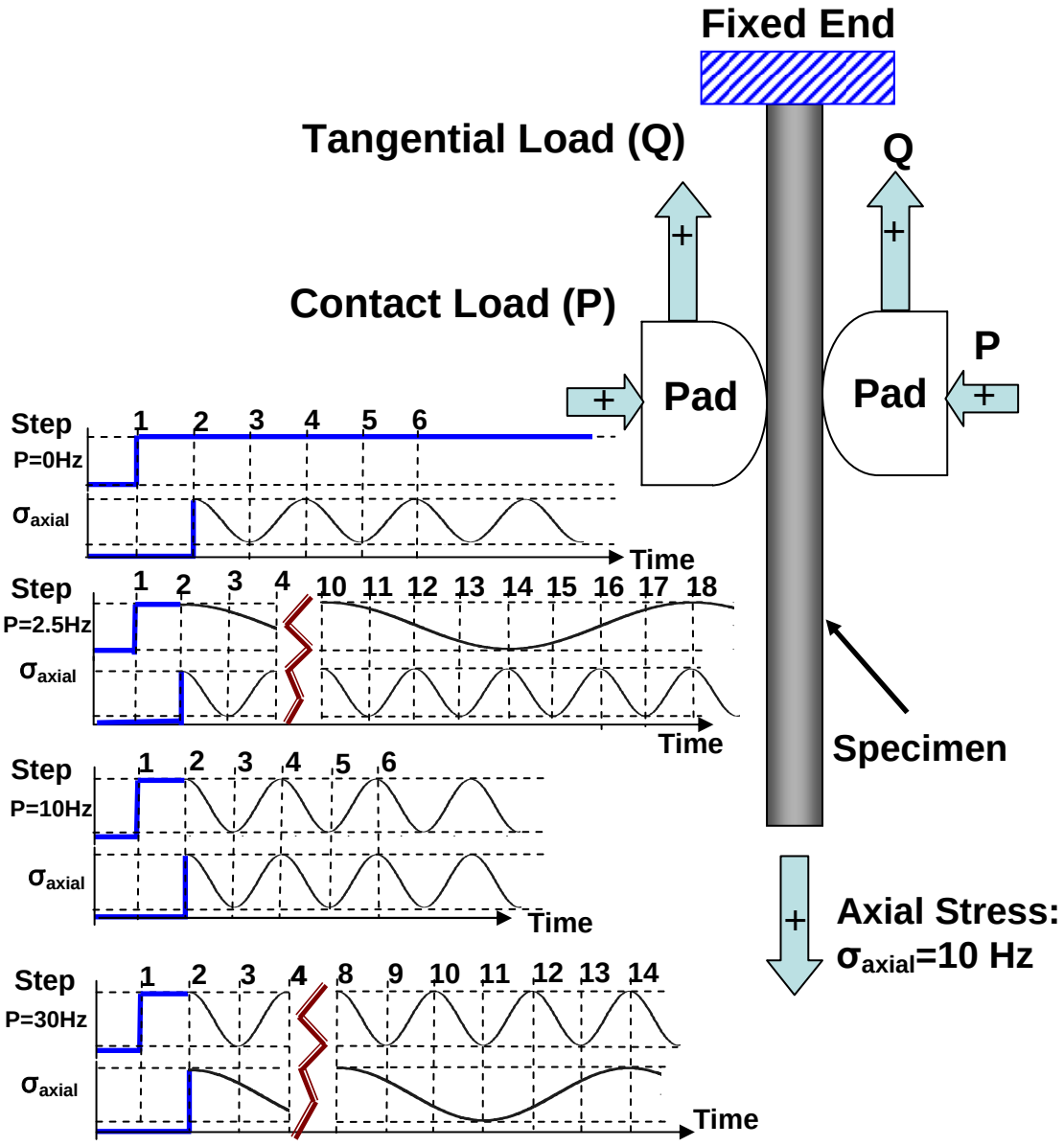

Figure 12. Determination of Experiment Applied Load

Table 1. Coefficient of Friction Measured in this Study

Shot-peened	Contact load (N)	Coefficient of friction (f)
N	2224	0.33
N	4448	0.34
Y	2224	0.27
Y	4448	0.31

Note:
Data measured before applying fretting fatigue cycles

Table 2. Test Loads Used in This Study (σ_{Freq} =10 Hz)

Test #	Shot peened	σ_{max} (MPa)	σ_{min} (MPa)	$\Delta\sigma$ (MPa)	R_σ	P_{max} (N)	P_{min} (N)	R_P	P_{Freq} (Hz)
1	N	600	60	540	0.1	2224	2224	1.0	0
2	N	600	60	540	0.1	4448	2224	0.5	0
3	N	600	60	540	0.1	4448	2224	0.5	2.5
4	N	600	60	540	0.1	4448	2224	0.5	30
5	N	270	-270	540	-1.0	2224	2224	1.0	0
6	N	270	-270	540	-1.0	4448	2224	0.5	0
7	N	270	-270	540	-1.0	4448	2224	0.5	2.5
8	N	270	-270	540	-1.0	4448	2224	0.5	30
9	Y	600	60	540	0.1	2224	2224	1.0	0
10	Y	600	60	540	0.1	4448	2224	0.5	0
11	Y	600	60	540	0.1	4448	2224	0.5	2.5
12	Y	600	60	540	0.1	4448	2224	0.5	10
13	Y	600	60	540	0.1	4448	2224	0.5	10
14	Y	600	60	540	0.1	4448	2224	0.5	30
15	Y	600	60	540	0.1	4448	2224	0.5	40
16	Y	600	-300	900	-0.5	2224	2224	1.0	0
17	Y	600	-300	900	-0.5	4448	2224	0.5	0
18	Y	600	-300	900	-0.5	4448	2224	0.5	2.5
19	Y	600	-300	900	-0.5	4448	2224	0.5	30
20	Y	270	-270	540	-1.0	2224	2224	1.0	0

Note:
The graphical explanation for load conditions is illustrated in Figure 12.

IV. Finite Element Analysis

The reason why finite element analyses (FEA) was needed for conducting fretting fatigue quantitative analysis in this study is elaborated in this chapter. Also, this chapter addresses the issues related to FEA analysis such as model development, load inputs, the coefficient of friction, model validation, and cyclic load effects. The present author also clarifies the maximum and minimum load conditions to enhance readability of the following sections.

4.1. Requirement for Finite Element Analysis

Finite element analysis segregates a continuum body into a finite number of elements. The basic premise is to formulate the governing equations at the discrete points, the nodes, which make up the elements, and then solve the equations as well as unknowns simultaneously to obtain the solution.

An infinite half-space assumption in fretting fatigue analysis is defined as half specimen thickness (b)/ contact half-width (a) >10. Finite specimen half-thickness can affect substrate compliance, and the stress components may differ for specimens with finite half-thickness. There is significant discrepancy between finite specimen half-thickness models and infinite half-space cases with respect to stress distribution within contact zone [48,49]. The infinite half-space assumption is a requirement for a FEA result to match an analytical solution obtained from the “Ruiz” program. As mentioned in Section 2.1, analytical solutions were developed based on infinite half-space assumption. However, throughout this study, $b/a_{Ruiz,max}$ ranged between 2.4~4.3 as displayed in Table 3, and the infinite half-space assumption was therefore violated. This explains why finite

element analysis, a numerical analysis technique that doesn't require an infinite half-space assumption to be met, is necessary for conducting quantitative analysis in this study. In addition, FEA can be used to determine the governing variables of fretting fatigue, such as contact stress, strain and displacement. These variables along with residual stress profiles and stress relaxation phenomenon can then be adopted to develop fretting fatigue predictive parameters which are addressed in Chapter V and VI.

4.2. Finite Element Model

A commercially available software, ABAQUS, was used for modeling the fretting fatigue configuration in this study as shown in Figure 13. In this study, four node, plain strain quadrilateral elements were used instead of eight node elements in order to eliminate the oscillation in the stress state along the contact interface introduced by the mid-side node of the eight node element. The contact condition was developed by using "master-slave" interfacial algorithm for modeling the finite element model of both shot-peened and un-peened experimental configuration. The model was consisted of three parts: rigid body constraint, fretting pad, and fretting specimen. The fretting pad was constrained in the x and y direction by the rigid body constraint. Multi-point constraint (MPC) was applied to the pad and specimen to keep it from rotating due to the application of loads as presented in Figure 13. Only one half of the fretting specimen was used in FEA model due to the symmetric nature to increase the computational efficiency of the analyses and to save memory resources. The half space of fretting specimen was constrained in the x and y direction along its boundary. The stiffness of the rigid body constraint was chosen to be very low for improved convergence of the finite element analysis. Moreover, very little load was transmitted from rigid body constraint to fretting

pad. The main purpose of this rigid body constraint was to restrict the fretting pad in the x and y-direction before the load steps were applied to FEA model. The contact load was applied at the top of the pad, the tangential load was applied on the left hand side of the fretting pad, and the axial stress was applied to the right hand side of half space of the specimen. A small sliding contact condition was used between the fretting specimen and fretting pad.

The mesh of the pad and the specimen were refined incrementally from the center of contact surface by changing certain geometric coordinates in the ABAQUS input file. The mesh near contact surface was refined to increase the accuracy of the stress, strain, and displacement distribution profile. On the other hand, coarse mesh far away from contact surface was designed for saving computing time and system resources. Half specimen thickness was determined to be 1.91 mm for un-peened specimens and 2.41 mm for shot-peened specimens. The material property of both the fretting pad and specimen was 126 GPa as modulus of elasticity and 0.3 as Poisson's ratio. A value of 0.5 was assigned to be the static coefficient of friction (f) for all models except for cases where $Q/P > 0.5$ from experimental result was violated. For these exceptions, $(Q/P)_{max}$ from experimental records was applied to avoid gross slip conditions between a pair of fretting pad and specimen. A summary of coefficients of friction used as the inputs for FEA is listed in Table 5, Chapter VI.

4.3. Load Inputs

For all FEA analysis, a maximum contact load was always applied as Step 1 and then kept constant until Step 2 to avoid gross slip condition. The maximum axial and tangential loads then followed as the second step. Among all tests, the frequency of axial

load was held at 10 Hz while changing stress range and stress ratio to achieve tension-tension and tension-compression configuration. Both frequencies and magnitude of the contact loads were varied to investigate the effects from its variation. After Step 2, applied loads were simulated as a sinusoidal function with predetermined peak/valley values for axial, contact, and measured tangential loads as documented in Table 5. A detailed explanation for the applied load sequence and numbering system used in this study is illustrated in Figure 14. The load step numbering convention indicated in Figure 14 is used throughout this study to improve the readability and comprehension.

4.4. Coefficient of Friction

As mentioned in Table 1, the difference among coefficients of friction was not significant for shot-peened and un-peened specimens. In addition, Iyer [21] showed that increasing friction from 0.37 to 0.5 (25% increase) caused no effect on contact half-width, 7% elevation on peak local cyclic stress range, and 15% raise in peak local cyclic shear stress range. Lykins [20] also observed increasing the coefficient of friction from 0.45 to 0.7 (66% increase) caused 20% increase in strain amplitude. In Sections 6.2, the author shows that increasing coefficients of friction from 0.4 to 1.0 (250% increase) only produced, at most, 27% variation in σ_{xx} stress profile and 16% elevation in MSSR parameter. Among these studies, a slight difference in a coefficient of friction didn't generate much deviation in stress profile, contact half-width, and so forth. Previous studies also found that the experimental stabilized static coefficient of friction ranged between 0.37~0.46 for un-peened Ti-6Al-4V specimens [18] and 0.33~0.46 for shot-peened Ti-6Al-4V specimens [1,9]. From these measurements, the shot-peening process

didn't modify the coefficient of friction significantly, and the value of a static coefficient of friction could be treated as the same for both shot-peened and un-peened specimens.

For this study, a constant value, 0.5, was used as the static coefficient of friction for all tests except for those cases in which Q/P <0.5 from experimental results was violated. For these exceptions, $(Q/P)_{max}$ from laboratory records was assigned as the coefficient of friction for FEA modeling. The detailed values for coefficients of friction used in FEA are listed in Table 5, Chapter VI.

4.5. Model Validation

Although the "Ruiz" FORTRAN program was developed on the basis of infinite half-space assumption under static applied contact and axial loads, it is still a useful tool for validating a FEA model by comparing their outputs. For verifying, results from FEA at Step 2 of Test 1 were chosen to compare with their counterparts calculated from Ruiz Program under the same load conditions. This validation was conducted by checking the contact half-width, the stress profile, Hertzian peak pressure, and nominal stress.

4.5.1. Contact Half-Width

Contact half-width can be solved analytically using Equation (11). Using this equation, contact half-width ($a_{analyticl}$) was calculated to be 0.566 mm at Step 2 of Test 1, identical to the value from Ruiz program. When compared to the value of contact half-width from FEA, 0.59 mm, the variation is less than 4%

From discussions above, contact half-width calculated from Equation (11) and the Ruiz program was identical to each other and close to the FEA solution. Since contact half-width is subjected to change all the time under variable contact loads, to simplify analysis and establish a practical reference, the contact half-width, $a_{Ruiz,max}$, calculated

from the Ruiz program at a step where a maximum axial, normal, and tangential loads occurred concurrently is used as a reference in the following chapters.

4.5.2. Stress State and Hertzian Peak Pressure

Since the Ruiz program is based upon the conditions that both contact and axial loads are applied statically, and the infinite half space criterion is met. In order to obtain these aforementioned conditions, Step 2 of Test 1 along the contact surface was chosen to validate stress profiles from FEA. Figure 15 demonstrates that the stress curves from FEA approach are close to those from the Ruiz program. The maximum values of σ_{xx} from FEA was determined as 927 MPa at $x/a_{Ruiz,max}$=0.942. In comparison with the outputs from the Ruiz program, the variation was calculated as 6 % in magnitude and 2 % in location along x-direction. Hertzian peak pressure (P_0) from FEA, shown in Figure 16, was determined as 399 MPa at $x/a_{Ruiz,max}$= 0.04. On comparison with values from the Ruiz program, the variation was 1% in magnitude and 4% in location along x-direction.

4.5.3. Applied Nominal Stress

The final criterion to validate FEA model is the nominal stress σ_{xx} far away the contact zone along x-direction. In principle, σ_{xx} from FEA analysis far away the contact region should be consistent with the applied axial stress. Figure 17 presents that at the location where $x/a_{Ruiz,max}$ = 7.18, the value of σ_{xx} from FEA calculation reached 602 MPa. On comparison with the applied axial stress of 600 MPa, the deviation is within 0.3 %.

4.6. Cyclic Load Effect and Steady State

Since the FEA axial loads in this study were applied cyclically, it is crucial to judge what the affect is from this alternating load condition and whether or not the FEA solutions can converge to a steady state. Test 1 was selected to investigate cyclically

applied load effect and the corresponding steady state phenomenon. Figure 18 demonstrates that when a cyclic load was introduced into the FEA model, an unsteady period occurred in stress profile. However, this unsteady phenomenon reached a steady state just after one load cycle was completed. It can also be seen from Figure 18 (a) and (c) that σ_{xy} was subjected to more deviation during transition from unsteady to steady state than σ_{xx}. That means σ_{xy} was more susceptible to the alternating load effect. Under variable load conditions, σ_{yy} stress profile was not varied at all, suggesting that σ_{yy} stress profile was independent on the effect introduced by cyclic axial loads.

Figure 18 also shows that the Ruiz solution could only approach FEA stress solution at Step 2 very well just as expected since this step indicates a quasi-static situation. Much more deviation was found after FEA solution reached a steady state after Step 4, i.e. after one load cycle. This observation indicated that the Ruiz program and analytic solution are much more effective in describing a fretting fatigue configuration under static applied axial and contact loads. On the other hand, FEA is necessary for fretting fatigue analysis under cyclic axial and/or contact loads configuration.

Based on observations achieved up to this point, FEA outputs in this study was elicited and analyzed only after a steady state was reached. In practice, that means FEA solutions were only collected and analyzed after either a normal or axial load cycle was completed, depending on which one had a lower frequency.

4.7. Maximum and Minimum Load Conditions

As illustrated in Figure 14, axial loads, contact loads, and tangential loads were all subjected to continuously changing magnitude during fretting fatigue cycles. Therefore, clarifying and defining maximum and minimum load conditions are helpful to improve

the readability and comprehension for the subsequent discussions. The maximum load condition is defined as a load step at which the maximum axial, contact, and tangential loads occur simultaneously under a variable loading condition. Also, the minimum load condition means a load step at which all minimum axial, contact, and tangential loads happen at the same time under a variable loading condition.

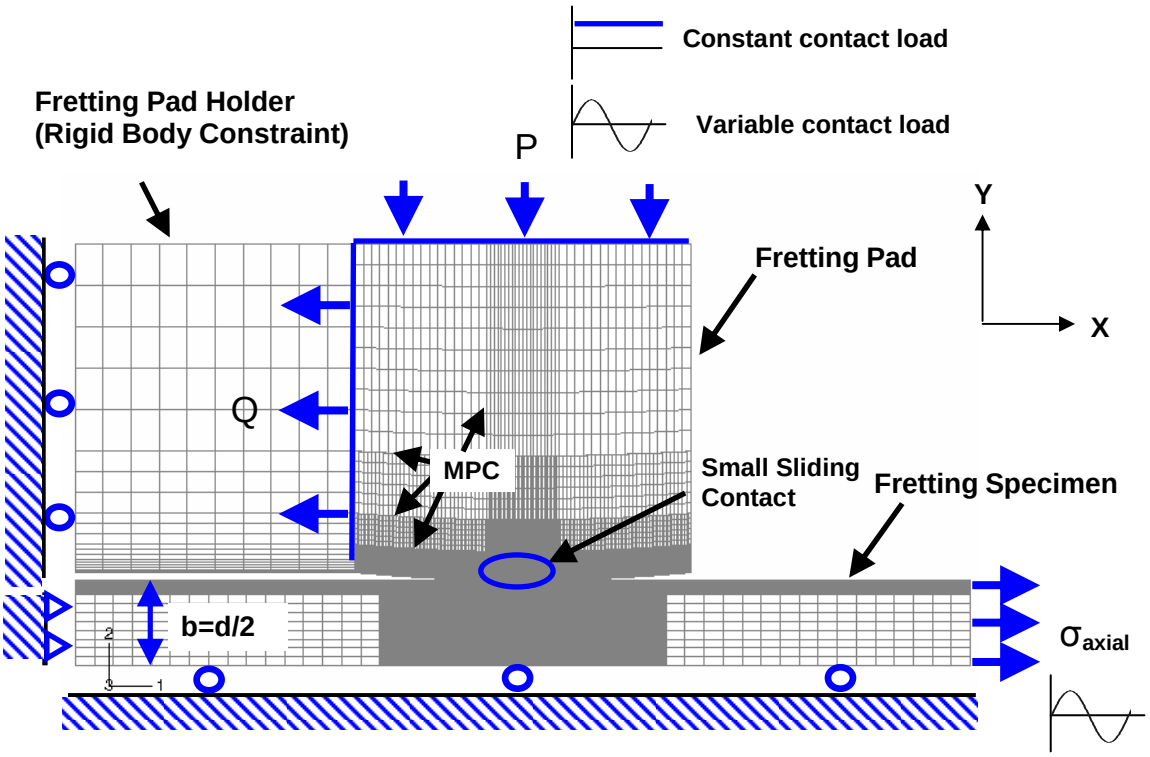

For shot-peened specimen: d = 4.83 mm
For un-peened-specimen: d = 3.81 mm

Figure 13. FEA Model with Load and Boundary Conditions

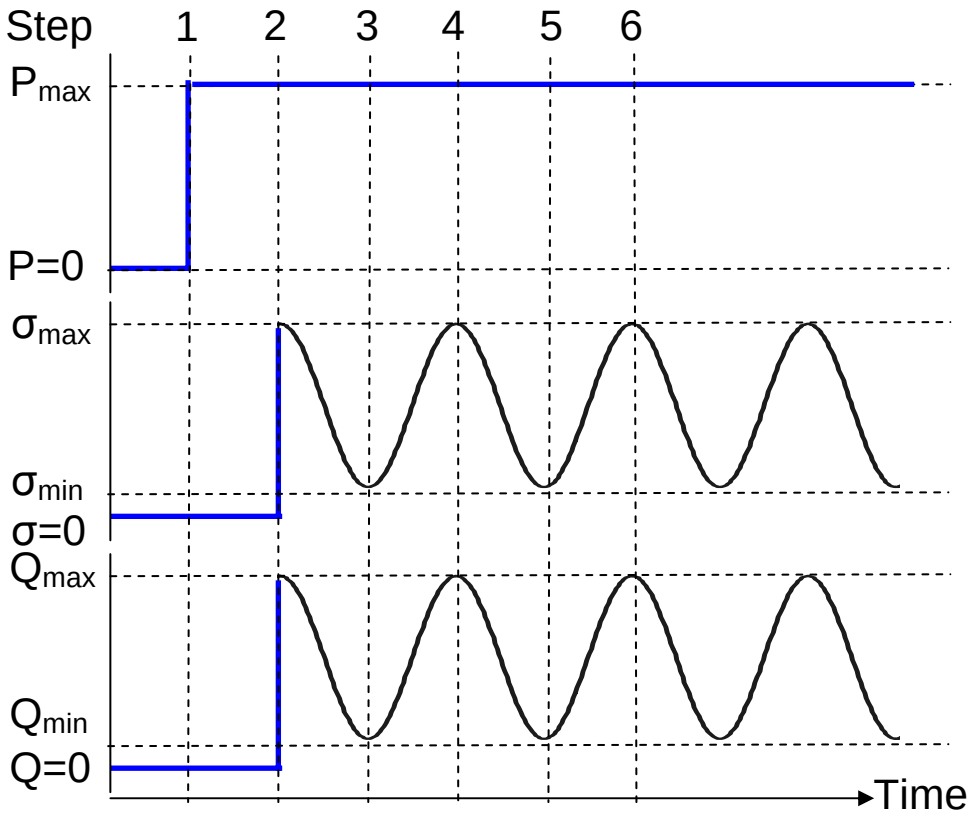

(a) 0 Hz Contact Load (σ_{axial} =10Hz)

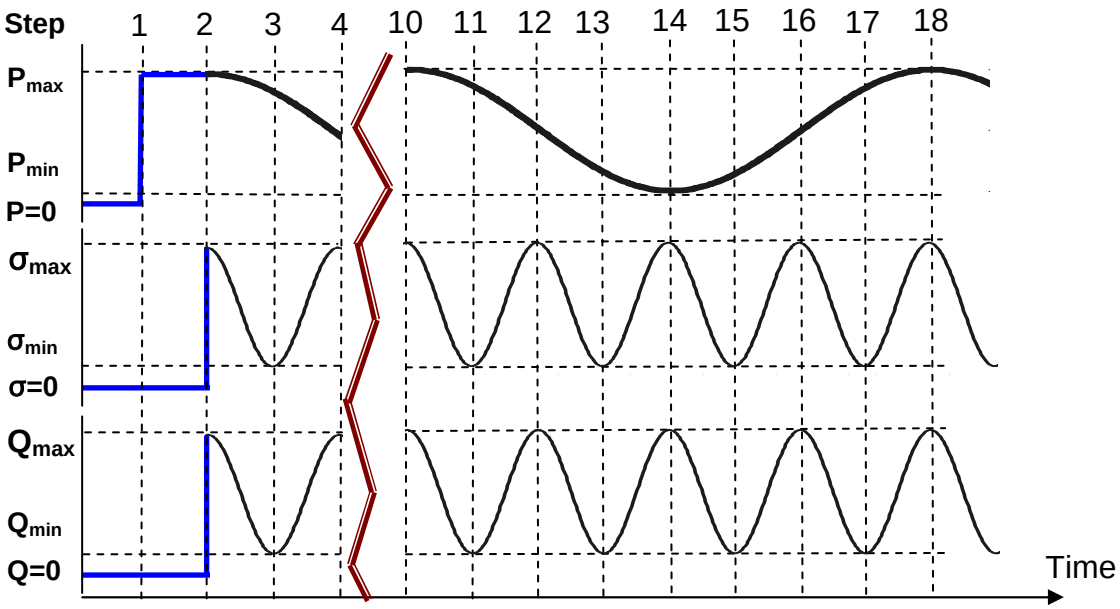

(b) 2.5 Hz Contact Load (σ_{axial} =10Hz)

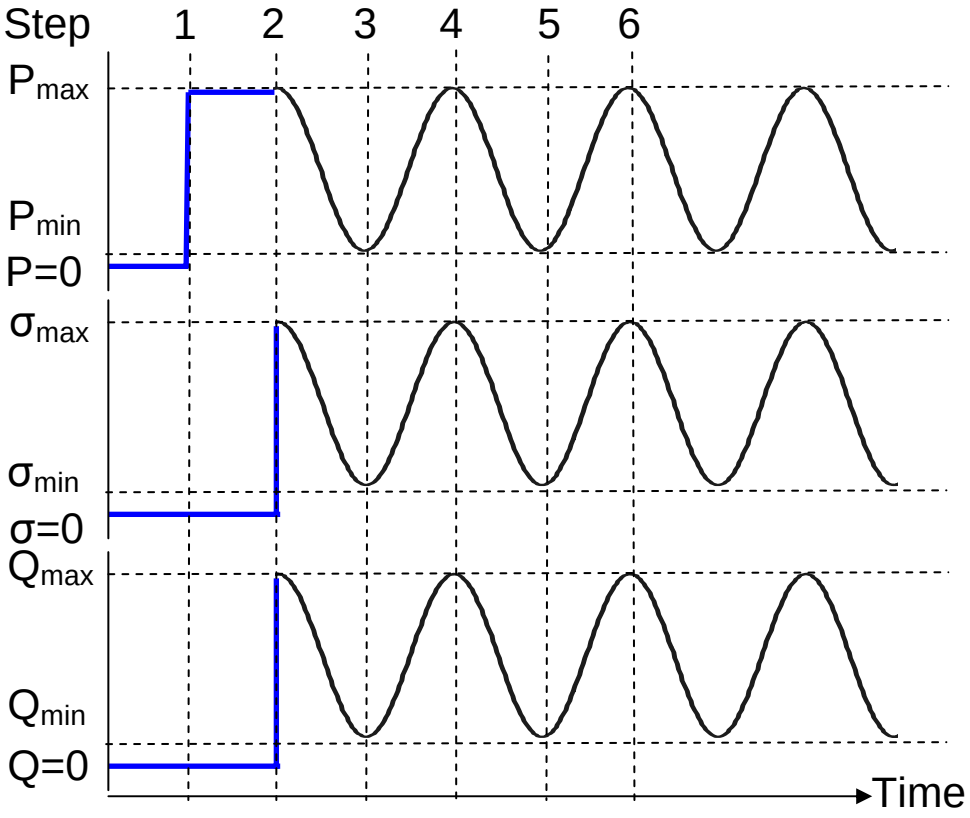

(c) 10 Hz Contact Load (σ_{axial} =10Hz)

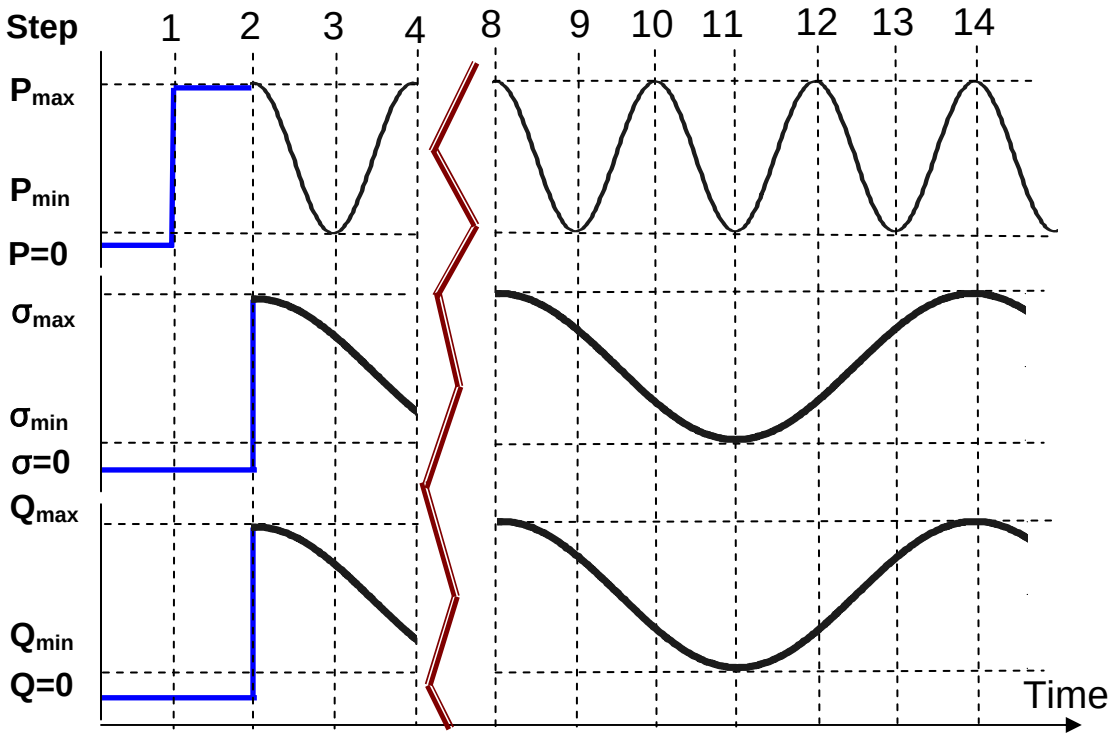

(d) 30 Hz Contact Load (σ_{axial} =10Hz)

Figure 14. Load Configuration and Sequence

Note:
The magnitude and frequency of the applied contact and axial loads are tabulated in Table 2, and the experimental measured tangential loads are recorded in Table 5 in Chapter VI.

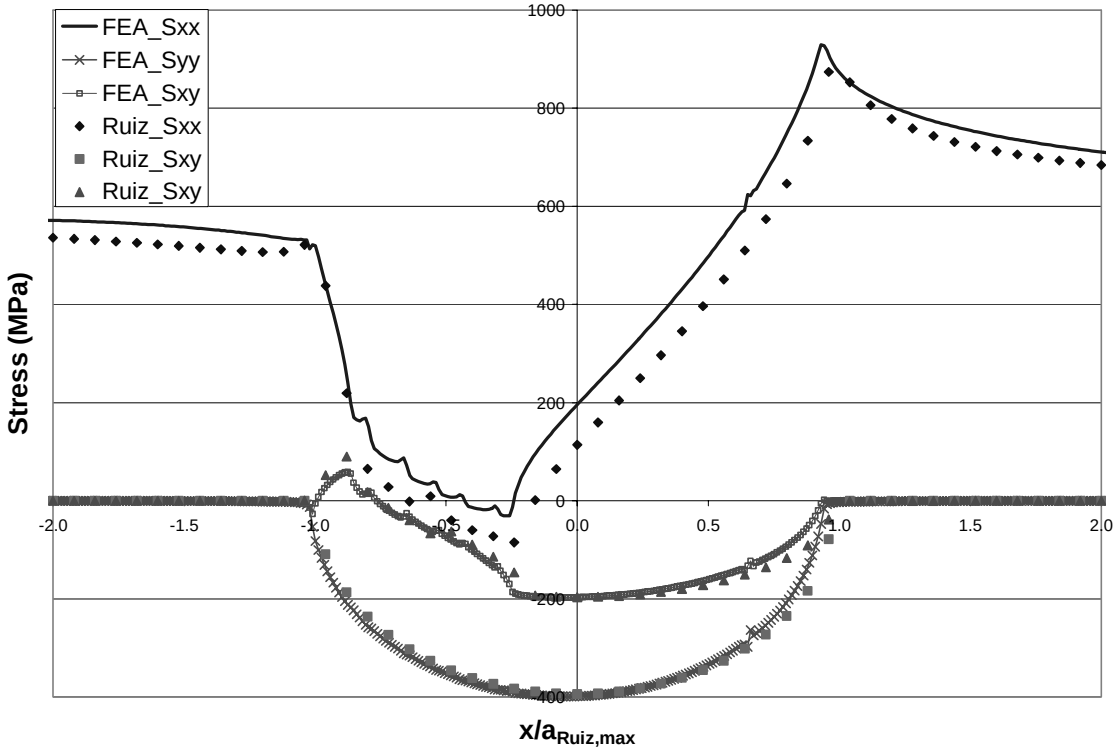

Figure 15. Stress Profile Calculated from FEA and Ruiz Program along Contact Surface at Step 2, Test 1

Note:

Load Condition: σ_{max} =600 MPa, σ_{min} =60 MPa, P_{max} =2224 N, P_{min} =2224 N, P_{Freq} =0 Hz
For FEA Solution: $b/a_{Ruiz,max} = 3.37$
For Ruiz Analytical Solution: $b/a_{Ruiz,max} = \infty$

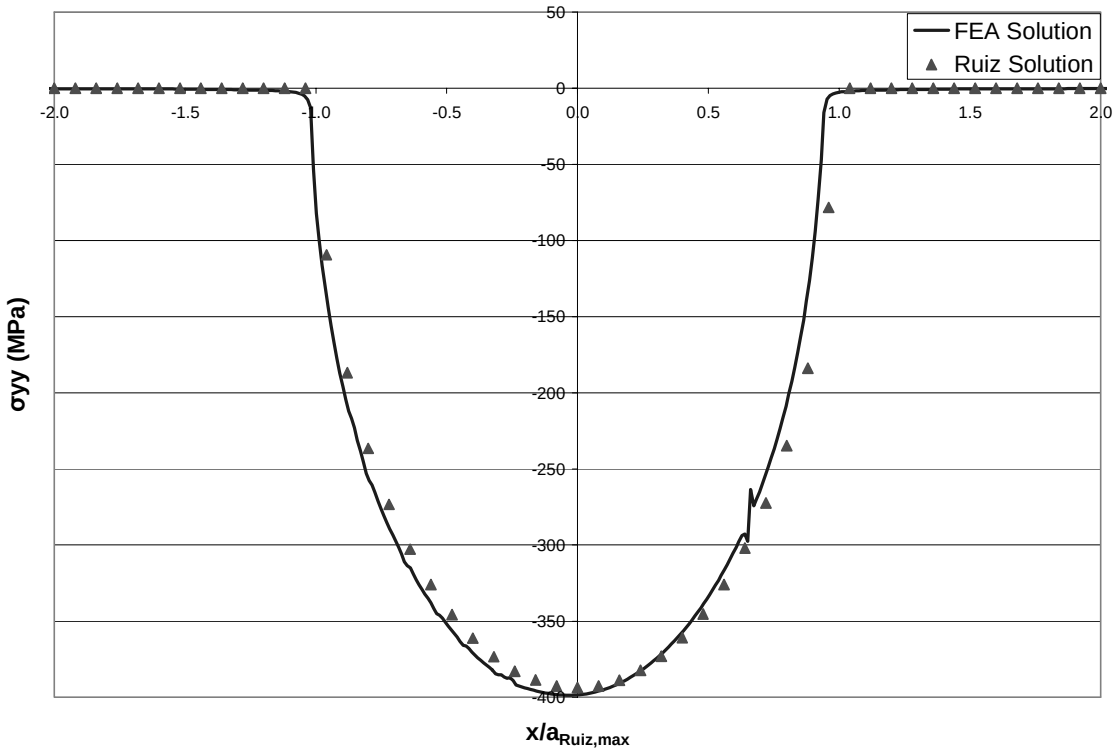

Figure 16. Stress Profile Calculated from FEA and Ruiz Program along Contact Surface at Step 2, Test 1 for Hertzian Peak Pressure

Note:

Load Condition: σ_{max} =600 MPa, σ_{min} =60 MPa, P_{max} =2224 N, P_{min} =2224 N, P_{Freq} =0 Hz
For FEA Solution: $b/a_{Ruiz,max} = 3.37$
For Ruiz Analytical Solution: $b/a_{Ruiz,max} = \infty$

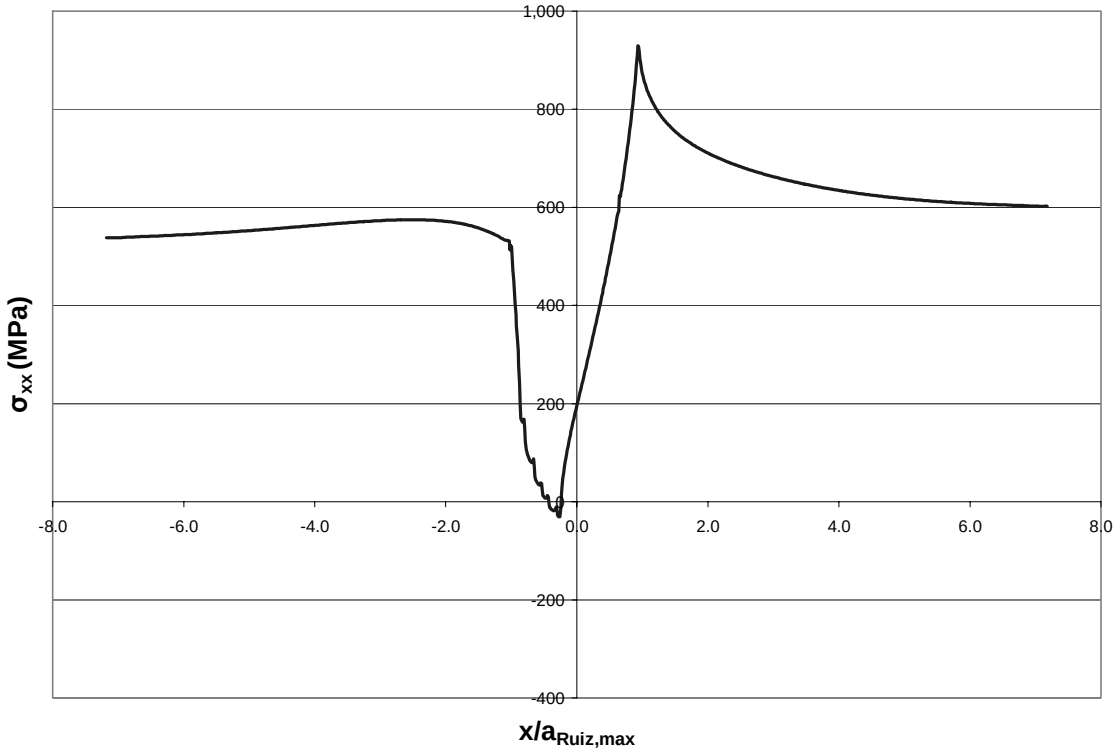

Figure 17. Stress Profile Calculated from FEA for σ_{xx} far away from the Contact Region at Step 2 of Test 1

Note:

Load Condition: σ_{max} =600 MPa, σ_{min} =60 MPa, P_{max} =2224 N, P_{min} =2224 N, P_{Freq} =0 Hz
For FEA Solution: $b/a_{Ruiz,max} = 3.37$
For Ruiz Analytical Solution: $b/a_{Ruiz,max} = \infty$

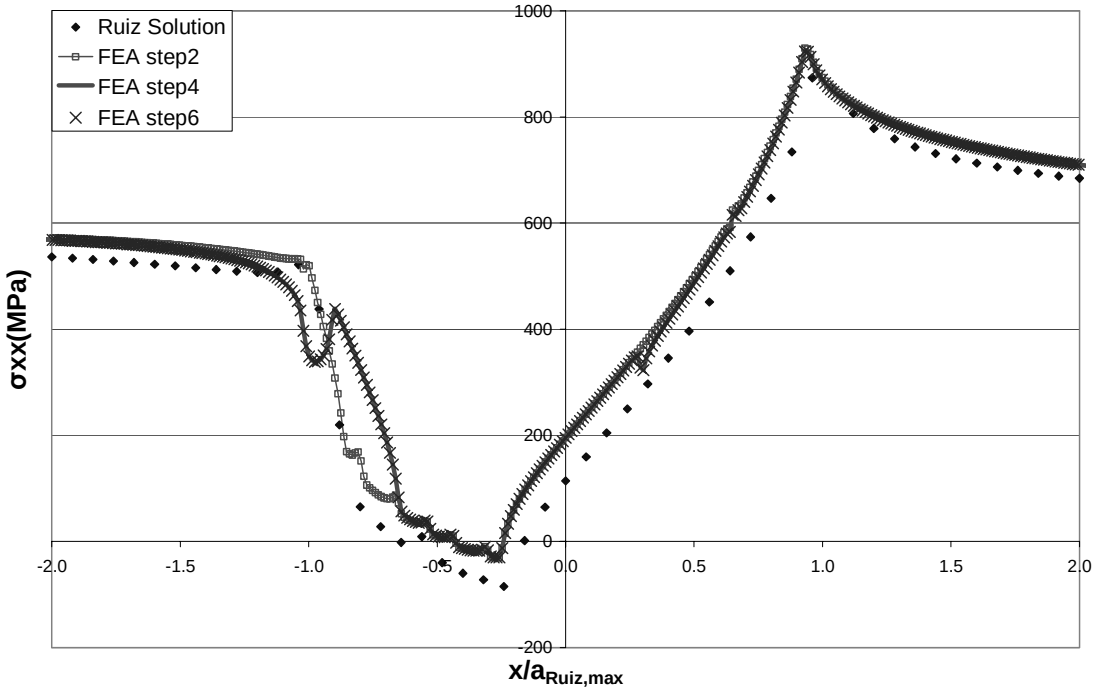

(a) Comparison of σ_{xx} Distribution along Contact Surface from Test 1 at Different Steps

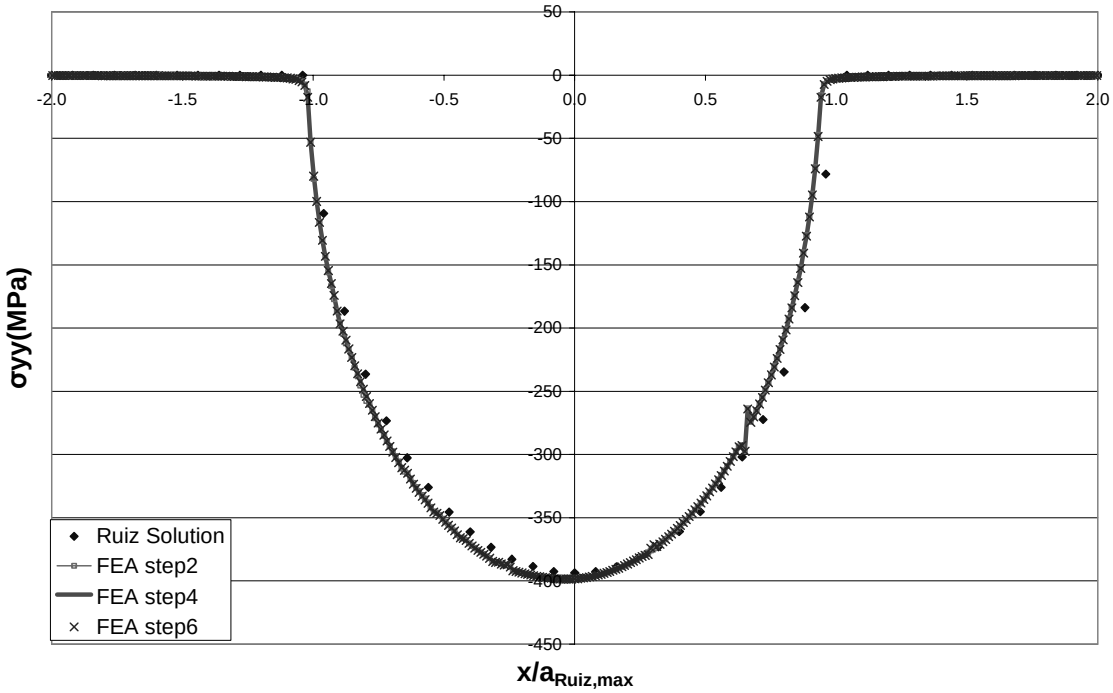

(b) Comparison of σ_{yy} Distribution along Contact Surface from Test 1 at Different Steps

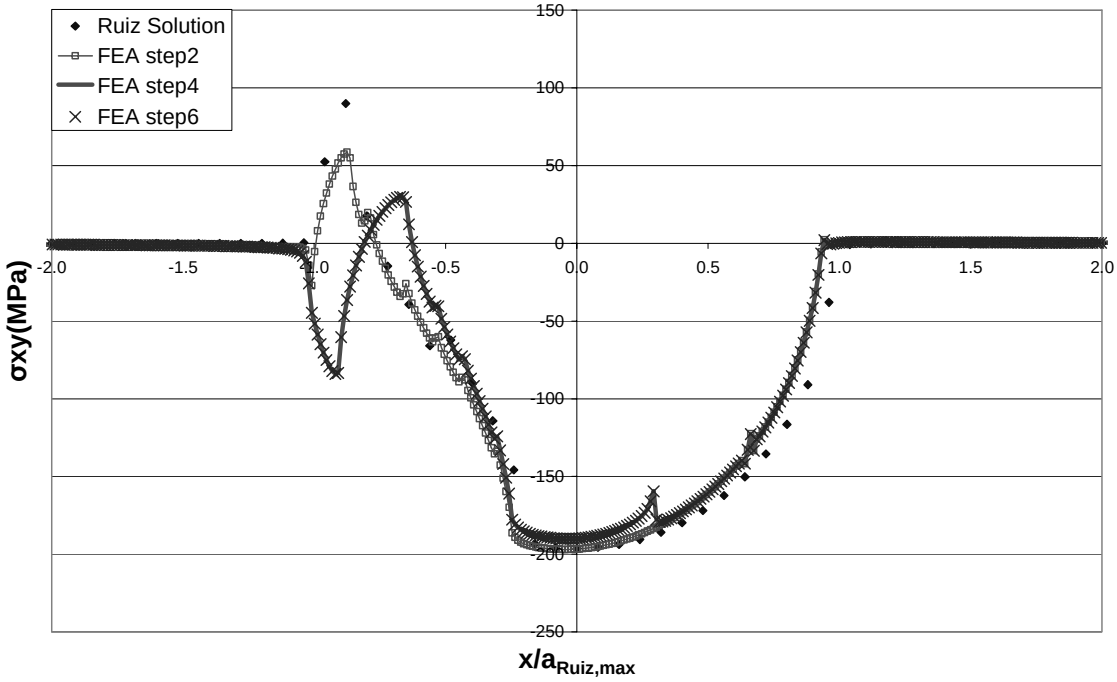

(c) Comparison of σ_{xy} Distribution along Contact Surface from Test 1 at Different Steps

Figure 18. Comparison of Stress Distribution along Contact Surface from Test 1 at Different steps

Note:

Load Condition: σ_{max} =600 MPa, σ_{min} =60 MPa, P_{max} =2224 N, P_{min} =2224 N, P_{Freq} =0 Hz
Un-peened Specimen

Table 3. Summary of $b/a_{Ruiz,max}$ in This Study (σ_{Freq} =10 Hz)

Test #	Shot peened	σ_{max} (MPa)	σ_{min} (MPa)	P_{max} (N)	P_{min} (N)	P_{Freq} (Hz)	$a_{Ruiz,max}$ (m)	b (m)	$b/a_{Ruiz,max}$
1	n	600	60	2,224	2,224	0	5.7E-04	1.9E-03	3.37
2	n	600	60	4,448	4,448	0	8.0E-04	1.9E-03	2.38
3	n	600	60	4,448	2,224	2.5	8.0E-04	1.9E-03	2.38
4	n	600	60	4,448	2,224	30	8.0E-04	1.9E-03	2.38
5	n	270	-270	2,224	2,224	0	5.7E-04	1.9E-03	3.37
6	n	270	-270	4,448	4,448	0	8.0E-04	1.9E-03	2.38
7	n	270	-270	4,448	2,224	2.5	8.0E-04	1.9E-03	2.38
8	n	270	-270	4,448	2,224	30	8.0E-04	1.9E-03	2.38
9	y	600	60	2,224	2,224	0	5.7E-04	1.9E-03	3.37
10	y	600	60	4,448	4,448	0	8.0E-04	2.4E-03	3.01
11	y	600	60	4,448	2,224	2.5	8.0E-04	2.4E-03	3.01
12	y	600	60	4,448	2,224	10	8.0E-04	2.4E-03	3.01
13	y	600	60	4,448	2,224	10	8.1E-04	2.4E-03	2.98
14	y	600	60	4,448	2,224	30	8.0E-04	2.4E-03	3.01
15	y	600	60	4,448	2,224	40	8.7E-04	2.4E-03	2.77
16	y	600	-300	2,224	2,224	0	5.7E-04	2.4E-03	4.26
17	y	600	-300	4,448	4,448	0	8.0E-04	2.4E-03	3.01
18	y	600	-300	4,448	2,224	2.5	8.0E-04	2.4E-03	3.01
19	y	600	-300	4,448	2,224	30	8.0E-04	2.4E-03	3.01
20	y	270	-270	2,224	2,224	0	5.7E-04	2.4E-03	4.26

V. MSSR Analysis

This chapter addresses the MSSR calculation procedure under fretting fatigue configuration for both constant and variable contact loads. Additionally, the method used in this study to account for shot-peening induced residual stress along with stress relaxation on the MSSR determination for shot-peened specimens is also elaborated.

5.1. MSSR Parameter

Based on the discussion mentioned in Section 2.5.7, the MSSR parameter was the only critical plane-based parameter which was more effective in predicting fretting fatigue life, crack initiation location, and crack initiation orientation simultaneously. Moreover, MSSR can also take into consideration the effects from multiaxial loading and stress concentration at the trailing edge as it should be the case under a fretting fatigue condition. Based on these observations, the MSSR parameter was adopted in this study as the only critical plane-based parameter to be used for predicting fretting fatigue behavior.

The formula defining the fatigue predictive parameter, MSSR, was explained in detail in Section 2.5.7, and it is expressed as Equation (43). In this study, comprehensive MSSR calculation was conducted using FEA stress outputs superimposed with the corresponding residual stress along all planes ranging from $-90^{o} \leq \theta \leq +90^{o}$ in 0.1° increment throughout the whole specimen, where θ is the orientation at which stress state in material is observed. Since two load steps are needed for the determination of MSSR, these two steps among several steps were first computed at the peak and valley of either axial or contact loads within the same test as illustrated in Figure 14 and tabulated in Table 4. After all MSSR between different step pairs in a test was determined, the MSSR with the greatest value among all others was then designated as the maximum MSSR

parameter of that test ($MSSR_{max}$). $MSSR_{max}$ was then analyzed in latter sections by its location, orientation, and correlation with fretting fatigue life under cyclic axial and/or variable contact load conditions.

In addition, MSSR was first reckoned for a full load cycle in a test to investigate whether or not the values of MSSR are symmetric with respect to a full load cycle as shown in Figure 19. Some results for MSSR determination, which were calculated by a full load cycle, are summarized in Table 4. This table presents that the values of MSSR are symmetric with respect to a completed load cycle in a test. Take Table 4 (b) for instance, MSSR obtained from Step 10-11 and Step 17-18 is close to each other, and MSSR from Step 11-12 and Step 16-17 is also similar in magnitude. Similar observations can also be found between Step 10-14 and Step 14-18, and so forth. These findings infers a practical simplification on the determination of MSSR, and the present author postulated that only half of the load cycle is needed for $MSSR_{max}$ determination since the values of MSSR between different step pairs are symmetric with respect to a full load cycle. To reduce analysis complexity and improve operation performance, the MSSR parameter in the remainder of this study was only conducted during one half of the load cycle.

Other observations from Table 4 are that the MSSR for un-peened specimens always occurs on the contact surface near the trailing edge regardless of the steps on which MSSR calculation was based. Nevertheless, the orientation for MSSR between different steps changes enormously, which ranges from 10˚ to 45˚ in Test 3 as seen in Table 4 (b). Figure 20 demonstrates the MSSR profile for Test 1 along with increasing depth for an un-peened specimen. The maximum value of MSSR in this plot takes place

on the contact surface, decreases near the surface, and becomes flat with the increasing depth.

5.2. Residual Stress

For shot-peened specimens, the determination of shot-peening induced residual stress is crucial because this residual stress must be superimposed to FEA stress solutions to carry out the MSSR parameter. Residual stress is considered as a bi-axial stress tensor, that is, $\sigma_{xx} = \sigma_{yy}$ and $\sigma_{xy} = 0$, except at the surface. In addition, residual stress profile can be distinguished into two portions, compressive stress near the peened surface and tensile stress in the interior of specimens after a specific depth. The compressive residual stress profile may be susceptible to shot-peening specifications, and the compensatory tensile stress distribution can be carried out via the formulas proposed by Namjoshi [9] as documented in Equation (22) to (26). Readers can refer to Section 2.3 for a comprehensive discussion on shot-peening process and the nature of the induced residual stress.

In this study with shot-peened specimens, the original compressive stress along the specimen surface was measured as -800 MPa by X-ray refraction technique, which was identical to the value obtained from Martinez's study for specimens shot-peened under 7A100 specification [2]. Therefore, the compressive stress profile from Martinez's study for 7A100 shot-peened specimens was adopted in this study. The tensile stress, on the other hand, was determined using the formulas listed in Equation (22) to (26), and the values for these constant coefficients were determined to be: $Y_0 = 164$ μm, p=56.38, q=586.67, r=1.41 and s=14.69. Using these constants, maximum tensile residual stress is about 277 MPa at a depth of 226 μm, maximum compressive stress is about -804 MPa at

25 μm depth, and the location where residual stress was zero occurred at 164 μm below the contact surface. The serpent curve for residual stress profile used in this study is presented as Figure 21.

5.3. Stress Relaxation

From Martinez's study [2], after specimens failed due to fretting fatigue cycles, residual stress within the contact zone was subjected to a complete (100%) relaxation. Additionally, Lee et al. [3,15] found that for specimens shot-peened under 7A100 specification, residual stress relaxation occurred evenly at different depths of specimens. Martinez [2] also observed that for specimens that were shot-peened under 4A100 and 10A100 specifications, these specimens, before failure occurred, were subjected to 20% and 40% stress relaxation within the contact region after 25,000 and 2 millions fretting fatigue cycles, respectively.

In summary, residual stress within the contact zone relaxed with the increasing fretting fatigue cycles, and the relaxation increased from 0% relaxation before applying fretting fatigue cycles until a complete (100%) relaxation happened at specimen failure. This relaxation phenomenon occurred evenly at locations with the same depth in a specimen. However, the exact correlation between fretting fatigue cycles and residual stress relaxation rate is still unclear.

In order to investigate the effects from residual stress and stress relaxation on the MSSR parameter, this study used residual stress profile presented in Figure 21 and assumed stress relaxation occurred uniformly at different depths of specimens. Further, 0%, 50%, 70%, and 100% stress relaxation were applied during the computation of MSSR, which will be discussed in Chapter VI. The present author also postulated a

different stress relaxation assumption to depict a better stress relaxation behavior as follows:

1) For tests with fretting fatigue life less than 100,000 cycles, shot-peened specimens are subjected to 20% stress relaxation.

2) For tests with fretting fatigue life between 100,000 and 1 million cycles, shot-peened specimens are subjected to 30% stress relaxation.

3) For tests with fretting fatigue life higher than 1 million cycles, shot-peened specimens are subjected to 40% relaxation.

This aforementioned assumption accompanied with uniform relaxation rate at different depths was used to determine the residual stress profile, which was then superimposed to FEA stress solution for MSSR determination. The MSSR calculation results under stress relaxation are discussed in depth in Chapter VI.

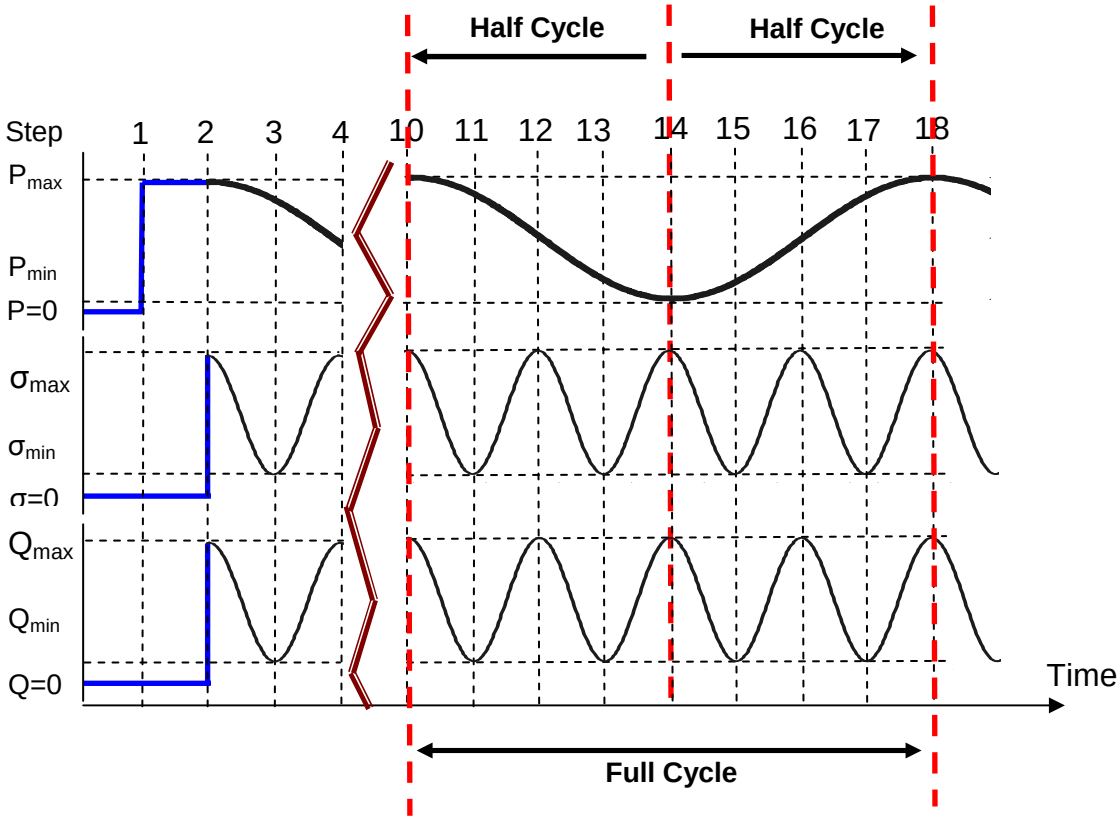

Figure 19. Explanation for Half Cycle Span and Full Cycle Span used in MSSR Calculation

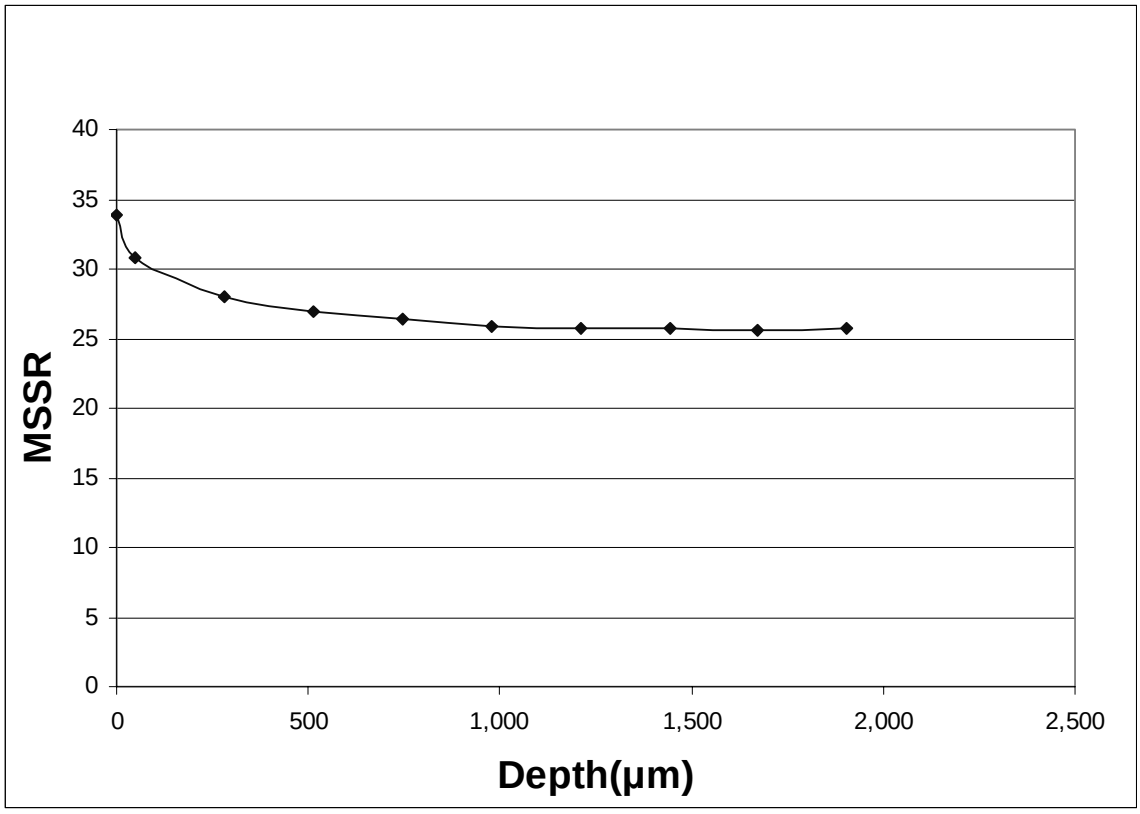

Figure 20. MSSR Profile along the Depth of Un-peened Specimen for Test 1, Step 4-5

Load Condition: σ_{max} =600 MPa, σ_{min} =60 MPa, P_{max} =2224 N, P_{min} =2224 N, P_{Freq} =0 Hz
Un-peened Specimen

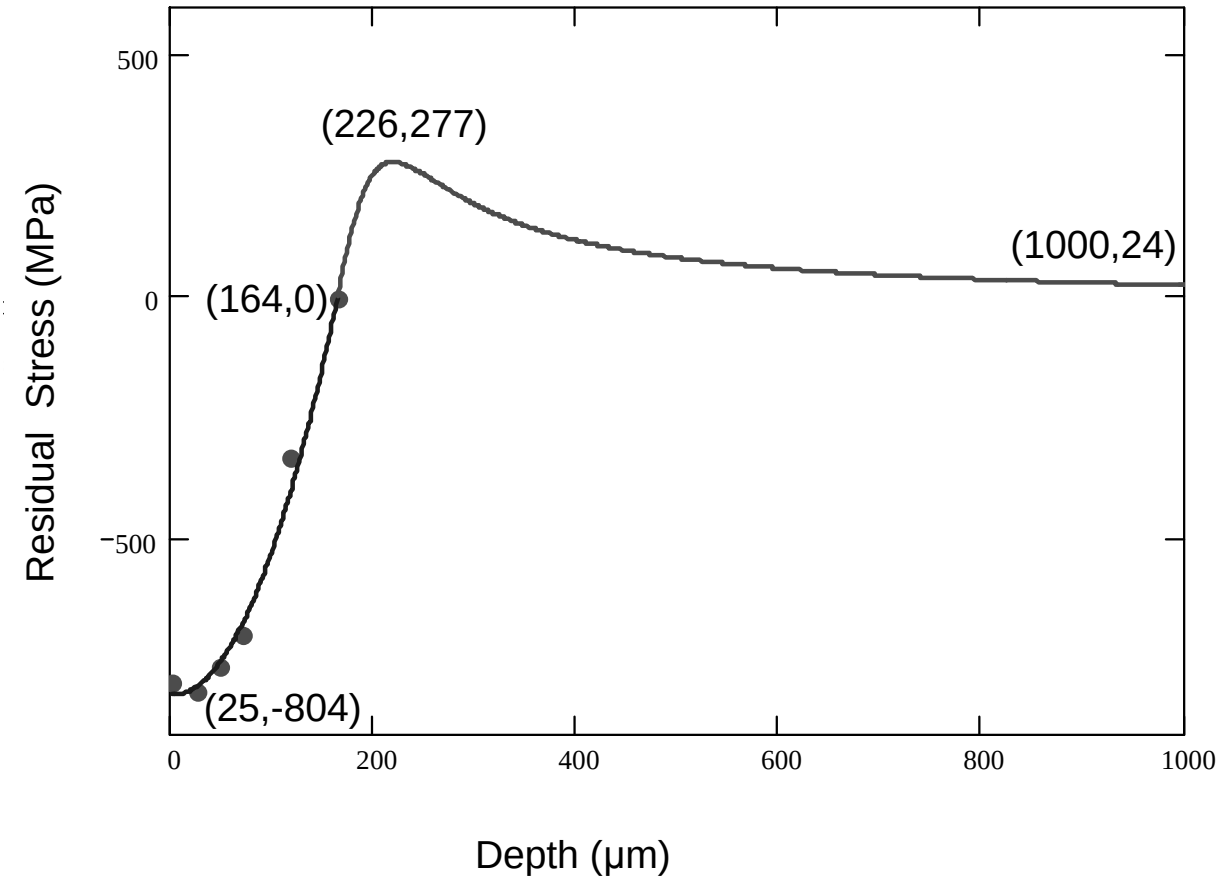

Figure 21. Residual Stress Profile Used in this Study for Shot-peened Specimen

Table 4. MSSR Determination under Variable Contact Loads with Different Frequencies

(a) MSSR for Test 1

Load Condition: σ_{max}=600 MPa, σ_{min}=60 MPa, P_{max}=2224 N, P_{min}=2224 N, P_{Freq}=0 Hz
Un-peened Specimen

Step	MSSR	$\Delta\tau$ (MPa)	$\Delta\tau_{crit}$ (MPa)	θ (deg)	$R_{\Delta\tau}$	σ_{max} (MPa)	σ_{min} (MPa)	depth (μm)	$x/a_{Ruiz,max}$
4-5	33.88	542	507	40	-0.1268	513	-131	0	0.93
5-6	33.79	527	492	41	-0.1331	523	-127	0	0.94

(b) MSSR for Test 3

Load Condition: σ_{max}=600 MPa, σ_{min}=60 MPa, P_{max}=4448 N, P_{min}=2224 N, P_{Freq}=2.5 Hz
Un-peened Specimen

Step	MSSR	$\Delta\tau$ (MPa)	$\Delta\tau_{crit}$ (MPa)	θ (deg)	$R_{\Delta\tau}$	σ_{max} (MPa)	σ_{min} (MPa)	depth (μm)	$x/a_{Ruiz,max}$
10-11	35.04	582	549	42	-0.1135	542	-91	0	0.94
11-12	35.07	528	507	36	-0.0784	588	-141	0	0.81
12-13	33.13	518	510	45	-0.0302	466	-14	0	0.82
13-14	33.80	502	472	39	-0.1218	545	-141	0	0.67
14-15	33.99	515	485	39	-0.1158	543	-143	0	0.67
15-16	33.14	518	510	45	-0.0306	467	-15	0	0.82
16-17	35.23	520	499	37	-0.0789	607	-142	0	0.82
17-18	35.01	583	549	42	-0.1147	541	-92	0	0.94
10-14	32.92	172	237	10	0.4399	521	812	0	0.75
14-18	32.88	171	240	10	0.4602	522	804	0	0.75

(c) MSSR for Test 4

Load Condition: σ_{max}=600 MPa, σ_{min}=60 MPa, P_{max}=4448 N, P_{min}=2224 N, P_{Freq}=30 Hz
Un-peened Specimen

Step	MSSR	$\Delta\tau$ (MPa)	$\Delta\tau_{crit}$ (MPa)	θ (deg)	$R_{\Delta\tau}$	σ_{max} (MPa)	σ_{min} (MPa)	depth (μm)	$x/a_{Ruiz,max}$
8-9	32.01	190	290	18	0.5384	397	658	0	0.70
9-10	30.22	213	179	12	-0.3753	725	243	0	0.68
10-11	20.82	77	120	19	0.5482	15	283	0	0.65
11-12	22.76	229	245	45	0.1200	215	32	0	0.98
12-13	30.27	314	311	149	-68.296	-144	516	0	0.73
13-14	32.00	189	290	18	0.5383	396	657	0	0.70
8-11	33.97	515	530	45	0.0505	496	27	0	0.94
11-14	33.99	516	531	45	0.0505	497	28	0	0.94

VI. Results and Discussion

This chapter addresses the results from experimental tests, FEA, and MSSR analysis. The analysis of fracture surface, crack initiation mechanism, fatigue life, stress solutions from FEA, MSSR prediction, and variable contact load effects are also summarized and discussed in this chapter.

6.1. Experimental Tests

Twenty tests were accomplished in this study, and the experimental results are summarized in Table 5. Among them, eight tests were conducted using un-peened specimens, and the other twelve were shot-peened ones. In addition, axial loads were manipulated to create tests under tension-tension and tension-compression fatigue conditions. It should be mentioned that Test 20 failed near the grip, which was far away from the contact region, after the application of 1.6 million cycles. Moreover, it was also noticed that relatively large gross slip and a sudden drop in tangential load during fretting fatigue cycles were observed for Test 13 and Test 15. Therefore, even though the experimental data from Test 13, 15, and 20 are recorded here, these three tests were not included in FEA and MSSR analysis to be discussed in the following sections.

6.1.1. Determination of Fretting Fatigue Condition

Fretting fatigue conditions were determined using hysteresis loop between a tangential load and an axial load as shown in Figure 22. These figures clearly show that partial slip fretting condition was met just after a few hundreds of fretting fatigue cycles. Figure 23 shows that after a steady fretting fatigue configuration was fulfilled, tangential loads remained stabilized from the beginning to the very end of a test. Combining Figure

22 and 23 together, it was obvious that for this study, partial slip fretting fatigue condition was met in a few hundreds of fretting fatigue cycles and then it was the case until the very end stage of experiments. In other words, steady state fretting fatigue configuration was quickly met among all tests after relatively few fretting fatigue cycles, and, after that, all fretting variables including coefficient of friction, contact load, tangential load, and axial load kept in stable through the majority fatigue life until the specimen broke into two pieces.

6.1.2. Q/P Ratio

The Q/P ratio was determined by dividing the tangential load (Q), by the contact load (P). The maximum Q/P, $(Q/P)_{max}$, ratio is considered as the lower boundary of the static coefficient of friction between a fretting specimen and pads in order to prevent gross slip condition. The maximum Q/P ratio was summarized in Table 5. From this table, $(Q/P)_{max}$ were less than 0.5 for most of these tests and had a small variation under different load conditions amid all tests. Figure 24 illustrates that under fretting fatigue phenomenon, Q/P was proportional to axial load under 0 Hz contact load condition and is subjected to variation in value over time. In other words, Q/P was changing dynamically all the time under fretting fatigue tests, but $(Q/P)_{max}$ presented much smaller variation among different tests.

6.1.3. Characteristics of Tangential Load

Typical characteristics of tangential load were presented in Figure 25. The tangential loads always demonstrated as a sinusoidal wave in phase with the corresponding axial load. Also, the frequency of tangential load was always identical to

that from axial loads. Contact loads only played a role in affecting the magnitude of tangential loads but had no effect on their waveform, frequency, and phase lag.

Figure 25 is also useful in highlighting the interactions between tangential loads, contact loads, and axial loads. This plot also provided the information about how to discretize a continuous load condition from experimental tests into discrete load steps for FEA modeling as mentioned before in Figure 14. Comparison of Figure 14 with Figure 25, they show the same pattern and feature in terms of load conditions, and hence the load inputs for FEA model was verified by these experimental outputs.

6.1.4. Fracture Surface

Fracture surfaces of specimens were examined with a scanning electron microscope. The observed general fracture topographies presented four distinguishable regions as shown in Figure 26(a); there were debris in Region 1, fine striations in Region 2, large dimples in Region 3, and catastrophic fracture in Region 4. Figure 26(b) explains the pattern observed from region 1, where crack initiated and grew at the early stage. This region is characterized by cleavage facets, steps, and oxidized debris. No striations could be found within this region. Region 2, illustrated in Figure 26(c), shows fine striations with grain boundary and was the main region for crack propagation. Large dimples with grain boundary definition were found in Region 3 as presented in Figure 26(d). The features of Region 4, where final, unstable crack growth occurred, were commonly associated with ductile tearing and shear lip, resulting catastrophic failure.

6.1.5. Fatigue Life

In order to explore the effects introduced by variable contact loads, experimental tests were categorized into 4 groups based on contact load configurations as well as

specimen surface condition, i.e. shot-peened vs. un-peened, as presented in Table 6 and Figure 27.

For un-peened specimens under constant contact loads, Category 1 shows that higher fatigue life occurred with a higher contact load, and the fatigue life from variable contact load cases was higher than that from constant contact loads. However, the observations from Category 2 were different from Category 1. In Category 2, higher constant contact loads reduced fatigue life when compared to lower constant contact loads, and the fatigue life from variable contact loads was located between its counterparts from corresponding high and low bounds of constant contact loads. For shot-peened specimens under constant contact loads, Category 3 demonstrates that higher fatigue life was found with higher contact loads, which was similar to the observation from Category 1. In Category 3, nevertheless, the fatigue life from variable contact loads was lower than that observed from constant contact load cases. Tests in Category 4 had similar fatigue life except for the test conducted under 30 Hz contact load. However, it should be emphasized that the variation among tests within the same category was less significant when the variation from different categories was taken into account.

When fatigue life from Category 1 was compared with Category 3, fatigue life was improved greatly due to a shot-peening process. Taking Category 1 and 2 into consideration, an extended fatigue life in Category 2 shows that the mean stress and stress ratio of an axial load played a crucial role in fretting fatigue life determination in addition to stress range. A similar fatigue life between Category 2 and Category 3 was found, inferring that the fatigue life improving mechanism from a shot-peening process resembled, in some extent, reducing mean stress value from axial loads. Finally,

combining Category 3 and Category 4 together, it was found that fatigue life was affected not only by tension axial stress but also compressive axial stress. That is, compressive stress also made contribution to fatigue life reduction under tension-compression axial stress configuration.

In summary, no obvious correlation between fatigue life and contact load conditions, in terms of frequency and magnitude, could be observed among these four categories, and fatigue life was primarily dominated by the applied axial load conditions as well as specimen surface treatment. This observation matched the findings from Iyer's [18] two-level block loading test using 200Hz axial load as well as Jutte's [25] study under bi-directional shear tests which was discussed in Section 2.4.3.

6.1.6. Stress Range and Effective Stress

Stress Range was defined in Equation (32), and effective stress in Equation (33). Using the X-ray diffraction technique and numerical approach, the shot-peening induced residual stress profile was determined in Figure 21, with maximum compressive stress -804 MPa at a depth of 25 μm and maximum tensile stress +277 MPa at 226 μm depth. Different stress relaxation rates were also applied to examine the effect on effective stress in this section. In addition, a different stress relaxation assumption made by the present author in Section 5.3, which is again mentioned in the following, was also used in discussing the influence on effective stress:

1) For tests with fretting fatigue life less than 100,000 cycles, shot-peened specimens are subjected to 20% relaxation.

2) For tests with fretting fatigue life between 100,000 and 1 million cycles, shot-peened specimens are subjected to 30% relaxation.

3) For tests with fatigue life higher than 1 million cycles, shot-peened specimens are subjected to 40% relaxation.

For comparison, the results from present study as well as previous experiments using similar test configuration were collected and summarized in Table 7. The data listed in this table was then used to plot $\Delta\sigma$-N_f and σ_{eff}-N_f curves as demonstrated in Figure 28 to 30. It should be mentioned, however, by using the scanning electron microscope technique documented in Section 6.1.8, crack initiation in this study for shot-peened specimens was found in the interior of specimens at a region where residual tensile stress existed and close to the maximum tensile stress similar to Namjoshi's observation [9]. For un-peened specimens, on the other hand, cracks were found to initiate along the contact surface.

Figure 28(a) and (b) shows that introduction of variable contact loads caused a bigger scatter associated with $\Delta\sigma$-N_f curve, especially for shot-peened specimens. Nevertheless, no clear correlation between contact load conditions, in terms of frequency and magnitude, and fatigue life was observed. When all test data was plotted in Figure 28(c), more deviation was found at a fatigue life around 100,000 cycles. However, from an overall outlook, all tests fell into a single curve within a large scatter band.

The effective stress was more successful in collapsing fatigue data into a single curve for un-peened specimens although accompanied with some scatter as demonstrated in Figure 29(a). On the other hand, the shot-peening process introduced more scatter into fatigue life distribution as shown in Figure 29(b) ~ (e), and no correlation between contact loads and fatigue life could be found, either. In addition, Figure 29(f) suggests that a different relaxation assumption was effective in collapsing fatigue data into a single

curve for shot-peened specimens. It was also noticed from Table 7 that effective stress reduced with the increase of stress relaxation.

A comparison between constant and variable contact loads using the effective stress for all tests is plotted in Figure 30. With 100% stress relaxation, all fatigue data lie in a curve with small deviation, but no clear relation between contact load conditions and fatigue life could be figured out. When different stress relaxations other than 100% relaxation were imposed, fatigue data from shot-peened and un-peened specimens were separated into two distinguishable trend lines. These trend lines also presented that a shot-peening process improved fretting fatigue life just as observed from experimental results. However, no obvious correlation between contact load conditions and fatigue data can be established for all tests.

6.1.7. Contact Half-Width

A typical scar pattern is illustrated in Figure 31. This photo showed clearly a stick zone with partial slip regions aside just as the deformed contact model presented in Figure 4. A contact region, termed as $2a_{Exp,max}$, was defined by incorporating both the stick zone and partial slip regions.

Contact half-widths from the Ruiz program, FEA calculation, and experimental measurements were collected and summarized in Table 8. On comparison contact half-widths from the Ruiz program with those from FEA outputs, the maximum variation was less than 4% at Step 1 and 7% at maximum load condition. Also, the maximum difference between the Ruiz solution and experimental measurements increased to 16%. However, it should be mentioned that a part of this variation was introduced by the vague scar boundary on the specimen surface caused by a severe slip condition at the final stage

of fretting tests that created difficulty in recognizing and measuring contact half-width from experimental scar. When examining contact half-widths from FEA outputs at Step 1 and at maximum load condition, an asymmetric distribution, introduced by the alternating axial load, with respect to the center of contact region up to 10% in terms of $a/a_{Ruiz,\ max}$ ratio was noticed. These measurements also confirmed that contact half-widths were only affected by the magnitude of contact load and independent upon the contact load frequencies and axial load conditions as predicted by Equation (11).

Overall, even if the Ruiz program was developed with infinite half space assumption under static axial and contact load conditions, it is still a practical tool for estimating contact half-width under cyclic load conditions with accuracy because the Ruiz program can save tremendous work in complex modeling and calculation.

6.1.8. Crack Initiation Location and Pattern

In general, crack initiation location in all tests, as shown in Figure 32, always occurred at a location where $x/a_{Exp,max} \approx +1$ along x-direction. For un-peened specimens, cracks always initiated at the contact surfaces as demonstrated in Figure 33. On the other hand, under the influence of a shot-peening process, crack initiation depths shifted from the contact surface to depths ranging from 180 ~ 240 μm within the interior as illustrated in Figure 34 . Crack initiation depths for all tests were examined by scanning electron microscope and summarized in Table 9.

Two patterns of crack initiation were observed and could be manifested as single crack initiation and multi-crack initiation as presented in Figure 35. A summary for crack initiation patterns is tabulated in Table 9. From this table, it is noticed that all un-peened specimens and some shot-peened specimens had the pattern of multi-crack initiation.

Nevertheless, no clear correlation between load conditions and crack initiation pattern could be realized from the present study.

6.1.9. Crack orientation

It is well documented in previous studies that under constant contact loads, crack initiation orientation was found about either +45˚ or -45˚ for un-peened specimens [20,22,23,25,50] and ranging from -37˚ to -54˚ for shot-peened specimens [1] as mentioned in Section 2.6.2. In this study, the present author was more interested in determining crack initiation orientation for specimens under variable contact loads. Since crack initiated in the interior of shot-peened specimens, it caused difficulty in measuring crack initiation orientation, un-peened specimens under variable contact loads with frequencies 2.5 Hz (Test 3) was selected to investigate crack initiation orientation. Photos from scanning electron microscopy presented in Figure 36 shows that crack initiation orientation was -50˚, which is equivalent to +40˚, for 2.5 Hz test. Comparing these observations to previous results, variable contact loads under different frequencies didn't alter crack initiation orientation significantly from constant contact load cases.

6.1.10. Summary of Contact Load Effects

Under either constant or variable contact loads, the tangential load was always a sinusoidal waveform in phase without any lag with its corresponding axial load. Variable loads made contribution to tangential loads only in magnitude but had no effect on the wave shape, frequency, and phase lag.

For all tests under constant and variable contact loads, there were four distinguishable regions found on the typical fracture topography, and they were debris at

Region 1, fine striation at Region 2, large dimples at Region 3, and catastrophic fracture at region 4.

When constant and variable contact load effects were compared in terms of fatigue life on the basis of the stress range and effective stress for un-peened specimens and shot-peened specimens with stress relaxation, no major different could be distinguished between contact load conditions and fatigue life. Fatigue life data from variable contact loads was about the same as that from constant contact load conditions with a narrow scatter band.

Two patterns of crack initiation were noticed, which were single-crack initiation and multi-crack initiation, and they were found to have no obvious dependence on contact load conditions.

The crack orientation for variable contact loads was found to be -50˚ for 2.5 Hz case, which were close to its counterpart from tests under constant contact loads.

6.2. Effects from Coefficient of Friction

Static coefficient of friction (f) used in this study was discussed in detail in Section 4.4 and tabulated in Table 5. So far, the determination of dynamic coefficient of friction under fretting fatigue is still unclear in the fretting fatigue literature. Moreover, Section 6.1.2 shows that Q/P under fretting conditions was varying over time and couldn't be treated as a constant at all. In order to highlight the effects introduced by variable contact loads, the coefficient of friction was assigned as 0.5 for all tests in this study except for those cases where experimental output $Q/P < 0.5$ was violated. For these exceptions, the maximum Q/P from experimental observations was applied as the static coefficient of friction instead.

Since a simplified assumption was made for the coefficient of friction, analyzing and understanding the repercussion on fretting fatigue variables such as stress profiles and MSSR parameter introduced by this assertion should be investigated and assessed before proceeding to further discussions. For this sake, four different values, 0.4, 0.5, 0.65, 0.8 and 1.0, were chosen as coefficients of friction and applied to Test 1 to clarify the influence on stress profile from FEA calculation and on MSSR computation. Figure 37(a) shows that increasing the coefficient of friction up to 250% (from 0.4 to 1.0), only increased maximum σ_{xx} by 27 % while the location of peak σ_{xx} remained invariant. More noticeable deviation from varying coefficient of friction was found on σ_{xy} stress profile as can be seen in Figure 37(c). However, there was no influence observed for σ_{yy} stress profile from Figure 37(b). That is, the coefficient of friction had no effect on the σ_{yy} stress distribution on the contact surface.

For MSSR determination, Figure 38(a) illustrates that for the coefficient of friction changing from 0.4 to 1.0, maximum MSSR only increased from 32.77 to 38.12 (15%) while keeping its location invariant. Moreover, for un-peened specimens, maximum MSSR always occurred on the contact surface despite the values of the coefficients of friction as displayed in Figure 38(b). This plot also demonstrates that the deviation was more pronounced near the contact surface and then became flattened along with the increase of depth. Deeper than a depth of 282 μm, no influence on $MSSR_{max}$ could be observed due to changing values for coefficients of friction.

Table 10 tabulates the details for MSSR computation under different coefficients of friction. It was observed that 15% increase in $MSSR_{max}$ occurred due to increasing coefficients of friction from 0.4 to 1.0. However, $MSSR_{max}$ always happened at $x/a_{Ruiz,max}$

=0.93 along contact surface, with a variation of 5˚ in crack orientation prediction. This shows that changing the coefficient of friction had no influence on MSSR crack location and orientation prediction and had only limited effect in crack initiation orientation determination.

6.3. Finite Element Analyses

With load details discussed in Section 4.3, the measured experimental load values tabulated in Table 5 were applied to FEA model to compute stress, strain, and displacement distribution within a whole specimen. The issues addressed in this section include thickness effect on FEA solutions, σ_{xx} stress concentration, asymmetric distribution of σ_{yy}, evolution of stress state, and influence on stress profile from residual stress.

6.3.1. Thickness Effects on Stress Profile

Since two different specimen thicknesses, 3.81 mm and 4.83 mm, were used in this study, the present study investigated the repercussions from different thicknesses on local stress distribution. Thickness effect on stress distribution is demonstrated in Figure 39. While specimen thicknesses changed from 3.81 mm to 4.83 mm (27% increase), maximum σ_{xx} increased from 929.34 MPa to 933.14 MPa (4% increase), and the location moved from $x/a_{Ruiz,max}$ = 0.931 to 0.953. In addition, maximum σ_{xy} changed from 58.65 MPa to 57.84 MPa (1.3%) with the location keeping unchanged at $x/a_{Ruiz,max}$ = -0.0875. Also, peak σ_{yy} was found to be invariant in both magnitude and location under the increase of thickness, which was 39.93 MPa at $x/a_{Ruiz,max}$ = 0.0337.

In summary, increasing specimen thickness up to 27% had only limited effect in stress profile, and stress curves from different thicknesses, 3.81 mm and 4.83 mm, matched each other very well.

6.3.2. Stress Concentration of σ_{xx}

Fretting fatigue configuration introduced stress concentration in σ_{xx} as displayed in Figure 39(a) Also, Equation (20) in Section 2.1 inferred that contributing factors to this concentration included contact load, tangential load as well as axial load. Take Step 2 of Test 1 for instance, maximum σ_{xx} concentration factor obtained by the Ruiz program, which assumed infinite half space was satisfied, was 1.457 at $x/a_{Ruiz,max}$ =0.96. When stress profiles were solved by FEA for Test 1 using 3.81 mm specimen thickness, with $b/a_{Ruiz,max}$ =3.37 at Step 2, the maximum σ_{xx} concentration factor raised to 1.548 at $x/a_{Ruiz,max}$ =0.931. On comparison FEA outputs to Ruiz solution, it was 6% increase in magnitude and 3 % deviation in location. FEA solutions from 3.81 mm specimen thickness and from 4.83 mm thickness showed that the location for the maximum σ_{xx} concentration factor shifted from $x/a_{Ruiz,max}$ =0.931 to 0.963, but no significant deviation in magnitude was observed.

In short, the maximum σ_{xx} concentration factor increased from 1.457 for infinite half-space cases to 1.548 (6% increase) for 3.81 mm specimen thickness cases. However, when specimen thickness increased from 3.81 mm to 4.83 mm (30% increase), no significant variation in magnitude was observed.

6.3.3. Asymmetric Distribution of σ_{yy}

The asymmetric distribution of σ_{yy} stress profile could be observed from Figure 39 (b). Here, Step 2 from Test 1 was chosen as an example to explain this asymmetric

property of σ_{yy} stress profile. From the Ruiz program, the Hertzian peak pressure was determined as -396.70 MPa at $x/a_{Ruiz,max} = 0$ with respect to the center of contact zone. Nevertheless, from FEA calculation for 3.81 mm specimen thickness, the location of Hertzian peak stress moved to $x/a_{Ruiz,max} = -0.00337$ while keeping magnitude unchanged. On the other hand, changing specimen thickness from 3.81 mm to 4.83 mm didn't alter significantly the magnitude and location of Hertzian peak pressure carried out by FEA stress solution.

6.3.4. Evolution of Stress Profiles

For Test 3, the maximum axial and tangential loads occurred at Step 10, 12, and 14 while the contact load reduced in magnitude from its maximum value at Step 10 to its minimum value at Step 14. Moreover, the load conditions at Step 10 and Step 18 were the same, which were both at the maximum load condition defined in Section 4.7. Figure 40(a) presents the evolution for σ_{xx} stress profile at different steps of Test 3. This figure explains that under different steps of Test 3, the maximum value of σ_{xx} changed continuously from 907 MPa with $x/a_{Ruiz,max} = 0.674$ at Step 10 to 1013 MPa with $x/a_{Ruiz,max} = 0.944$ at Step 14. Furthermore, Figure 40(b) indicates that Hertzian peak pressure increased from -399 MPa with $x/a_{Ruiz,max} = -0.0475$ at Step 10 to -570 MPa at Step 14 with unchanged location.

When two steps of Test 3, Step 10 and Step 18, were compared together in Figure 40(d), it shows that stress profiles were only affected by the load condition at that step. In other words, stress profile determination was independent of applied load sequence and the adjacent steps, and a stress profile was only determined by the applied loads at that specific step. However, it should be noticed that among different tests, stress profiles at

maximum load conditions were no longer identical to each other even under the same axial and contact loads as demonstrated in Figure 41. Theses variation on stress profiles among different tests probably came from the difference in tangential loads measured in each test.

6.3.5. Stress Profile with Residual stress

Figure 42 presents stress profiles at different depths for a shot-peened specimen at Step 4 of Test 1 under 100% stress relaxation. From this figure, maximum σ_{xx} reduced from 931 MPa with $x/a_{Ruiz,max} = 0.95$ on contact surface to 657 MPa with $x/a_{Ruiz,max} = 2.03$ at a depth of 226 μm. Additionally, Hertzian peak pressure varied from -399 MPa with $x/a_{Ruiz,max} = -0.06$ on the contact surface to -398 MPa with $x/a_{Ruiz,max} = -0.21$ at 226 μm depth.

The influence on stress profiles from stress relaxation on contact surface at Step 4 of Test 9 is illustrated in Figure 43. These figures show maximum σ_{xx} decreased from 931 MPa at $x/a_{Ruiz,max} = 0.95$ under 100% relaxation to 138 MPa at the same location under 0% relaxation. Hertzian peak pressure was also lowered from -397 MPa at $x/a_{Ruiz,max} = -0.06$ under 100% relaxation to -1190 MPa with the location unchanged under 0% relaxation. No effect on σ_{xy} stress distribution from stress relaxations was found as expected since residual stress was assumed as bi-axial distribution, $\sigma_{xx} = \sigma_{yy}$ and $\tau_{xy=0}$, and resulted in no contribution on σ_{xy} stress profile.

At a location 226 μm below the contact surface, the influence on stress profiles under stress relaxations is also demonstrated in Figure 44. The maximum σ_{xx} raised from 657 MPa at $x/a_{Ruiz,max} = 1.86$ under 100% relaxation to 934 MPa at $x/a_{Ruiz,max} = 2.01$ under 0% relaxation. Hertzian peak pressure also increased from -398 MPa at $x/a_{Ruiz,max} = -0.02$

under 100% relaxation to -121 MPa under 0% relaxation while the location was unchanged. No effect on σ_{xy} stress profile from different relaxation rates was noticed just like the case observed along contact surface.

On comparison of stress profiles on the contact surface with 100% relaxation to those at a depth of 226 μm, maximum σ_{xx} decreased from 931 MPa to 657 MPa. Also, the gradient of σ_{xx} stress profile became flat with the increasing depth. However, when taking stress profiles under 0% relaxation into account, maximum σ_{xx} raised from 138 MPa along contact surface to 934 MPa at 226 μm depth due to the residual compressive stress near the contact surface and tensile stress within the interior of the specimen.

6.4. MSSR

A comprehensive MSSR calculation was conducted. The maximum MSSR for each test used in this study was then determined and compared with the data from previous researches. The correlation between MSSR fretting fatigue life was investigated, and the effects from stress relaxations are also discussed. The effectiveness of MSSR prediction is looked into in terms of fatigue life, crack initiation location and orientation.

6.4.1. Determination of the Maximum MSSR

The fatigue predictive parameter, MSSR, was defined in Equation (43), and a detailed discussion for MSSR is presented in Section 2.5.7. As mentioned in Section 5.1, the values of MSSR parameter were symmetric with respect to a full load cycle. In addition, two load steps were needed for the MSSR determination. In this study, the peak and valley of either normal or axial loads were sampled and numbered into discrete steps as shown in Figure 14. To determine the MSSR parameter between two steps in a test, an exhaustive MSSR calculation between different step pairs with different amount of stress

relaxation rates was executed for each test, and the results are listed in Table 11. Among them, the MSSR with the greatest value was chosen as the maximum MSSR of that test ($MSSR_{max}$) and is further summarized in Table 12(a) and Table 13. In order to compare the data from this study to that from previous researches, MSSR results from several former investigations using similar test configuration, 50.8 mm radius cylindrical-end fretting pads, was also put together into Table 12(b)~(d), which will be discussed in latter sections.

From Table 13, the maximum MSSR occurred between different step pairs among test groups with different contact load frequencies. On the other hand, for test groups with the same contact load frequency, the maximum MSSR was found to happen at the same step pair even though the mean stress and stress range of axial loads were different.

6.4.2. MSSR under Residual Stress Relaxation

It should be mentioned that, in practice, 100% stress relaxation is equivalent to 0% residual stress imposed, which defines a condition where no residual stress is imposed into stress and MSSR calculation. From Table 12(a) for shot-peened specimens, the $MSSR_{max}$ with 100% stress relaxation had the highest value. Once stress relaxation other than 100% relaxation was imposed, which ranged between 0% ~ 50% in this study, the $MSSR_{max}$ parameter always happened at a depth of 226 μm instead of on the contact surface. The increase of stress relaxation from 0% to 50% was accompanied with the decreasing magnitude of $MSSR_{max}$, but the depth for $MSSR_{max}$ occurrence was always at 226 μm below the contact surface.

Table 13 provides crack initiation location and orientation with different stress relaxations. The $MSSR_{max}$ was found near the trailing edge at locations where $x/a_{Ruiz,max}$ =

0.81 ~ 1.46 for all tests regardless of stress relaxations. For 100% stress relaxation, the $MSSR_{max}$ occurred on the contact surface for all tests but at 226 μm depth when other amount of relaxations was imposed into shot-peened specimens. Due to the influence of stress relaxations, MSSR prediction on crack orientation varied between 34˚ ~ 45˚. For tests under the same stress relaxation, however, contact loads had no effect on the determination of crack initiation depth, limited effect on crack orientation prediction which was about 8˚ at most, and produced maximum variation of about 0.41in the value of $x/a_{Ruiz,max}$ along x-direction. For a test with different relaxations, the $MSSR_{max}$ always occurred between the same two steps. That is, changing stress relaxations didn't change the step pair at which the $MSSR_{max}$ happened.

Figure 45 illustrates MSSR with different stress relaxations along with depths under different contact load frequencies. With 100% stress relaxation, the greatest MSSR parameter always occurred on the contact surface and reduced in magnitude with the increase of depth. When different stress relaxation rates other than 100% were considered, the highest MSSR shifted to 226 μm below the contact surface. Furthermore, MSSR behavior presented in Figure 45 showed a similar pattern with each other regardless of contact load conditions in terms of frequencies and magnitudes.

6.4.3. Fatigue Life

Tests conducted in this study were divided in four categories based on axial load configuration and surface treatment as illustrated in Figure 46. For un-peened specimens under constant contact loads, the greater $MSSR_{max}$ was found with the higher constant contact loads. The $MSSR_{max}$ for variable contact loads was located between its counterparts from corresponding high and low bounds of constant contact loads.

However, it should be clarified that even though these observed trends were distinguishable, they were relatively less significant when compared with deviations under different categories. When stress relaxations other than 100% were imposed to shot-peened specimens, there was no significant variation found on $MSSR_{max}$ within the same category, and no strong correlation between $MSSR_{max}$ and contact load configurations could be drawn.

Figure 47 shows the comparison for the $MSSR_{max}$ results from this study and previous researches using similar test configuration. No significant distinction from contact load variation can be noticed for un-peened specimens, and all $MSSR_{max}$ collapsed into a single curve well within a scatter band. When stress relaxations other than 100% were imposed for shot-peened specimens, no significant dependence on contact load conditions could be found even if shot-peening process introduced more scatter into these plots. Different stress relaxation hypothesis postulated in Section 5.3 by the present author seems to be effective in further collapsing $MSSR_{max}$-N_f into a curve with even narrow deviation as shown in Figure 47(f).

When contact loads were categorized and considered as only constant or variable conditions, a comparison of $MSSR_{max}$-N_f relation is presented in Figure 48. These MSSR data from constant and variable contact loads fell into a single curve with small deviation for un-peened tests, and similar phenomenon was also observed for shot-peened experiments with stress relaxations other than 100% relaxation. Again, when different relaxation assumption was applied in Figure 48(e), MSSR parameter was effective in collapsing data from both un-peened and shot-peened specimens into a single curve, regardless of the contact load conditions.

6.4.4. Crack Initiation Details

MSSR predictions for crack initiation locations and orientations under stress relaxations are summarized in Table 13. For un-peened specimens, $MSSR_{max}$ always occurred on the contact surface with $x/a_{Ruiz,max} = 0.81 \sim 0.94$ as observed from experimental counterparts. Constant and variable contact loads had limited effect in crack orientation prediction, which was 9˚ at most, and no effect in crack initiation location prediction.

For shot-peened specimens under stress relaxations other than 100% relaxation, the location of $MSSR_{max}$ shifted to 226 μm in the interior of specimens with $x/a_{Ruiz,max}$ ranging between 0.81 and 1.46, which also matched the observation from experimental counterparts. Constant and variable contact loads had only limited effect on crack initiation orientation and location prediction, 8˚ in crack orientation and 0.41variation in value for $x/a_{Ruiz,max}$ at most.

From Table 13, MSSR predicted crack initiation orientation for un-peened specimens under 2.5 Hz contact load (Test 3) was 36˚, which matched experimental observations -50˚ (equivalent to +40˚). Comparing with previous studies, crack initiation orientation were either -45^{o} or $+45^{o}$ with a variation of $\pm 15^{o}$ under constant contact load configuration for un-peened specimens as discussed in Section 2.6.2. It can be seen that variable contact loads didn't have any significant effect on crack orientation. Overall, the MSSR parameter could predict the crack initiation location, depth, and orientation very well for both shot-peened and un-peened specimens regardless of contact load configuration.

6.4.5. Summary of Contact Load Effects on MSSR

For test groups categorized by contact load frequencies, $MSSR_{max}$ occurred between different step pairs among different groups. On the other hand, $MSSR_{max}$ was always found at the same step pairs for tests with the same contact load frequency even though shot-peened specimens were subjected to stress relaxations. For all tests, $MSSR_{max}$ always occurred along contact surface with 100% stress relaxation and at a depth of 226 μm when stress relaxations other than 100% took place. Constant or variable contact load configurations had no effect on MSSR crack initiation depth prediction and had only limited contribution on crack orientation and location predictions, which were, at most, 9˚ difference in crack orientation and 0.41 variation in the value of $x/a_{Ruiz,max}$.

When tests were divided as different categories based on axial load conditions and surface treatment, only relatively small variation in fatigue life was found for the same group, and the dependence on contact load conditions were vague. No consistent correlation between contact load configurations and $MSSR_{max}$ or fatigue life could be concluded.

As contact loads were considered as only constant or variable conditions, MSSR parameter was effective to collapse fatigue life into a single curve within an acceptable scatter band for un-peened specimens regardless of contact load conditions. Also, similar conclusion could be made for tests using shot-peened specimens with other than 100% stress relaxation. Furthermore, different relaxation assumption was more effective in further reducing the deviation in the fatigue life relationships. Under different relaxation assumption, $MSSR_{max}$ from shot-peened specimens appears to have greater value than that from un-peened specimens.

.

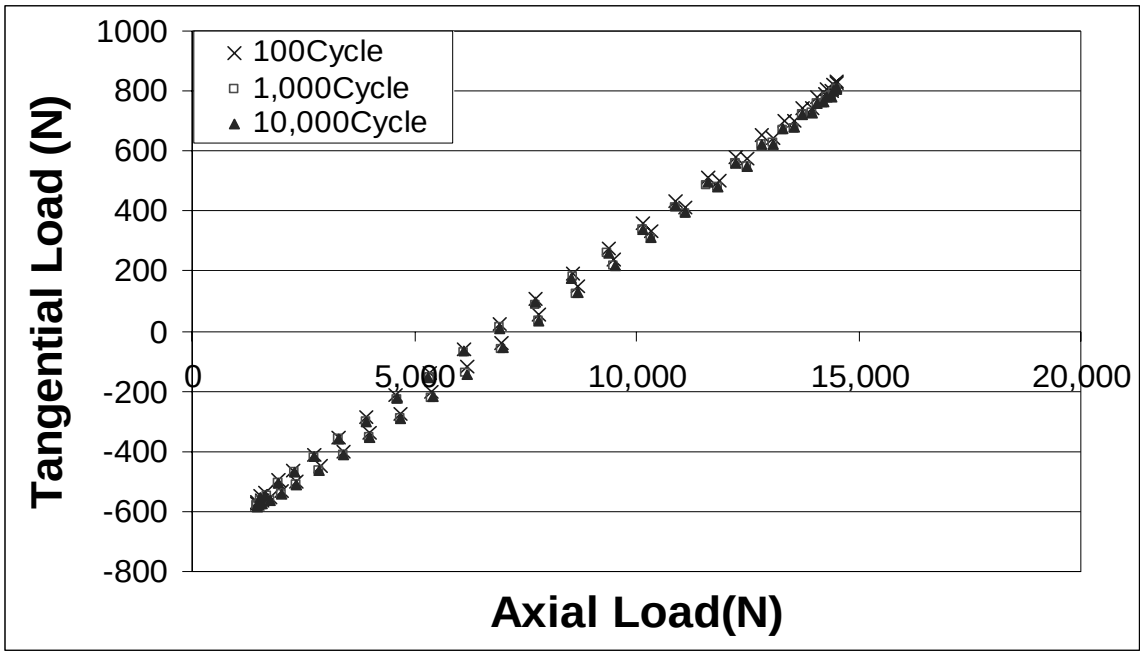

(a) Typical Hysteresis Loop for Test 1
Load Condition: σ_{max} =600 MPa, σ_{min} =60 MPa, P_{max} =2224 N, P_{min} =2224 N, P_{Freq} =0 Hz

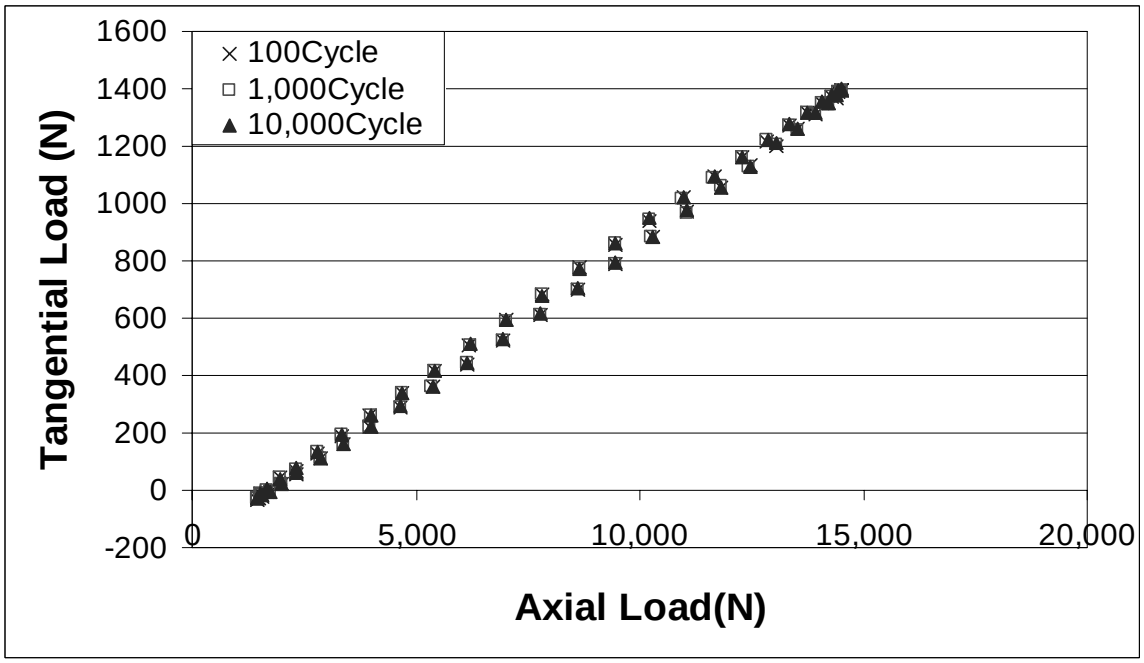

(b) Typical Hysteresis Loop for Test 2
Load Condition: σ_{max} =600 MPa, σ_{min} =60 MPa, P_{max} =4448 N, P_{min} =4448 N, P_{Freq} =0 Hz

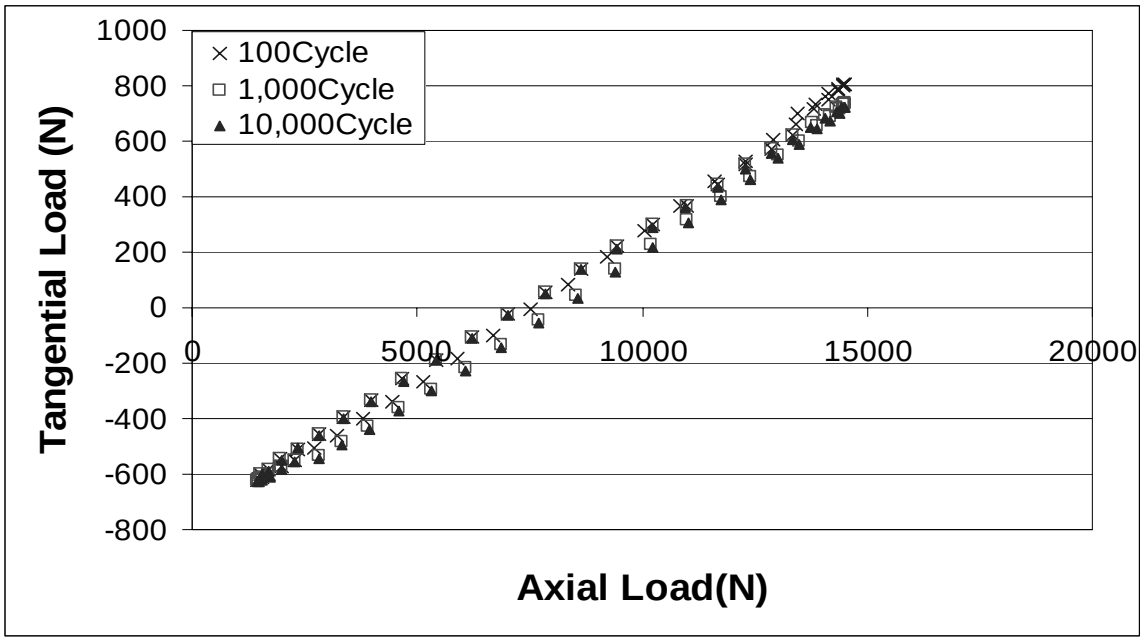

(c) Typical Hysteresis Loop for Test 3
Load Condition: σ_{max}=600 MPa, σ_{min}=60 MPa, P_{max}=4448 N, P_{min}=2224 N, P_{Freq}=2.5 Hz

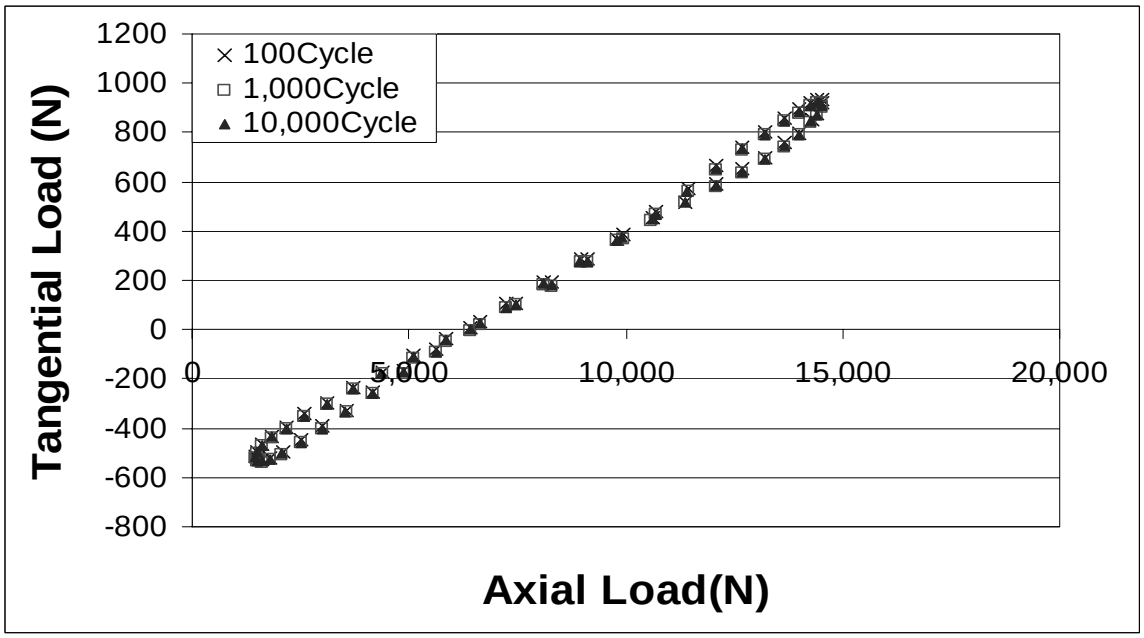

(d) Typical Hysteresis Loop for Test 4
Load Condition: σ_{max} =600 MPa, σ_{min} =60 MPa, P_{max} =4448 N, P_{min} =2224 N, P_{Freq} =30 Hz

Figure 22. Typical Hysteresis Loop of Tangential Load vs. Axial Load

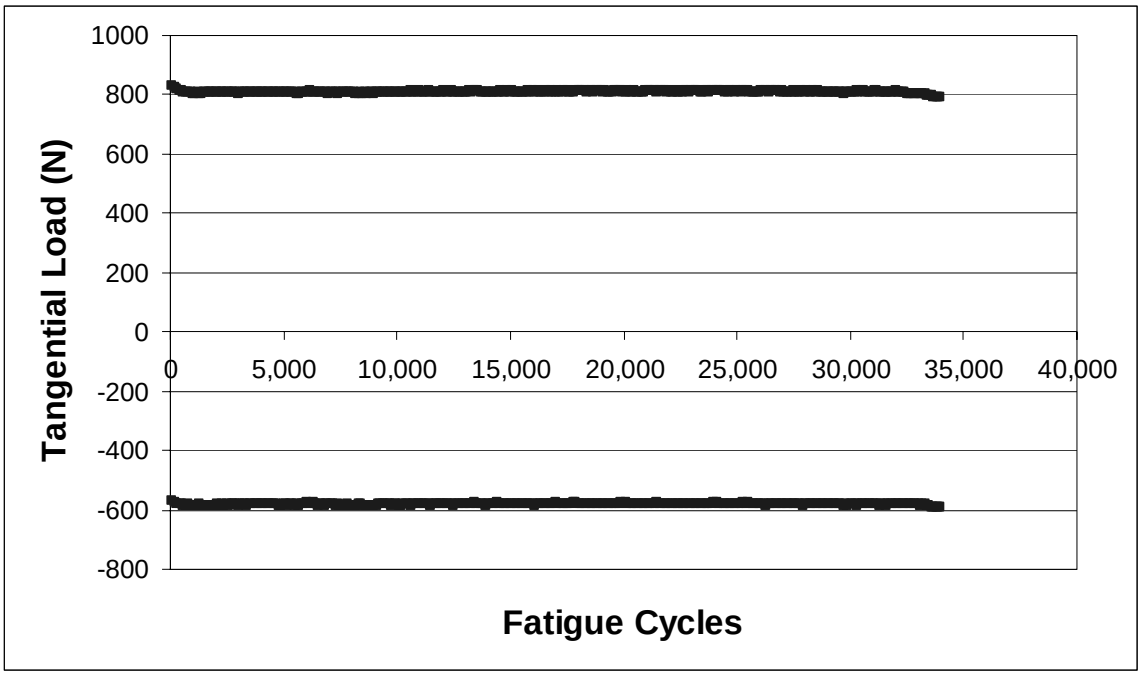

(a) Qmax & Qmin vs. Fatigue Life for Test 1
Load Condition: σ_{max} =600 MPa, σ_{min} =60 MPa, P_{max} =2224 N, P_{min} =2224 N, P_{Freq} =0 Hz

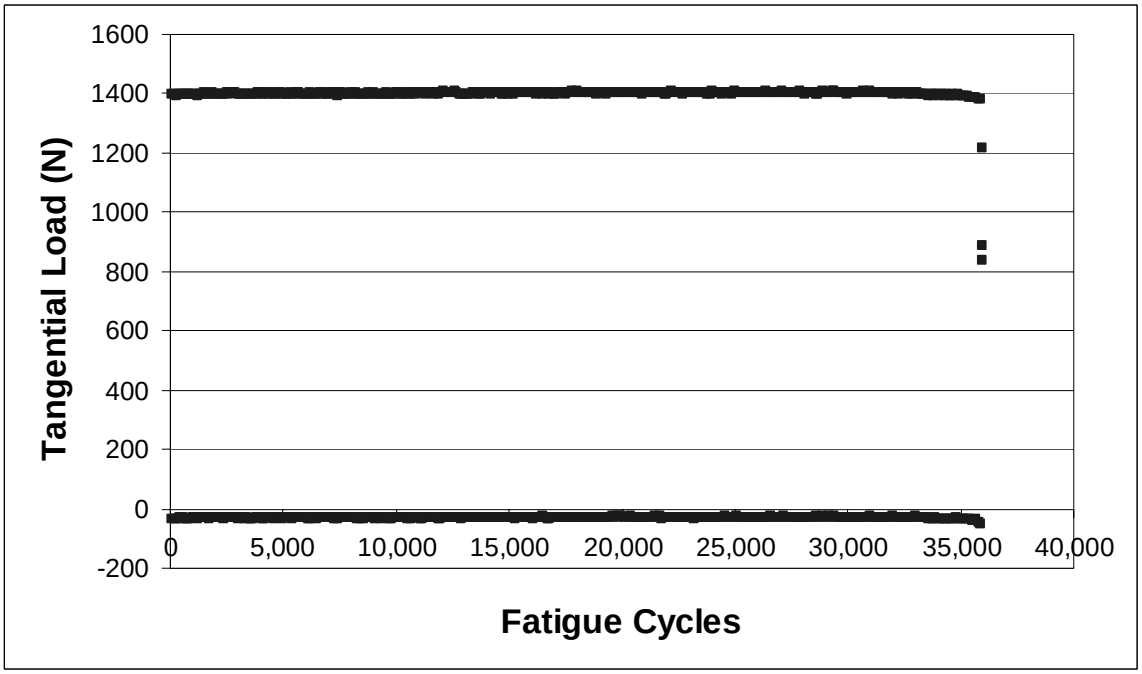

(b) Qmax & Qmin vs. Fatigue Life for Test 2
Load Condition: σ_{max} =600 MPa, σ_{min} =60 MPa, P_{max} =4448 N, P_{min} =4448 N, P_{Freq} =0 Hz

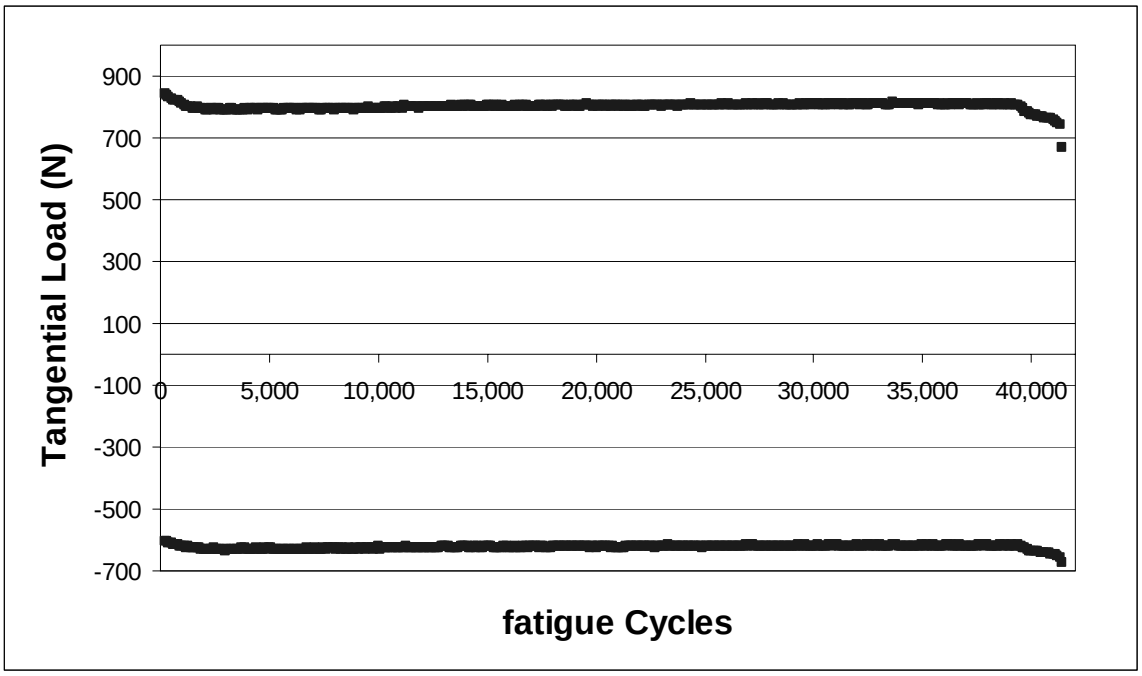

(c) Qmax & Qmin vs. Fatigue Life for Test 3
Load Condition: σ_{max}=600 MPa, σ_{min}=60 MPa, P_{max}=4448 N, P_{min}=2224 N, P_{Freq}=2.5 Hz

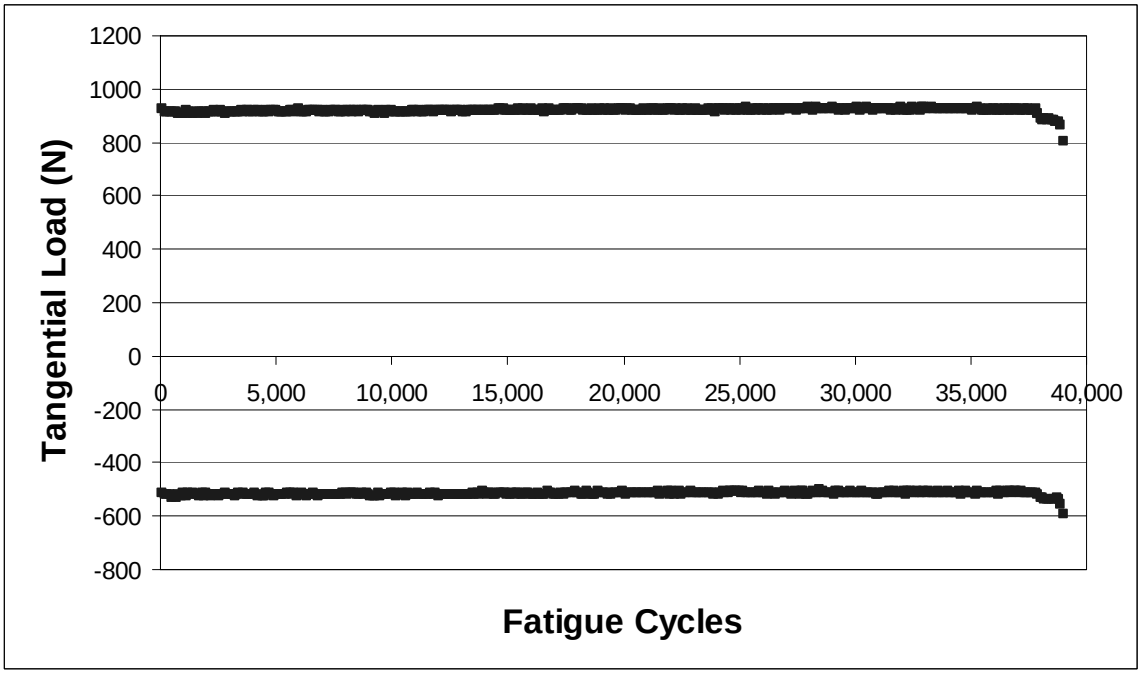

(d) Qmax & Qmin vs. Fatigue Life for Test 4
Load Condition: σ_{max} =600 MPa, σ_{min} =60 MPa, P_{max} =4448 N, P_{min} =2224 N, P_{Freq} =30 Hz

Figure 23. Qmax & Qmin vs. Fatigue Life

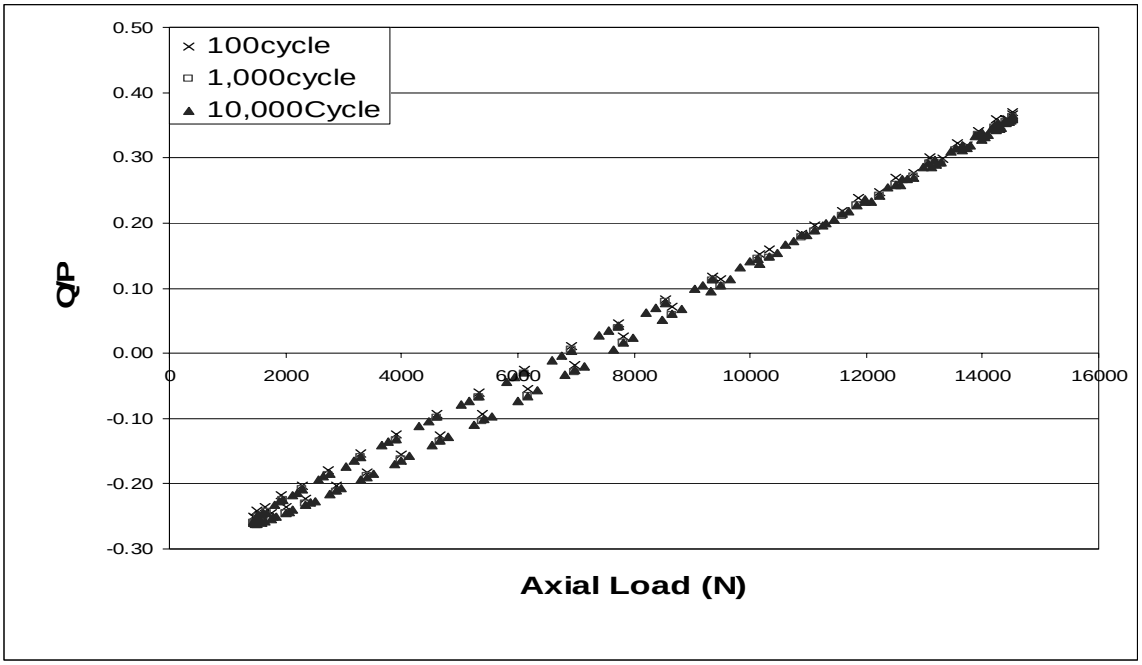

(a) Q/P vs. Axial Load

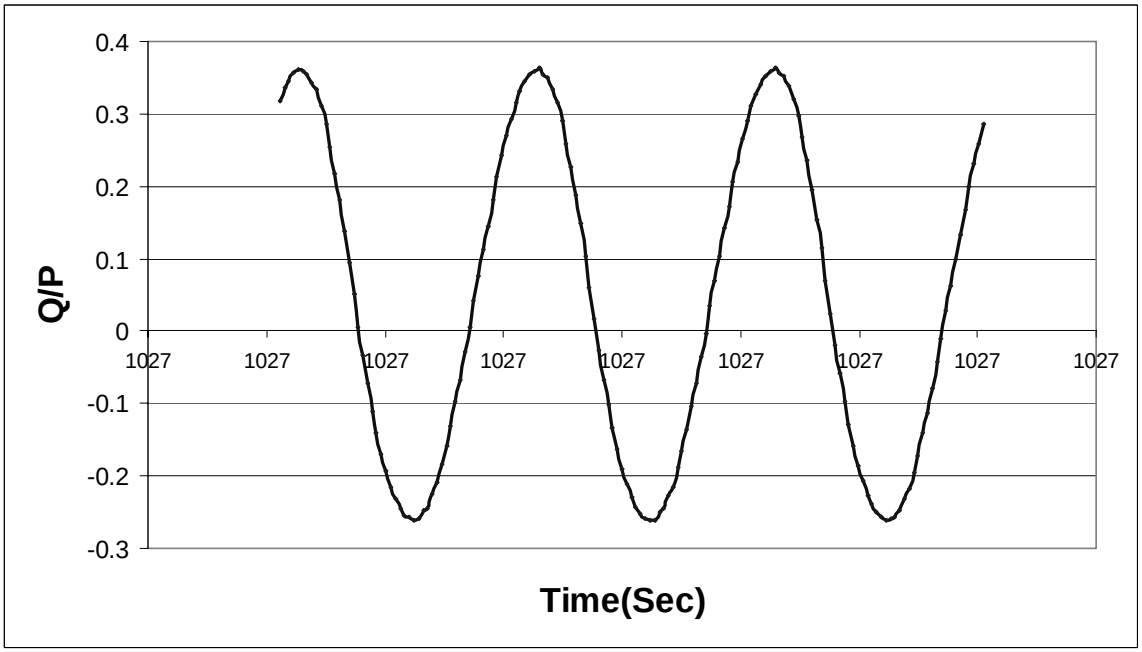

(b) Q/P vs. Time at 10,000th Cycle

Figure 24. Q/P Ratio for Test1
Load Condition: σ_{max} =600 MPa, σ_{min} =60 MPa, P_{max} =2224 N, P_{min} =2224 N, P_{Freq} =0 Hz

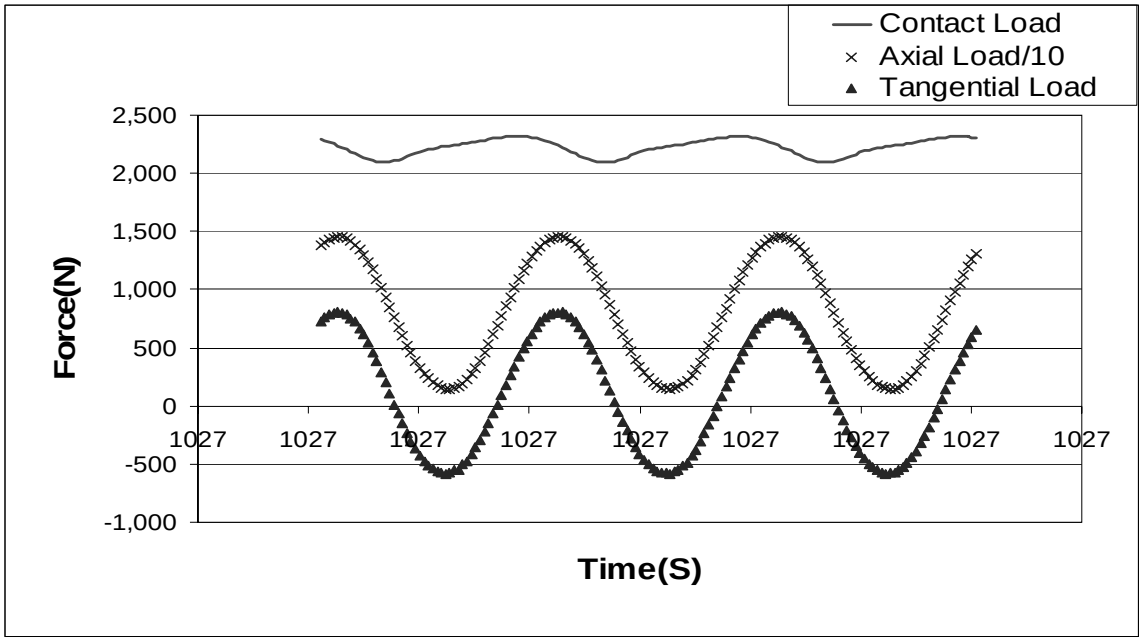

(a) Experimental Data Measured from Test 1

Load Condition: σ_{max} =600 MPa, σ_{min} =60 MPa, P_{max} =2224 N, P_{min} =2224 N, P_{Freq} =0 Hz

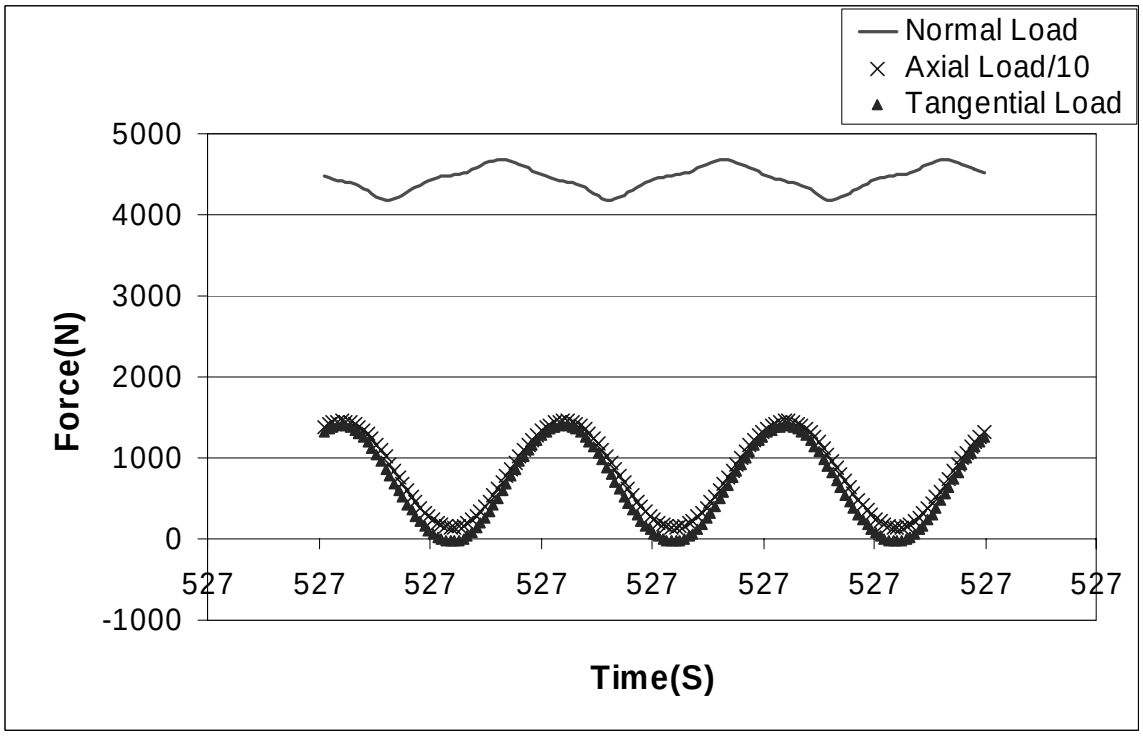

(b) Experimental Data Measured from Test 2

Load Condition: σ_{max} =600 MPa, σ_{min} =60 MPa, P_{max} =4448 N, P_{min} =4448 N, P_{Freq} =0 Hz

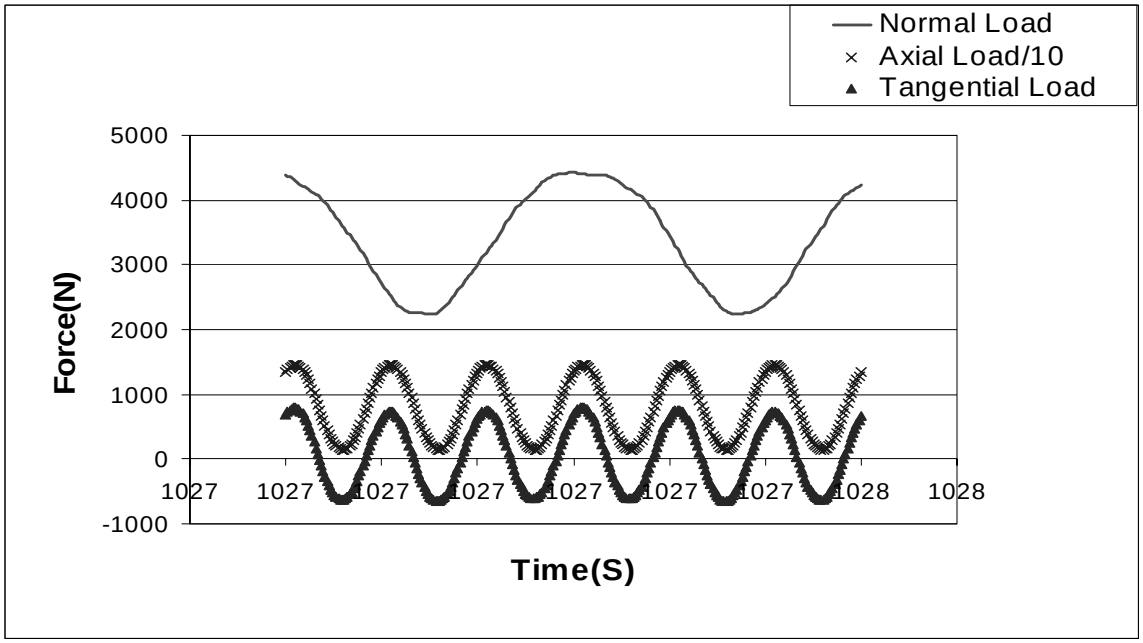

(c) Experimental Data Measured from Test 3
Load Condition: σ_{max}=600 MPa, σ_{min}=60 MPa, P_{max}=4448 N, P_{min}=2224 N, P_{Freq}=2.5 Hz

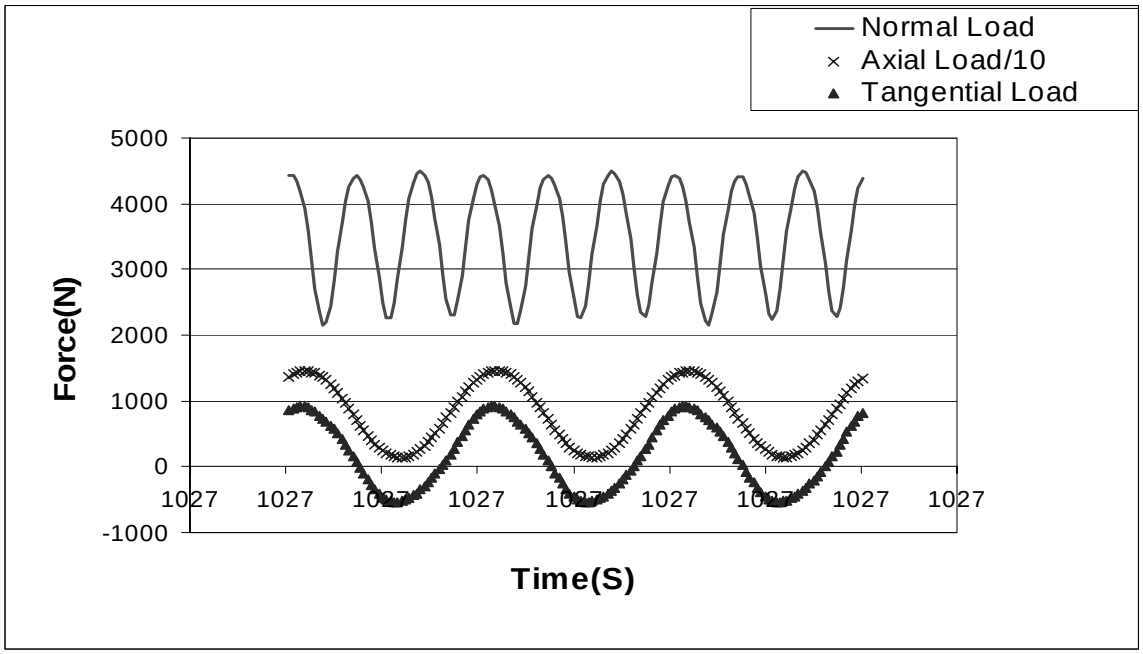

(d) Experimental Data Measured from Test 4
Load Condition: σ_{max}=600 MPa, σ_{min}=60 MPa, P_{max}=4448 N, P_{min}=2224 N, P_{Freq}=30 Hz

Figure 25. Relations among Axial Load, Contact Load, Tangential Load at 10,000th Cycle

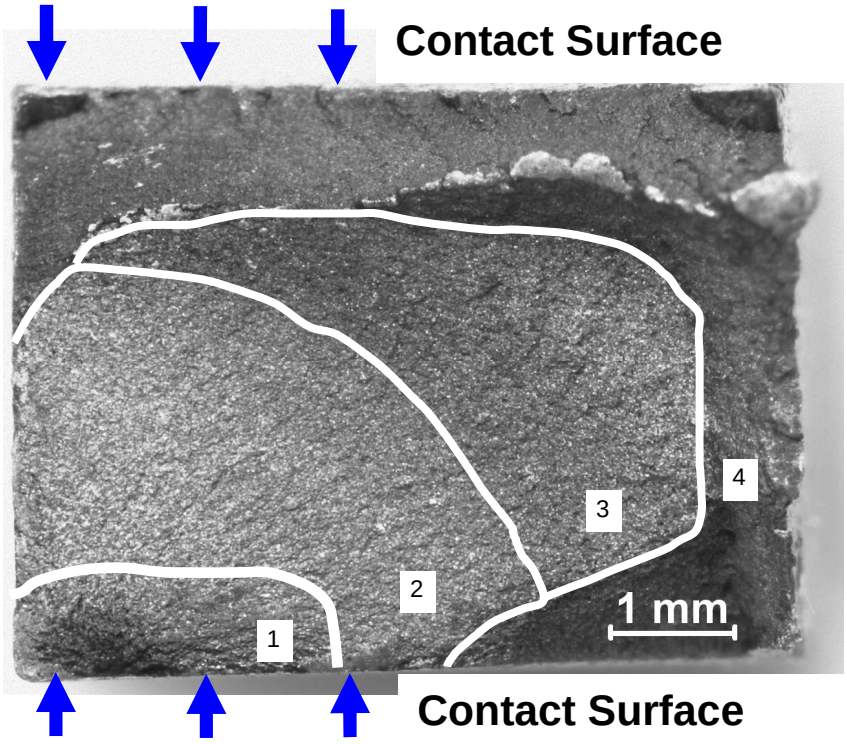

(a) Typical Fracture Surface with Four Distinguishable Regions

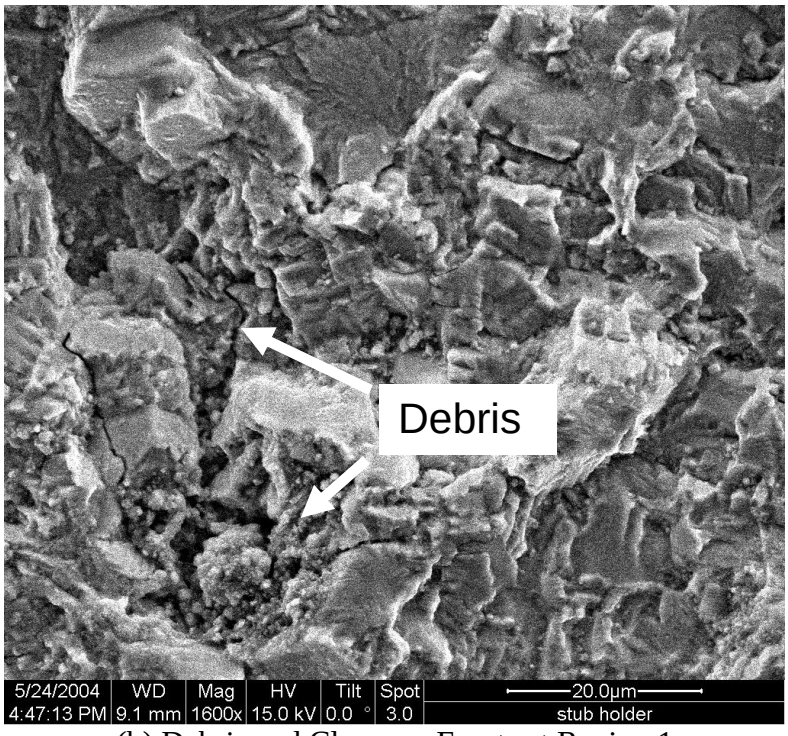

(b) Debris and Cleavage Facets at Region 1

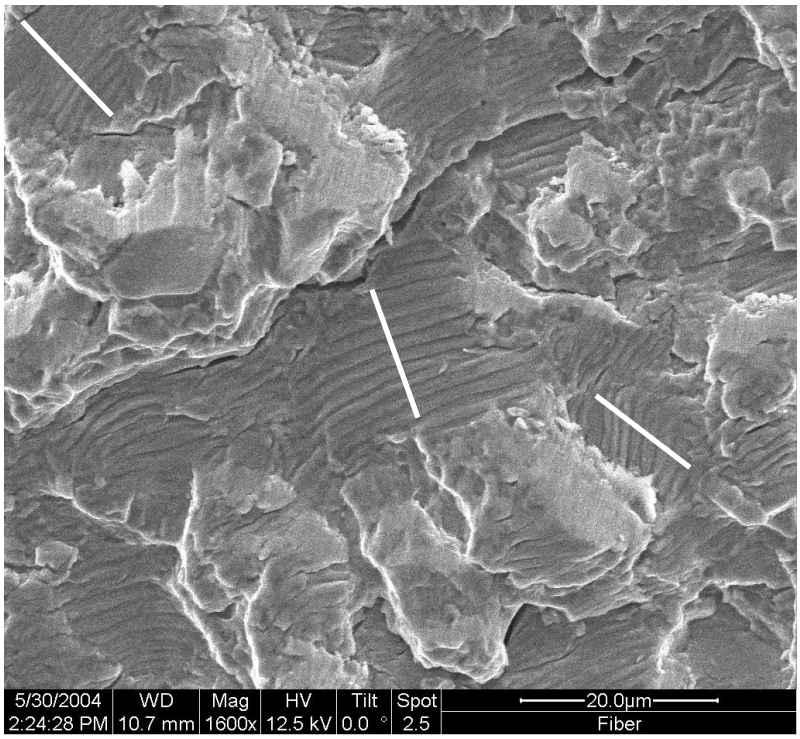

(c) Fine Striations at Region 2

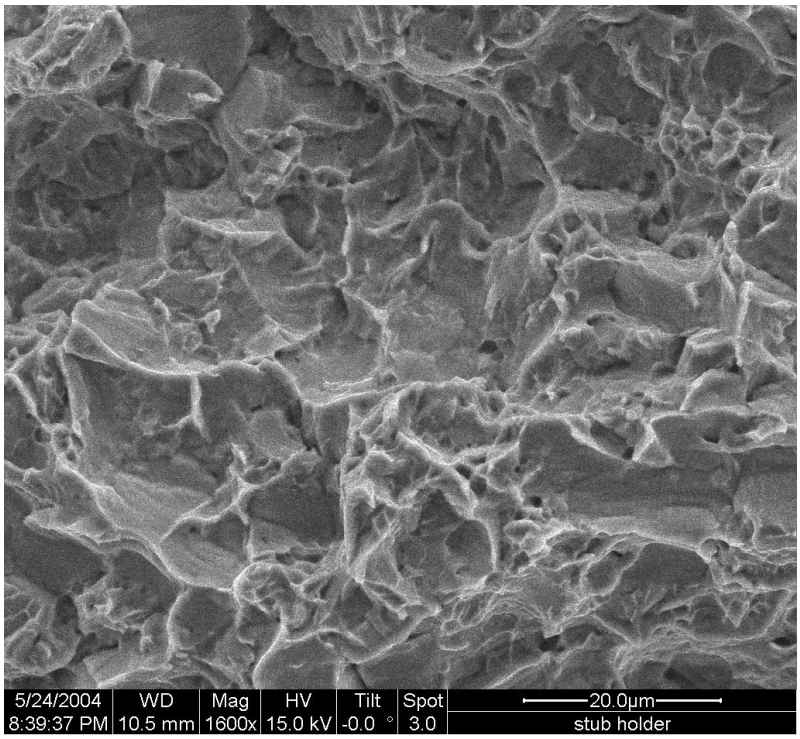

(d) Large Dimples at Region 3

Figure 26. Fracture Surface for Test 14
Load Condition: σ_{max} =600 MPa, σ_{min} =60 MPa, P_{max} =4448 N, P_{min} =2224 N, P_{Freq} =30 Hz
Shot-peened Specimen

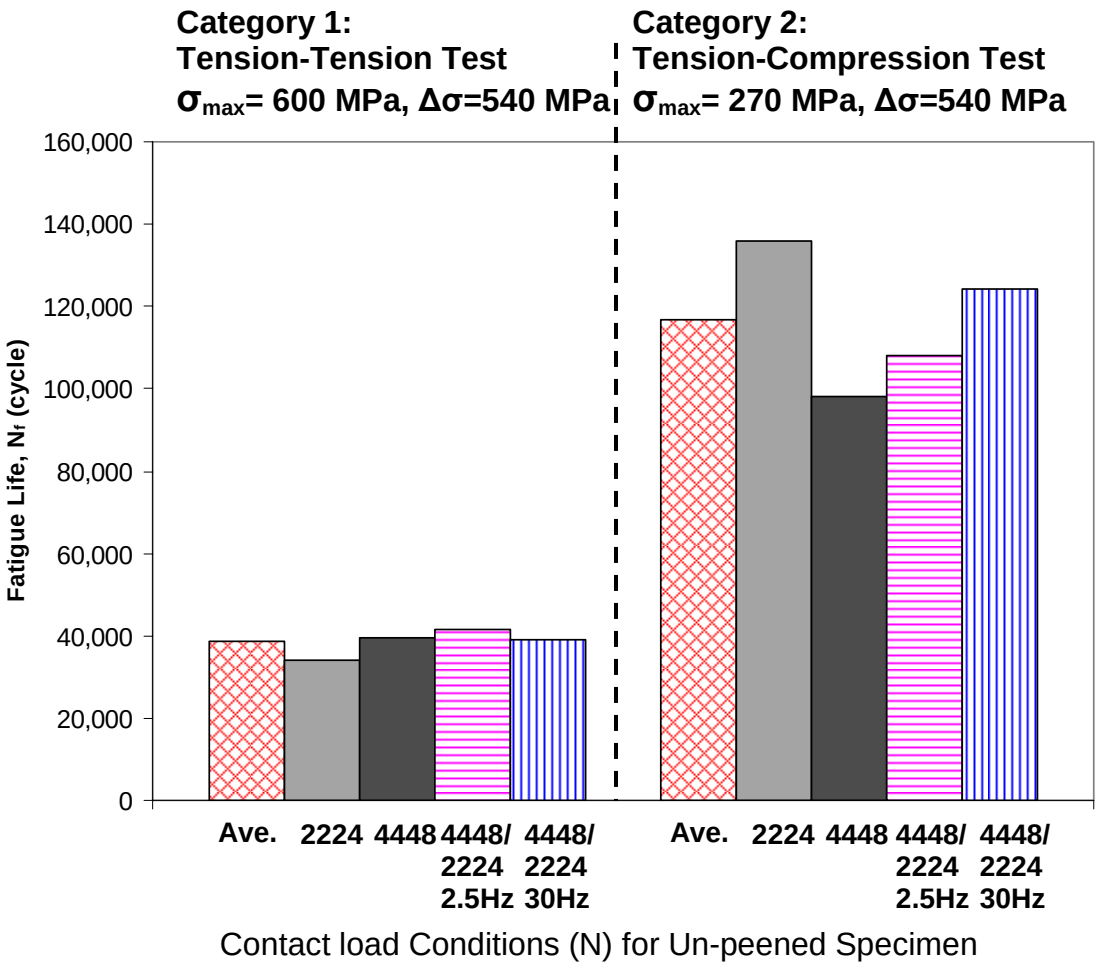

(a) Fatigue life Comparisons for Un-peened Specimens

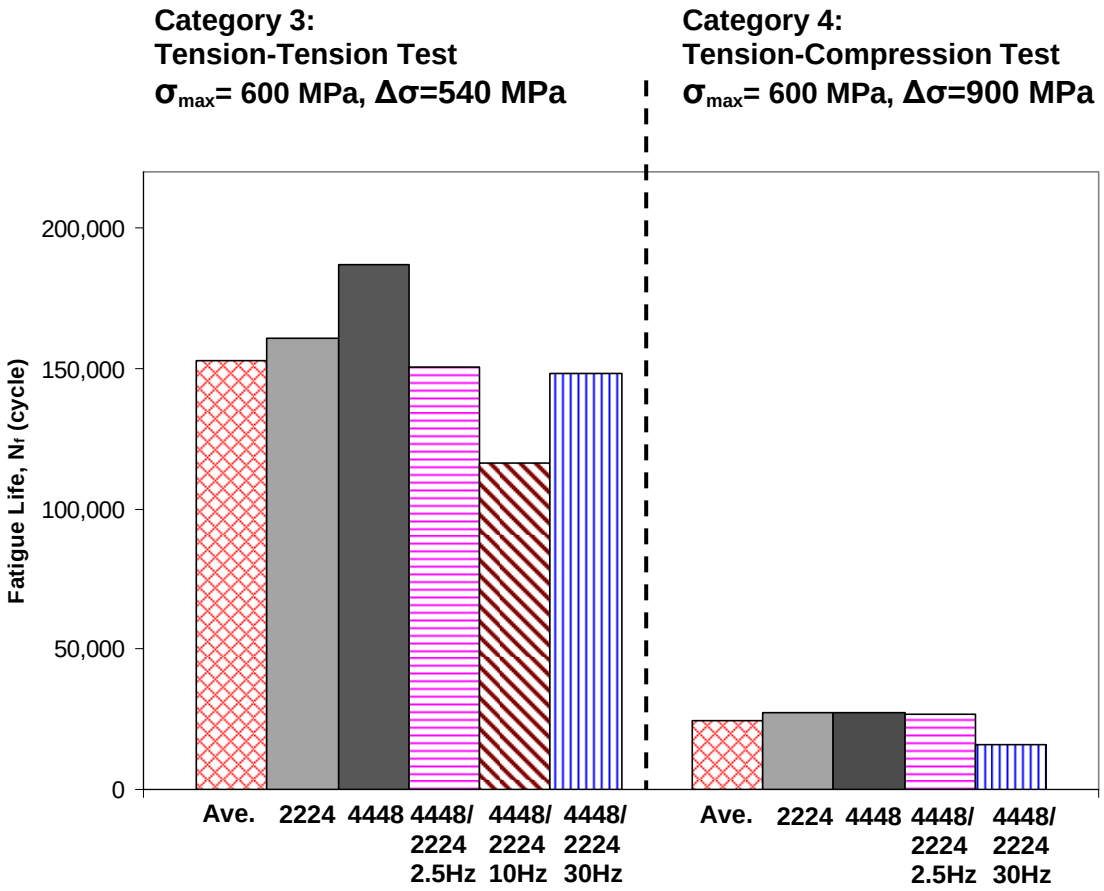

(b) Fatigue Life Comparisons for Shot-peened Specimens

Figure 27. Fatigue Life Comparisons for Various Contact Loading Conditions (Data from Table 6)

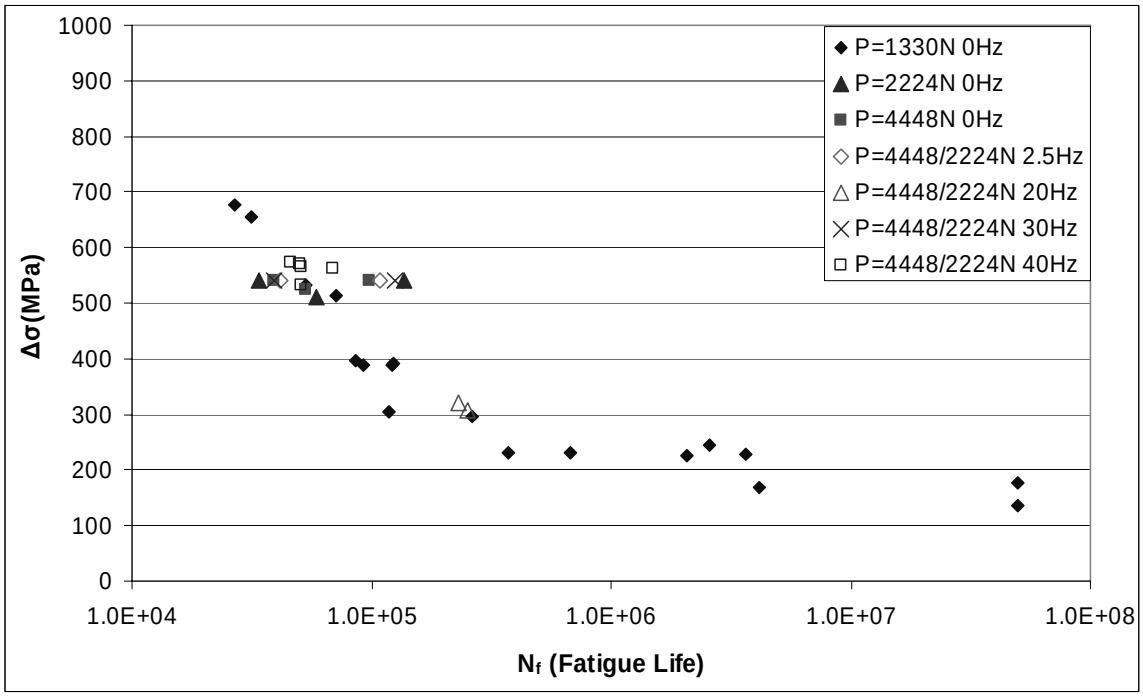

(a) Δσ-Nf for Un-peened Specimens

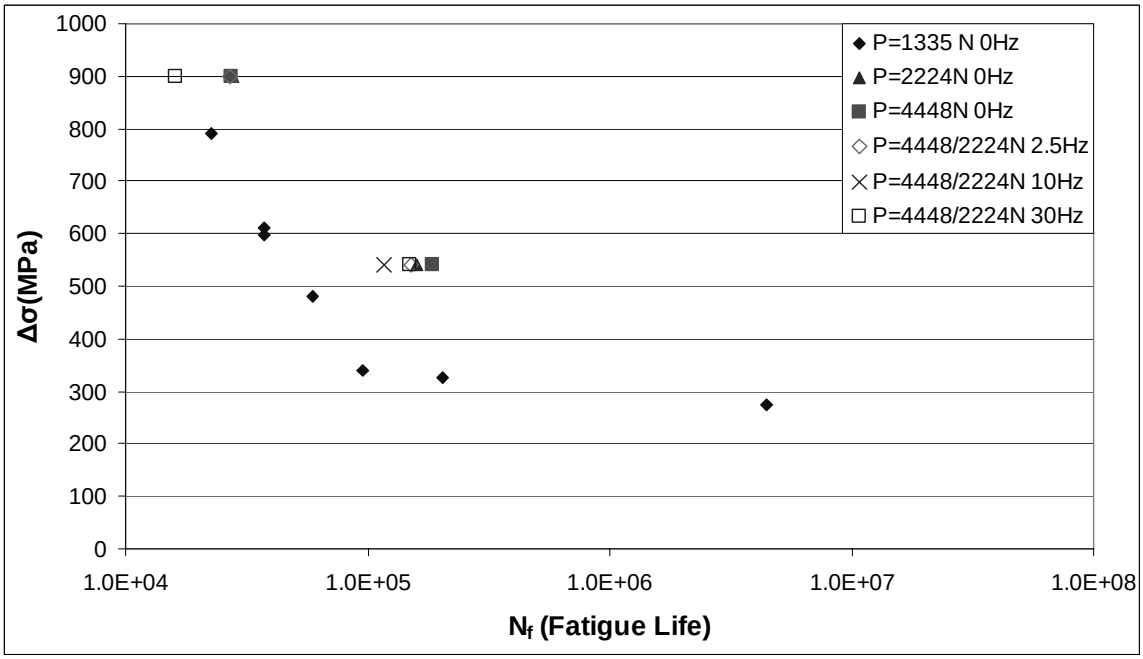

(b) Δσ-Nf for Shot-peened Specimens

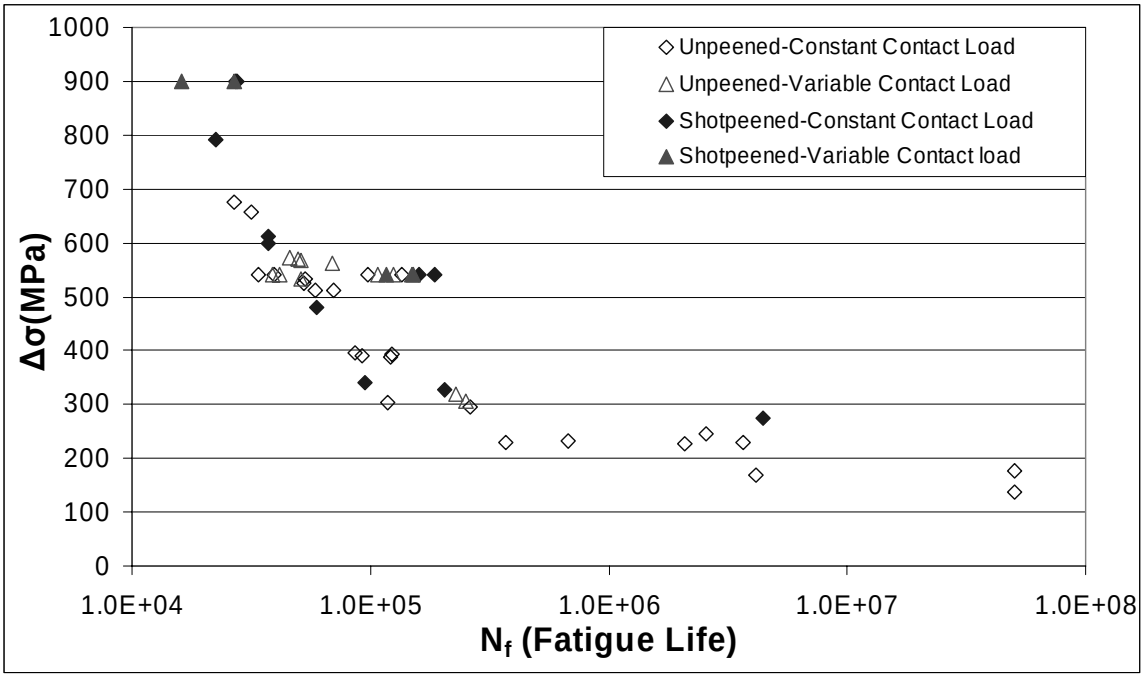

(c) Comparison of $\Delta\sigma$-N_f for Shot-peened & Un-peened Specimens

Figure 28. $\Delta\sigma$-N_f from Experimental Tests (Data from Table 7)

Note:

It should be mentioned that stress range parameter can't account for the effect introduced by different stress ratios. In addition, the experimental data adopted in this figure is obtained from tests conducted with various stress ranges and stress ratios.

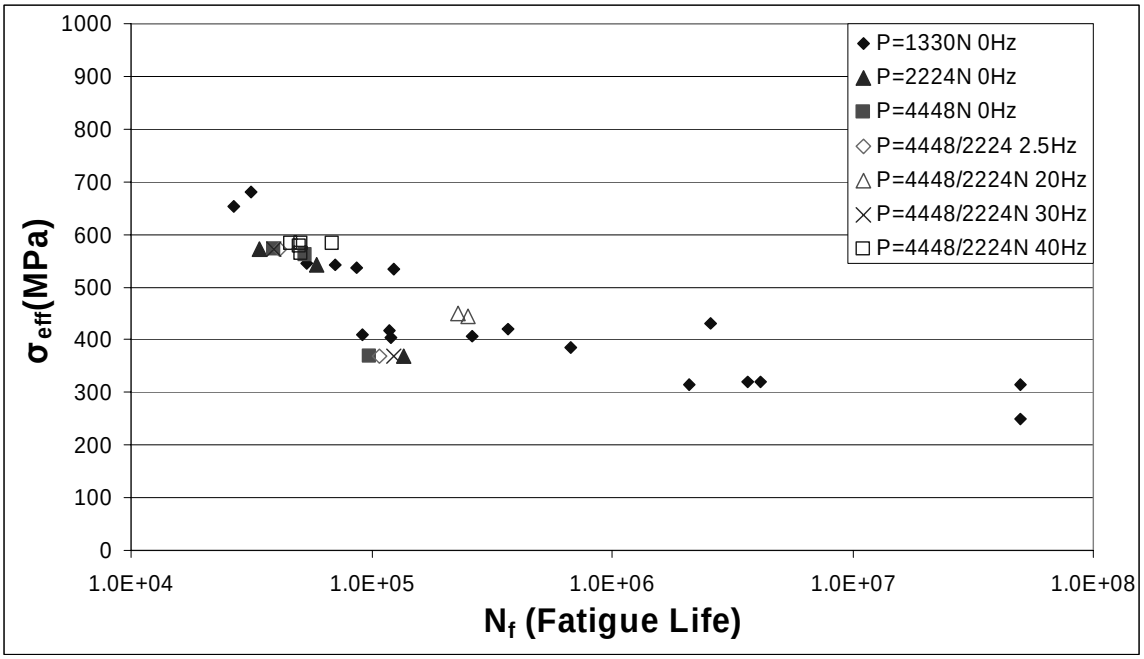

(a) σ_{eff}-N_f for Un-peened Specimens

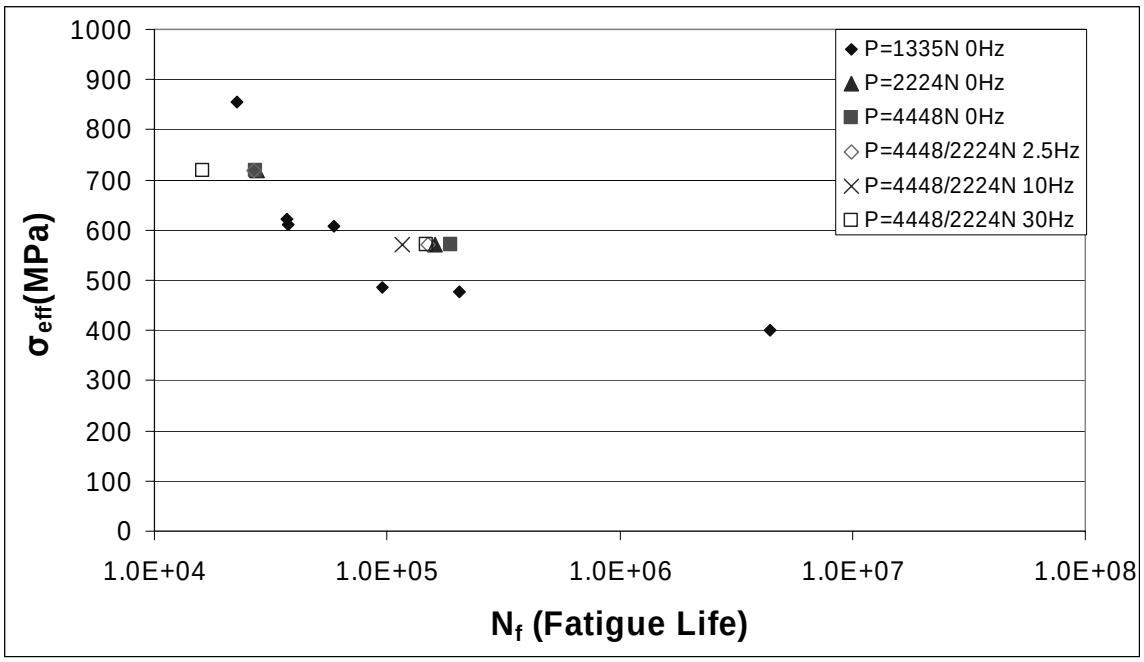

(b) σ_{eff}-N_f for Shot-peened Specimens with 100% Stress Relaxation

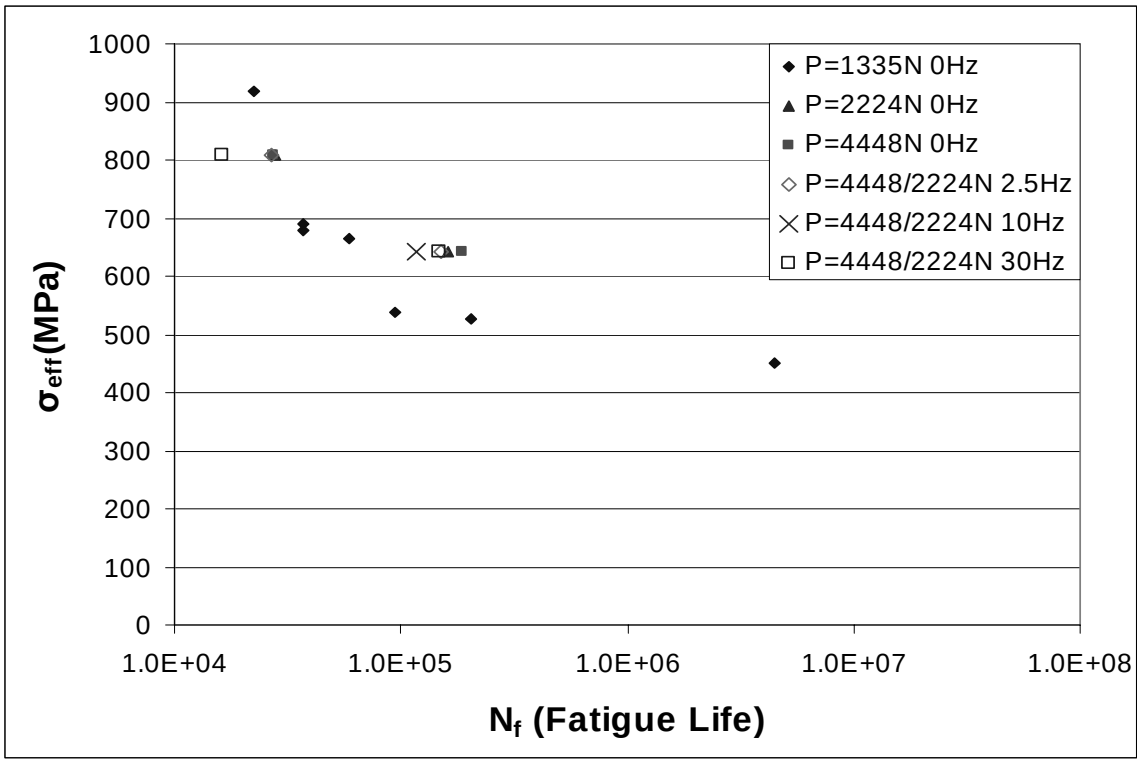

(c) σ_{eff}-N_f for Shot-peened Specimens with 50% Stress Relaxation

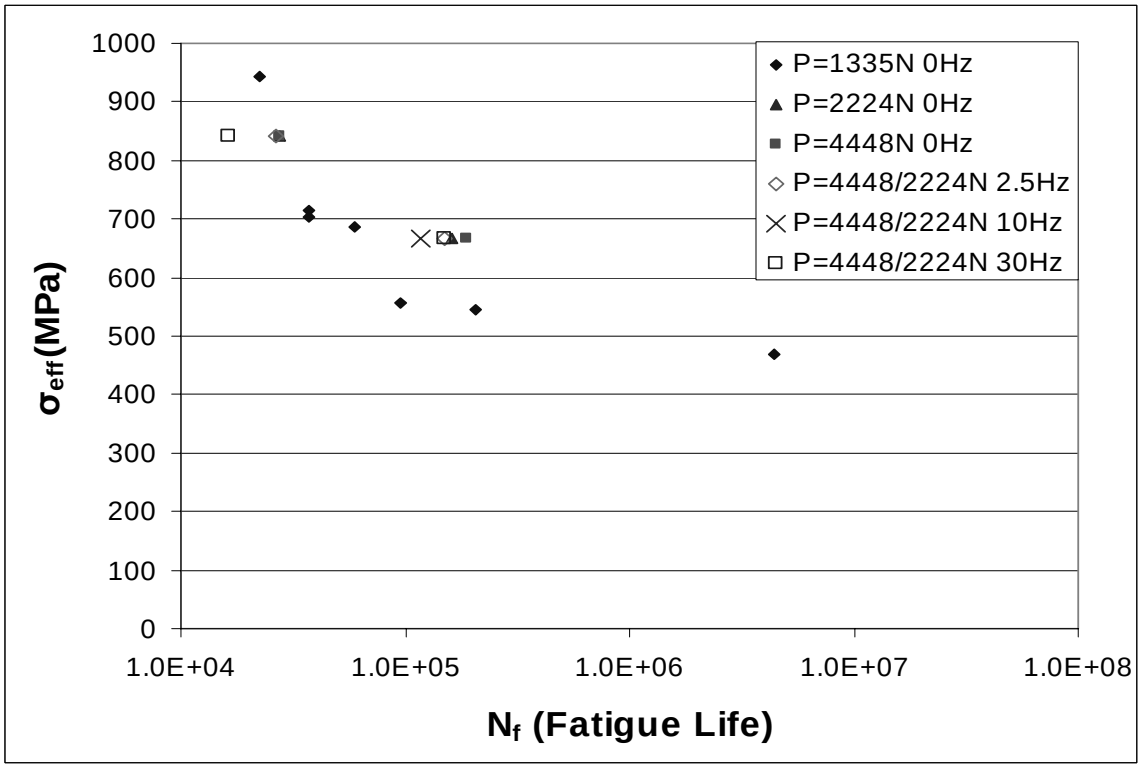

(d) σ_{eff}-N_f for Shot-peened Specimens with 30% Stress Relaxation

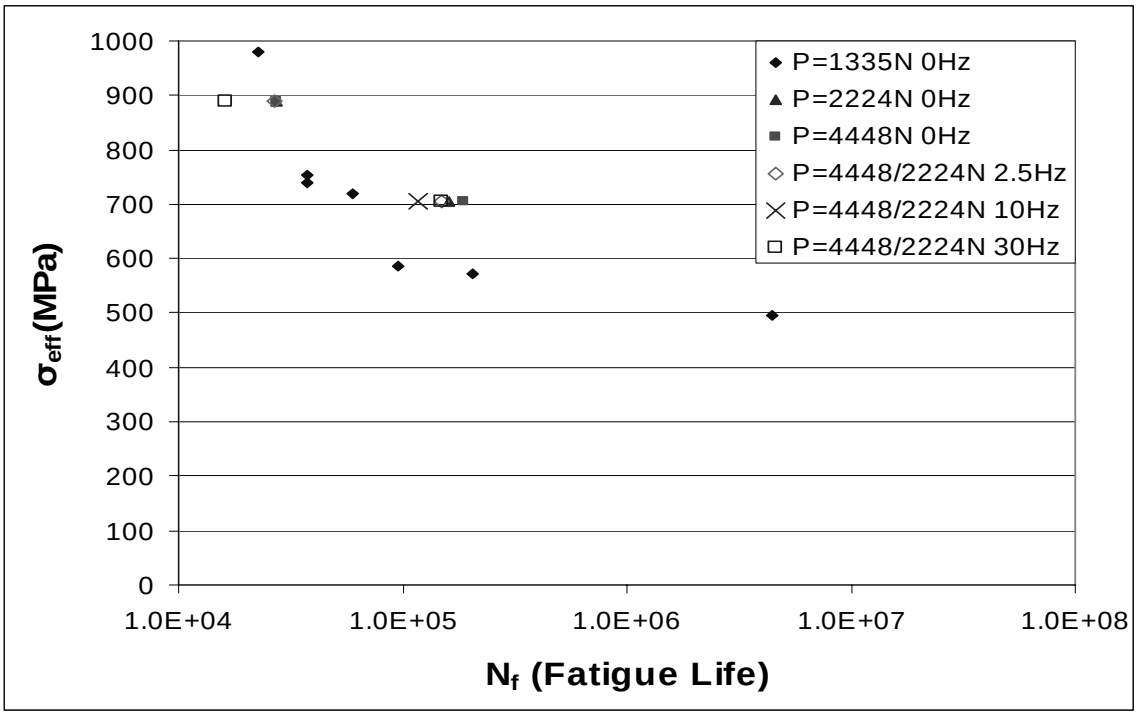

(e) σ_{eff}-N_f for Shot-peened Specimens with 0% Stress Relaxation

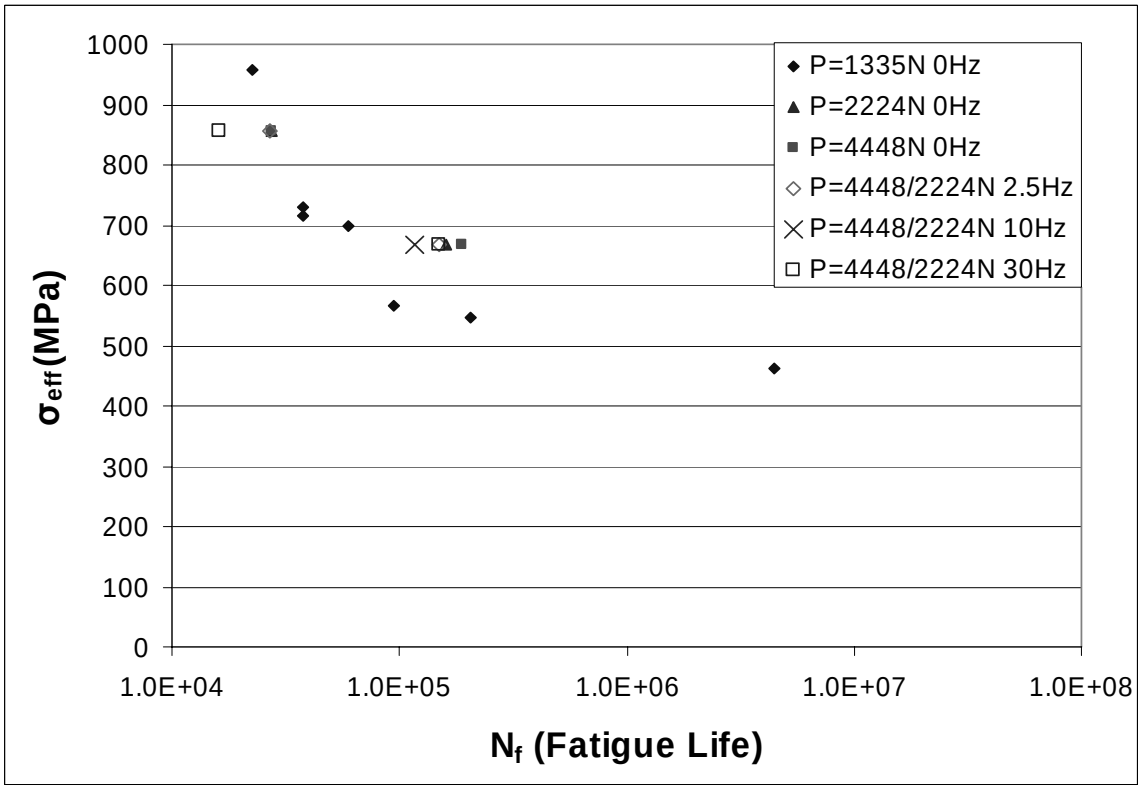

(f) σ_{eff}-Nf for Shot-peened Specimens with Different Stress Relaxation Assumption

Figure 29. σ_{eff}-N_f for Shot-peened & Un-peened Specimens (Data from Table 7)

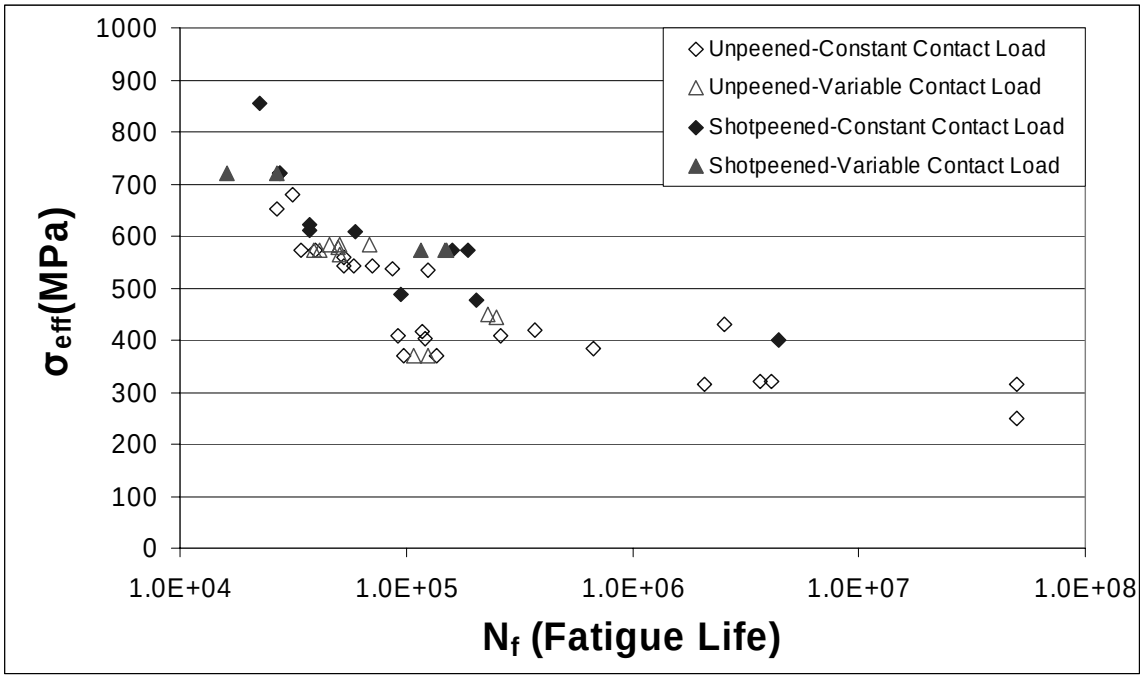

(a) σ_{eff}-N_f for Constant and Variable Contact Load with 100% Stress Relaxation

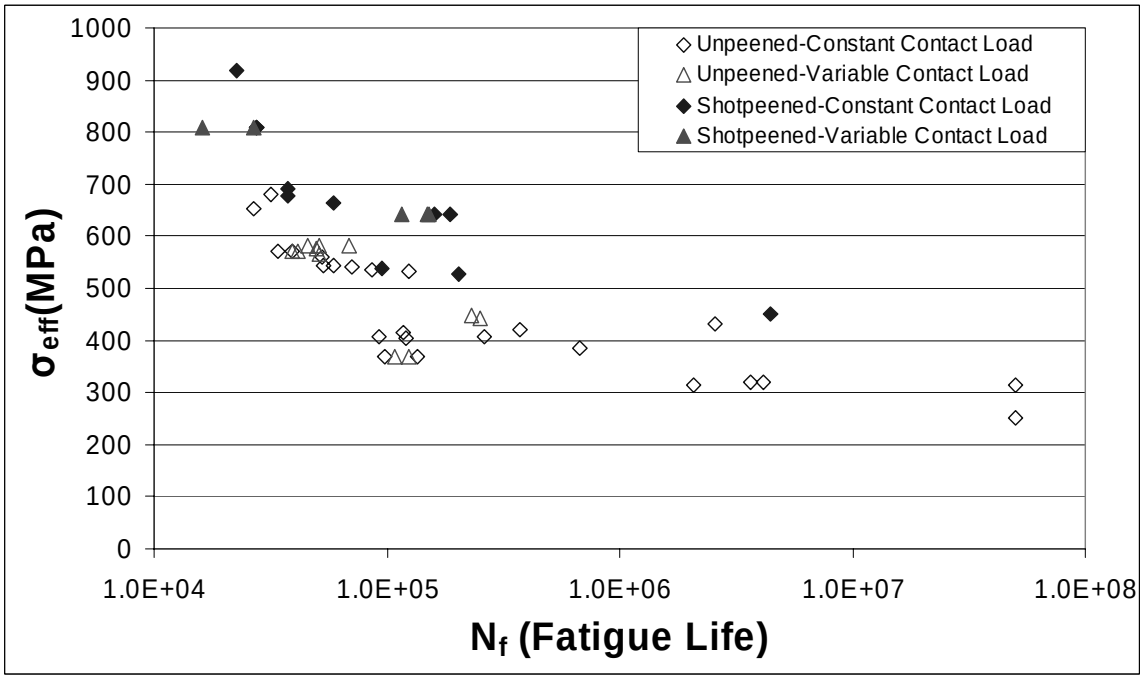

(b) σ_{eff}-N_f for Constant and Variable Contact Load with 50% Stress Relaxation

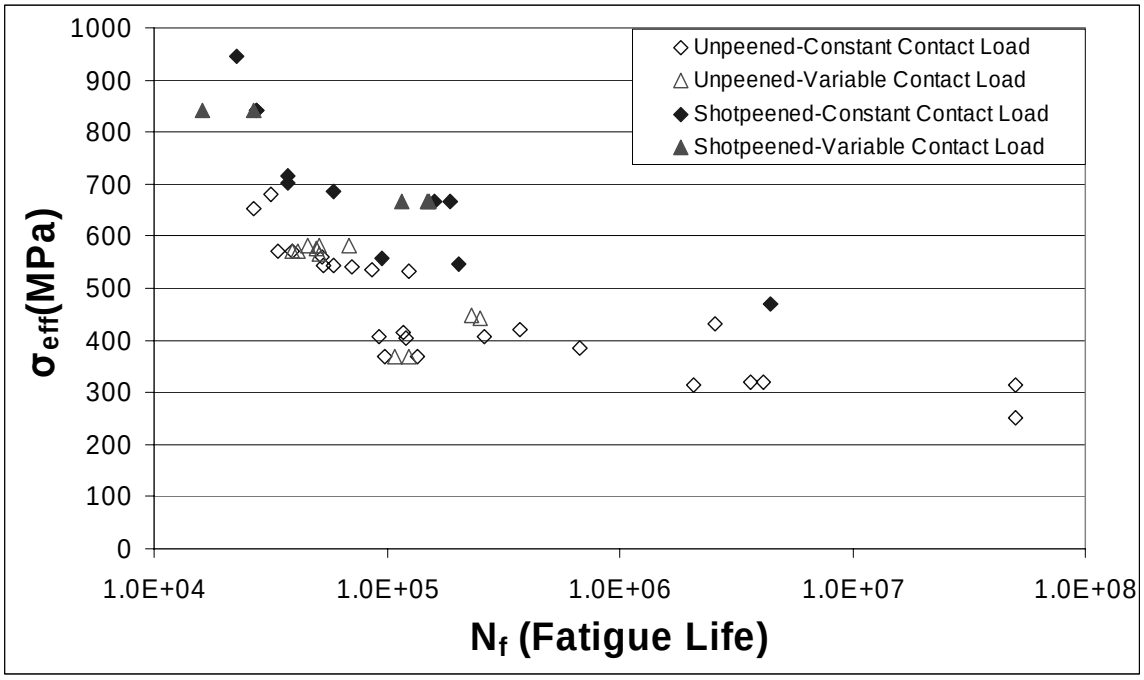

(c) σ_{eff}-N_f for Constant and Variable Contact Load with 30% Stress Relaxation

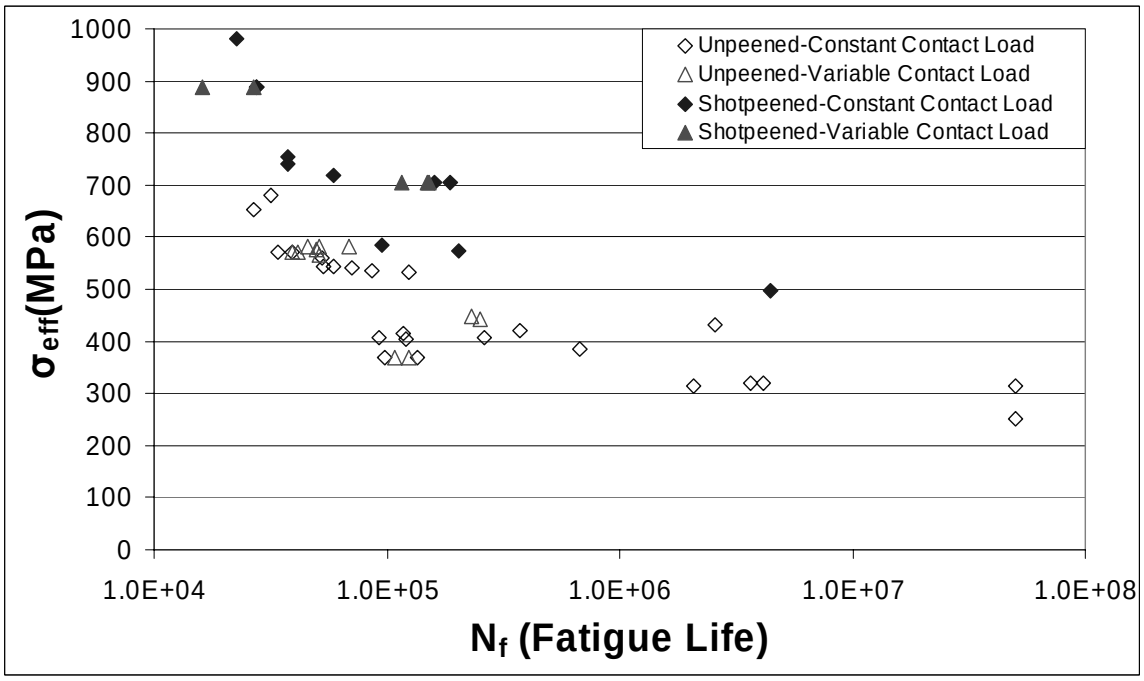

(d) σ_{eff}-N_f for Constant and Variable Contact Load with 0% Stress Relaxation

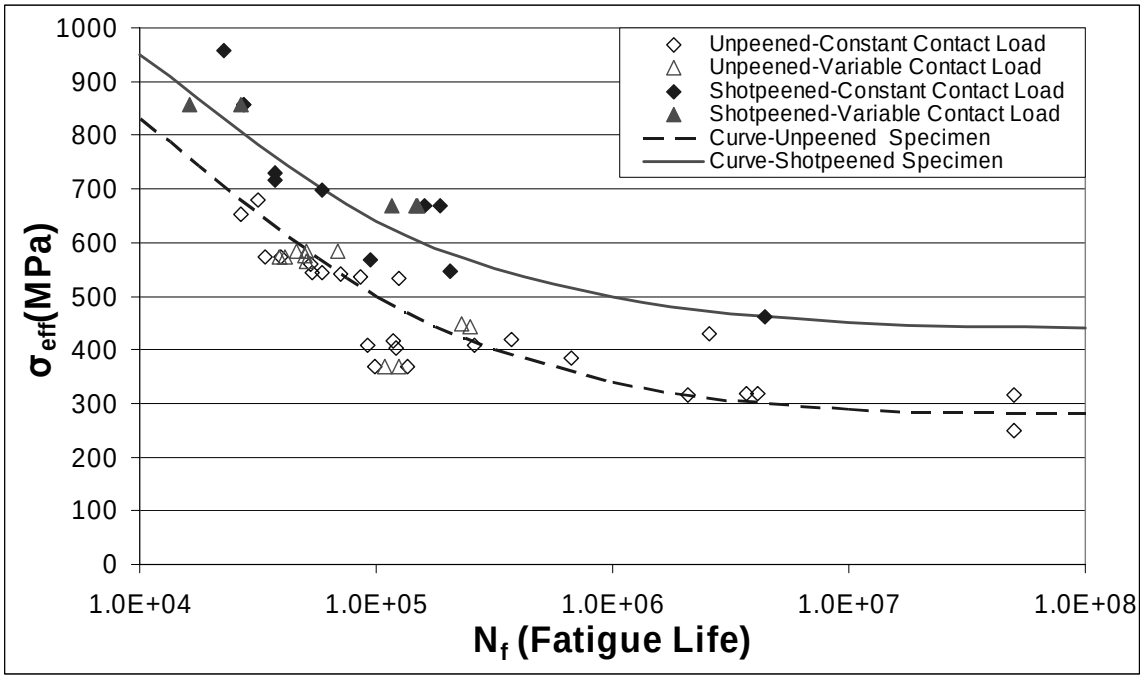

(e) σ_{eff}-N_f for Constant and Variable Contact Load with Different Relaxation Assumption

Figure 30. σ_{eff}-N_f for Constant & Variable Contact Load (Data from Table 7)

Note:
The fitting curve shown in Figure 30 (e) is used to approximately demonstrate the trend observed from fatigue life data.

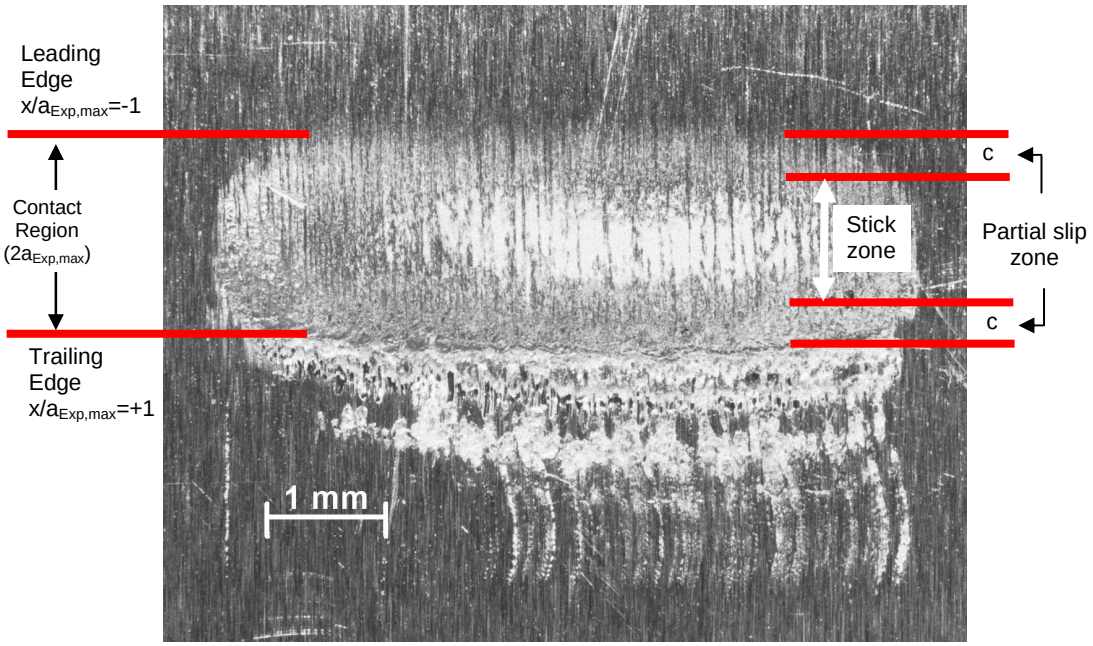

Figure 31. Scar Pattern from Test 4

Load Condition: σ_{max} =600 MPa, σ_{min} =60 MPa, P_{max} =4448 N, P_{min} =2224 N, P_{Freq} =30 Hz
Un-peened Specimen

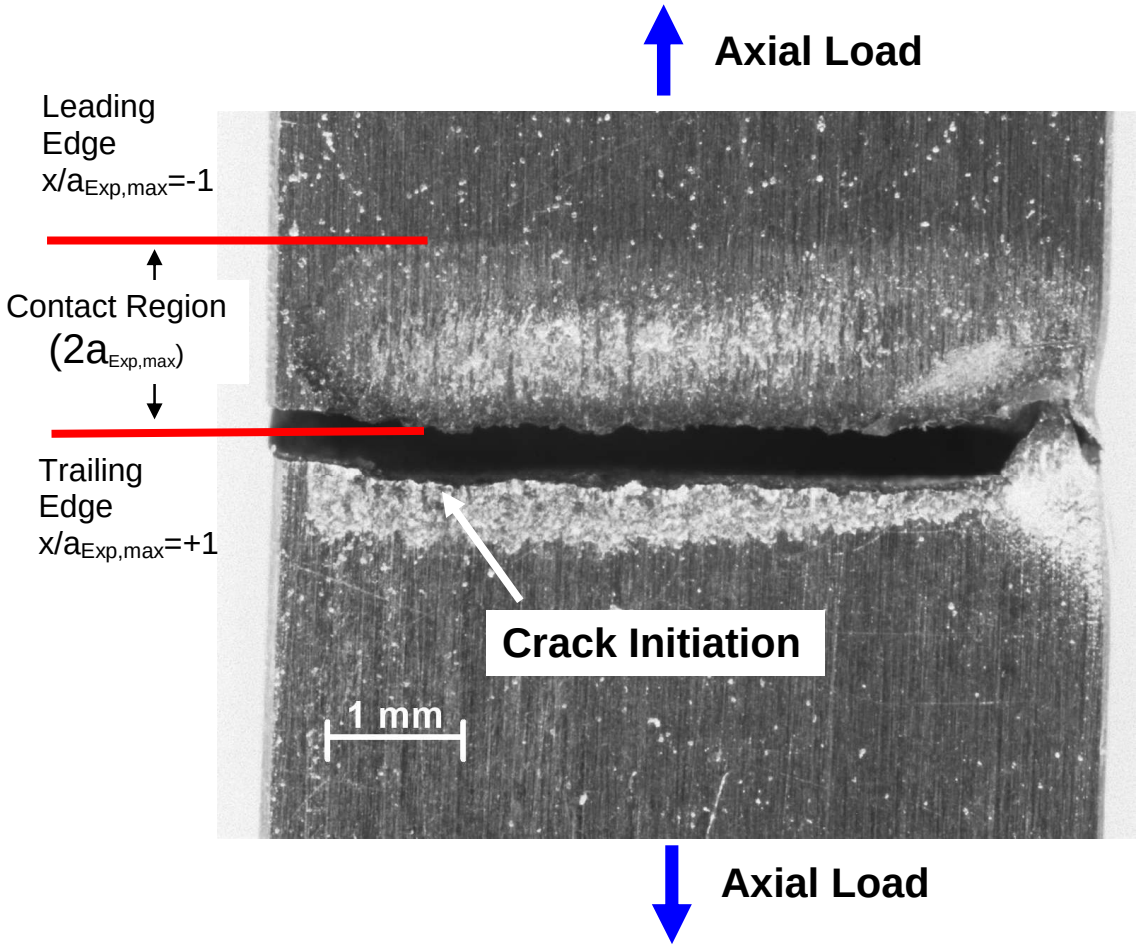

Figure 32. Crack Initiation Location

Crack Initiation at Location near $x/a_{Exp,max} = +1$ (Photo from Test 1)
Load Condition: σ_{max} =600 MPa, σ_{min} =60 MPa, P_{max} =2224 N, P_{min} =2224 N, P_{Freq} =0 Hz

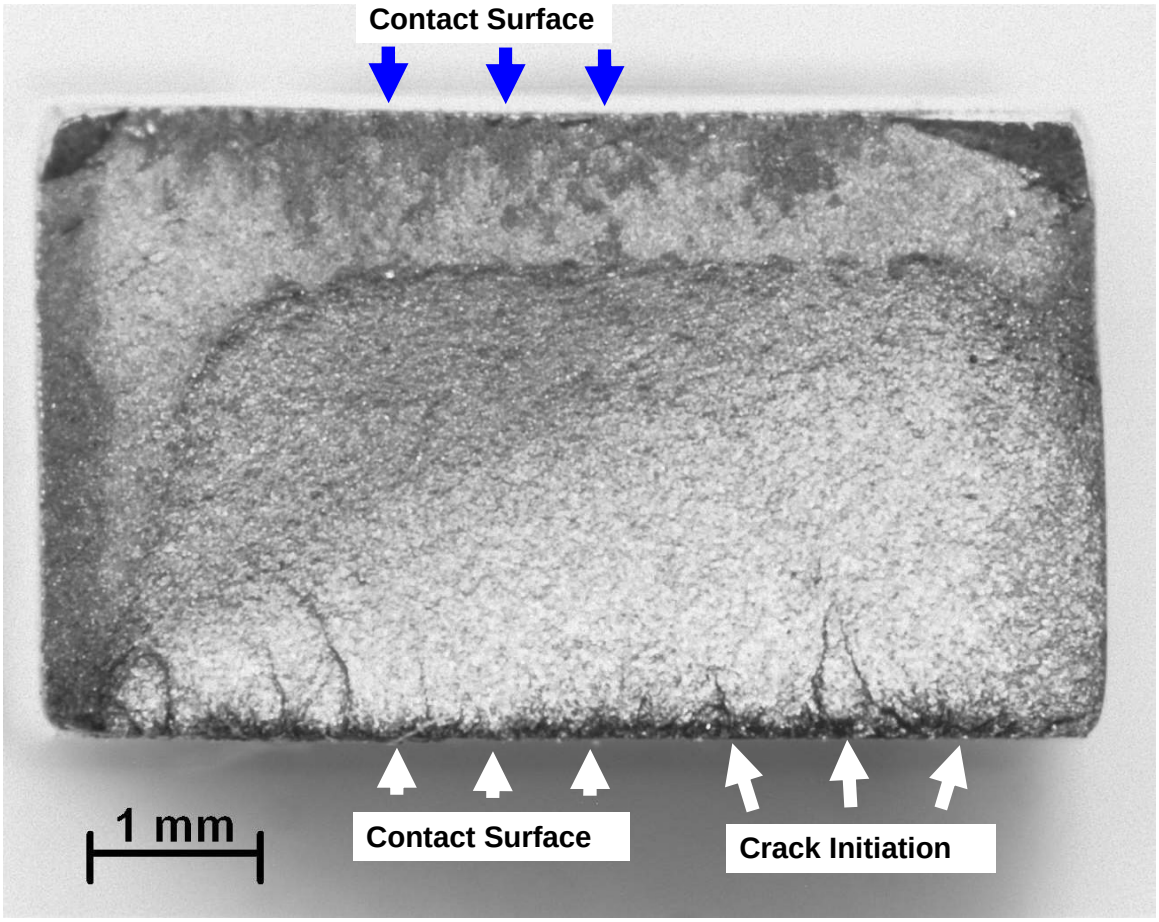

(a) Crack Initiation Observed on Contact Surface (under Lower Magnification)

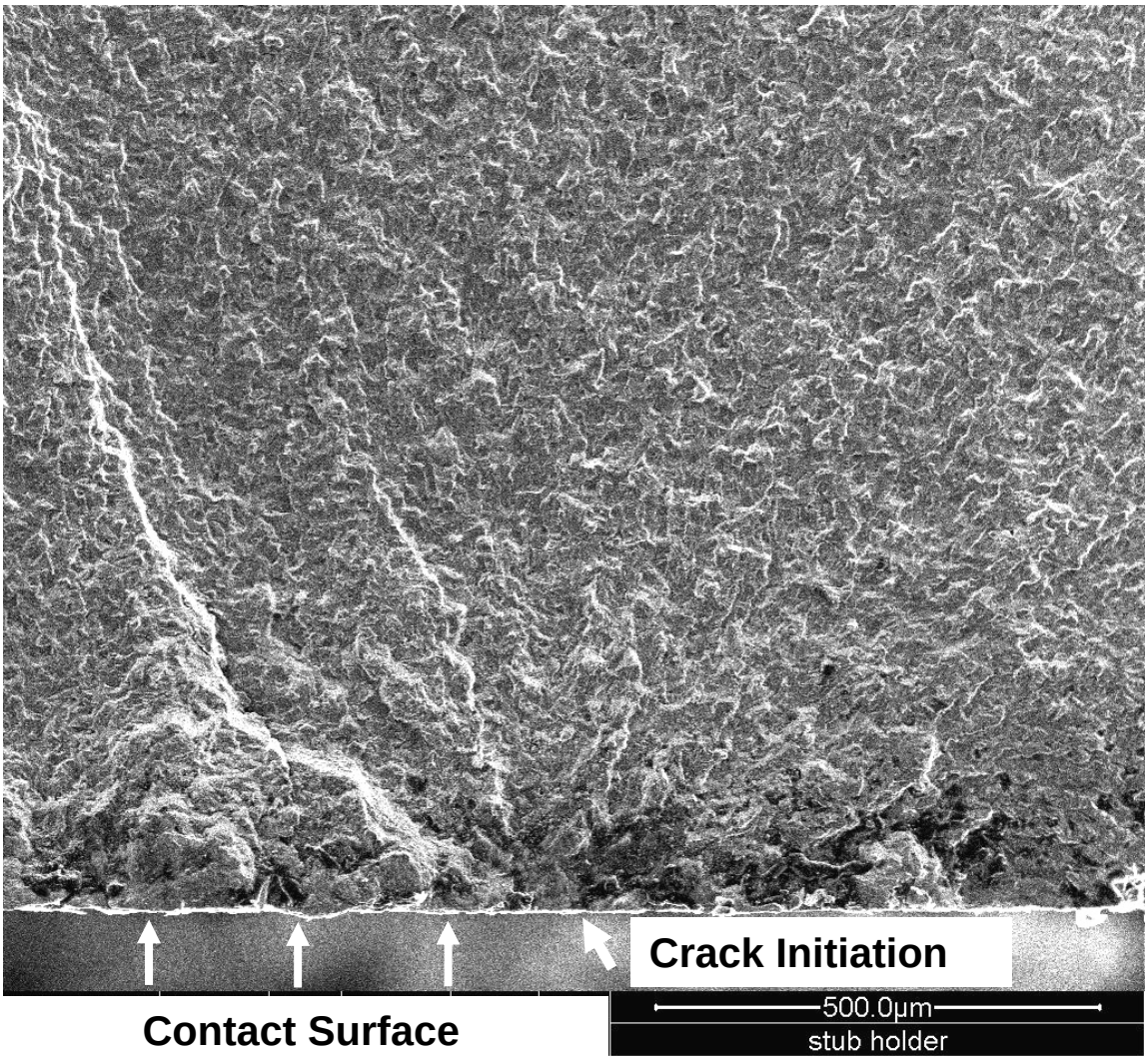

(b) Crack Initiation Observed on Contact Surface (under Higher Magnification)

Figure 33. Surface Crack Initiation for Un-peened Specimens (Test 3)

Load Condition: σ_{max}=600 MPa, σ_{min}=60 MPa, P_{max}=4448 N, P_{min}=2224 N, P_{Freq}=2.5 Hz
Un-peened Specimen

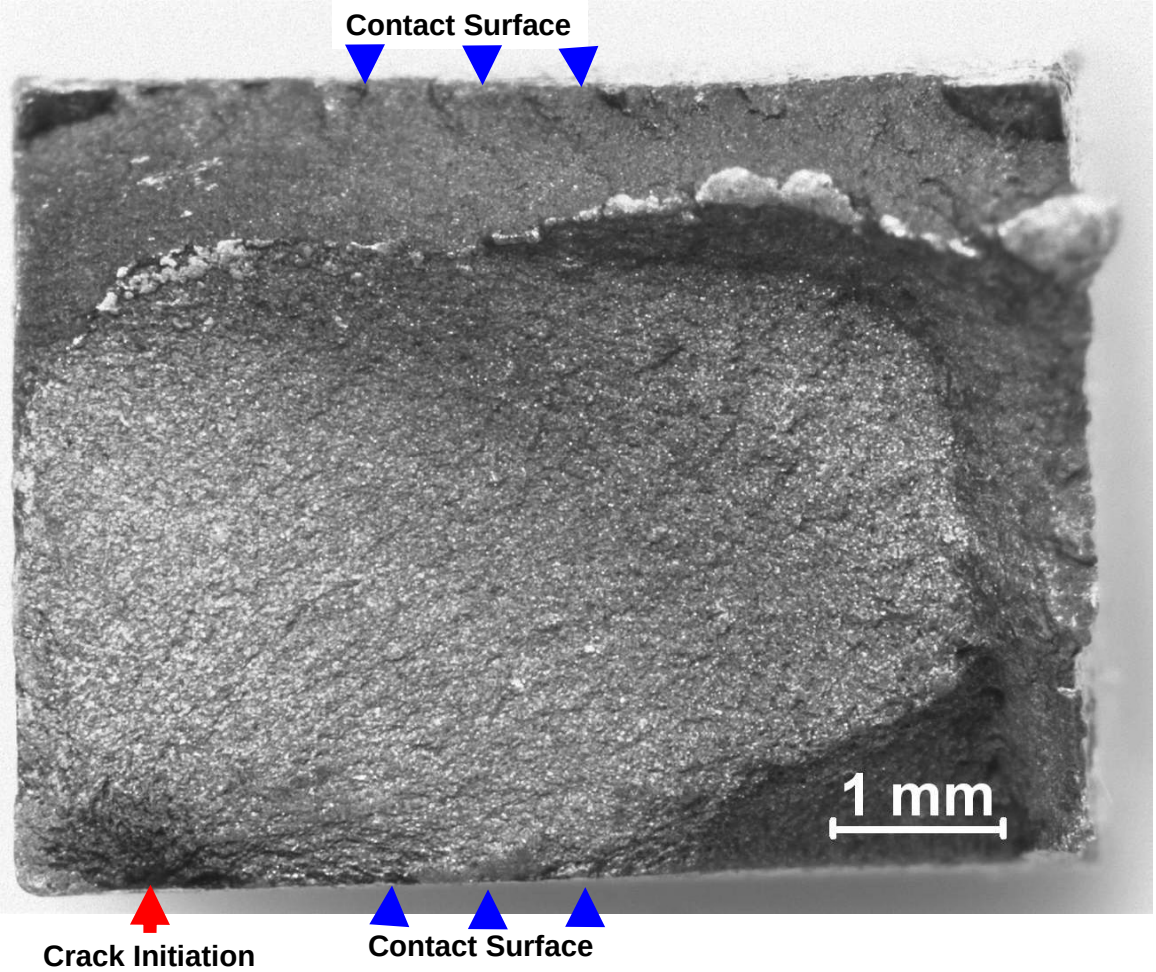

(a) Crack Initiation Observed in the Interior of Specimen (under Lower Magnification)

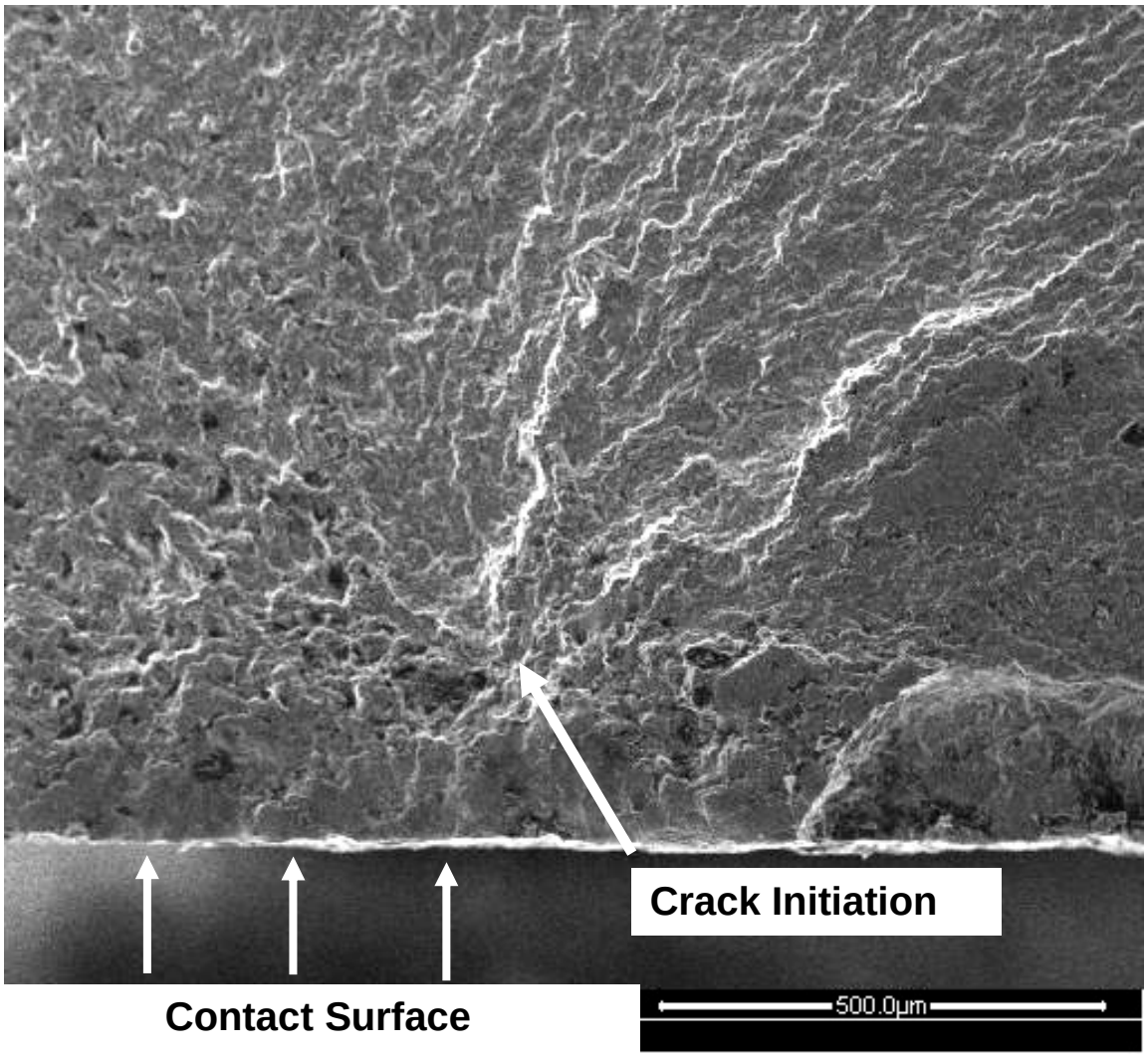

(b) Crack Initiation Observed in the Interior of Specimen (under Higher Magnification)

Figure 34. Deep Crack Initiation for Shot-peened Specimens (Photo from Test 13)

Load Condition: σ_{max} =600 MPa, σ_{min} =60 MPa, P_{max} =4448 N, P_{min} =2224 N, P_{Freq} =10 Hz
Shot-peened Specimen

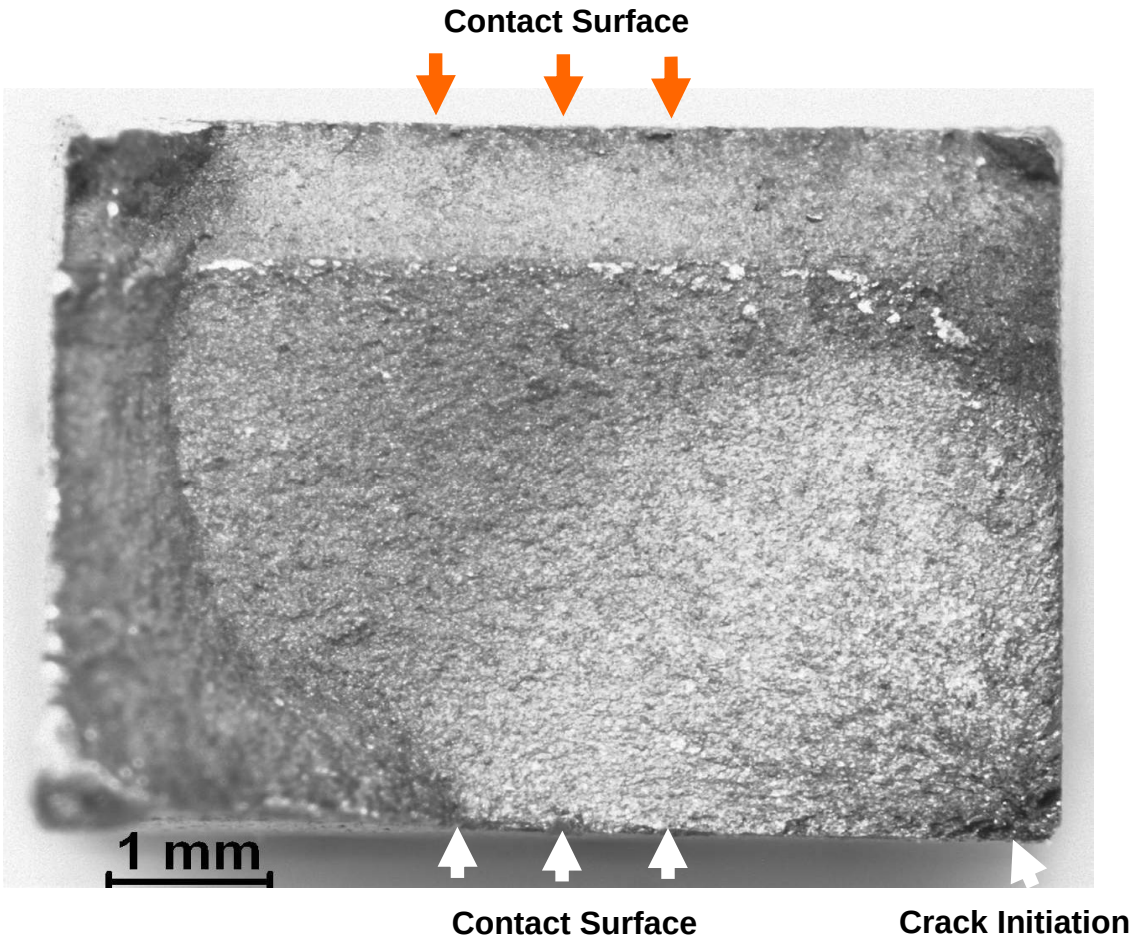

(a) Single Crack Initiation Location Pattern (Test 9)
Load Condition: σ_{max} =600 MPa, σ_{min} =60 MPa, P_{max} =2224 N, P_{min} =2224 N, P_{Freq} =0 Hz
Shot-peened specimen

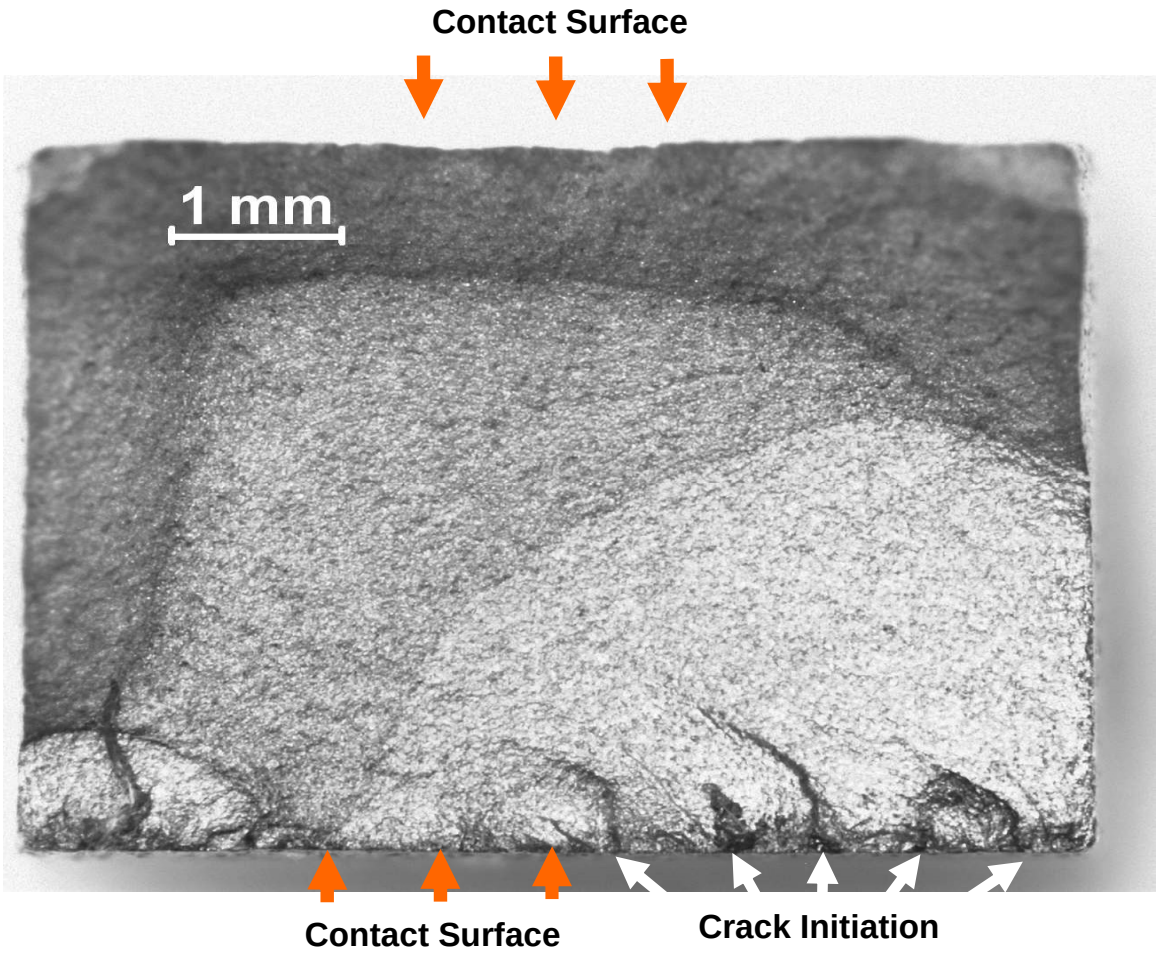

(b) Multi Crack Initiation Location Pattern (Test 10)
Load Condition: σ_{max} =600 MPa, σ_{min} =60 MPa, P_{max} =4448 N, P_{min} =4448 N, P_{Freq} =0 Hz
Shot-peened specimen

Figure 35. Crack Initiation Location Pattern

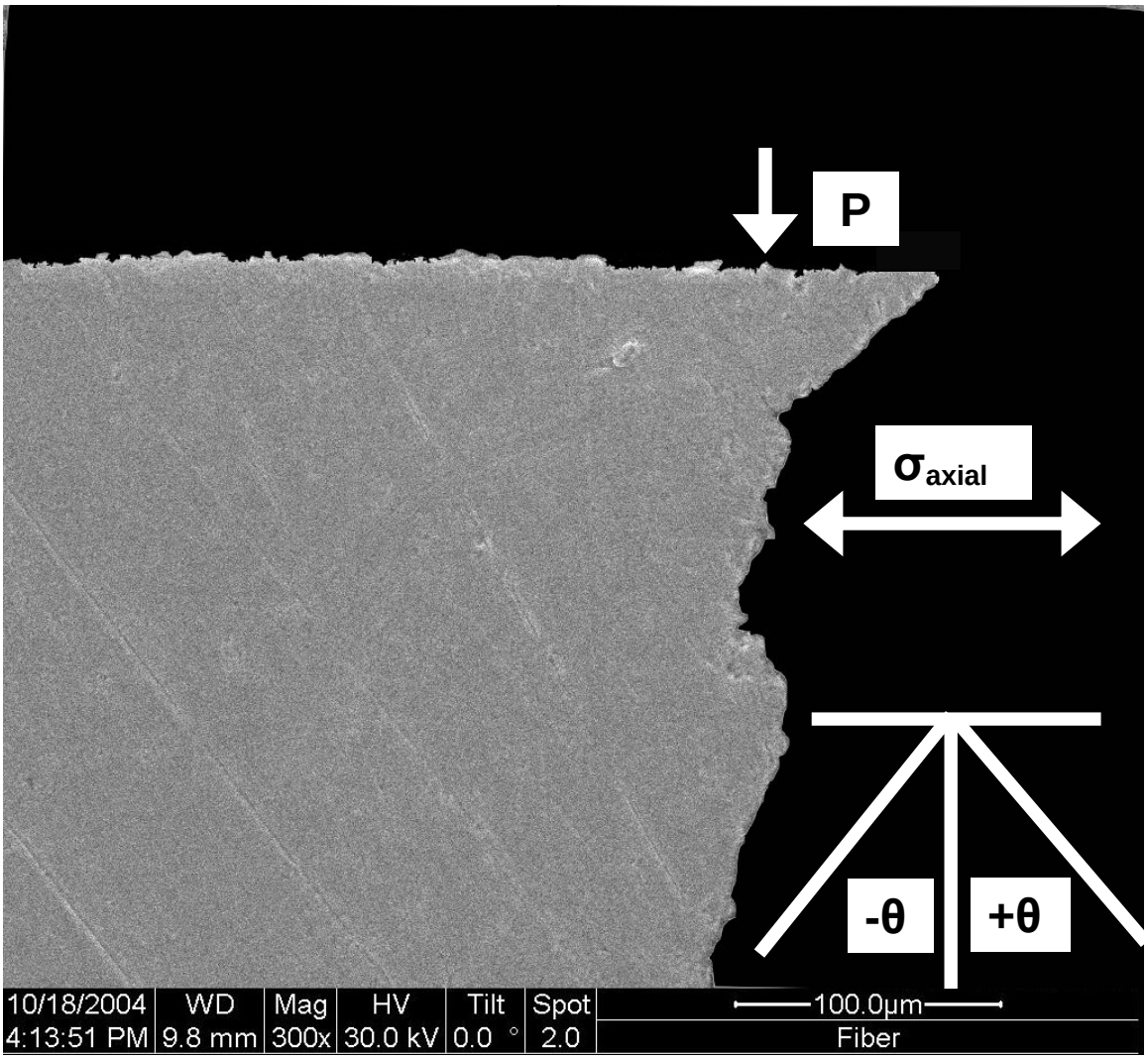

Figure 36. Crack Initiation Orientation for Test 3, θ = -50˚ (equivalent to +40˚)

Photo Taken from Test 3
Load Condition: σ_{max}=600 MPa, σ_{min}=60 MPa, P_{max}=4448 N, P_{min}=2224 N, P_{Freq}=2.5 Hz

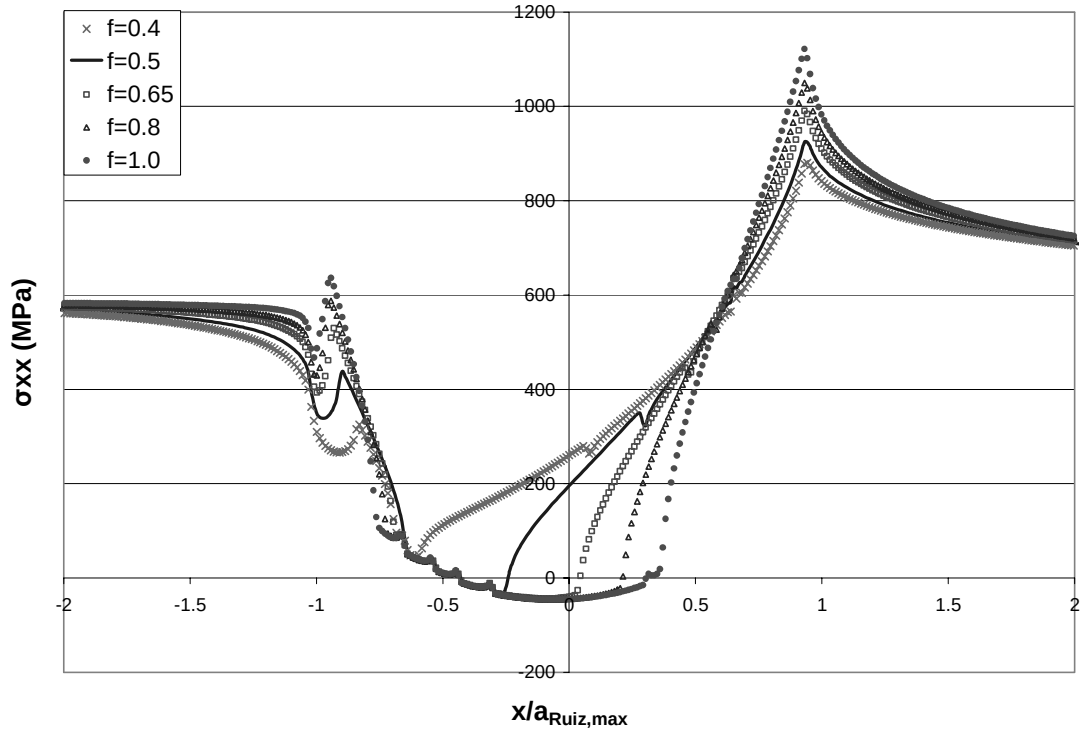

(a) σ_{xx} Stress Profile from Different Coefficients of Friction for Test 1, Step 4

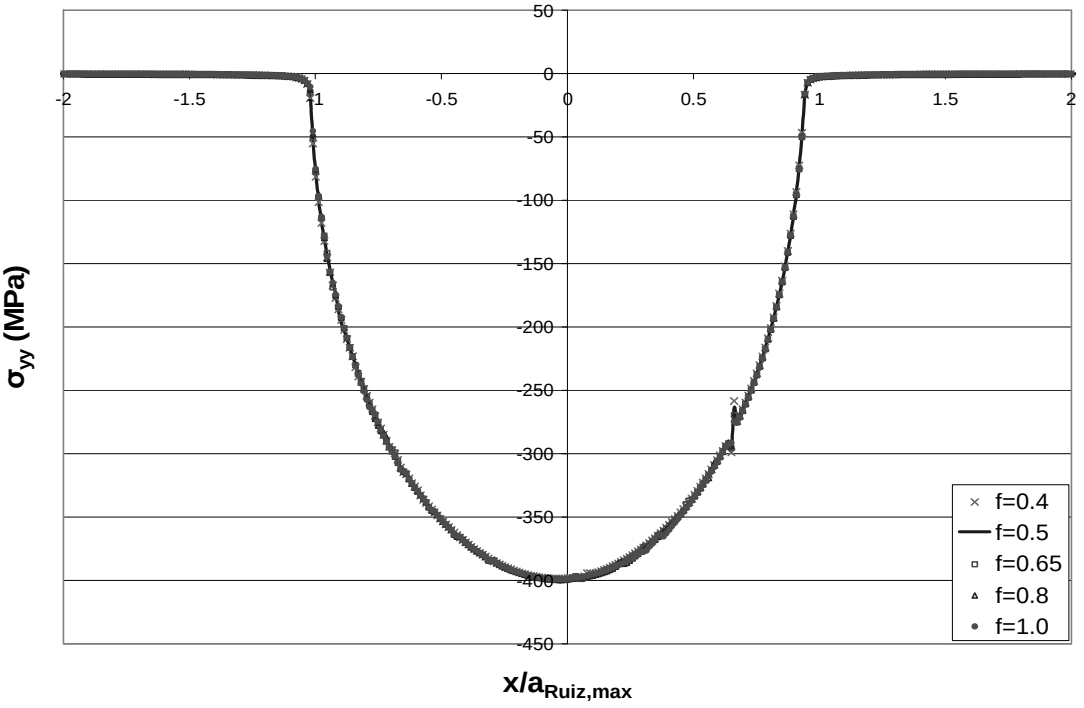

(b) σ_{yy} Stress Profile from Different Coefficients of Friction for Test 1, Step 4

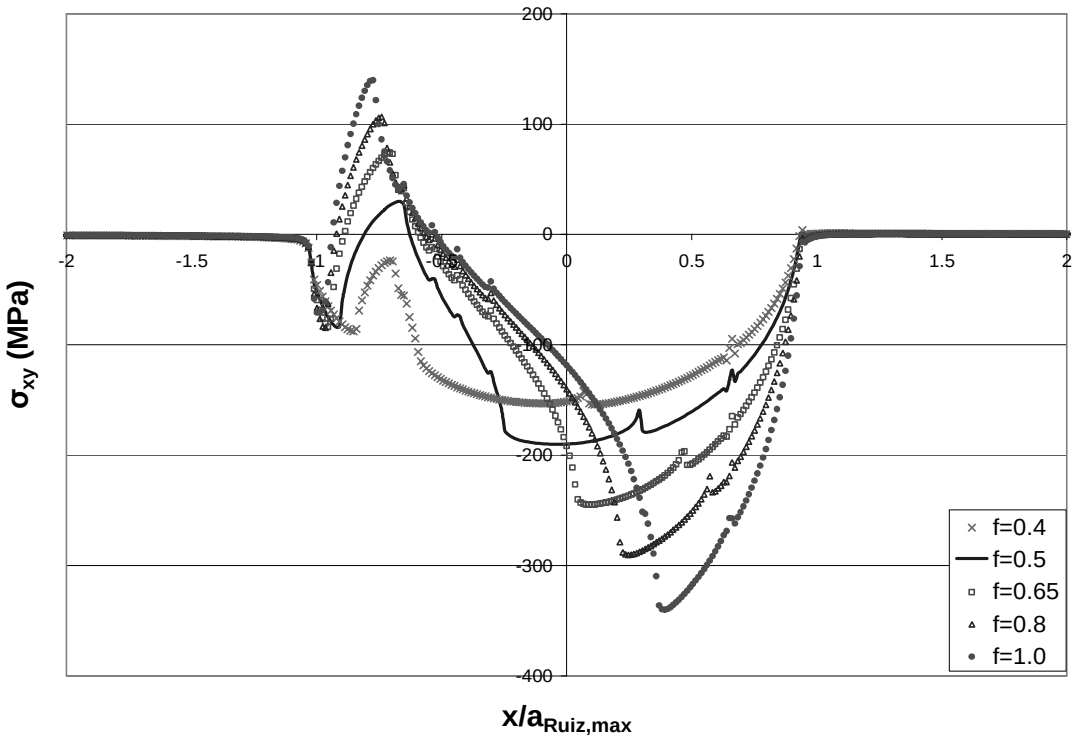

(c) σ_{xy} Stress Profile from Different Coefficients of Friction for Test 1, Step 4

Figure 37. Stress Profile from Different Coefficients of Friction for Test 1, Step 4

Data from FEA calculation
Load Condition: σ_{max} =600 MPa, σ_{min} =60 MPa, P_{max} =2224 N, P_{min} =2224 N, P_{Freq} =0 Hz
Un-peened Specimen

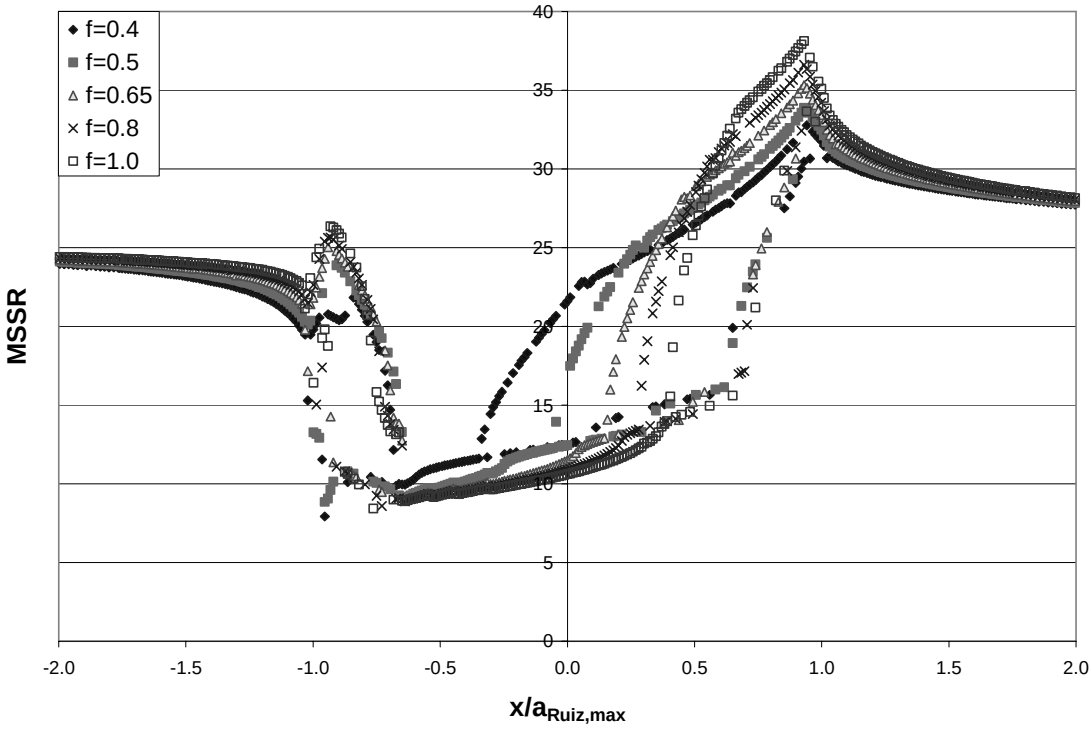

(a) MSSR Distribution along Contact Surface

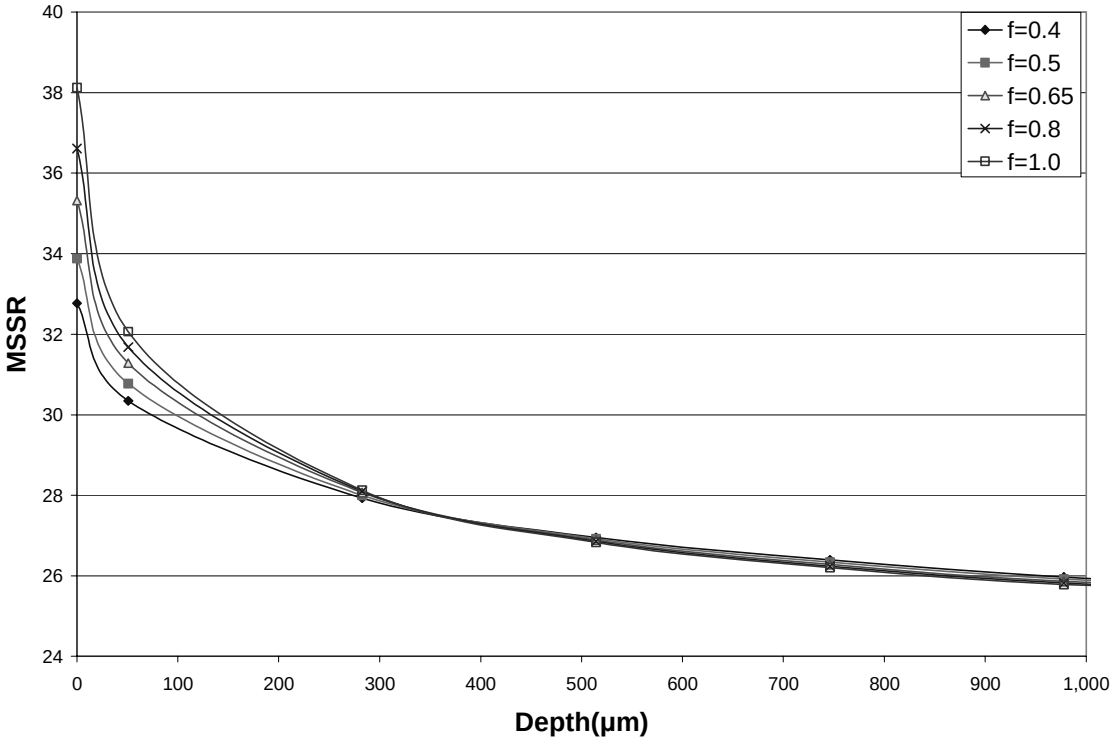

(b) MSSR Distribution along the Depth of the Specimen

Figure 38. MSSR Profile under Different Coefficients of Friction for Test 1, Step 4-5

Load Condition: σ_{max} =600 MPa, σ_{min} =60 MPa, P_{max} =2224 N, P_{min} =2224 N, P_{Freq} =0 Hz
Un-peened Specimen

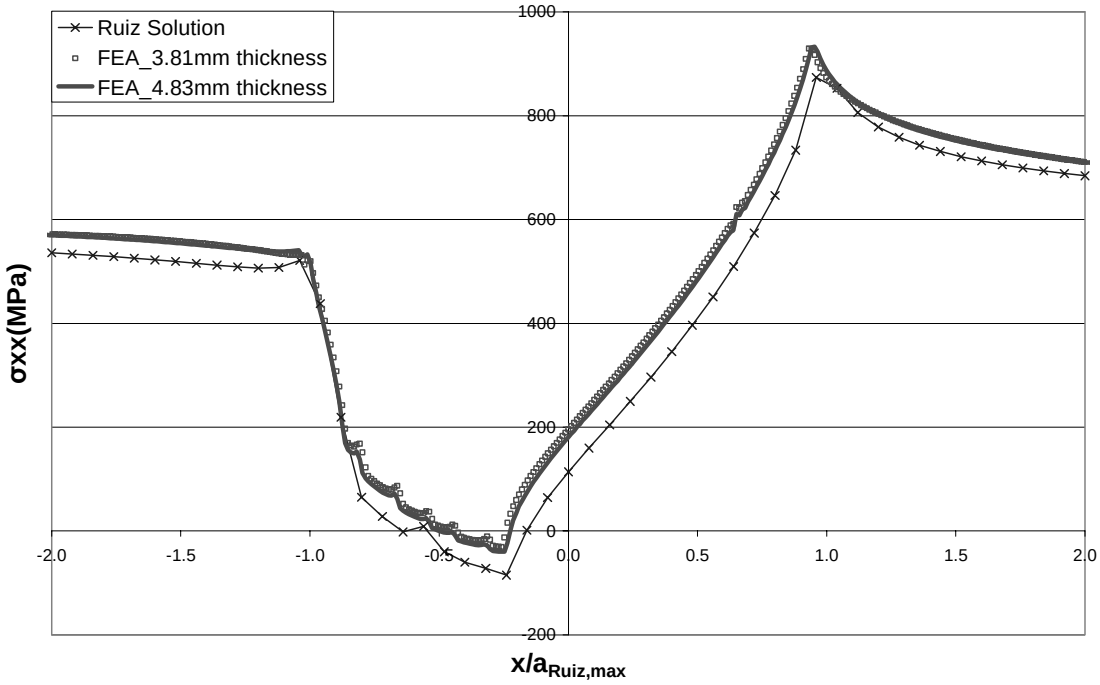

(a) Thickness Effect on σ_{xx} Stress Profile

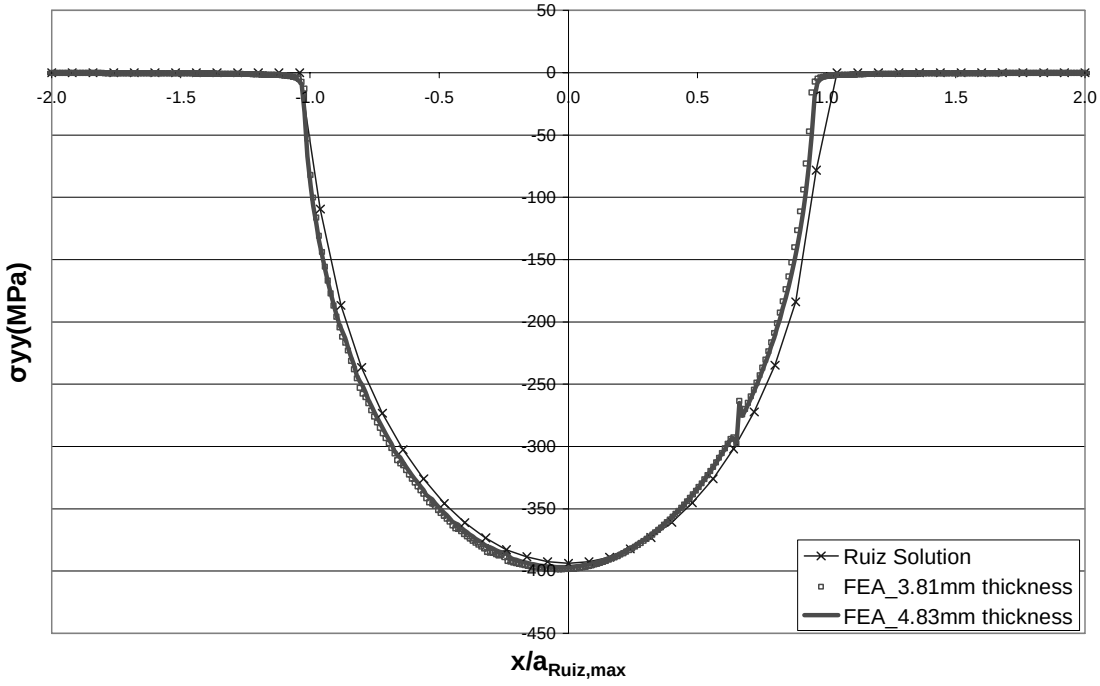

(b) Thickness Effect on σ_{yy} Stress Profile

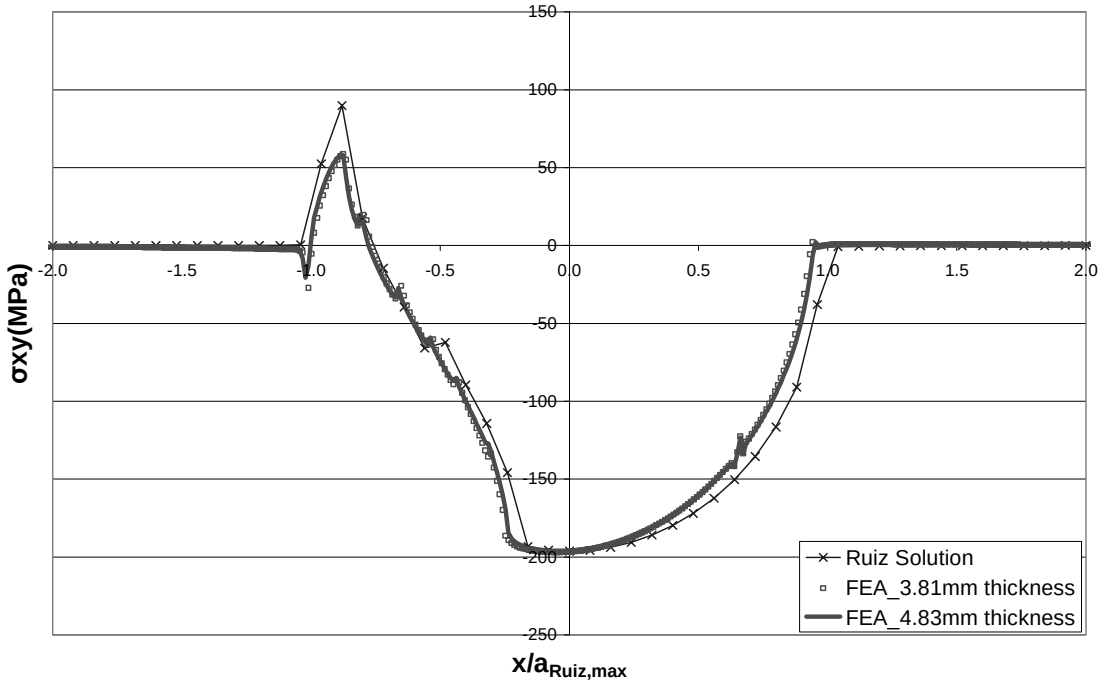

(c) Thickness Effect on σ_{xy} Stress Profile

Figure 39. Thickness Effect on Stress Profile along the Contact Surface for Step 2, Test 1

Load Condition: σ_{max} =600 MPa, σ_{min} =60 MPa, P_{max} =2224 N, P_{min} =2224 N, P_{Freq} =0 Hz
Un-peened Specimen

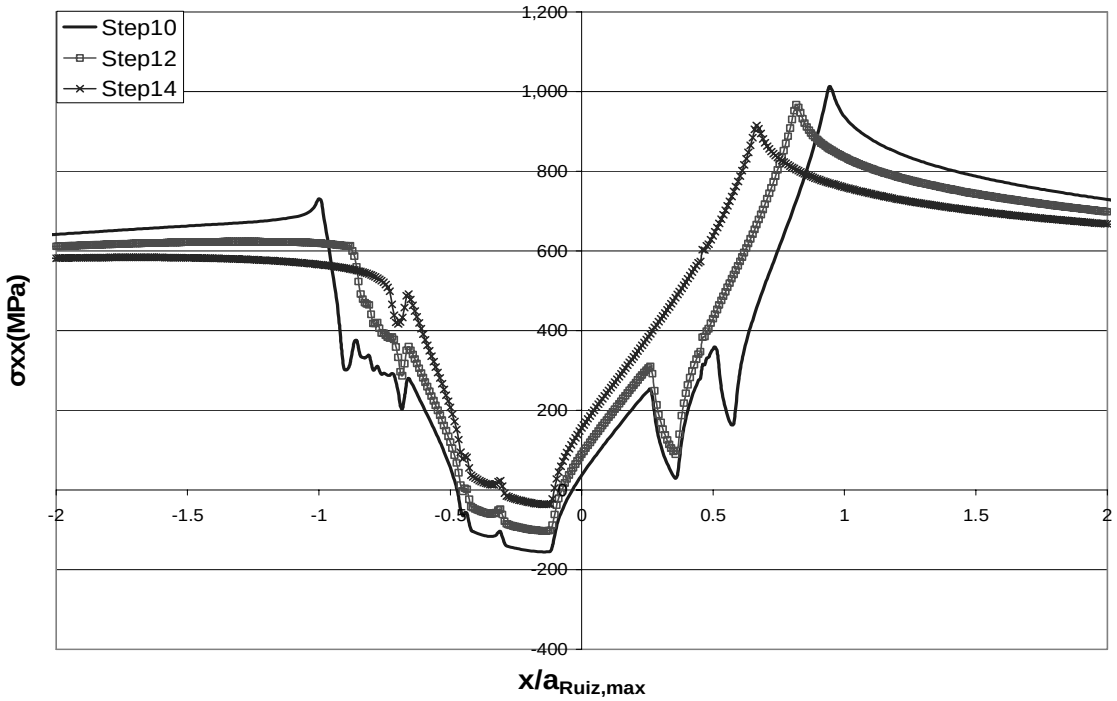

(a) σ_{xx} at Different Steps

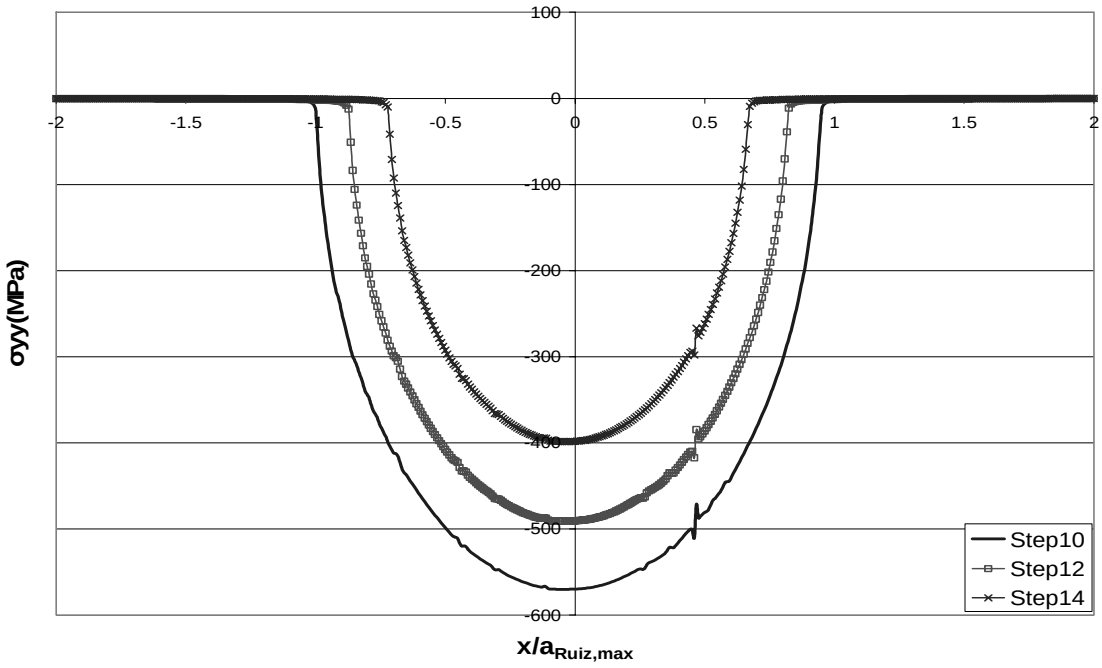

(b) σ_{yy} at Different Steps

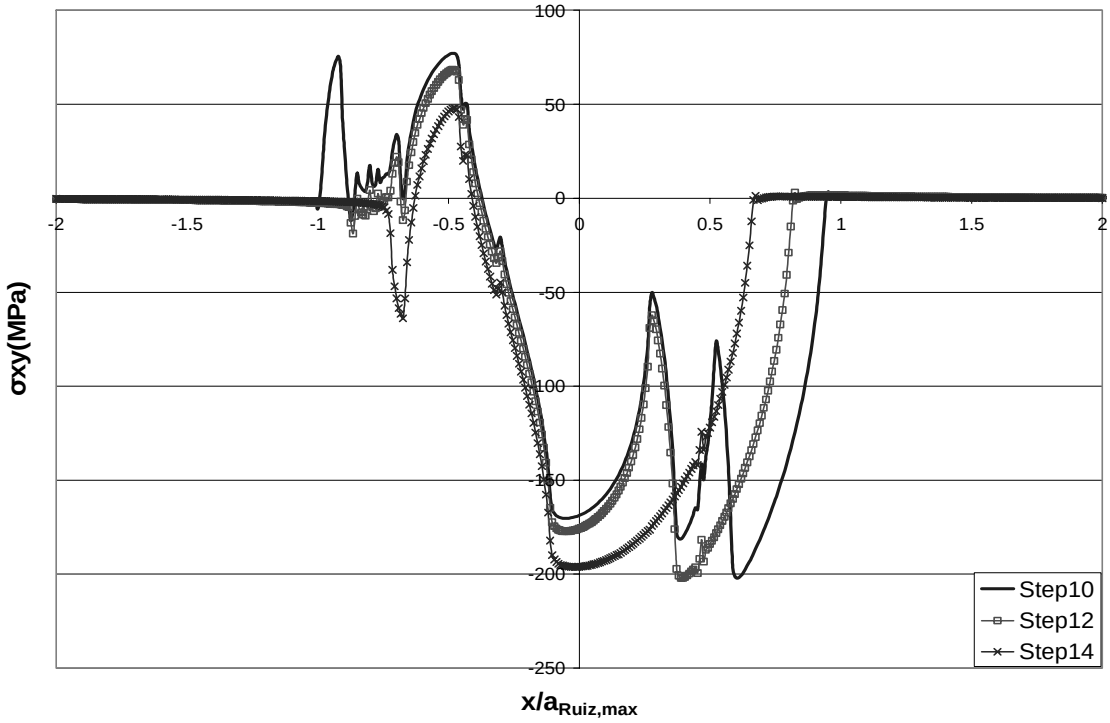

(c) σ_{xy} at Different Steps

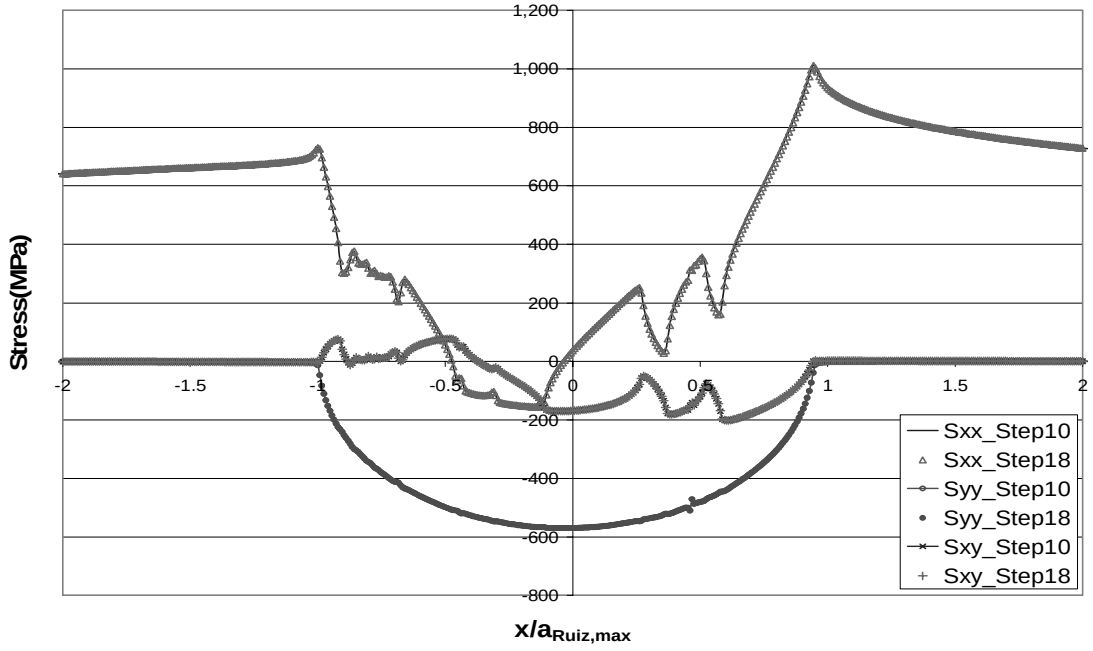

(d) Stress Profile at Step 10 and Step 18

Figure 40. Evolution of Stress Profile along Contact Surface for Test 3
Load Condition: σ_{max}=600 MPa, σ_{min}=60 MPa, P_{max}=4448 N, P_{min}=2224 N, P_{Freq}=2.5 Hz
Un-peened Specimen

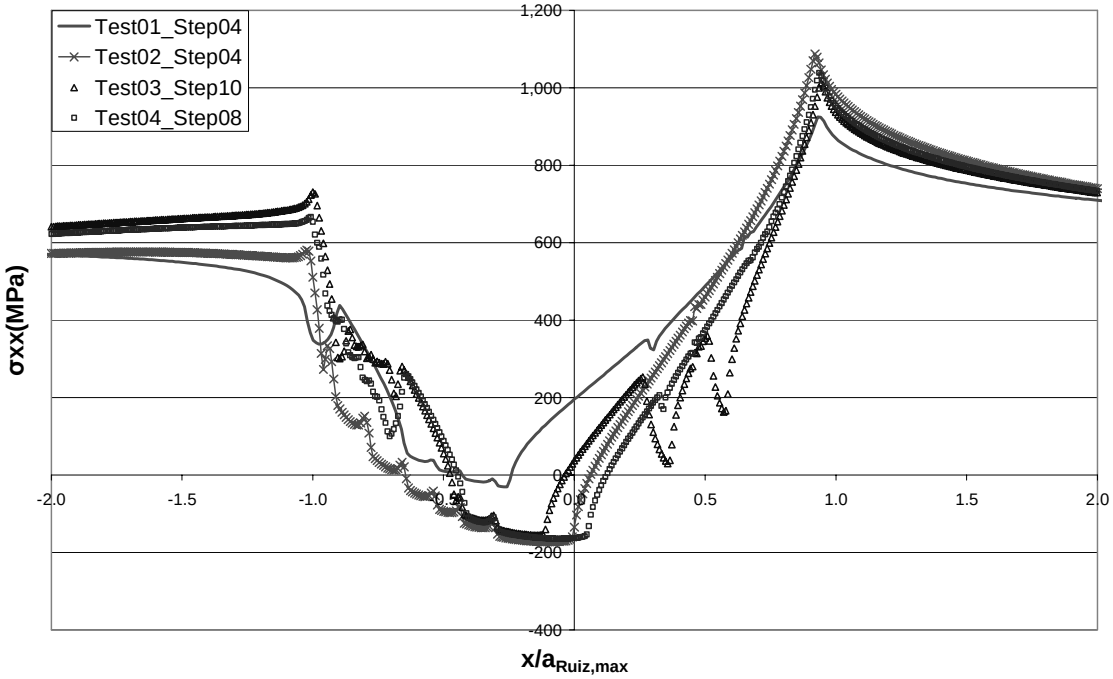

Figure 41. Comparison of Maximum Load Condition along Contact Surface among Different tests

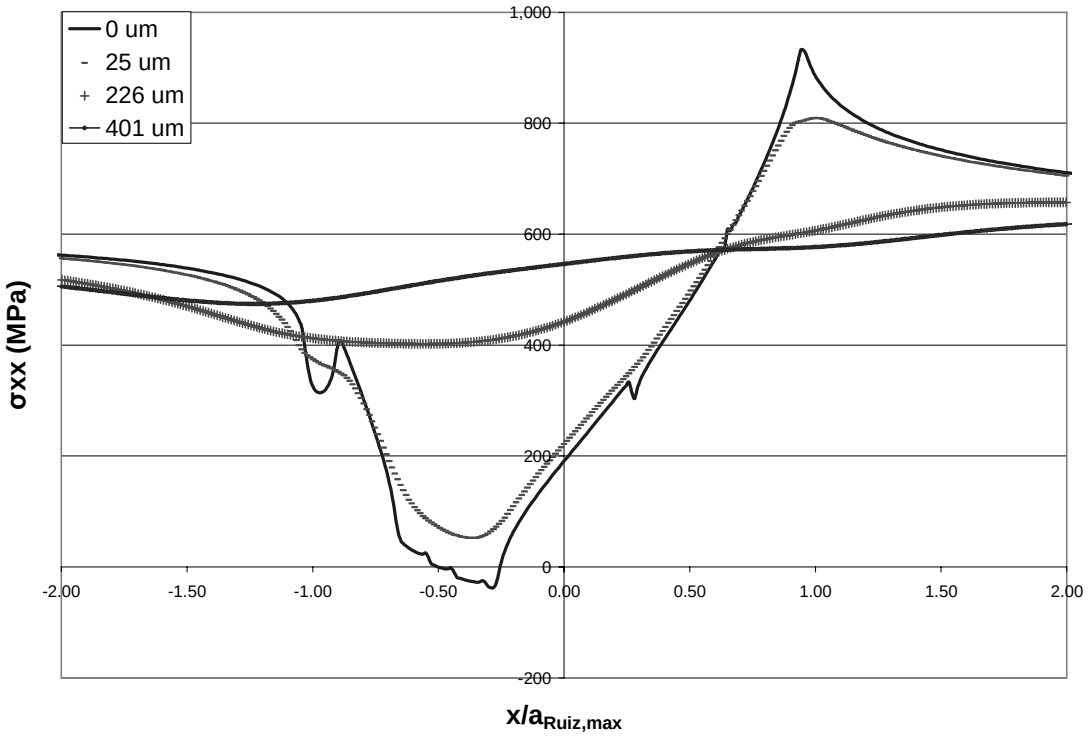

(a) σ_{xx} Stress Profile at Different Depths without Residual Stress

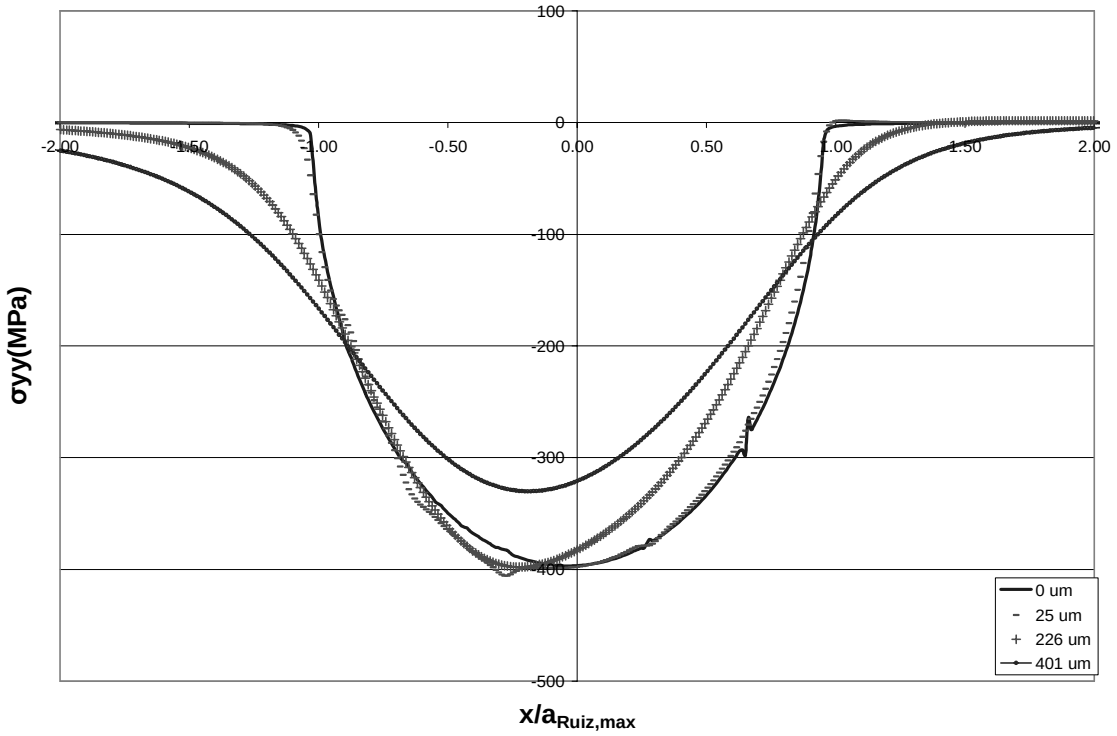

(b) σ_{yy} Stress Profile at Different Depths without Residual Stress

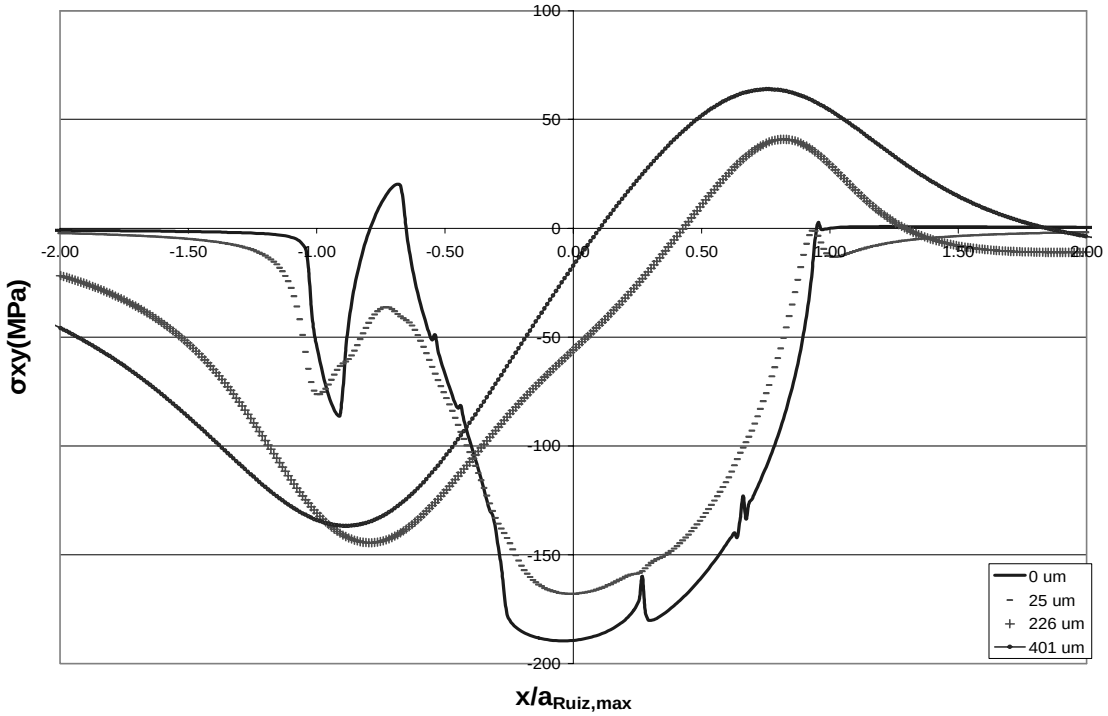

(c) σ_{xy} Stress Profile at Different Depths without Residual Stress

Figure 42. Comparison of Stress Profile at Different Depths for Test 9, Step 4

Load Condition: σ_{max} =600 MPa, σ_{min} =60 MPa, P_{max} =2224 N, P_{min} =2224 N, P_{Freq} =0 Hz
Shot-peened Specimen

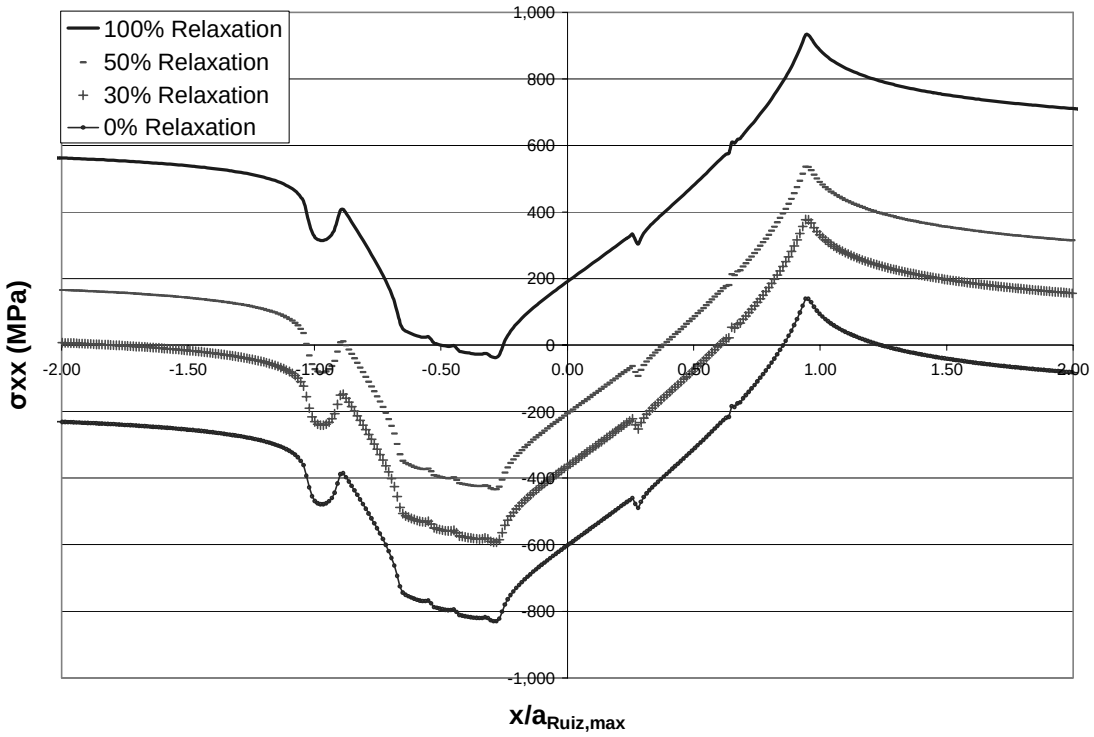

(a) σ_{xx} Stress Profile on Contact Surface with Different Residual Stress Relaxation

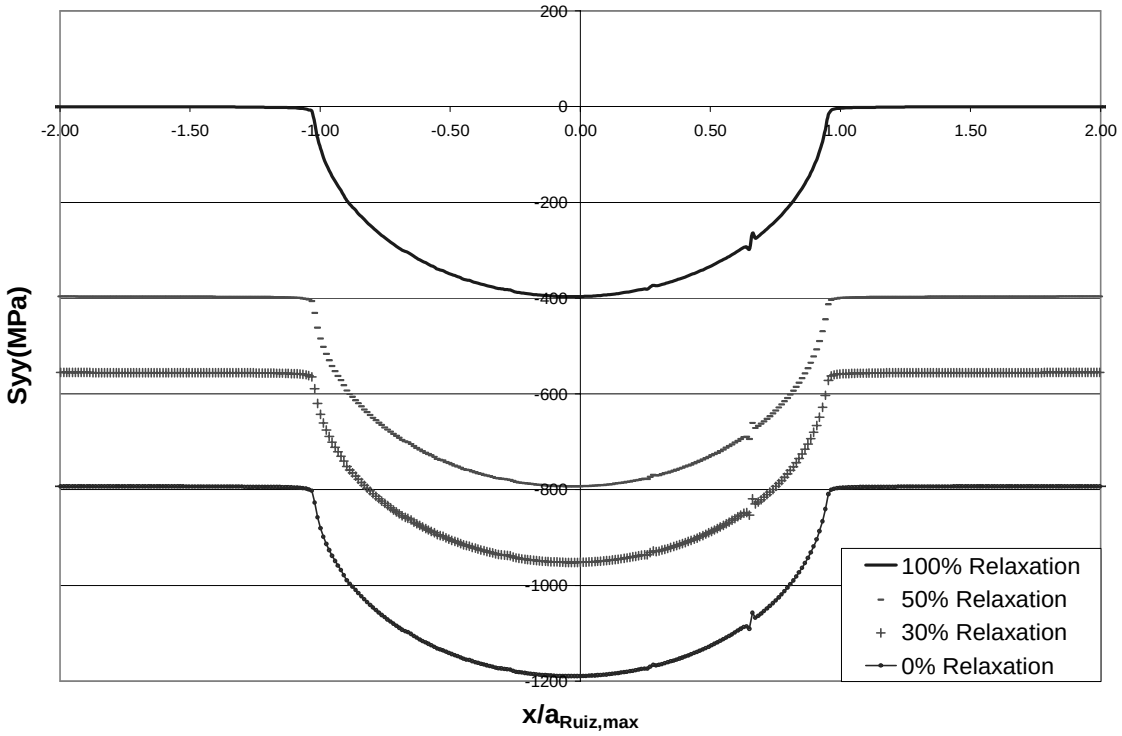

(b) σ_{yy} Stress Profile on Contact Surface with Different Residual Stress Relaxation

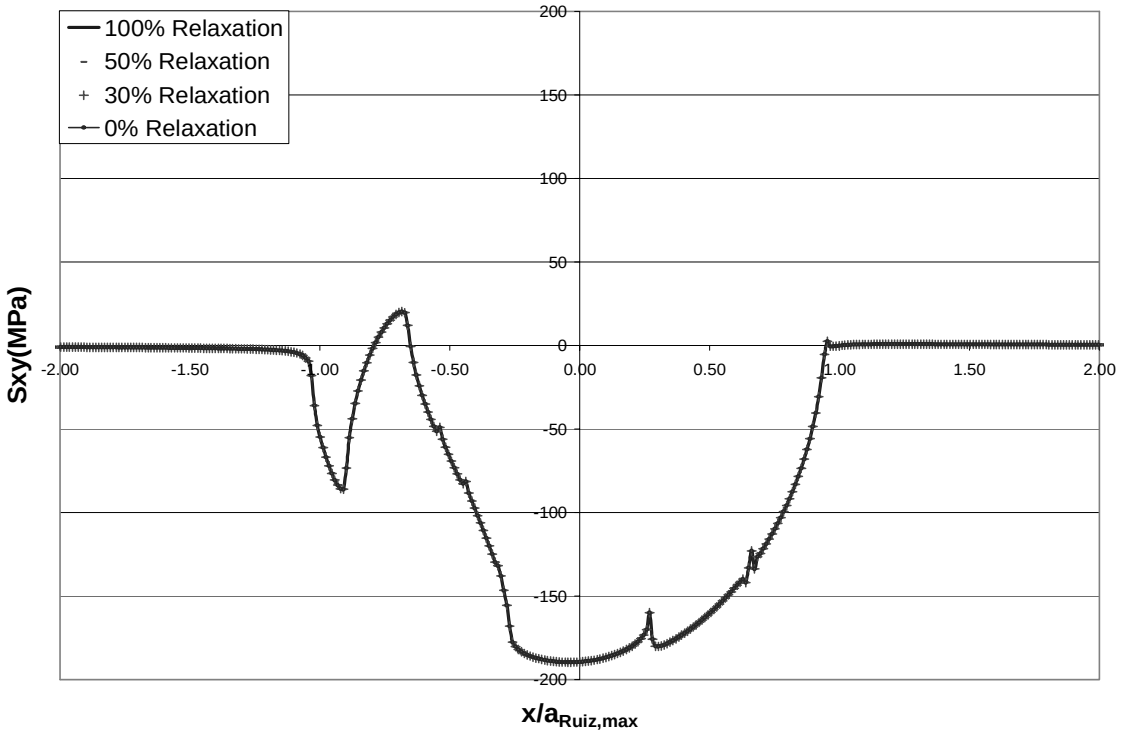

(c) σ_{xy} Stress Profile on Contact Surface with Different Residual Stress Relaxation

Figure 43. Comparison of Stress Profile under Influence of Residual Stress Relaxation along Contact Surface for Test 9, Step 4

Load Condition: σ_{max} =600 MPa, σ_{min} =60 MPa, P_{max} =2224 N, P_{min} =2224 N, P_{Freq} =0 Hz
Shot-peened Specimen

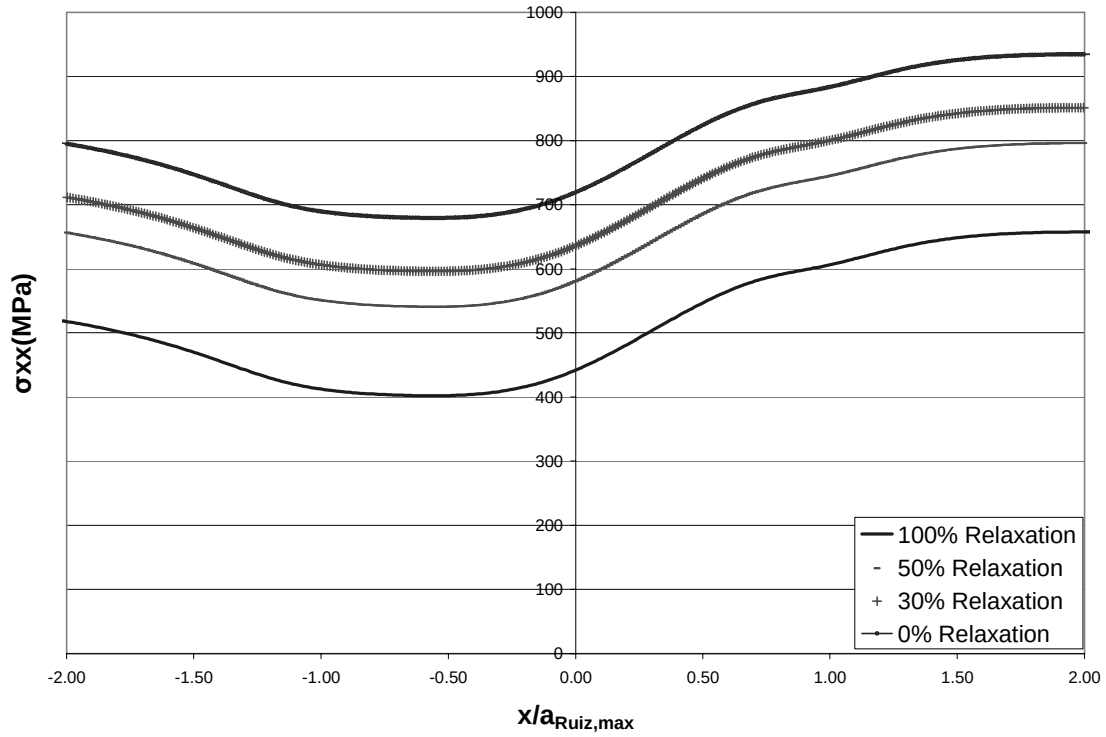

(a) σ_{xx} Stress Profile at 226 μm Depth with Different Residual Stress Relaxation

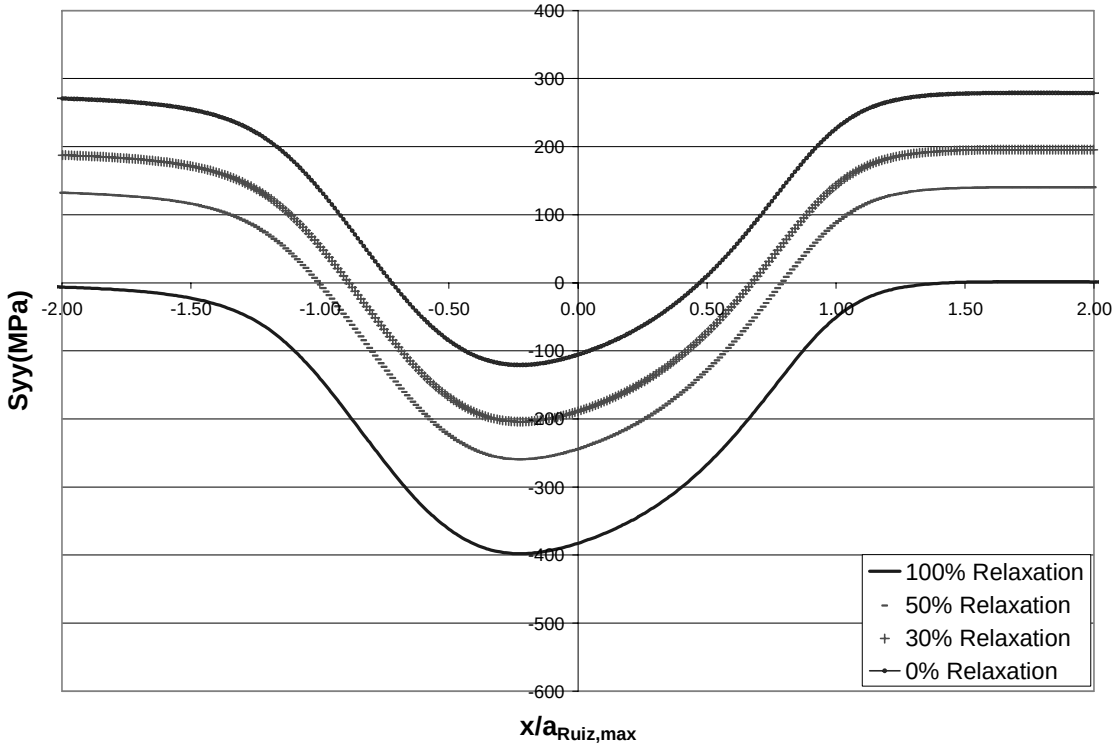

(b) σ_{yy} Stress Profile at 226 μm Depth with Different Residual Stress Relaxation

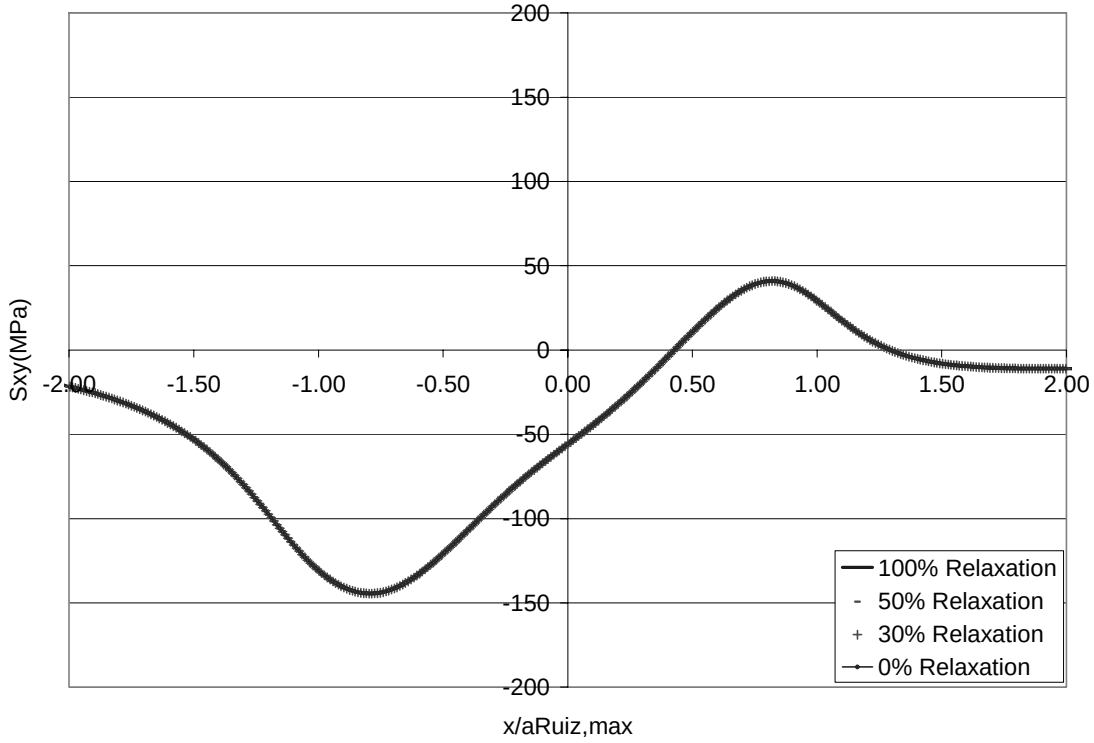

(c) σ_{xy} Stress Profile at 226 μm Depth with Different Residual Stress Relaxation

Figure 44. Comparison of Stress Profile under Influence of Residual Stress Relaxation at 226 μm Depth for Test 9, Step 4

Load Condition: σ_{max} =600 MPa, σ_{min} =60 MPa, P_{max} =2224 N, P_{min} =2224 N, P_{Freq} =0 Hz
Shot-peened Specimen

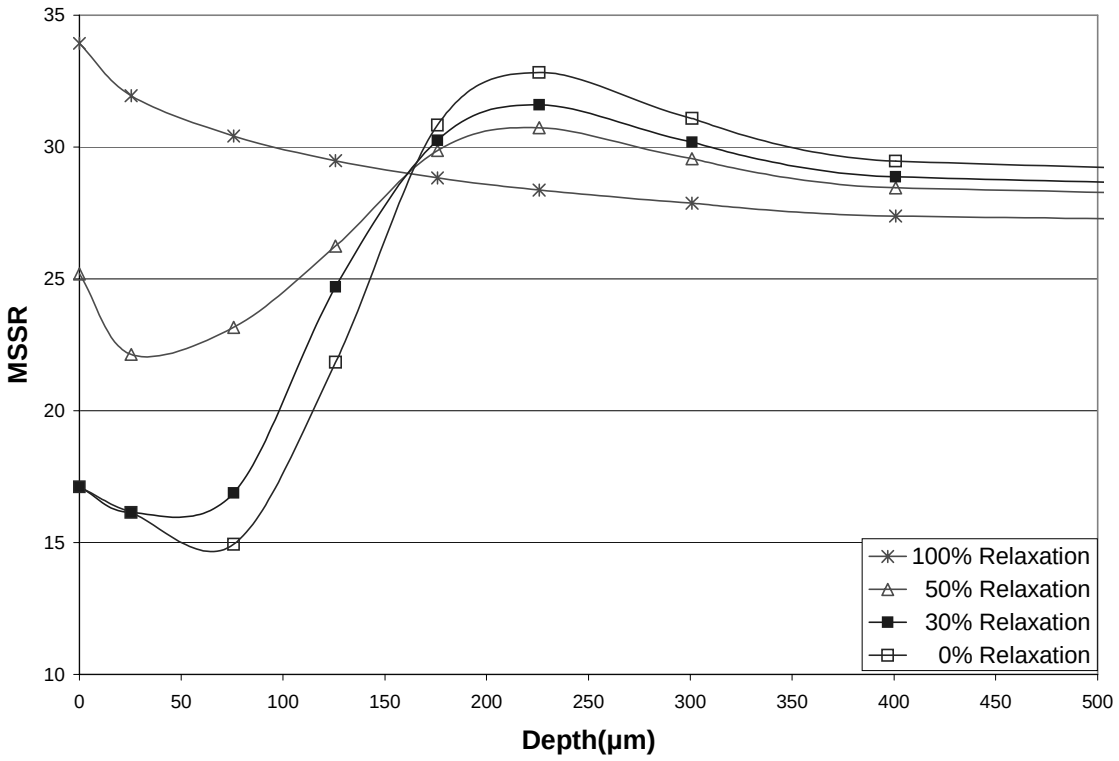

(a) MSSR at Different Depths for Test 9, Step 4-5

Load Condition: σ_{max} =600 MPa, σ_{min} =60 MPa, P_{max} =2224 N, P_{min} =2224 N, P_{Freq} =0 Hz
Shot-peened Specimen

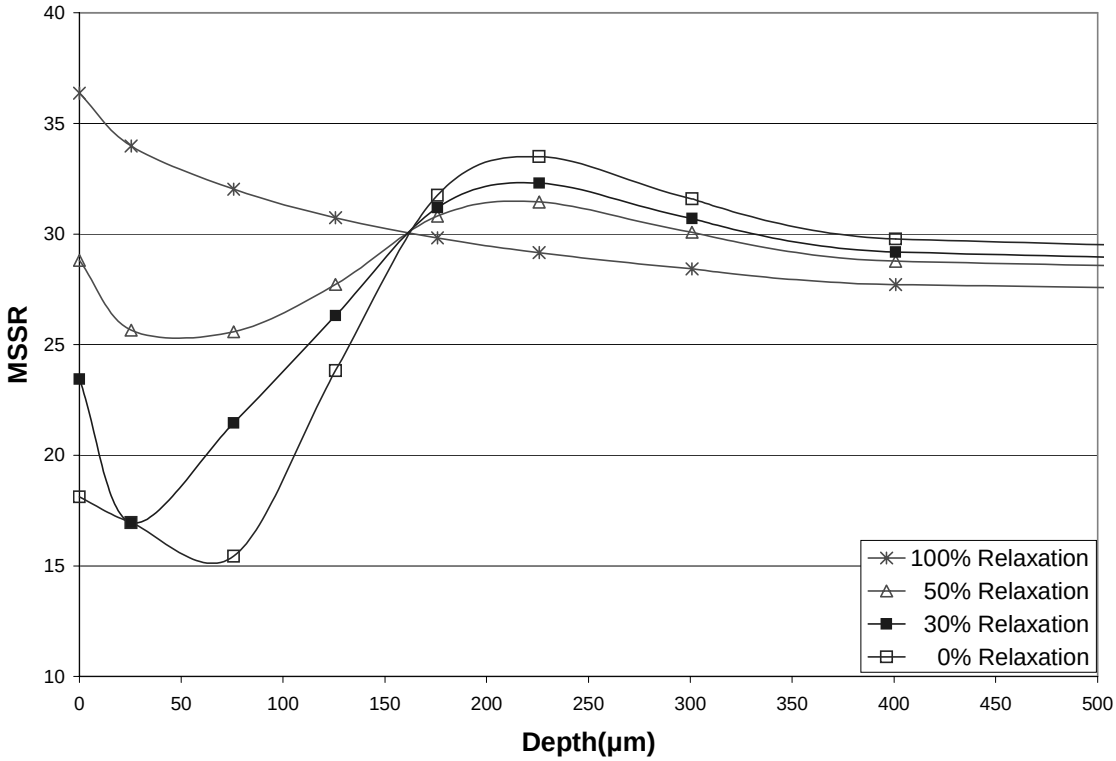

(b) MSSR at Different Depths for Test 10, Step 4-5

Load Condition: σ_{max} =600 MPa, σ_{min} =60 MPa, P_{max} =4448 N, P_{min} =4448 N, P_{Freq} =0 Hz
Shot-peened Specimen

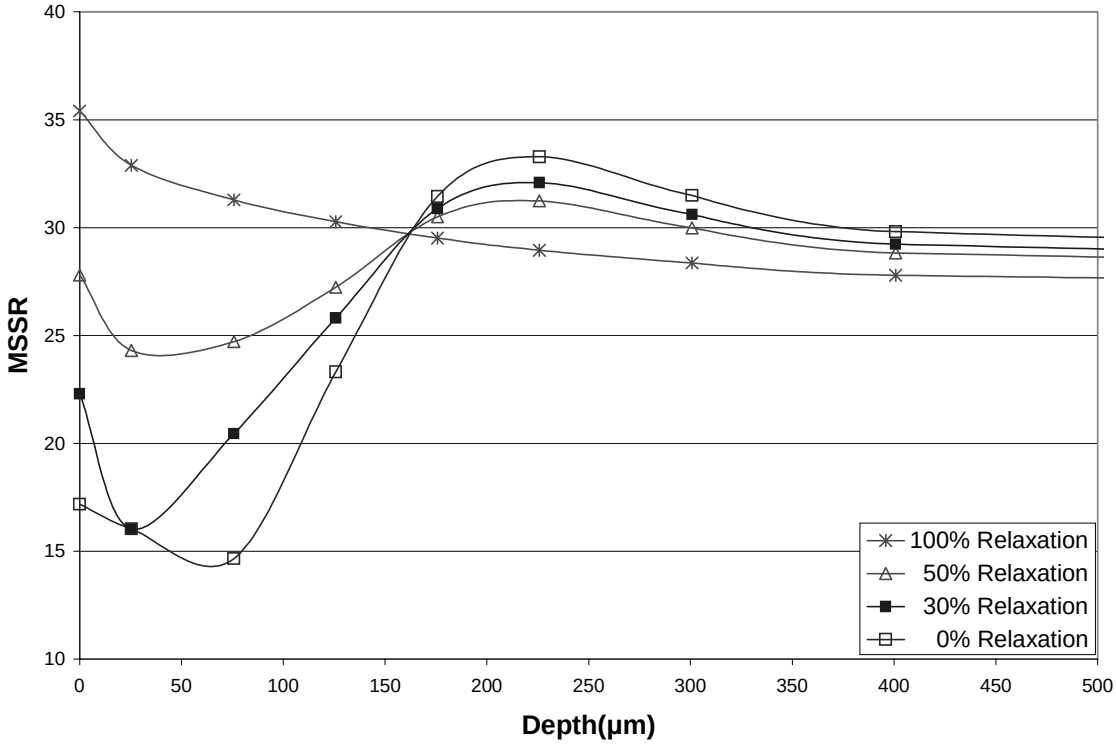

(c) MSSR at Different Depths for Test 11, Step 11-12

Load Condition: σ_{max}=600 MPa, σ_{min}=60 MPa, P_{max}=4448 N, P_{min}=2224 N, P_{Freq}=2.5 Hz
Shot-peened Specimen

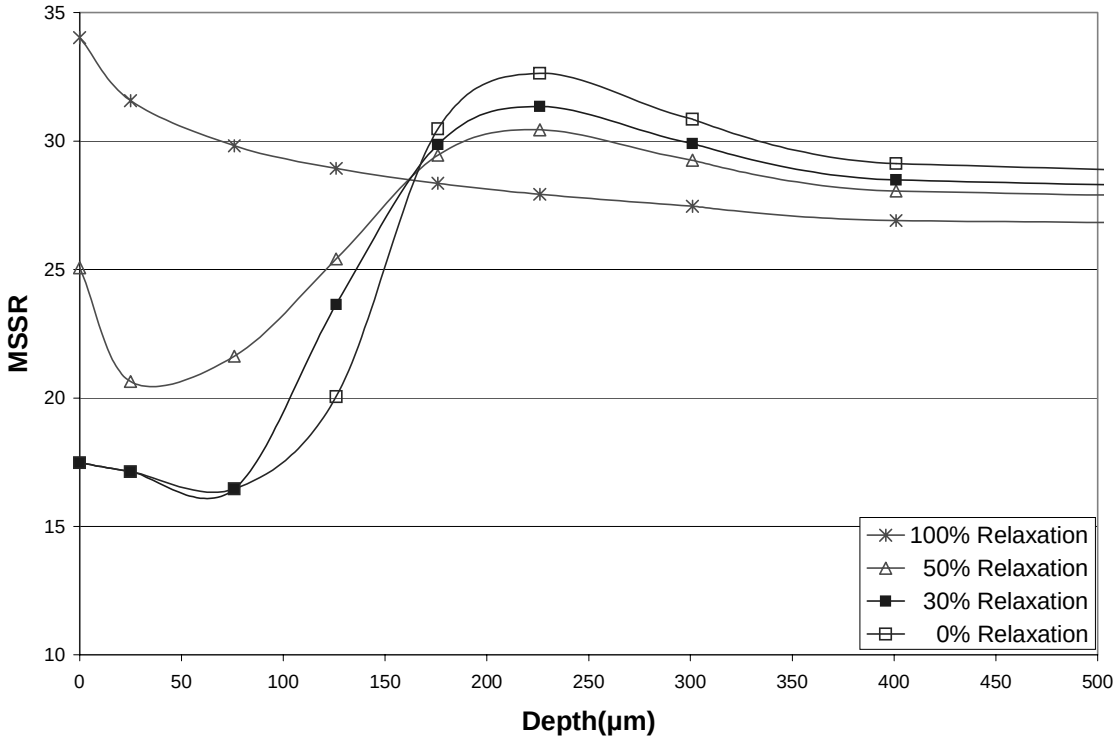

(d) MSSR at Different Depths for Test 14, Step 8-11

Load Condition: σ_{max} =600 MPa, σ_{min} =60 MPa, P_{max} =4448 N, P_{min} =2224 N, P_{Freq} =30 Hz
Shot-peened Specimen

Figure 45. MSSR under Influence of Residual Stress Relaxation at Different Depths

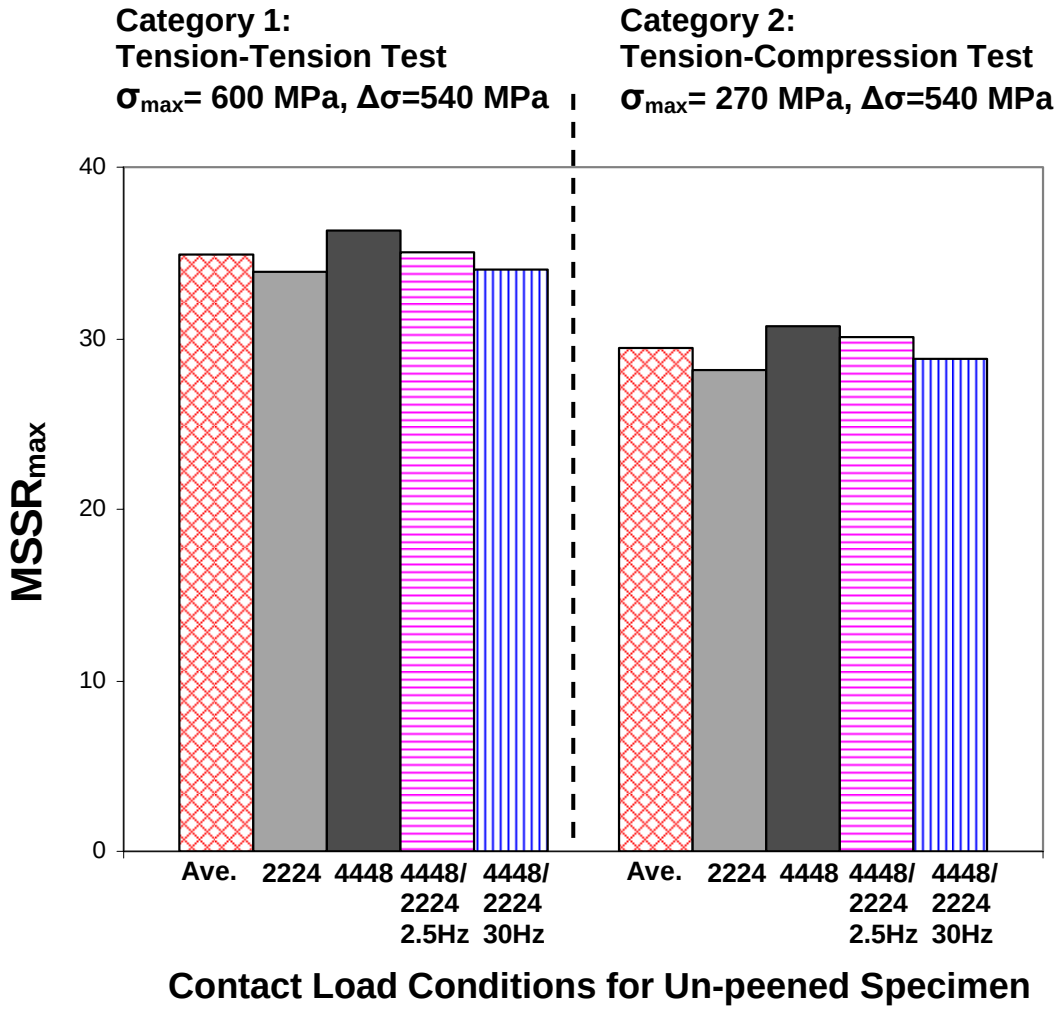

(a) For Un-peened Specimens

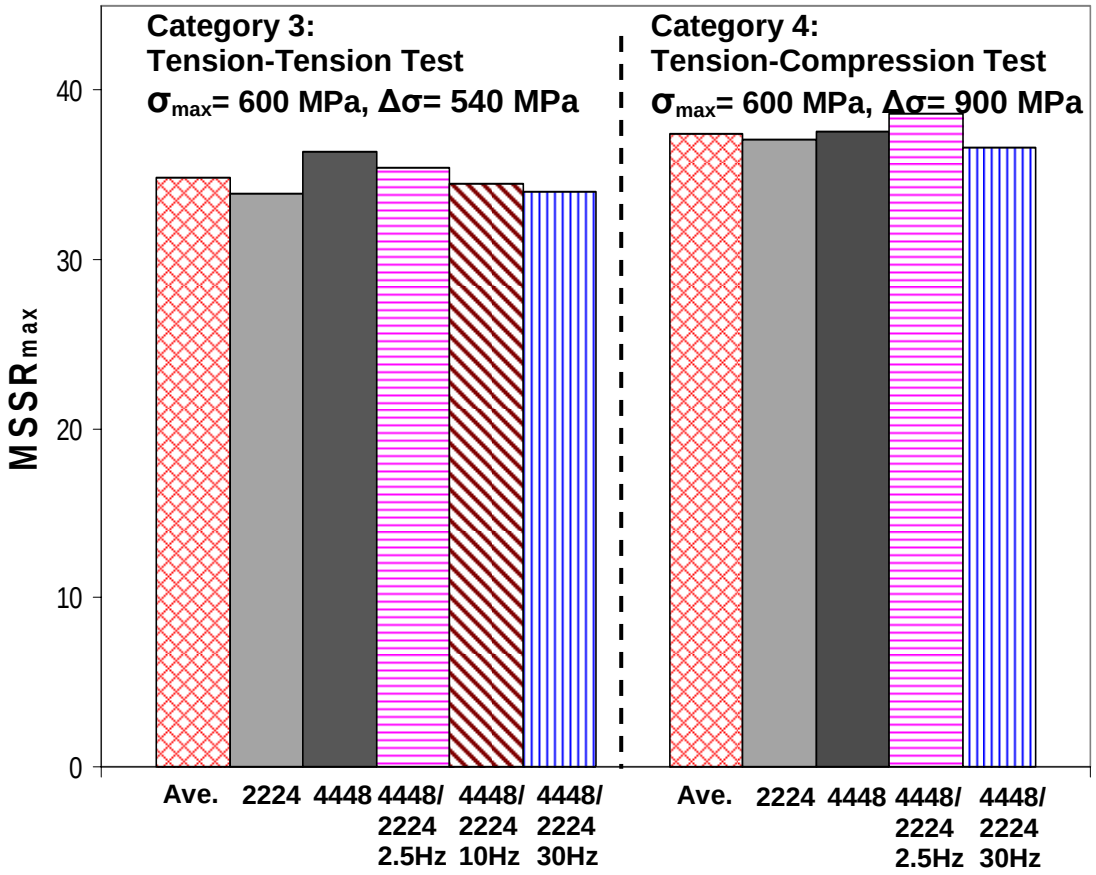

(b) Shot-peened Specimens with 100% Stress Relaxation

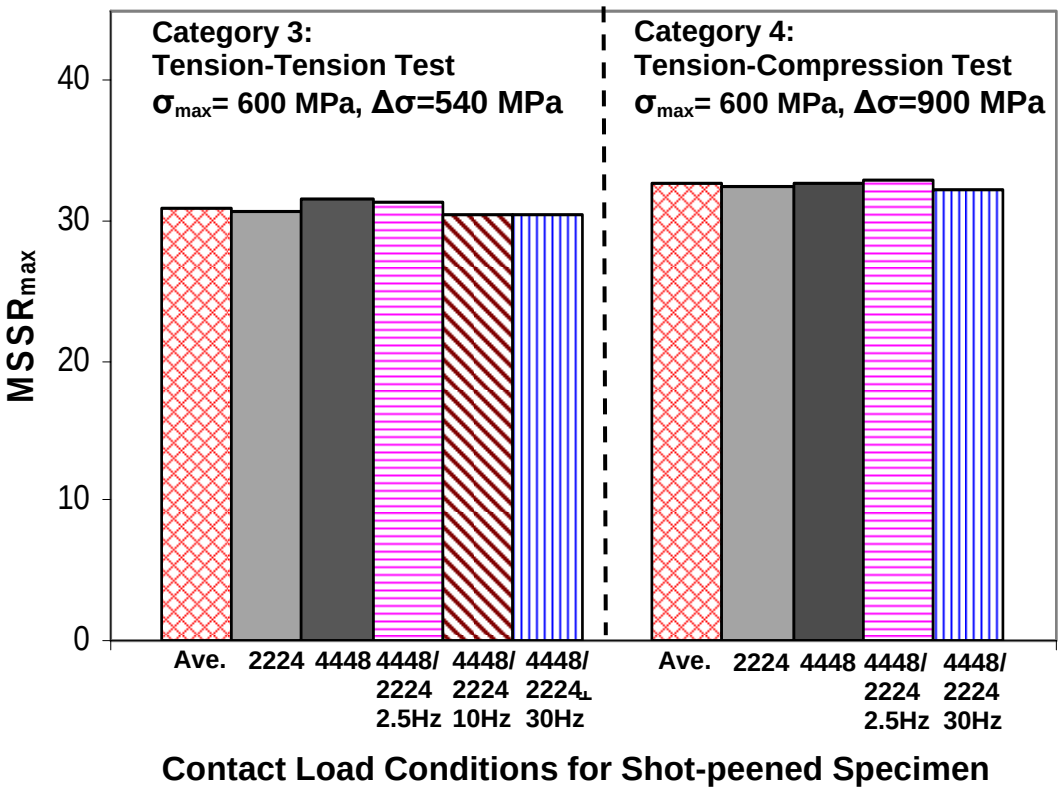

(c) For Un-peened Specimens 50% Stress Relaxation

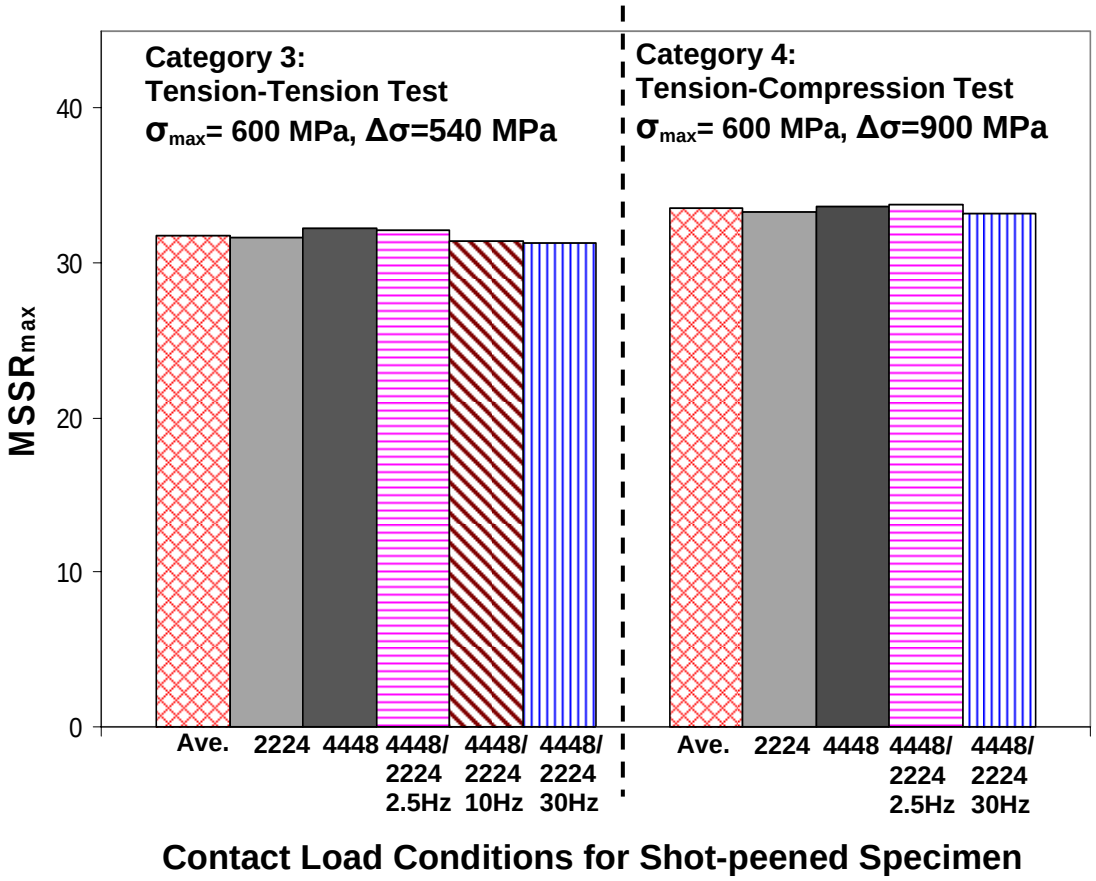

(d) For Shot-peened Specimens with 30% Stress Relaxation

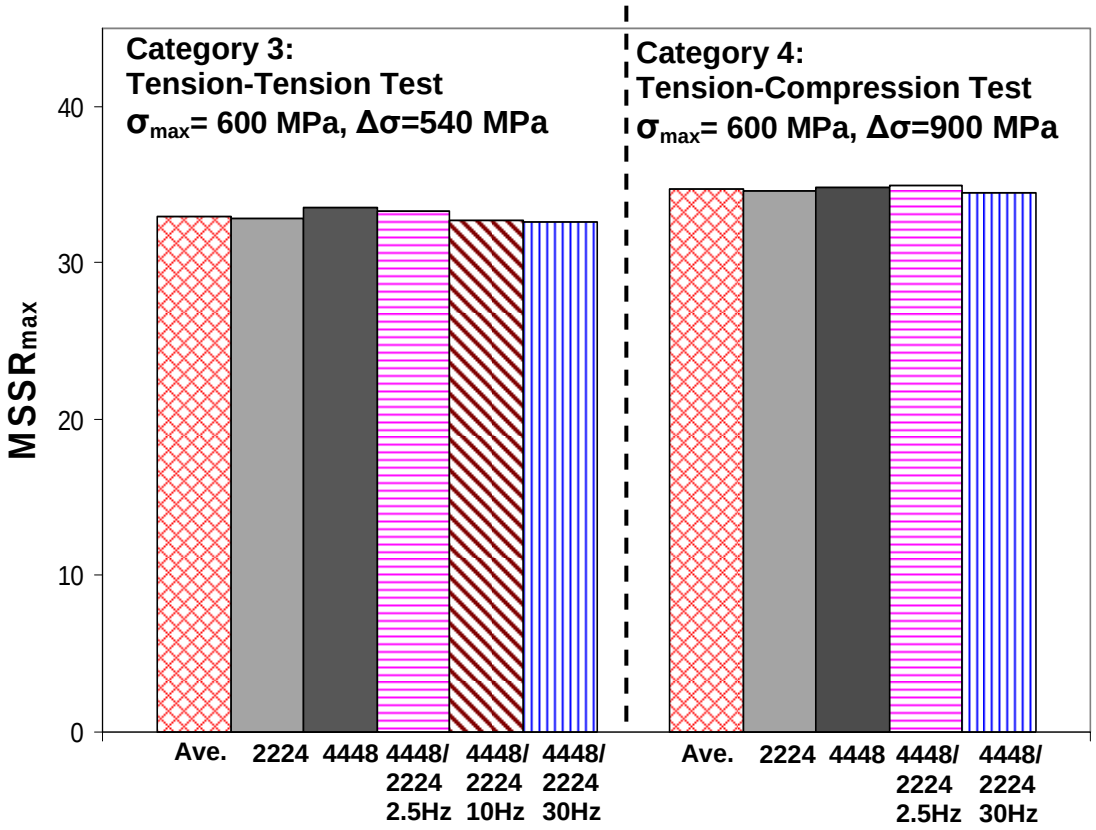

(e) For Shot-peened Specimens with 0% Stress Relaxation

Figure 46. $MSSR_{max}$ Comparisons for Various Contact Loading Conditions (Data from Table 12(a))

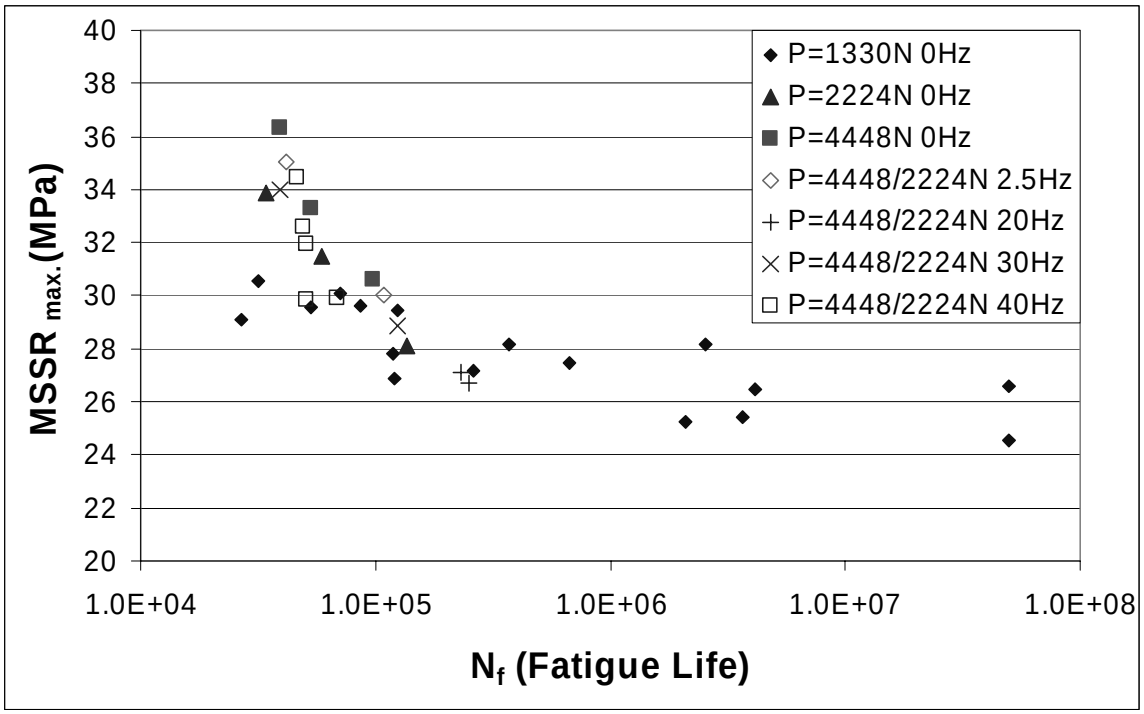

(a) $MSSR_{max}$ –N_f for Un-peened Specimens

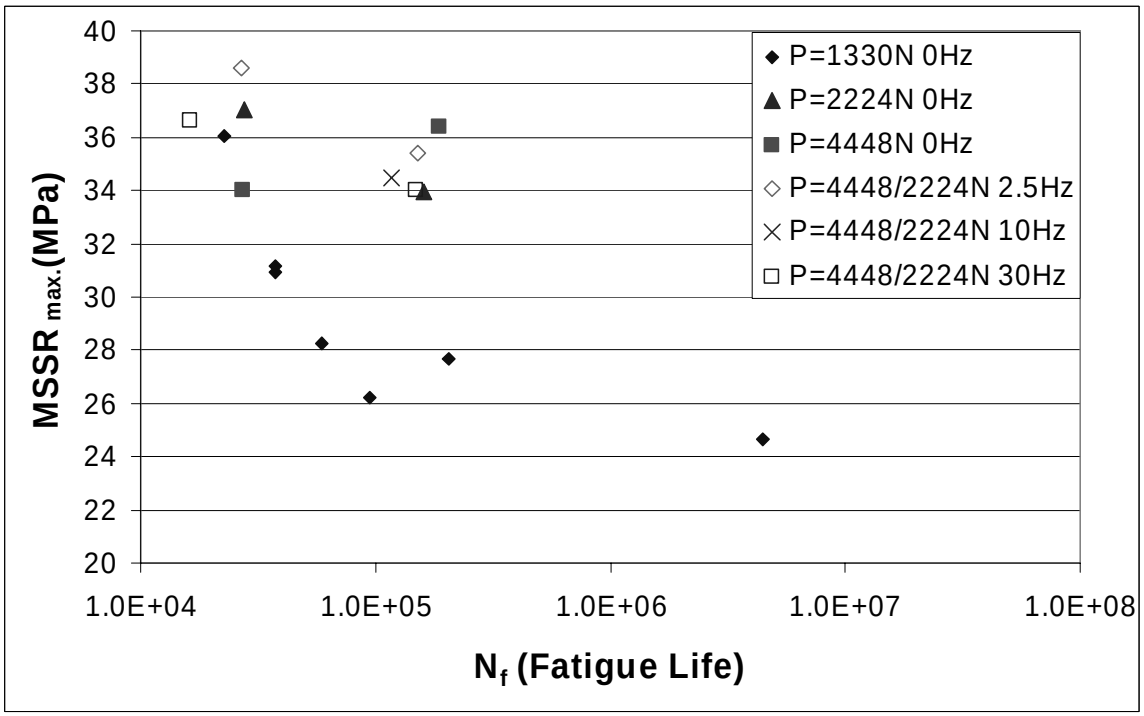

(b) $MSSR_{max}$ –N_f for Shot-peened Specimens with 100% Stress Relaxation

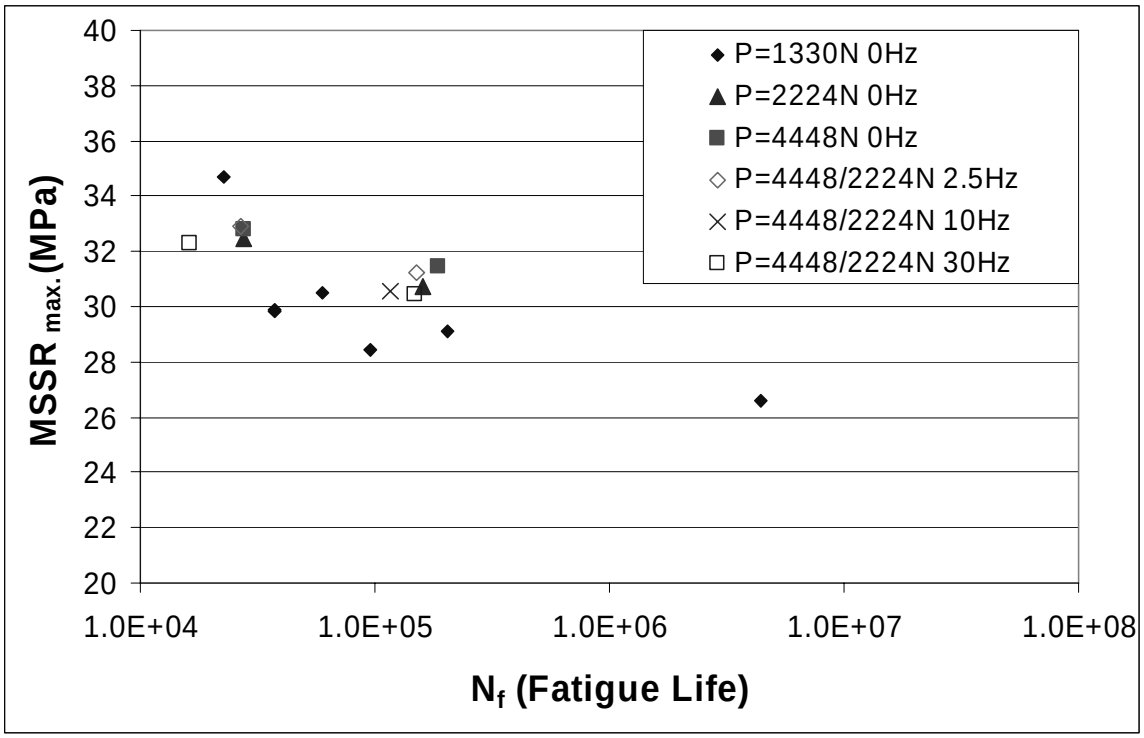

(c) $MSSR_{max}$ –N_f for Shot-peened Specimens with 50% Stress Relaxation

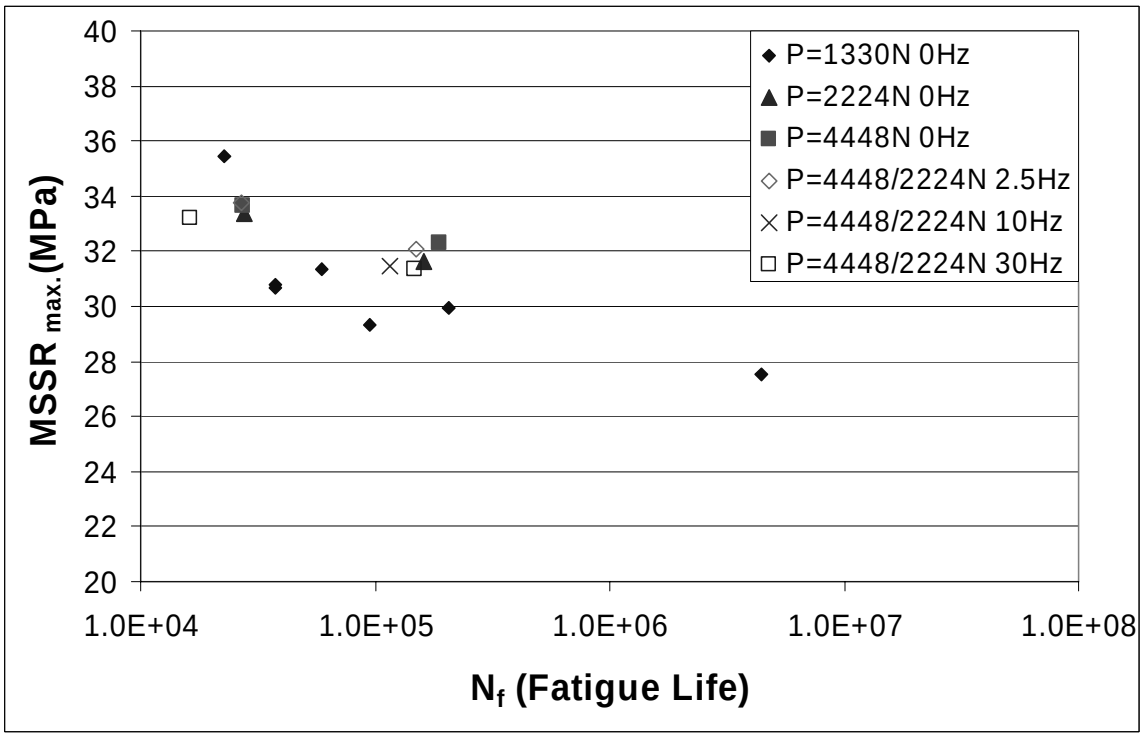

(d) $MSSR_{max}$ –N_f for Shot-peened Specimens with 30% Stress Relaxation

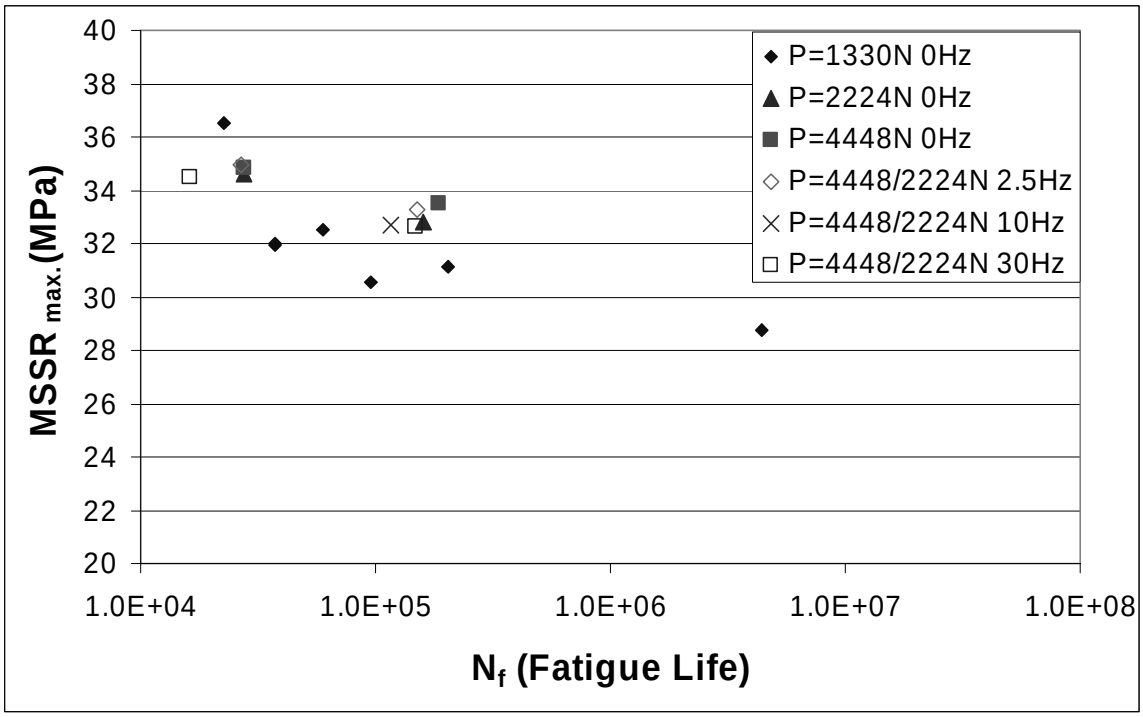

(e) $MSSR_{max}$ –N_f for Shot-peened Specimens with 0% Stress Relaxation

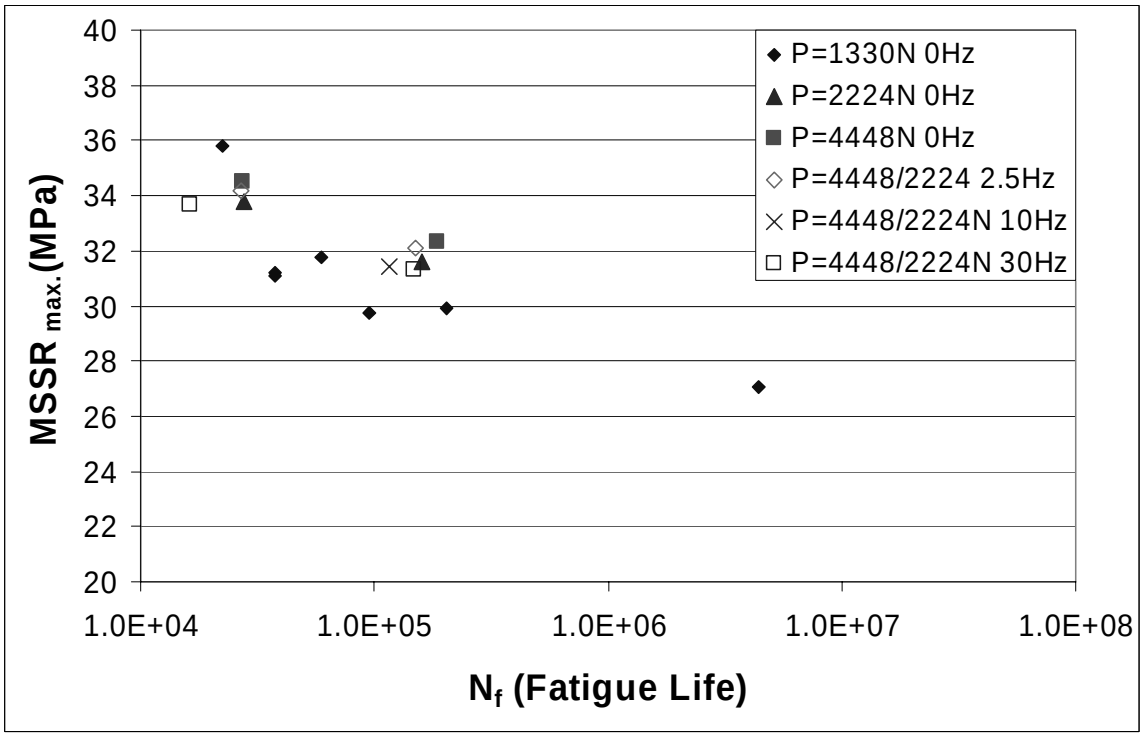

(f) $MSSR_{max}$ –N_f for Shot-peened Specimens with Different Stress Relaxation

Figure 47. $MSSR_{max}$-N_f for Un-peened and Shot-peened Specimens
(Data from Table 12)

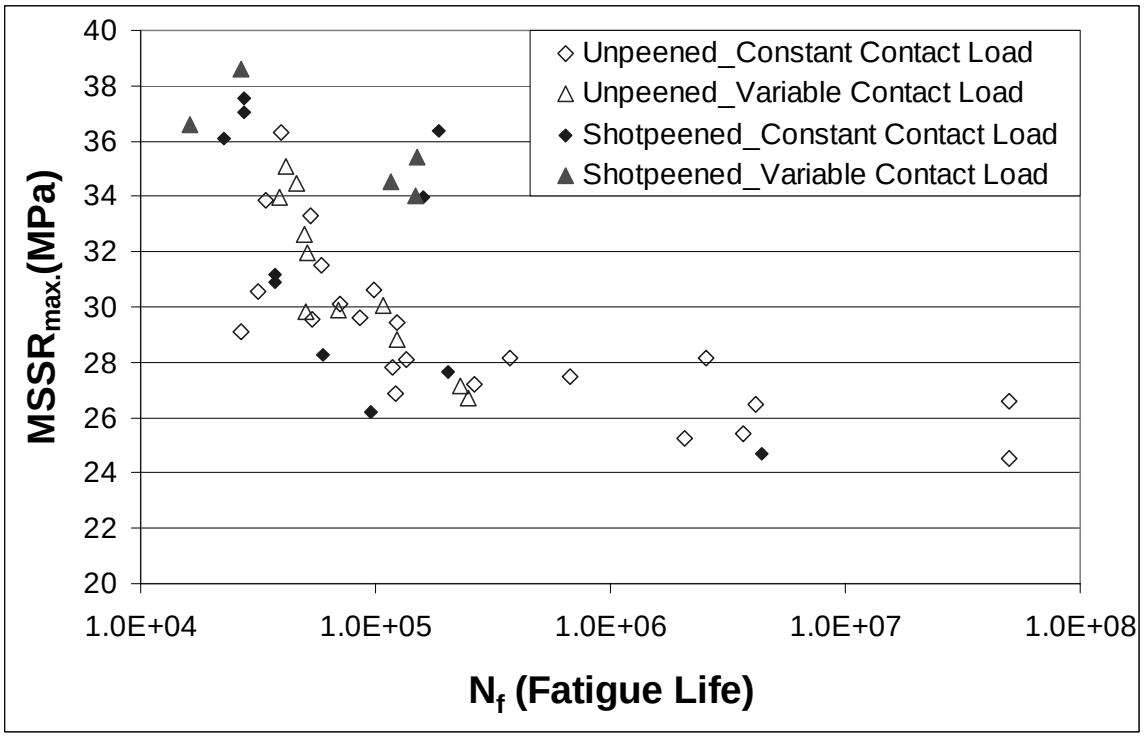

(a) $MSSR_{max}$ –N_f for Constant and Variable Contact Load with 100% Stress Relaxation

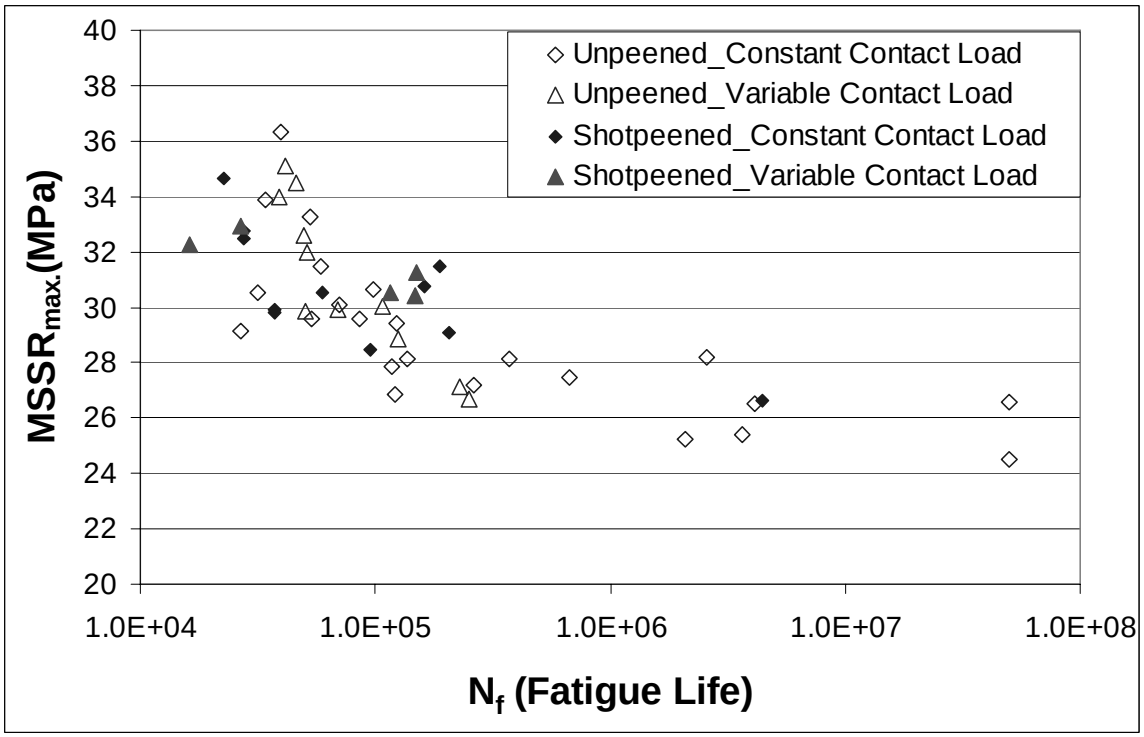

(b) $MSSR_{max}$ –N_f for Constant and Variable Contact Load with 50% Stress Relaxation

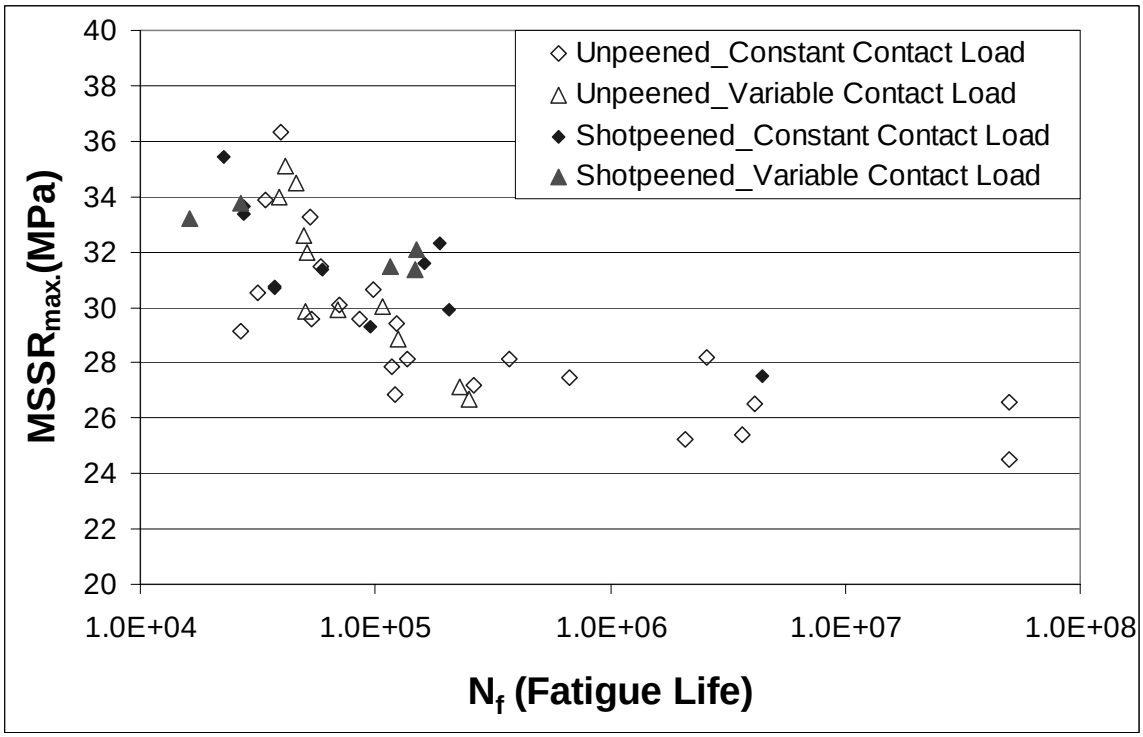

(c) $MSSR_{max}$ –N_f for Constant and Variable Contact Load with 30% Stress Relaxation

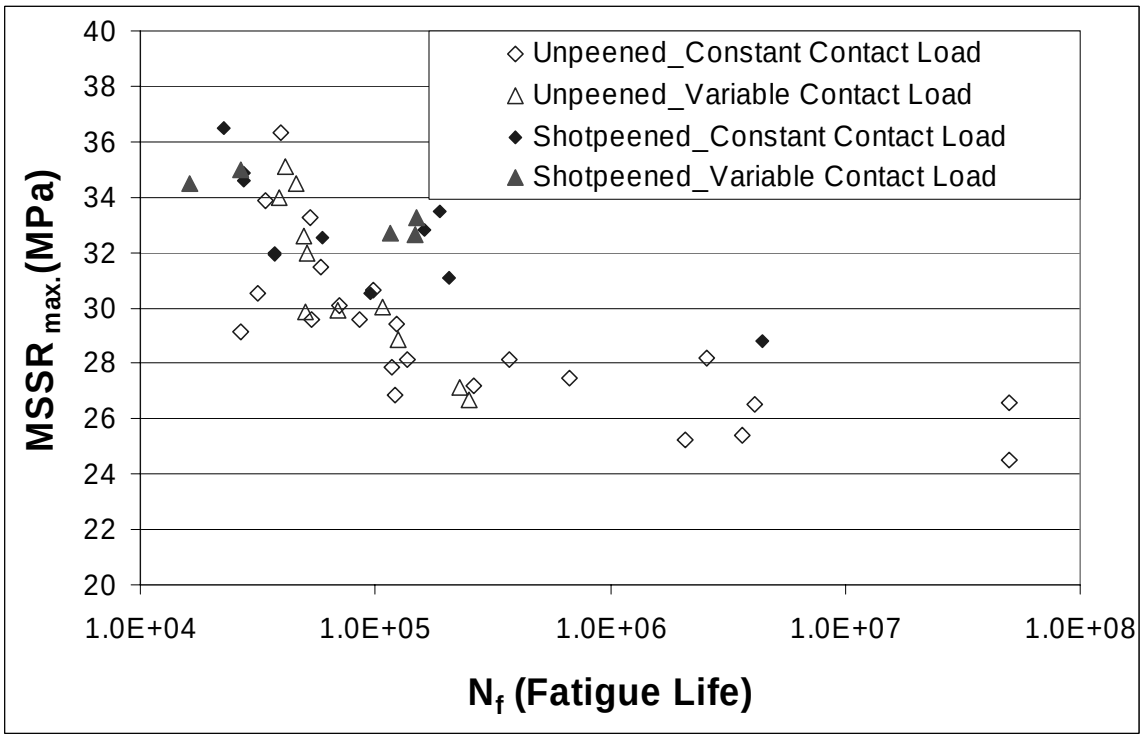

(d) $MSSR_{max}$ –N_f for Constant and Variable Contact Load with 0% Stress Relaxation

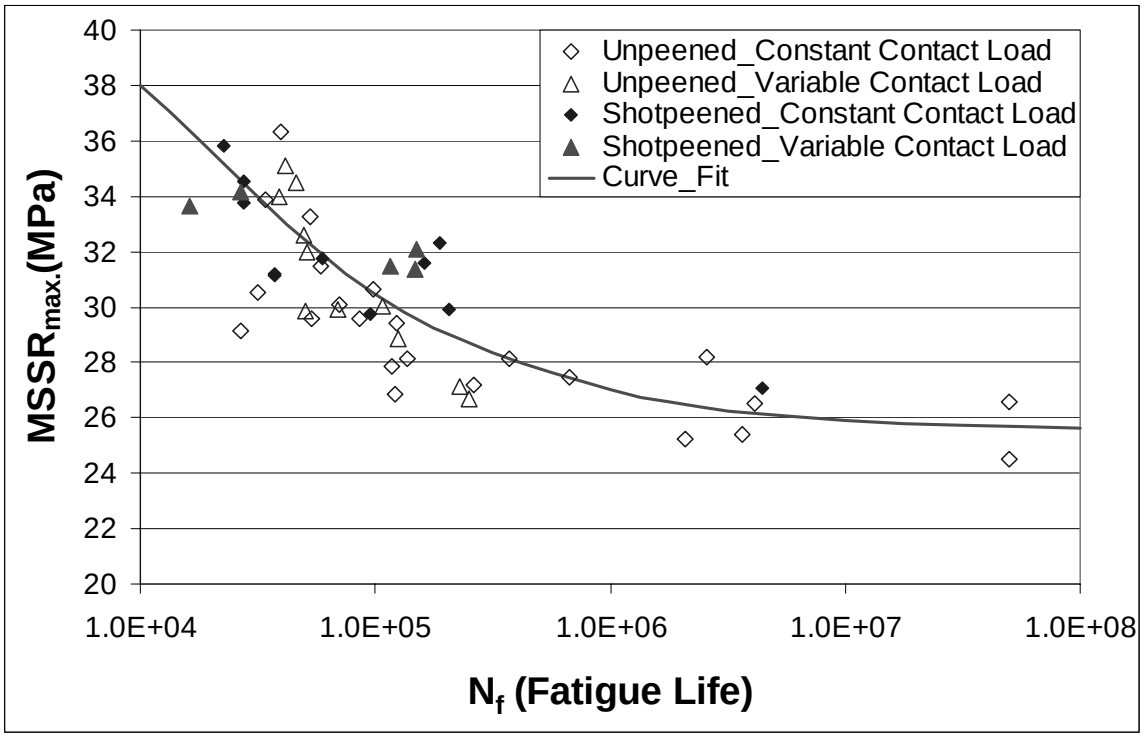

(e) $MSSR_{max}$–N_f for Constant and Variable Contact Load with Different Stress Relaxation

Figure 48. $MSSR_{max}$-N_f for Constant and Variable Contact Load
(Data from Table 12)

Note:
The fitting curve shown in Figure 48 (e) is used to approximately demonstrate the trend observed from $MSSR_{max}$.

Table 5. Summary of Experimental Results

Test #	Shot peened	σ_{max} (MPa)	σ_{min} (MPa)	P_{max} (N)	P_{min} (N)	P_{Freq} (Hz)	Q_{max} (N)	Q_{min} (N)	N_f (Cycle)	Crack Initiation Depth (μm)	Q/P Max.	f_{FEA}
1	n	600	60	2,224	2224	0	806	-580	34,072	Surface	0.36	0.5
2	n	600	60	4,448	4448	0	1,399	-27	39,434	Surface	0.32	0.5
3	n	600	60	4,448	2,224	2.5	730	-590	41,400	Surface	0.29	0.5
4	n	600	60	4,448	2,224	30	920	-532	39,004	Surface	0.34	0.5
5	n	270	-270	2,224	2224	0	649	-650	136,092	Surface	0.30	0.5
6	n	270	-270	4,448	4448	0	771	-586	98,072	Surface	0.18	0.5
7	n	270	-270	4,448	2,224	2.5	719	-616	108,056	Surface	0.28	0.5
8	n	270	-270	4,448	2,224	30	740	-650	124,417	180-220	0.30	0.5
9	y	600	60	2,224	2224	0	836	-598	160,474	200-240	0.38	0.5
10	y	600	60	4,448	4448	0	1,223	-340	186,797	200-220	0.28	0.5
11	y	600	60	4,448	2,224	2.5	880	-540	150,520	180-210	0.35	0.5
12	y	600	60	4,448	2,224	10	1,176	-430	116,414	180-210	0.27	0.5
13	y	600	60	4,448	2,224	10	1,180	-418	412,801	180-210	0.27	0.5
14	y	600	60	4,448	2,224	30	1,030	-540	148,437	180-210	0.34	0.5
15	y	600	60	4,448	2,224	40	920	-600	254,277	180-200	0.37	0.5
16	y	600	-300	2,224	2224	0	1,132	-1,335	27,619	180-200	0.61	0.65
17	y	600	-300	4,448	4448	0	1,249	-1,001	27,414	200-230	0.29	0.5
18	y	600	-300	4,448	2,224	2.5	1,119	-1,330	26,824	180-200	0.60	0.65
19	y	600	-300	4,448	2,224	30	1,360	-1,183	16,169	180-220	0.52	0.55
20	y	270	-270	2,224	2224	0	731	-682	1,608,111	-	0.34	0.5

Note:
Relatively large gross slip and a sudden drop in tangential load during fretting fatigue cycles were observed for Test 13 and Test 15. Additionally, Test 20 fractured near the grip, which was far away from the contact region.

Table 6. Four Categories of Fatigue Life from Experimental Records

Category	Test #	Shot peened	σ_{max} (MPa)	σ_{min} (MPa)	P_{max} (N)	P_{min} (N)	P_{Freq} (Hz)	Q_{max} (N)	Q_{min} (N)	N_f (Cycle)	$N_{f,ave}$ (Cycle)	Deviation (%)
1 (T-T)	1	n	600	60	2,224	2224	0	806	-580	34,072	38,478	-11
	2	n	600	60	4,448	4448	0	1,399	-27	39,434		2
	3	n	600	60	4,448	2,224	2.5	730	-590	41,400		8
	4	n	600	60	4,448	2,224	30	920	-532	39,004		1
2 (T-C)	5	n	270	-270	2,224	2224	0	649	-650	136,092	116,659	17
	6	n	270	-270	4,448	4448	0	771	-586	98,072		-16
	7	n	270	-270	4,448	2,224	2.5	719	-616	108,056		-7
	8	n	270	-270	4,448	2,224	30	740	-650	124,417		7
3 (T-T)	9	y	600	60	2,224	2224	0	836	-598	160,474	152,528	5
	10	y	600	60	4,448	4448	0	1,223	-340	186,797		22
	11	y	600	60	4,448	2,224	2.5	880	-540	150,520		-1
	12	y	600	60	4,448	2,224	10	1,176	-430	116,414		-24
	14	y	600	60	4,448	2,224	30	1,030	-540	148,437		-3
4 (T-C)	16	y	600	-300	2,224	2224	0	1,132	-1,335	27,619	24,507	13
	17	y	600	-300	4,448	4448	0	1,249	-1,001	27,414		12
	18	y	600	-300	4,448	2,224	2.5	1,119	-1,330	26,824		9
	19	y	600	-300	4,448	2,224	30	1,360	-1,183	16,169		-34

Note:
T-T: Tension-Tension Test
T-C: Tension-Compression Test

Table 7. Summary of Stress Range and Effective Stress from Experimental Records
(a) From This Study

Test #	Shot peen	σ_{max} (MPa)	$\Delta\sigma$ (MPa)	σ_{eff} (MPa) Relaxation Rate						P_{max} (N)	P_{min} (N)	P_{Freq} (Hz)	N_f (cycle)
				0%	20%	30%	40%	50%	100%				
1	n	600	540	-	-	-	-	-	572	2224	2224	0	34,072
2	n	600	540	-	-	-	-	-	572	4448	4448	0	39,434
3	n	600	540	-	-	-	-	-	572	4448	2224	2.5	41,400
4	n	600	540	-	-	-	-	-	572	4448	2224	30	39,004
5	n	270	540	-	-	-	-	-	369	2224	2224	0	136,092
6	n	270	540	-	-	-	-	-	369	4448	4448	0	98,072
7	n	270	540	-	-	-	-	-	369	4448	2224	2.5	108,056
8	n	270	540	-	-	-	-	-	369	4448	2224	30	124,417
9	y	600	540	706	681	668	655	642	572	2224	2224	0	160,474
10	y	600	540	706	681	668	655	642	572	4448	4448	0	186,797
11	y	600	540	706	681	668	655	642	572	4448	2224	2.5	150,520
12	y	600	540	706	681	668	655	642	572	4448	2224	10	116,414
14	y	600	540	706	681	668	655	642	572	4448	2224	30	148,437
16	y	600	900	888	857	841	825	808	720	2224	2224	0	27,619
17	y	600	900	888	857	841	825	808	720	4448	4448	0	27,414
18	y	600	900	888	857	841	825	808	720	4448	2224	2.5	26,824
19	y	600	900	888	857	841	825	808	720	4448	2224	30	16,169

(b) From Lykin's Research [20]

(50.8 mm Radius Cylindrical-end Pads using Un-peened Specimens)

Test #	Shot peen	σ_{max} (MPa)	$\Delta\sigma$ (MPa)	σ_{eff} (MPa) Relaxation Rate						P_{max} (N)	P_{min} (N)	P_{Freq} (Hz)	N_f (cycle)
				0%	20%	30%	40%	50%	100%				
1	n	636	675	-	-	-	-	-	653	1330	1330	0	26,700
2	n	700	656	-	-	-	-	-	679	1330	1330	0	31,600
3	n	552	534	-	-	-	-	-	544	1330	1330	0	53,400
4	n	566	513	-	-	-	-	-	542	1330	1330	0	70,600
5	n	687	396	-	-	-	-	-	536	1330	1330	0	86,200
6	n	425	389	-	-	-	-	-	408	1330	1330	0	91,900
7	n	538	305	-	-	-	-	-	416	1330	1330	0	118,000
8	n	416	388	-	-	-	-	-	403	1330	1330	0	121,000
9	n	686	392	-	-	-	-	-	533	1330	1330	0	124,000
10	n	529	297	-	-	-	-	-	408	1330	1330	0	262,000
11	n	687	231	-	-	-	-	-	420	1330	1330	0	371,000
12	n	582	231	-	-	-	-	-	384	1330	1330	0	672,000
13	n	413	227	-	-	-	-	-	315	1330	1330	0	2,080,000
14	n	686	244	-	-	-	-	-	431	1330	1330	0	2,560,000
15	n	420	229	-	-	-	-	-	320	1330	1330	0	3,660,000
16	n	540	168	-	-	-	-	-	319	1330	1330	0	4,140,000
17	n	507	176	-	-	-	-	-	315	1330	1330	0	50,000,000
18	n	410	137	-	-	-	-	-	250	1330	1330	0	50,000,000

(c) From Jutte's Study [25]

(50.8 mm Radius Cylindrical-end Pads using Un-peened Specimens)

Test #	Shot peen	σ_{max} (MPa)	$\Delta\sigma$ (MPa)	σ_{eff} (MPa) Relaxation Rate						P_{max} (N)	P_{min} (N)	P_{Freq} (Hz)	N_f (cycle)
				0%	20%	30%	40%	50%	100%				
11	n	600	306	-	-	-	-	-	443	4448	2224	20	250,000
12	n	592	320	-	-	-	-	-	449	4448	2224	20	230,000
15	n	569	512	-	-	-	-	-	543	2224	2224	0	59,000
17	n	590	525	-	-	-	-	-	560	4448	4448	0	53,000
18	n	599	563	-	-	-	-	-	583	4448	2224	36	69,000
19	n	582	570	-	-	-	-	-	577	4448	2224	36	50,000
20	n	596	566	-	-	-	-	-	582	4448	2224	36	51,000
21	n	591	573	-	-	-	-	-	583	4448	2224	40	46,000
22	n	592	533	-	-	-	-	-	565	4448	2224	40	51,000

(d) From Namjoshi's Study [1]

(50.8 mm Radius Cylindrical-end Pads using Shot-peened Specimens)

Test #	Shot peen	σ_{max} (MPa)	$\Delta\sigma$ (MPa)	σ_{eff} (MPa) Relaxation Rate						P_{max} (N)	P_{min} (N)	P_{Freq} (Hz)	N_f (cycle)
				0%	20%	30%	40%	50%	100%				
16	y	547	275	497	479	470	461	451	401	1335	1335	0	4,438,031
17	y	621	598	740	716	703	691	678	611	1335	1335	0	37,401
18	y	632	612	753	728	716	703	690	623	1335	1335	0	37,352
19	y	650	326	573	555	546	536	527	476	1335	1335	0	204,504
20	y	653	340	585	567	557	548	538	487	1335	1335	0	95,149
21	y	738	480	718	697	687	676	665	608	1335	1335	0	59,373
22	y	910	791	981	957	944	932	919	854	1335	1335	0	22,561

Table 8. Summary of Contact Half-width

Test #	Ruiz Solution	FEA Output								Exp. Measurement	
		at Step 1				at Max. Load Condition					
	$a_{Ruiz,max}$ (m)	-a (m)	+a (m)	$a_{FEA,step1}$ (m)	Error (%)	-a (m)	+a (m)	$a_{FEA,max}$ (m)	Error (%)	$a_{Exp,max}$ (m)	Error (%)
1	5.7E-04	5.9E-04	5.9E-04	5.9E-04	4	6.1E-04	5.7E-04	5.9E-04	4	6.6E-04	16
2	8.0E-04	8.1E-04	8.1E-04	8.1E-04	1	8.3E-04	7.5E-04	7.9E-04	2	8.5E-04	6
3	8.0E-04	8.1E-04	8.1E-04	8.1E-04	1	8.1E-04	8.0E-04	8.1E-04	1	8.5E-04	6
4	8.0E-04	8.1E-04	8.1E-04	8.1E-04	1	8.7E-04	8.2E-04	8.4E-04	5	8.2E-04	3
5	5.7E-04	5.8E-04	5.8E-04	5.8E-04	3	6.1E-04	6.0E-04	6.0E-04	7	6.4E-04	12
6	8.0E-04	8.1E-04	8.1E-04	8.1E-04	1	8.2E-04	8.1E-04	8.2E-04	2	8.5E-04	6
7	8.0E-04	8.0E-04	8.1E-04	8.0E-04	0	8.3E-04	8.0E-04	8.2E-04	2	8.6E-04	7
8	8.0E-04	8.0E-04	8.1E-04	8.0E-04	0	8.2E-04	8.0E-04	8.1E-04	1	8.2E-04	2
9	5.7E-04	5.8E-04	5.8E-04	5.8E-04	3	6.0E-04	5.7E-04	5.8E-04	3	6.5E-04	15
10	8.0E-04	8.1E-04	8.1E-04	8.1E-04	1	8.3E-04	7.7E-04	8.0E-04	0	9.0E-04	13
11	8.0E-04	8.1E-04	8.1E-04	8.1E-04	1	8.2E-04	7.7E-04	8.0E-04	1	9.3E-04	16
12	8.0E-04	8.1E-04	8.1E-04	8.1E-04	1	8.3E-04	7.7E-04	8.0E-04	1	8.1E-04	1
14	8.0E-04	8.1E-04	8.1E-04	8.1E-04	1	8.3E-04	7.9E-04	8.1E-04	1	9.3E-04	16
16	5.7E-04	5.8E-04	5.8E-04	5.8E-04	3	6.1E-04	5.6E-04	5.8E-04	3	6.5E-04	15
17	8.0E-04	8.1E-04	8.1E-04	8.1E-04	1	8.3E-04	7.2E-04	7.7E-04	4	8.7E-04	9
18	8.0E-04	8.1E-04	8.1E-04	8.1E-04	1	8.3E-04	7.8E-04	8.0E-04	0	8.7E-04	9
19	8.0E-04	8.1E-04	8.1E-04	8.1E-04	1	8.3E-04	7.9E-04	8.1E-04	1	8.7E-04	9

Note:

$$Error(\%) = \frac{\left|a_{Ruiz,\max} - a\right|}{a_{Ruiz,\max}} * 100, \text{ where } a \text{ is either } a_{FEA,step\ 1},\ a_{FEA,\max} \text{ or } a_{Exp,\max}$$

Table 9. Summary of crack initiation depth & pattern

Test #	Shot peen	σ_{max} (MPa)	σ_{min} (MPa)	P_{max} (N)	P_{min} (N)	P_{Freq} (Hz)	Q_{max} (N)	Q_{min} (N)	N_f	Crack Initiation Depth (μm)	Crack Initiation Point
1	n	600	60	2224	2224	0	806	-580	3.4E+04	Surface	Multi
2	n	600	60	4448	4448	0	1399	-27	3.9E+04	Surface	Multi
3	n	600	60	4448	2224	2.5	730	-590	4.1E+04	Surface	Multi
4	n	600	60	4448	2224	30	920	-532	3.9E+04	Surface	Multi
5	n	270	-270	2224	2224	0	649	-650	1.4E+05	Surface	Multi
6	n	270	-270	4448	4448	0	771	-586	9.8E+04	Surface	Multi
7	n	270	-270	4448	2224	2.5	719	-616	1.1E+05	Surface	Multi
8	n	270	-270	4448	2224	30	740	-650	1.2E+05	Surface	Multi
9	y	600	60	2224	2224	0	836	-598	160,474	180-220	Single
10	y	600	60	4448	4448	0	1223	-340	186,797	200-240	Single
11	y	600	60	4448	2224	2.5	880	-540	150,520	200-220	Single
12	y	600	60	4448	2224	10	1176	-430	116,414	180-210	Multi
13	y	600	60	4448	2224	10	1180	-418	412,801	180-210	Single
14	y	600	60	4448	2224	30	1030	-540	148,437	180-210	Single
15	y	600	60	4448	2224	40	920	-600	254,277	180-210	Multi
16	y	600	-300	2224	2224	0	1132	-1335	27,619	180-200	Multi
17	y	600	-300	4448	4448	0	1249	-1001	27,414	180-200	Multi
18	y	600	-300	4448	2224	2.5	1119	-1330	26,824	200-230	Multi
19	y	600	-300	4448	2224	30	1360	-1183	16,169	180-200	Multi

Table 10. Summary of MSSR Parameter under Different Coefficient of Friction

Friction f_{FEA}	MSSR max	$\Delta\tau$ (MPa)	$\Delta\tau_{crit}$ (MPa)	θ (MPa)	$R_{\Delta\tau}$	σ_{max} (MPa)	σ_{min} (MPa)	Depth μm	$x/a_{Ruiz,max}$
0.40	32.77	490	464	41.5	-0.1014	490	-124	0	0.94
0.50	33.88	542	507	40.2	-0.1268	513	-131	0	0.93
0.65	35.32	593	547	39.2	-0.1588	562	-127	0	0.93
0.80	36.61	638	582	38.2	-0.1840	610	-119	0	0.93
1.00	38.12	692	623	37.0	-0.2109	669	-105	0	0.93

Note:
Data from Test1, Step 4-5
Load Condition: σ_{max}=600 MPa, σ_{min}=60 MPa, P_{max}=2224 N, P_{min}=2224 N, P_{Freq}=0 Hz
Un-peened Specimen

Table 11. MSSR Calculation for This Study

(a) Un-peened Specimens

Test #	Step	MSSR	$\Delta\tau$ (MPa)	$\Delta\tau_{crit}$ (MPa)	Θ (deg)	$R_{\Delta\tau}$	σ_{max} (MPa)	σ_{min} (MPa)	depth (μm)	$x/a_{Ruiz,max}$
1	4-5	33.88	542	507	40	-0.13	513	-131	0	0.93
2	4-5	36.32	581	572	39	-0.03	601	-91	0	0.91
3	10-11	35.04	582	549	42	-0.11	542	-91	0	0.94
	11-12	35.07	528	507	36	-0.08	588	-141	0	0.81
	12-13	33.13	518	510	45	-0.03	466	-14	0	0.82
	13-14	33.80	502	472	39	-0.12	545	-141	0	0.67
	10-14	32.92	172	237	10	0.44	521	812	0	0.75
4	8-9	32.01	190	290	18	0.54	397	658	0	0.70
	9-10	30.22	213	179	12	-0.38	725	243	0	0.68
	10-11	20.82	77	120	19	0.55	15	283	0	-0.65
	8-11	33.97	515	530	45	0.05	496	27	0	0.94
5	4-5	28.12	540	398	40	-0.74	307	-329	0	0.94
6	4-5	30.64	573	448	40	-0.56	387	-316	0	0.94
7	10-11	30.03	593	455	42	-0.62	350	-289	0	0.94
	11-12	29.72	507	385	37	-0.65	400	-359	0	0.82
	12-13	28.07	504	394	45	-0.57	309	-182	0	0.82
	13-14	28.40	522	387	39	-0.72	331	-353	0	0.67
	10-14	27.66	183	182	180	-0.01	159	547	0	0.69
8	08-09	26.35	231	298	44	0.37	319	140	0	0.94
	09-10	24.20	199	159	9	-2.01	386	-67	0	0.68
	10-11	12.56	405	281	52	-0.95	-120	-238	0	0.67
	08-11	28.84	515	429	45	-0.40	315	-149	0	0.94

(b) Shot-peened Specimens under 100% Relaxation

Test #	Step	MSSR	$\Delta\tau$ (MPa)	$\Delta\tau_{crit}$ (MPa)	θ (deg)	$R_{\Delta\tau}$	σ_{max} (MPa)	σ_{min} (MPa)	depth (μm)	$x/a_{Ruiz,max}$
9	4-5	33.94	546	503	41	-0.16	521	-139	0	0.95
10	4-5	36.37	591	565	41	-0.09	611	-119	0	0.94
11	10-11	35.17	601	559	42	-0.14	541	-101	0	0.95
	11-12	35.41	542	510	37	-0.12	606	-167	0	0.82
	12-13	33.34	524	512	45	-0.04	476	-20	0	0.82
	13-14	34.31	547	509	39	-0.14	538	-161	0	0.67
	10-14	32.84	166	232	10	0.46	535	815	0	0.76
12	4-5	34.50	526	540	45	0.05	518	26	0	0.94
14	8-9	32.22	171	251	13	0.50	437	735	0	0.68
	9-10	31.50	243	237	17	-21.18	210	708	0	0.67
	10-11	19.70	97	104	10	0.12	-1	258	0	-0.64
	8-11	34.03	528	538	45	0.03	492	19	0	0.94
16	4-5	37.05	857	659	41	-0.61	563	-424	0	0.93
17	4-5	37.53	814	653	41	-0.49	600	-394	0	0.94
18	10-11	38.62	920	718	41	-0.57	610	-420	0	0.94
	11-12	38.40	850	663	38	-0.57	647	-446	0	0.82
	12-13	36.53	848	673	45	-0.52	518	-294	0	0.82
	13-14	36.97	829	632	40	-0.64	584	-439	0	0.67
	10-14	34.89	228	265	5	0.24	583	914	0	0.71
19	8-9	33.12	313	440	45	0.46	538	271	0	0.94
	9-10	31.21	417	370	29	-4.10	-147	501	0	0.63
	10-11	14.59	102	101	151	-61.10	-349	89	0	-0.66
	8-11	36.61	781	664	45	-0.34	531	-202	0	0.94

(c) Shot-peened Specimens under 50% Relaxation

Test #	Step	MSSR	$\Delta\tau$ (MPa)	$\Delta\tau_{crit}$ (MPa)	θ (deg)	$R_{\Delta\tau}$	σ_{max} (MPa)	σ_{min} (MPa)	depth (μm)	$x/a_{Ruiz,max}$
9	4-5	30.74	313	305	36	-0.05	553	182	226	1.17
10	4-5	31.46	323	321	36	-0.01	577	200	226	1.15
11	10-11	30.92	318	312	37	-0.04	556	193	226	1.13
	11-12	31.24	320	308	34	-0.07	581	193	226	1.09
	12-13	30.49	313	313	38	0.00	527	186	226	0.85
	13-14	30.94	315	306	35	-0.05	564	184	226	0.87
	10-14	29.61	91	178	160	0.70	571	684	226	0.84
12	4-5	30.55	320	333	42	0.07	505	179	226	1.43
14	8-9	27.65	116	210	148	0.66	500	484	226	0.94
	9-10	27.86	178	187	25	11.70	312	550	226	1.09
	10-11	20.66	184	204	47	0.17	164	176	226	0.80
	8-11	30.44	319	331	42	0.07	502	177	226	1.46
16	4-5	32.48	530	400	37	-0.67	544	-60	226	0.87
17	4-5	32.78	526	406	38	-0.60	555	-39	226	1.17
18	10-11	32.73	538	409	38	-0.65	548	-45	226	1.20
	11-12	32.90	533	402	36	-0.67	567	-57	226	1.11
	12-13	32.32	533	404	39	-0.65	529	-48	226	1.02
	13-14	32.60	529	399	36	-0.67	552	-62	226	0.90
	10-14	29.53	80	161	160	0.72	602	712	226	0.83
19	8-9	28.17	138	231	43	0.61	500	360	226	1.56
	9-10	27.02	278	220	30	-1.90	91	449	226	1.10
	10-11	17.90	148	150	56	40.41	135	52	226	1.18
	8-11	32.28	565	447	41	-0.53	479	-33	226	0.86

(d) Shot-peened Specimens under 30% Relaxation

Test #	Step	MSSR	$\Delta\tau$ (MPa)	$\Delta\tau_{crit}$ (MPa)	θ (deg)	$R_{\Delta\tau}$	σ_{max} (MPa)	σ_{min} (MPa)	depth (μm)	$x/a_{Ruiz,max}$
9	4-5	31.60	318	310	36	-0.05	602	236	226	1.22
10	4-5	32.30	323	321	36	-0.01	632	256	226	1.15
11	10-11	31.78	322	317	38	-0.03	604	246	226	1.19
	11-12	32.08	320	308	34	-0.07	636	248	226	1.09
	12-13	31.37	313	313	38	0.00	582	241	226	0.85
	13-14	31.80	317	308	35	-0.05	617	239	226	0.89
	10-14	30.39	91	178	160	0.70	626	740	226	0.84
12	4-5	31.45	320	333	42	0.07	561	234	226	1.43
14	8-9	28.55	116	210	148	0.66	556	540	226	0.94
	9-10	28.73	179	191	26	9.30	366	600	226	1.10
	10-11	22.12	184	204	47	0.17	219	232	226	0.80
	8-11	31.34	319	331	42	0.07	557	233	226	1.46
16	4-5	33.35	532	401	37	-0.67	597	-4	226	1.26
17	4-5	33.64	526	406	38	-0.60	610	17	226	1.17
18	10-11	33.59	538	409	38	-0.65	604	10	226	1.21
	11-12	33.75	533	402	36	-0.67	623	-2	226	1.11
	12-13	33.20	533	404	39	-0.65	584	7	226	1.02
	13-14	33.47	529	399	36	-0.67	608	-6	226	0.90
	10-14	30.30	80	161	160	0.72	657	767	226	0.83
19	8-9	29.08	138	231	43	0.61	556	416	226	1.56
	9-10	27.98	279	222	30	-1.93	147	502	226	1.10
	10-11	19.54	151	150	56	-125.69	190	110	226	1.17
	8-11	33.20	566	449	41	-0.52	533	22	226	0.85

(e) Shot-peened Specimens under 20% Relaxation

Test #	Step	MSSR	$\Delta\tau$ (MPa)	$\Delta\tau_{crit}$ (MPa)	θ (deg)	$R_{\Delta\tau}$	σ_{max} (MPa)	σ_{min} (MPa)	depth (μm)	$x/a_{Ruiz,max}$
16	4-5	33.77	532	401	37	-0.67	625	24	226	1.26
17	4-5	34.05	526	406	38	-0.60	638	44	226	1.17
18	10-11	34.01	538	409	38	-0.65	631	38	226	1.20
	11-12	34.16	533	402	36	-0.67	650	26	226	1.11
	12-13	33.63	534	406	39	-0.64	609	36	226	1.05
	13-14	33.88	529	399	36	-0.67	635	21	226	0.90
	10-14	30.67	80	161	160	0.72	685	795	226	0.83
19	8-9	29.51	138	231	43	0.61	584	443	226	1.56
	9-10	28.43	279	222	30	-1.93	175	530	226	1.10
	10-11	20.27	157	152	56	-15.94	216	140	226	1.14
	8-11	33.65	566	449	41	-0.52	560	50	226	0.85

(f) Shot-peened Specimens under 0% Relaxation

Test #	Step	MSSR	$\Delta\tau$ (MPa)	$\Delta\tau_{crit}$ (MPa)	θ (deg)	$R_{\Delta\tau}$	σ_{max} (MPa)	σ_{min} (MPa)	depth (μm)	$x/a_{Ruiz,max}$
9	4-5	32.83	318	310	36	-0.05	686	319	226	1.22
10	4-5	33.50	323	321	36	-0.01	715	339	226	1.15
11	10-11	33.01	322	318	38	-0.03	686	329	226	1.20
	11-12	33.28	321	310	34	-14.60	331	717	226	1.09
	12-13	32.62	311	316	38	0.03	662	324	226	0.81
	13-14	33.01	319	310	36	-0.05	697	322	226	0.90
	10-14	31.51	91	178	160	0.70	709	823	226	0.84
12	4-5	32.72	320	333	42	0.07	644	317	226	1.43
14	8-9	29.83	119	213	148	0.66	634	621	226	0.94
	9-10	29.96	179	192	26	8.54	448	681	226	1.11
	10-11	24.01	184	204	47	0.17	302	315	226	0.80
	8-11	32.64	371	379	42	0.04	579	320	226	0.81
16	4-5	34.58	532	401	37	-0.67	680	79	226	1.26
17	4-5	34.86	526	406	38	-0.60	693	100	226	1.17
18	10-11	34.82	538	410	38	-0.64	686	94	226	1.21
	11-12	34.96	533	402	36	-0.67	706	81	226	1.11
	12-13	34.45	534	406	39	-0.64	665	91	226	1.05
	13-14	34.69	529	399	36	-0.67	691	77	226	0.90
	10-14	31.40	83	173	157	0.74	704	825	226	0.81
19	8-9	30.35	138	231	43	0.61	639	499	226	1.49
	9-10	29.31	280	223	30	-1.95	231	584	226	1.11
	10-11	21.61	164	154	57	-8.36	269	197	226	1.12
	8-11	34.51	566	449	41	-0.52	616	105	226	0.85

Table 12. Summary of $MSSR_{max}$

(a) Summary of $MSSR_{max}$ from this Study

Test #	Shot peen	σ_{max} (MPa)	σ_{min} (MPa)	P_{max} (N)	P_{min} (N)	P_{Freq} (Hz)	N_f	$MSSR_{max}$ Stress Relaxation					
								100%	50%	40%	30%	20%	0%
1	n	600	60	2224	2224	0	34,072	33.88	-	-	-	-	-
2	n	600	60	4448	4448	0	39,434	36.32	-	-	-	-	-
3	n	600	60	4448	2224	2.5	41,400	35.07	-	-	-	-	-
4	n	600	60	4448	2224	30	39,004	33.97	-	-	-	-	-
5	n	270	-270	2224	2224	0	136,092	28.12	-	-	-	-	-
6	n	270	-270	4448	4448	0	98,072	30.64	-	-	-	-	-
7	n	270	-270	4448	2224	2.5	108,056	30.03	-	-	-	-	-
8	n	270	-270	4448	2224	30	124,417	28.84	-	-	-	-	-
9	y	600	60	2224	2224	0	160,474	33.94	30.74	-	31.60	-	32.83
10	y	600	60	4448	4448	0	186,797	36.37	31.46	-	32.30	-	33.50
11	y	600	60	4448	2224	2.5	150,520	35.41	31.24	-	32.08	-	33.28
12	y	600	60	4448	2224	10	116,414	34.50	30.55	-	31.45	-	32.72
14	y	600	60	4448	2224	30	148,437	34.03	30.44	-	31.34	-	32.64
16	y	600	-300	2224	2224	0	27,619	37.05	32.48	-	33.35	33.77	34.58
17	y	600	-300	4448	4448	0	27,414	37.53	32.78	-	33.64	34.52	34.86
18	y	600	-300	4448	2224	2.5	26,824	38.62	32.90	-	33.75	34.16	34.96
19	y	600	-300	4448	2224	30	16,169	36.61	32.28	-	33.20	33.65	34.51

(b) Summary of $MSSR_{max}$ from Lykin's Study [20]

(50.8 mm Radius Cylindrical-end Pads with Un-peened Specimens)

Test	Shot	σ_{max}	σ_{min}	P_{max}	P_{min}	P_{Freq}	N_f	$MSSR_{max}$					
								Stress Relaxation					
#	peen	(MPa)	(MPa)	(N)	(N)	(Hz)		100%	50%	40%	30%	20%	0%
1	n	636	-40	1330	1330	0	2.7E+04	29.1	-	-	-	-	-
2	n	700	44	1330	1330	0	3.2E+04	30.5	-	-	-	-	-
3	n	552	18	1330	1330	0	5.3E+04	29.6	-	-	-	-	-
4	n	566	53	1330	1330	0	7.1E+04	30.1	-	-	-	-	-
5	n	687	291	1330	1330	0	8.6E+04	29.6	-	-	-	-	-
7	n	538	233	1330	1330	0	1.2E+05	27.8	-	-	-	-	-
8	n	416	29	1330	1330	0	1.2E+05	26.9	-	-	-	-	-
9	n	686	294	1330	1330	0	1.2E+05	29.4	-	-	-	-	-
10	n	529	232	1330	1330	0	2.6E+05	27.2	-	-	-	-	-
11	n	687	456	1330	1330	0	3.7E+05	28.2	-	-	-	-	-
12	n	582	351	1330	1330	0	6.7E+05	27.5	-	-	-	-	-
13	n	413	186	1330	1330	0	2.1E+06	25.3	-	-	-	-	-
14	n	686	442	1330	1330	0	2.6E+06	28.2	-	-	-	-	-
15	n	420	191	1330	1330	0	3.7E+06	25.4	-	-	-	-	-
16	n	540	372	1330	1330	0	4.1E+06	26.5	-	-	-	-	-
17	n	507	331	1330	1330	0	5.0E+07	26.6	-	-	-	-	-
18	n	410	273	1330	1330	0	5.0E+07	24.5	-	-	-	-	-

(c) Summary of $MSSR_{max}$ from Jutte's Study [25]

(50.8 mm Radius Cylindrical-end Pads with Un-peened Specimens)

Test	Shot	σ_{max}	σ_{min}	P_{max}	P_{min}	P_{Freq}	N_f	$MSSR_{max}$					
								Stress Relaxation					
#	peen	(MPa)	(MPa)	(N)	(N)	(Hz)		100%	50%	40%	30%	20%	0%
11	n	600	294	4448	2224	20	250,000	26.7	-	-	-	-	-
12	n	592	272	4448	2224	20	230,000	27.1	-	-	-	-	-
15	n	569	57	2224	2224	0	58,600	31.5	-	-	-	-	-
17	n	590	65	4448	4448	0	53,000	33.3	-	-	-	-	-
18	n	599	36	4448	2224	36	69,000	29.9	-	-	-	-	-
19	n	582	12	4448	2224	36	49,500	32.6	-	-	-	-	-
20	n	596	30	4448	2224	36	50,700	29.9	-	-	-	-	-
21	n	591	18	4448	2224	40	46,000	34.5	-	-	-	-	-
22	n	592	59	4448	2224	40	51,000	32.0	-	-	-	-	-

(d) Summary of $MSSR_{max}$ from Yuksel's Study [20]

(50.8 mm Radius Cylindrical-end Pads with Shot-peened Specimens)

Test #	Shot peen	σ_{max} (MPa)	σ_{min} (MPa)	P_{max} (N)	P_{min} (N)	P_{Freq} (Hz)	N_f	$MSSR_{max}$ Stress Relaxation					
								100%	50%	40%	30%	20%	0%
16	y	547	272	1335	1335	0	4438031	24.7	26.6	27.1	27.5	27.9	28.8
17	y	621	24	1335	1335	0	37,401	31.2	29.8	30.3	30.7	31.1	31.9
18	y	632	20	1335	1335	0	37,352	30.9	29.9	30.4	30.8	31.2	32.0
19	y	650	324	1335	1335	0	204,504	27.7	29.1	29.5	29.9	30.3	31.1
20	y	653	313	1335	1335	0	95,149	26.2	28.5	28.9	29.3	29.7	30.5
21	y	738	257	1335	1335	0	59,373	28.3	30.5	30.9	31.3	31.7	32.5
22	y	910	120	1335	1335	0	22,561	36.1	34.7	35.1	35.4	35.8	36.5

Table 13. Crack Initiation Location and Orientation under Stress Relaxation

100% Relaxation						50% Relaxation				
Test #	**Step**	**MSSR max**	**θ (deg)**	depth (μm)	$x/a_{Ruiz,max}$	**Step**	**MSSR max**	**θ (deg)**	depth (μm)	$x/a_{Ruiz,max}$
1	4-5	33.88	40	0	0.93	-	-	-	-	-
2	4-5	36.32	39	0	0.91	-	-	-	-	-
3	11-12	35.07	36	0	0.81	-	-	-	-	-
4	8-11	33.97	45	0	0.94	-	-	-	-	-
5	4-5	28.12	40	0	0.94	-	-	-	-	-
6	4-5	30.64	40	0	0.94	-	-	-	-	-
7	10-11	30.03	42	0	0.94	-	-	-	-	-
8	08-11	28.84	45	0	0.94	-	-	-	-	-
9	4-5	33.94	41	0	0.95	4-5	30.74	36	226	1.17
10	4-5	36.37	41	0	0.94	4-5	31.46	36	226	1.15
11	11-12	35.41	37	0	0.82	11-12	31.24	34	226	1.09
12	4-5	34.50	45	0	0.94	4-5	30.55	42	226	1.43
14	8-11	34.03	45	0	0.94	8-11	30.44	42	226	1.46
16	4-5	37.05	41	0	0.93	4-5	32.48	37	226	0.87
17	4-5	37.53	41	0	0.94	4-5	32.78	38	226	1.17
18	10-11	38.62	41	0	0.94	11-12	32.90	36	226	1.11
19	8-11	36.61	45	0	0.94	8-11	32.28	41	226	0.86

30% Relaxation						0% Relaxation				
Test #	**Step**	**MSSR max**	**θ (deg)**	depth (μm)	$x/a_{Ruiz,max}$	**Step**	**MSSR max**	**θ (deg)**	depth (μm)	$x/a_{Ruiz,max}$
1	-	-	-	-	-	-	-	-	-	-
2	-	-	-	-	-	-	-	-	-	-
3	-	-	-	-	-	-	-	-	-	-
4	-	-	-	-	-	-	-	-	-	-
5	-	-	-	-	-	-	-	-	-	-
6	-	-	-	-	-	-	-	-	-	-
7	-	-	-	-	-	-	-	-	-	-
8	-	-	-	-	-	-	-	-	-	-
9	4-5	31.60	36	226	1.22	4-5	32.83	36	226	1.22
10	4-5	32.30	36	226	1.15	4-5	33.50	36	226	1.15
11	11-12	32.08	34	226	1.09	11-12	33.28	34	226	1.09
12	4-5	31.45	42	226	1.43	4-5	32.72	42	226	1.43
14	8-11	31.34	42	226	1.46	8-11	32.64	42	226	0.81
16	4-5	33.35	37	226	1.26	4-5	34.58	37	226	1.26
17	4-5	33.64	38	226	1.17	4-5	34.86	38	226	1.17
18	11-12	33.75	36	226	1.11	11-12	34.96	36	226	1.11
19	8-11	33.20	41	226	0.85	8-11	34.51	41	226	0.85

VII. Summary, Conclusions, and Recommendations

7.1. Summary

Nearly all work accomplished to date has assumed a constant contact load while investigating fretting fatigue, and only little effort has been devoted to investigate the effects from variable contact loads. In reality, mechanic components of a turbine engine are operated under a complicate vibratory environment, experiencing both variable axial loads and contact loads at the same time. Therefore, a better understanding of how variation in the contact load affects the fretting fatigue behavior can help engineers to better account for its effects, and hence more explorations focusing on the variable contact load effects are imperative. The main objective of this study was therefore to investigate the effects from variable contact loads on fretting fatigue behavior. Twenty tests were conducted, including eight un-peened and twelve shot-peened specimens, and the thicknesses for un-peened and shot-peened specimens were 3.81 mm and 4.83 mm, respectively. Axial loads were manipulated to produce tension-tension as well as tension-compression fatigue conditions, and contact loads were applied with four frequencies: 0 Hz, 2.5 Hz, 10 Hz, and 30 Hz. These global loads were applied by a computer-controlled bi-axial servo-hydraulic test machine, using a peak valley compensator to reduce the variation between control and feedback signals. Applied load outputs were monitored and recorded continuously until specimens fractured into two pieces, and induced tangential loads were determined as the half of difference between lower axial load and upper axial load. These experimental load outputs were then utilized as the load inputs for FEA modeling.

A scanning electron microscope was used to examine the fracture surface, crack initiation locations, and crack orientations. The determination of crack initiation location for shot-peened specimens was then utilized for superimposing of residual stress into MSSR calculation. Also, both crack initiation locations and orientations were used to verify the applicability of MSSR predictions on crack initiation mechanism.

Since the infinite half space assumption was violated in this study, analytical solutions were no longer valid, and FEA, a numerical method that doesn't require the infinite half-space assumption to be satisfied, was imperative. Also, the commercial available software, ABAQUS, was used for conducting FEA in this study. For all simulations, the experimentally measured maximum contact load was always applied initially as the first step to prevent the occurrence of gross slip conditions, followed by the measured maximum axial load as the second step. After step 2, the load sequence was applied based on the experimental peak/valley values and frequencies. The static coefficient of friction was chosen as a constant, 0.5, for all tests except for those where maximum $Q/P < 0.5$ from experimental results was not satisfied. For these exceptions, the maximum Q/P from experimental observations was applied as the static coefficients of friction instead. The validation of the FEA model was accomplished by comparing with the Ruiz solutions for contact half-width, stress profiles, Hertzian peak value, and applied nominal loads. Effect of different variables such as specimen thicknesses, σ_{xx} stress concentration, σ_{yy} asymmetric distribution, cyclic load effects, and the steady state in FEA model were also conducted in detail. In order to enhance readability and comprehension, a maximum load condition was defined as a time when all maximum global loads occurred simultaneously. Additionally, a minimum load condition was

described as a step where all these global loads were all at their minimum values at the same time.

A shot-peening process introduced residual stresses into peened specimens, which was compressive near the peened surface and tensile after some depth within the interior. During fretting cycles, residual stress was subjected to relaxation, which was 0% before applying fretting fatigue cycles and 100% after a specimen broke into two pieces within the contact zone. This relaxation occurred uniformly throughout the specimen at all depths. However, the correlation between relaxation rates and fretting fatigue life is still unclear. In addition to a constant relaxation assumption, which assumed that the relaxation rate was the same for all tests under different fatigue regimes, a different relaxation rate hypothesis was also postulated by the present author. This hypothesis assumed that the amount of stress relaxation increase with the increasing fretting fatigue cycles. Once the corresponding stress relaxations were determined, they were then superimposed into FEA stress solutions to investigate the performance of fatigue parameters in fretting fatigue mechanism prediction.

Three fatigue parameters: the stress range, effective stress, and MSSR were investigated for their effectiveness on predictions on fatigue life and crack initiation mechanisms. The stress range parameter was formulated based on global applied axial loads and didn't take into account residual stress as well as local stress distribution. The effective stress parameter, on the other hand, was able to take residual stress into consideration but doesn't include the effect from local stress concentration. A critical plane-based fatigue parameter, MSSR, incorporates the influence from residual stress and contact stress, which should be the case since fretting fatigue configuration introduced a

non-uniform stress distribution near a contact region. MSSR was discussed in depth about its fretting fatigue mechanism predictions including fatigue life, crack initiation location, and orientation.

7.2. Conclusions

1. Under variable contact load conditions, the induced tangential loads always remained in phase with the applied axial load. In other words, the tangential load had the same frequency and zero phase lag with the corresponding axial loads. Contact loads affected neither the tangential load frequency nor the phase lag.
2. No distinguishing correlation between fatigue life and contact load conditions, in terms of magnitudes and frequencies, was observed for tests conducted in this study. Fatigue life was primarily dominated by the applied axial load conditions.
3. Based on the effective stress for un-peened specimens, magnitudes and frequencies of contact loads had no significant effect on fatigue life. Similar conclusion can be drawn for shot-peened specimens when stress relaxation other than 100% was imposed.
4. From effective stress parameter, shot-peening process improved fretting fatigue resistance under both constant and variable contact load conditions when compared to un-peened specimens.
5. The analytical solution, based on half-space assumption, for contact half-width determination was able to predict contact half-width with a very good accuracy for the cases where the infinite half space assumption was violated.

6. Without cyclic axial loads, contact half-widths were symmetric with respect to the center of contact zone. Once a cyclic axial load was applied to the specimens, the contact half-width became asymmetric.
7. Cracks initiated near the trailing edge in all tests. For un-peened specimens, cracks occurred on the contact surface; however, for shot-peened specimens, cracks initiated at a depth within the interior of a specimen where residual tensile stress was maximum.
8. Crack initiation orientation under variable contact loads for un-peened specimens was observed similar to that from constant contact load tests.
9. Changing values for coefficients of friction from 0.4 to 1.0 produced much less deviation on stress profiles as well as in MSSR value.
10. Under fretting fatigue configuration with alternating axial loads applied, the maximum stress concentration for σ_{xx} was noticed to occur near the trailing edge, and the σ_{yy} stress distribution was no longer symmetric with respect to the center of a contact zone.
11. For un-peened specimens and shot-peened specimens with 100% stress relaxation, the maximum MSSR was determined to occur along a contact surface near the trailing edge despite the frequency and magnitude of contact loads. Once stress relaxation from 0% up to 50% was imposed to shot-peened specimens, the maximum MSSR moved to 226 μm below the contact surface near the trailing edge regardless of the contact load conditions.
12. Based on the MSSR parameter, no significant correlation between fatigue life and contact load conditions could be noticed. This observation was even more obvious

for shot-peened specimens. The applied axial loads played the dominant role in fatigue life determination.

13. The MSSR parameter was effective to collapse fatigue life data into a single curve for un-peened specimens regardless of the contact load conditions. Similar results were also observed for shot-peened specimens. When the different stress relaxation assumption was invoked into shot-peened specimens, MSSR parameter is effective in collapsing fatigue data from both un-peened and shot-peened specimens into a single trend line.
14. On comparison with constant contact loads, variable contact loads didn't alter significantly the MSSR prediction in crack location and orientation.
15. The MSSR parameter was effective in predicting crack initiation location and crack initiation orientation for fretting fatigue behavior under both constant and variable contact load conditions.

7.3. Recommendations for Future Work

This study performed fretting fatigue analysis on titanium alloy under both constant and variable contact loads with 50.8 mm radius cylindrical-end pads in a laboratory environment at about 25˚ C. Since the dovetail joint shape between disk and blade in real aircraft engine is more complicated, and the geometry of fretting pads plays a crucial role in fatigue life determination, further efforts should be devoted to investigate the significance of different pad geometry under variable contact load conditions. Moreover, the operating temperature in gas turbine engine is much higher than room temperature, that means variable contact loads with an elevated temperature test condition is an interesting subject for future study. When airplanes are deployed in a

place near coastal shore or with muggy climate, environmental corrosion impairs mechanical component fatigue resistance even further than in dry-air situation. Variable contact loads accompanied with synthetic seawater corrosion will make contribution in clarifying the importance of fretting fatigue under environmental corrosion. In some cases, turbine engine components are made of different materials, and this suggests a possibility to conduct a fretting fatigue test under dissimilar materials between fretting pads and specimens under variable contact load configuration.

Due to the limitation on the hydraulic test machine capacity, the maximum contact load frequency adopted in this study was chosen as 30 Hz. Nonetheless, in a real turbine engine, the vibration frequency is much greater than this value, and thus a higher contact load frequency such as 200 Hz should be included in future work to better understanding the nature of fretting fatigue phenomenon.

In spite of the shot-peening process itself, there are still several controlling variables: Almen intensity and surface coverage, for instance, which can produce different residual stress profiles. As material performance under fretting fatigue configuration is susceptible to residual stress profile, more investigations using different surface treatments, such as laser-peening approach, and specifications should be also conducted under variable contact loads.

Surface treatments such as a shot-peening process produce residual stress distribution, and this residual stress has reported to be subject to relaxation with fretting fatigue cycles. Although residual stress within a contact region would complete relax after a specimen broke into two pieces, the correlation between relaxation rate and fretting fatigue cycles is still a mystery. A quantitative analysis about stress relaxation

phenomenon under a fretting fatigue test using variable contact load could provide more knowledge into this fretting fatigue mechanism.

Shot-peening improves material performance in terms of fatigue resistance; however, this process also increases manufacturing cost. Even though shot-peening can reduce expenses in terms of maintenance and inspection, it does raise the complexity in fabrication and price in procurement. An optimization analysis between the enhanced operating performance and increasing costs should be investigated to determine whether or not shot-peening is a good choice in turbine engine build-up.

MSSR uses critical plane method at a specific point to determine fatigue life, crack location, and crack orientation. An alternate form of MSSR parameter described in Equation (44) should be investigated to verify whether this alternate form could provide equivalent or even better prediction in fretting fatigue mechanism.

Appendix A

Due to the shot-peening induced residual stress, crack may initiate either at or below the contact surface for shot-peened specimens. The comparison of shot-peened specimens with surface and inside crack initiation location is first addressed in terms of stress range, effective stress, and MSSR parameter. The local σ_{xx} stress evolution near the trailing edge under variable contact load conditions is also discussed. Also, the approach postulated by the present author using average MSSR parameter to correlate fatigue life for 2.5 Hz contact load tests is elaborated in this appendix.

A.1 Comparison of Surface and Inside Crack Initiation

A shot-peening process introduces residual stress into specimens, and this residual stress is subject to relaxation during fretting fatigue. Under the influence of residual stress, crack initiation location may shift from the contact surface to a location within the interior of a shot-peened specimen. Figure 49 compares shot-peened specimens with surface and inside crack initiation location in terms of stress range and effective stress along with different amount of stress relaxation. From these figures, no significant variation can be observed for specimens with these two crack initiation locations. Figure 50 demonstrates $MSSR_{max}$ vs. N_f for shot-peened specimens under the influence of stress relaxation. It is clear different stress relaxation assumption can be used in collapsing fatigue life for shot-peened specimens, regardless of crack initiation location. In summary, when applying different stress relaxation assumption for shot-peened specimens, no significant difference can be found based on crack initiation location in terms of stress range, effective stress, and MSSR parameter.

A.2 Characteristics of Local σ_{xx} Evolution

The effective stress written as Equation (33) in Section 2.5.2 is founded based on the global applied axial load. However, under fretting fatigue configuration, stress concentration of σ_{xx} near the trailing edge is observed, and this concentration effect should be included into fatigue predictive parameter. Figure 51 shows local σ_{xx} evolution near the trailing edge for un-peened specimens under variable contact loads. As can be seen, local σ_{xx} always has the same frequency with its corresponding global axial load, despite the contact load frequency. For tests conducted under 0 Hz and 30 Hz, the local σ_{xx} evolution history resembles the corresponding global axial load, regular loading conditions with the coincidence of peak and valley between local and global σ_{xx}. Nevertheless, for tests under 2.5 Hz variable contact loads, the local σ_{xx} presents highly irregular variations among different load steps. Under plain fatigue, Dowling [51] suggests using "rain-flow cycle counting" to correlate fatigue life with irregular loading conditions, but this approach must be revised before applying to fretting fatigue. Using local σ_{xx} evolution instead of using global axial load has the potential to develop effective fretting fatigue predictive parameter, and more work should be devoted in this field for future researches.

A.3 MSSR Parameter Prediction Using Average MSSR

As seen in Figure 51, for tests conducted under contact load frequencies other than 2.5 Hz, the maximum MSSR always occurs between the peak and valley of the applied global axial load. On the other hand, more variation for MSSR distribution is observed for tests with 2.5 Hz contact load. In order to account for the effect from MSSR variation, an average MSSR ($MSSR_{ave}$) is applied instead of $MSSR_{max}$ for tests executed under 2.5 Hz contact load conditions. Figure 52 shows the correlation between MSSR

parameter and fatigue life. In these plots, $MSSR_{max}$ is adopted for tests with contact load frequencies other than 2.5 Hz, and $MSSR_{ave}$ is used for 2.5 Hz contact load frequency. In this figures, no significant difference can be found although $MSSR_{max}$ is replaced by $MSSR_{ave}$ for 2.5 Hz contact load tests. However, MSSR determination under variable contact load conditions is still unclear, and more investigation is needed to correlate MSSR parameter and fatigue life under variable load conditions.

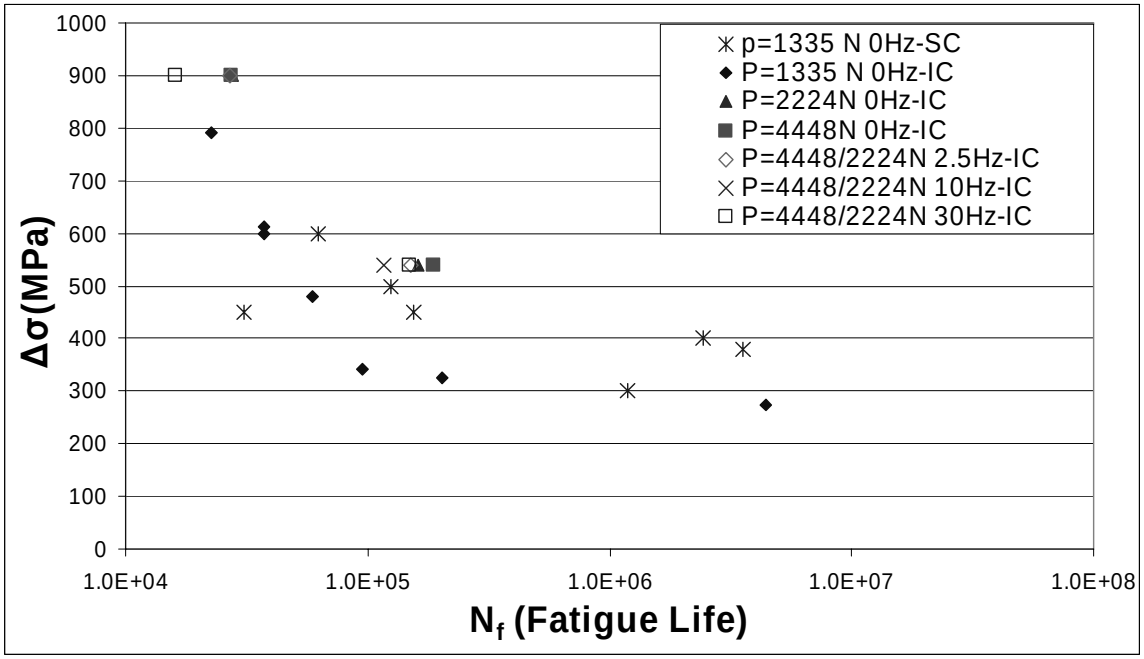

(a) Comparison of Δσ-Nf for Shot-peened Specimens with Surface and Inside Crack Initiation Location

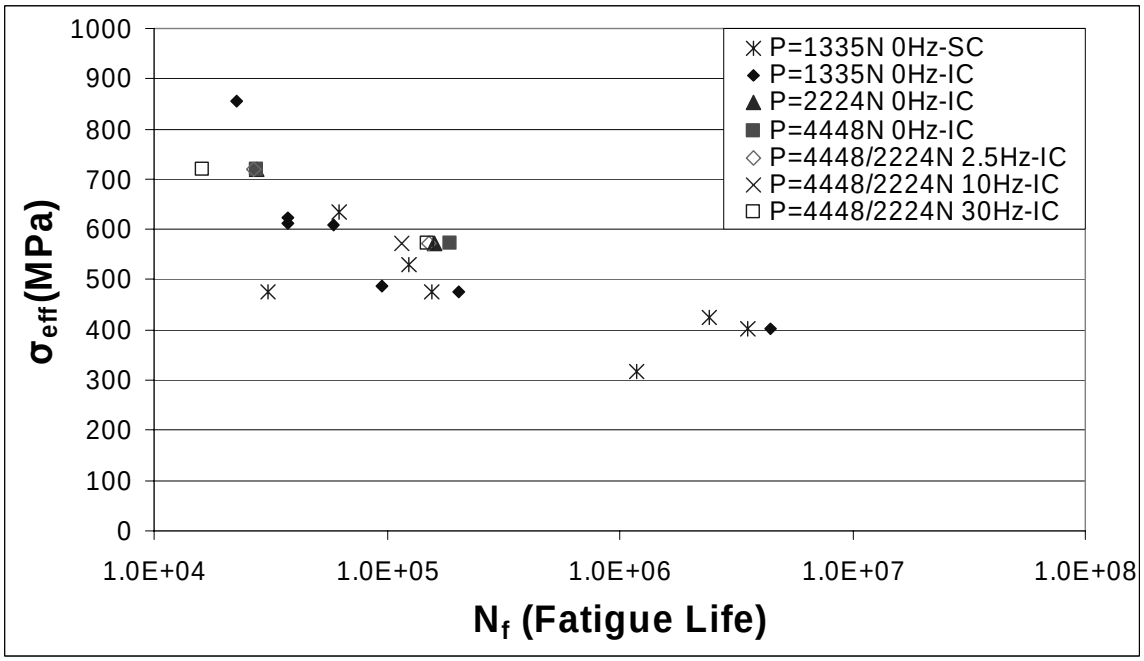

(b) Comparison of σeff-Nf for Shot-peened Specimens under 100% Stress Relaxation with Surface and Inside Crack Initiation Location

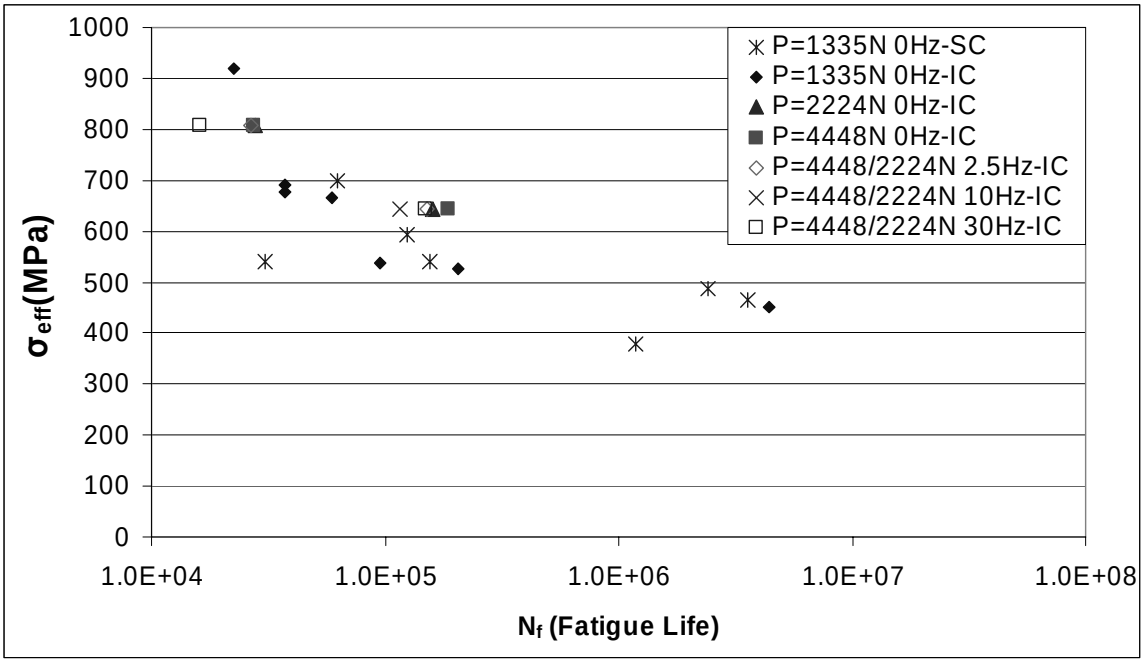

(c) Comparison of σ_{eff}-N_f for Shot-peened Specimens under 50% Stress Relaxation with Surface and Inside Crack Initiation Location

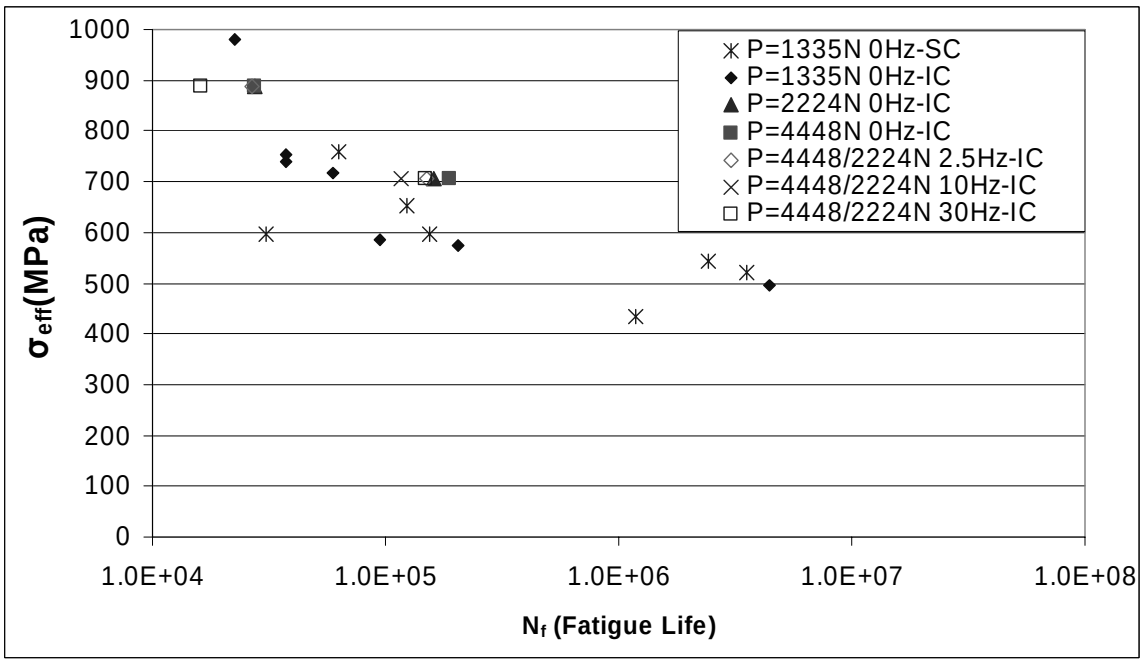

(d) Comparison of σ_{eff}-N_f for Shot-peened Specimens under 0% Stress Relaxation with Surface and Inside Crack Initiation Location

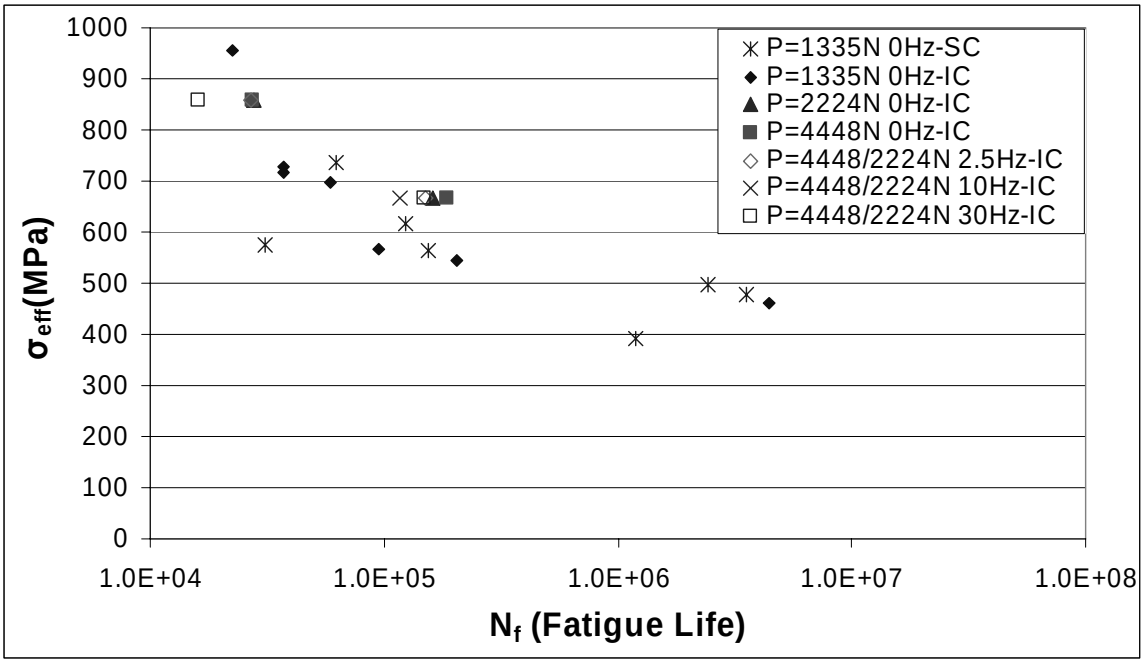

(e) Comparison of σ_{eff}-N_f for Shot-peened Specimens under different Stress Relaxation with Surface and Inside Crack Initiation Location

Figure 49. Comparison of $\Delta\sigma$ & σ_{eff} for Shot-peened Specimens with Surface and Inside Crack Initiation Location (Data from Table 7 and Table 14)

Note:

1. Except for Lee's investigation under 1335 N constant contact load, cracks initiated below the contact surface for all shop-peened specimens presented in these figures.
2. The values of σ_{eff} listed in these figures are calculated by applying Equation (33) defined in Section 2.5.2.
3. SC: Surface Crack Initiation
   IC : Inside Crack Initiation

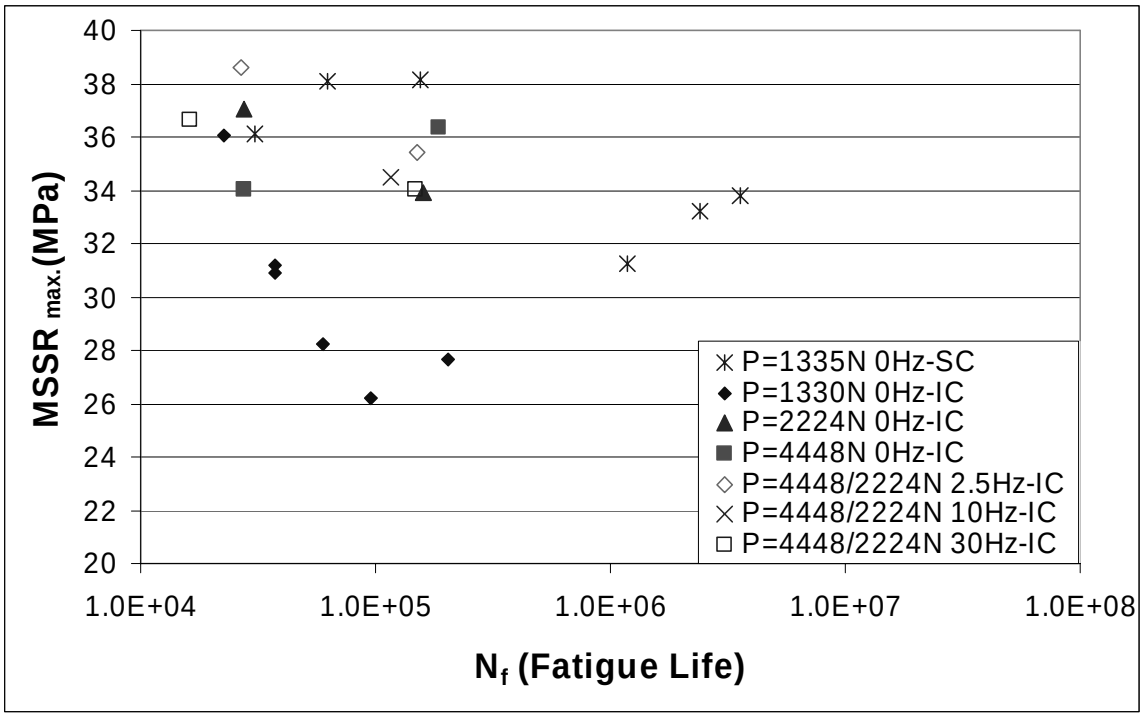

(a) Comparison of $MSSR_{max}$ -N_f for Shot-peened Specimens under 100% Stress Relaxation with Surface and Inside Crack Initiation Location

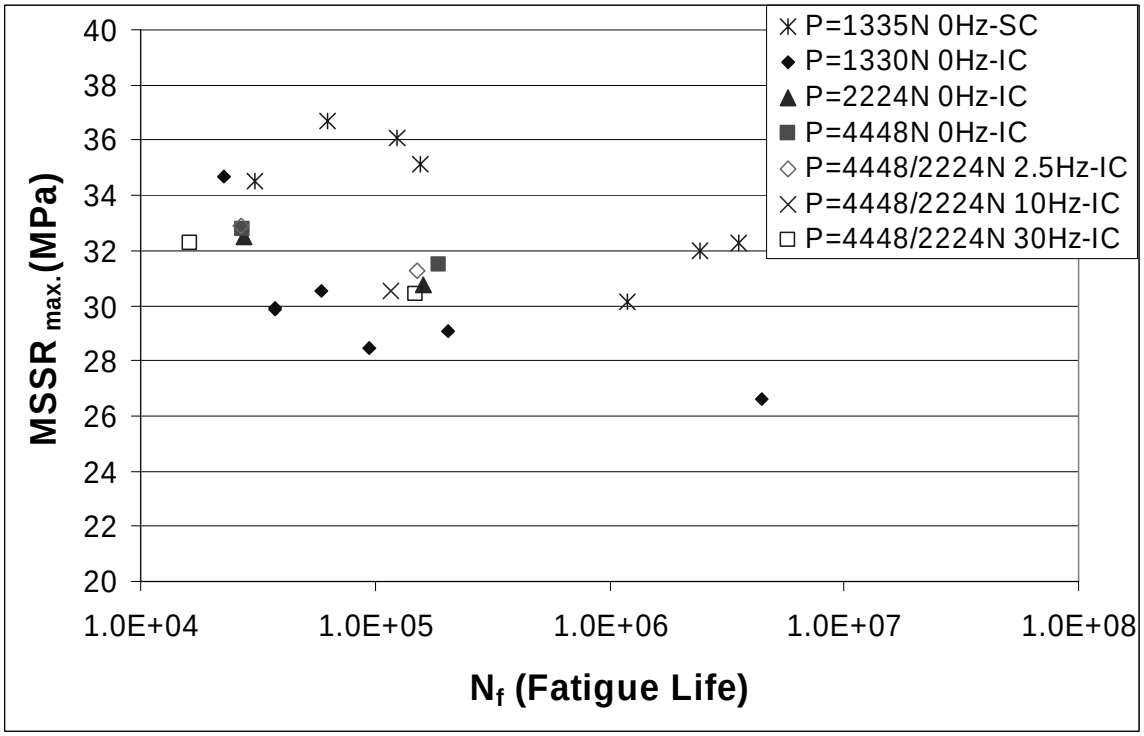

(b) Comparison of $MSSR_{max}$ -N_f for Shot-peened Specimens under 50% Stress Relaxation with Surface and Inside Crack Initiation Location

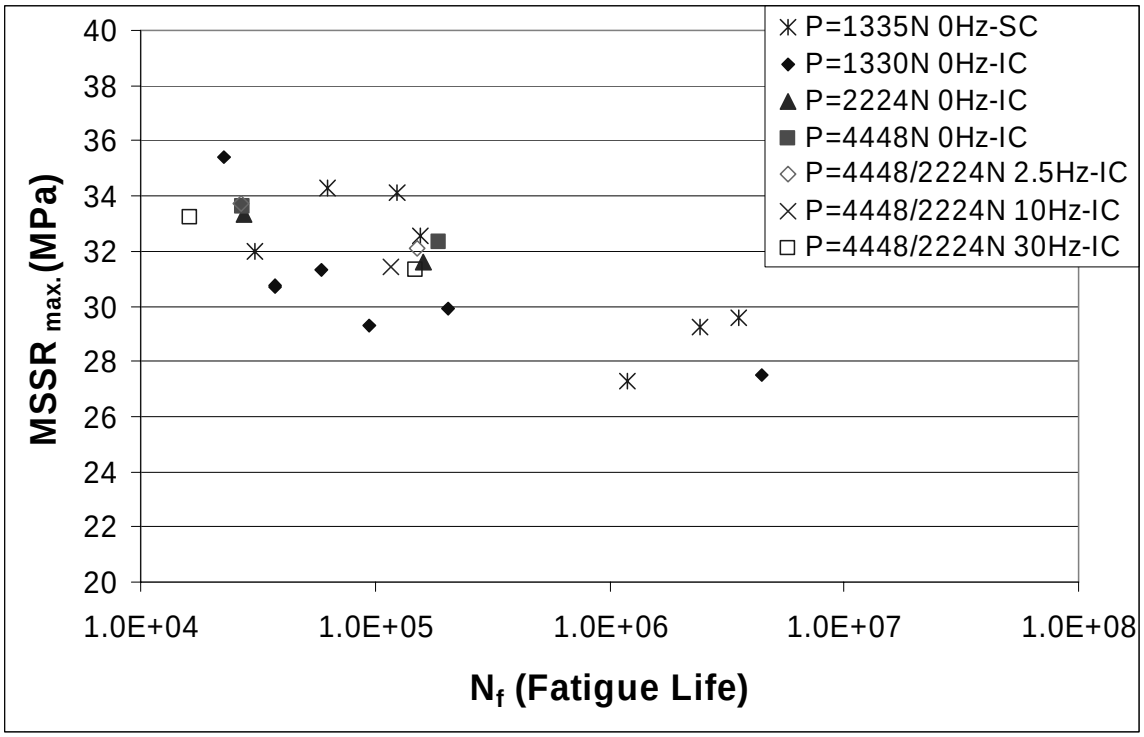

(c) Comparison of $MSSR_{max}$ -N_f for Shot-peened Specimens under 30% Stress Relaxation with Surface and Inside Crack Initiation Location

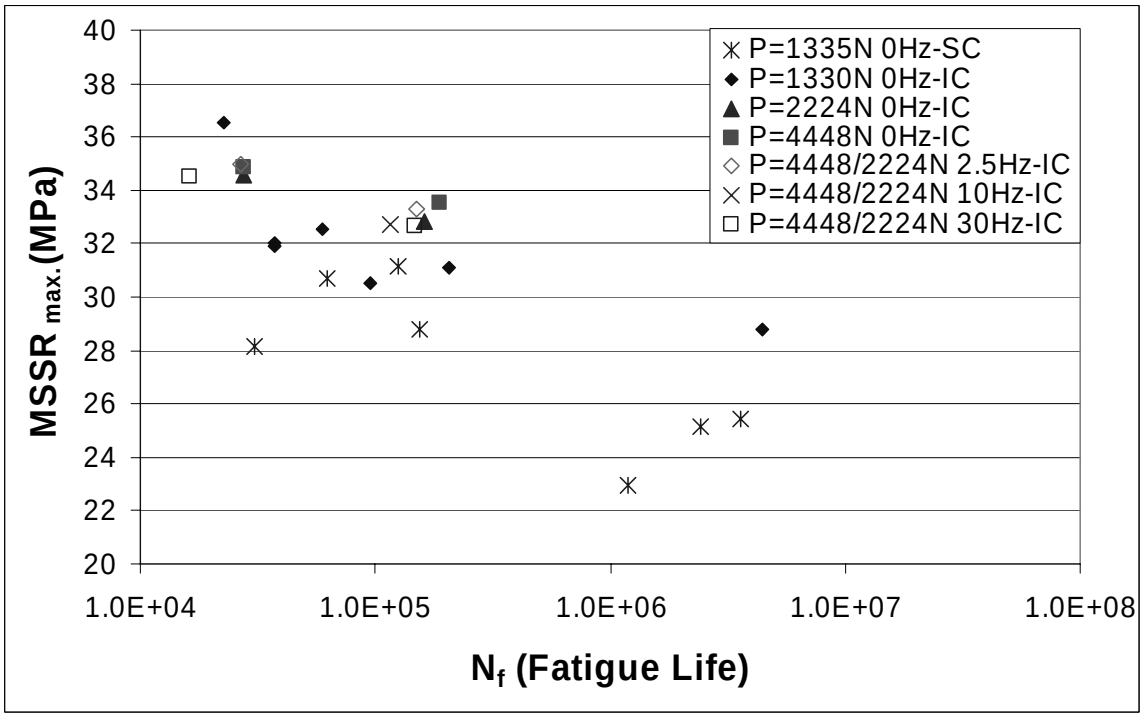

(d) Comparison of $MSSR_{max}$ -N_f for Shot-peened Specimens under 0% Stress Relaxation with Surface and Inside Crack Initiation Location

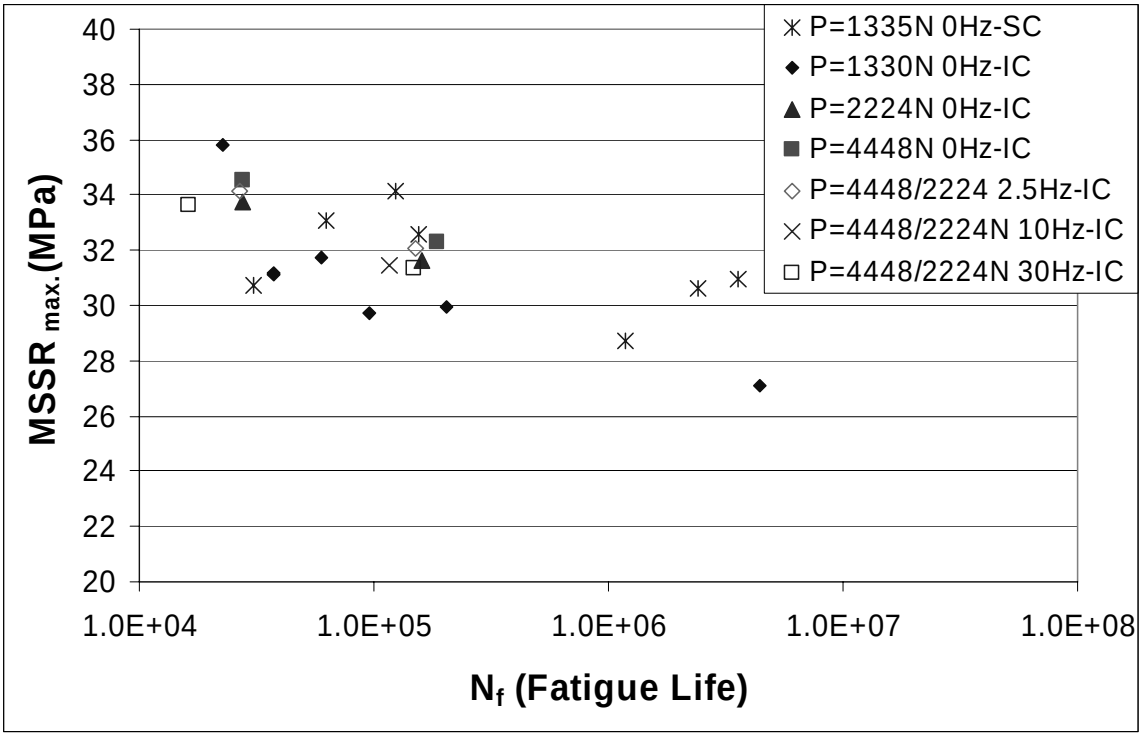

(e) Comparison of $MSSR_{max}$ -N_f for Shot-peened Specimens under Different Stress Relaxation with Surface and Inside Crack Initiation Location

Figure 50. Comparison of $MSSR_{max}$ for Shot-peened Specimens with Surface and Inside Crack Initiation Location (Data from Table 12 and Table 15)

Note:

1. Except for Lee's investigation under 1335 N constant contact load, cracks initiated below the contact surface for all shop-peened specimens presented in these figures.
2. The values of $MSSR_{max}$ from Lee's research are computed on the contact surface only while others are calculated throughout a whole specimen.
3. SC: Surface Crack Initiation
   IC : Inside Crack Initiation

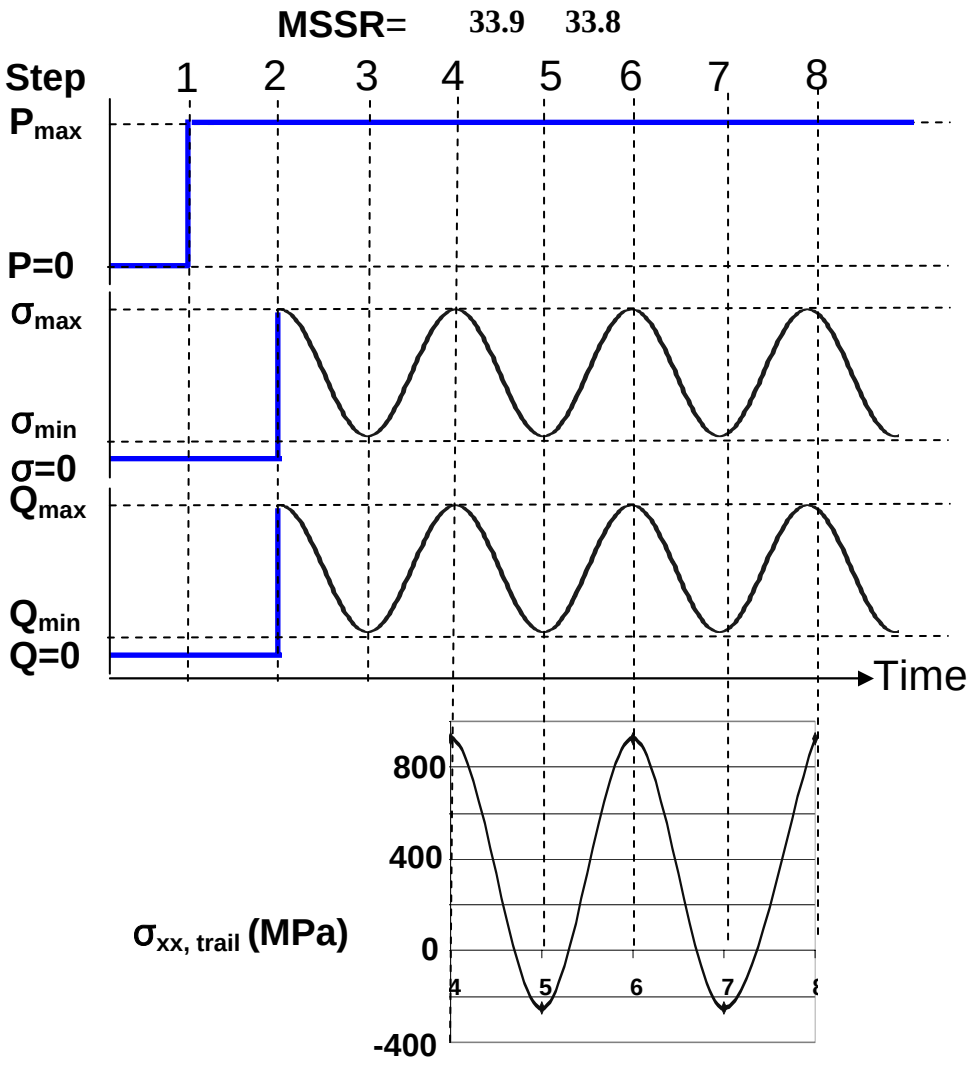

(a) For Test 1 at $x/a_{Ruiz,max}$ = 0.94 at Contact Surface
Load Condition: σ_{max} =600 MPa, σ_{min} =60 MPa, P_{max} =2224 N, P_{min} =2224 N, P_{Freq} =0 Hz
Un-peened Specimen

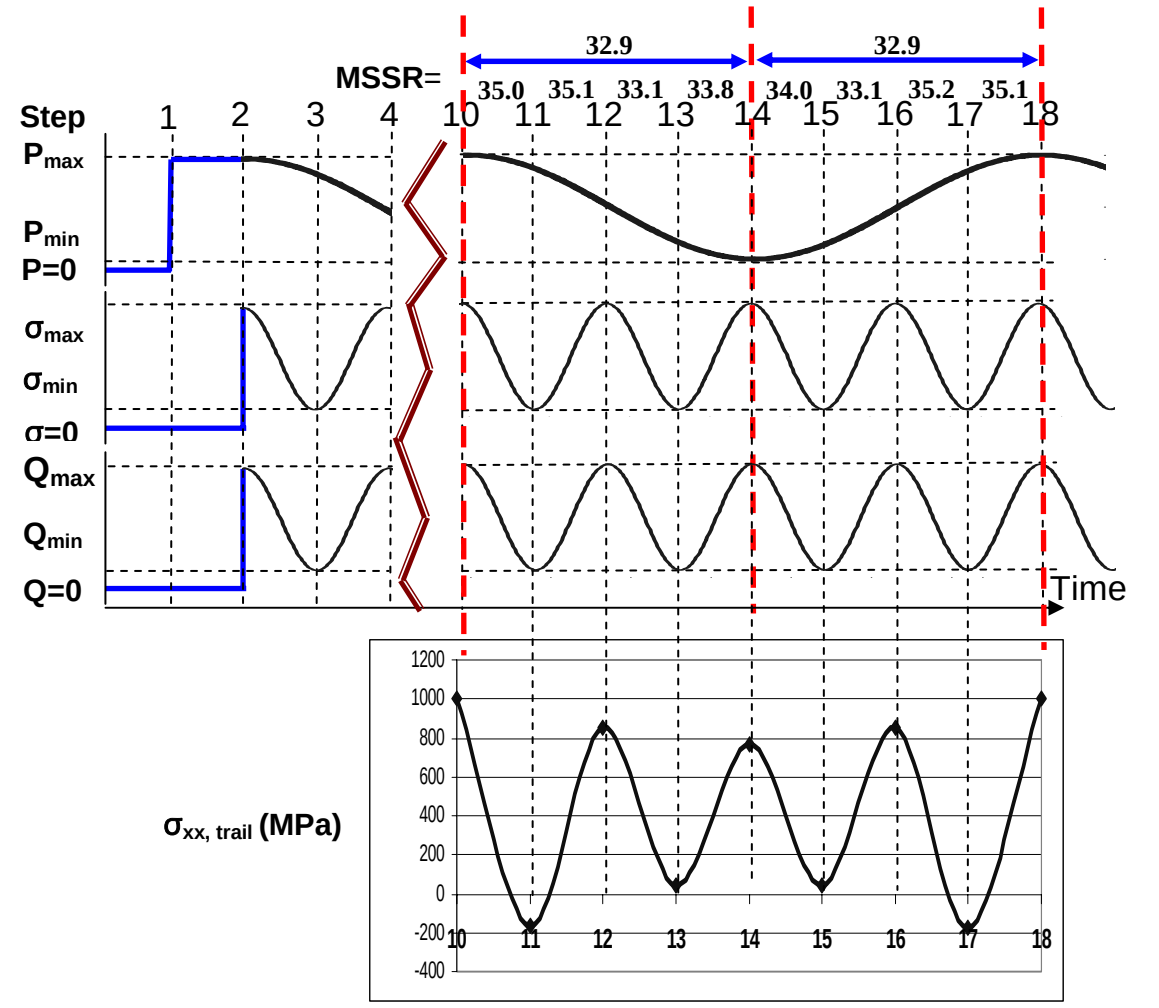

(b) For Test 3 at $x/a_{Ruiz,max}$ = 0.95 at Contact Surface
Load Condition: σ_{max}=600 MPa, σ_{min}=60 MPa, P_{max}=4448 N, P_{min}=2224 N, P_{Freq}=2.5 Hz
Un-peened Specimen

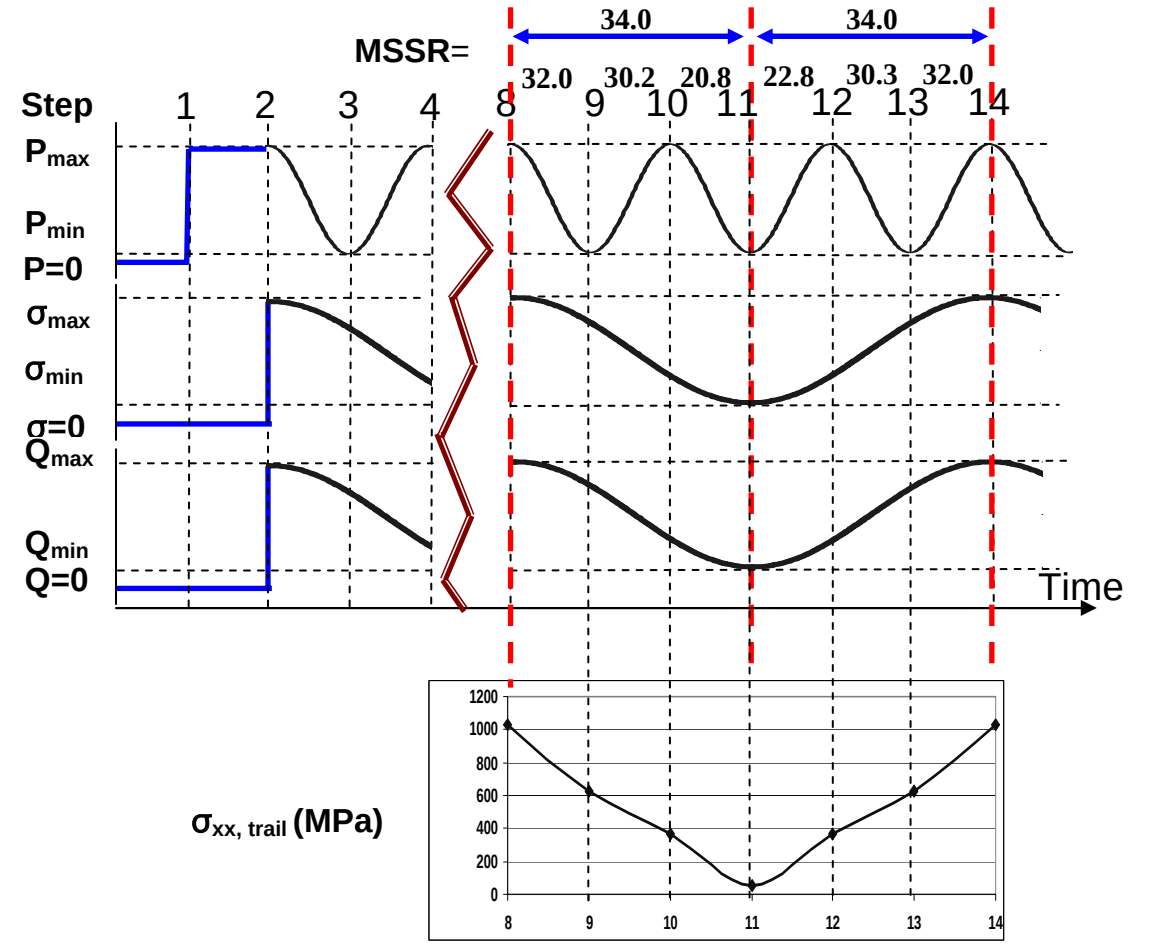

(c) For Test 4 at $x/a_{Ruiz,max}$ = 0.94 at Contact Surface
Load Condition: σ_{max} =600 MPa, σ_{min} =60 MPa, P_{max} =4448 N, P_{min} =2224 N, P_{Freq} =30 Hz
Un-peened Specimen

Figure 51. Relations among MSSR, Global Loads, and Local σ_{xx} near the Trailing Edge at Contact Surface under Variable Contact Load Condition

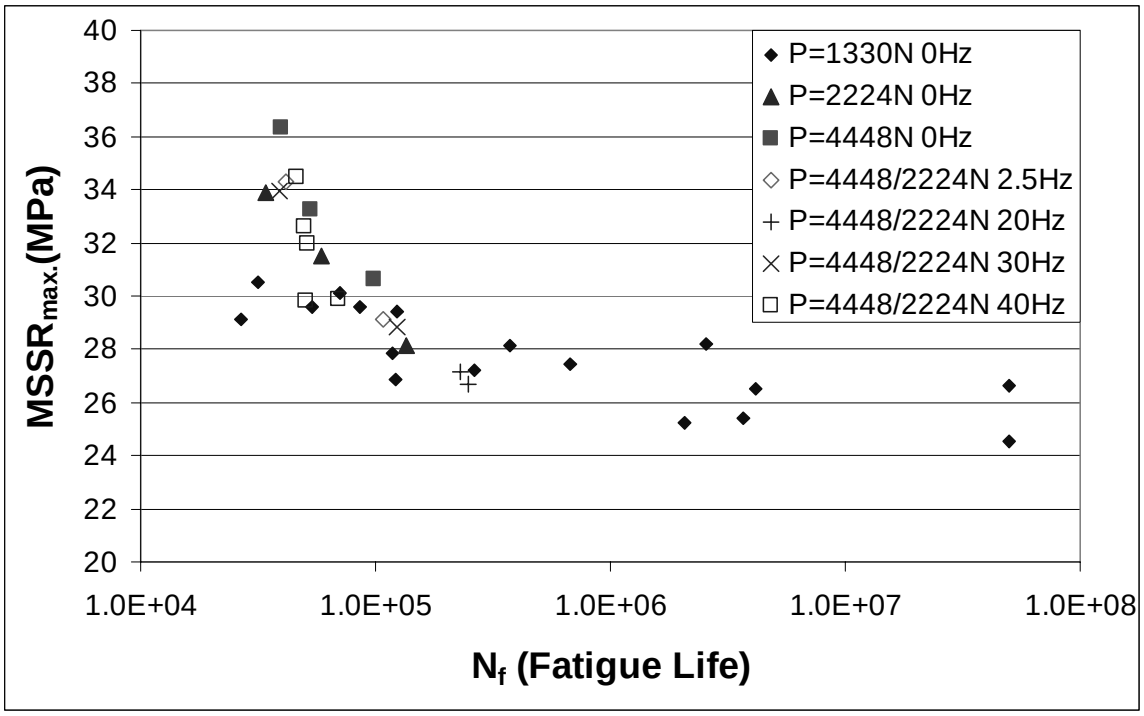

(a) $MSSR_{max}$-N_f for Un-peened Specimen

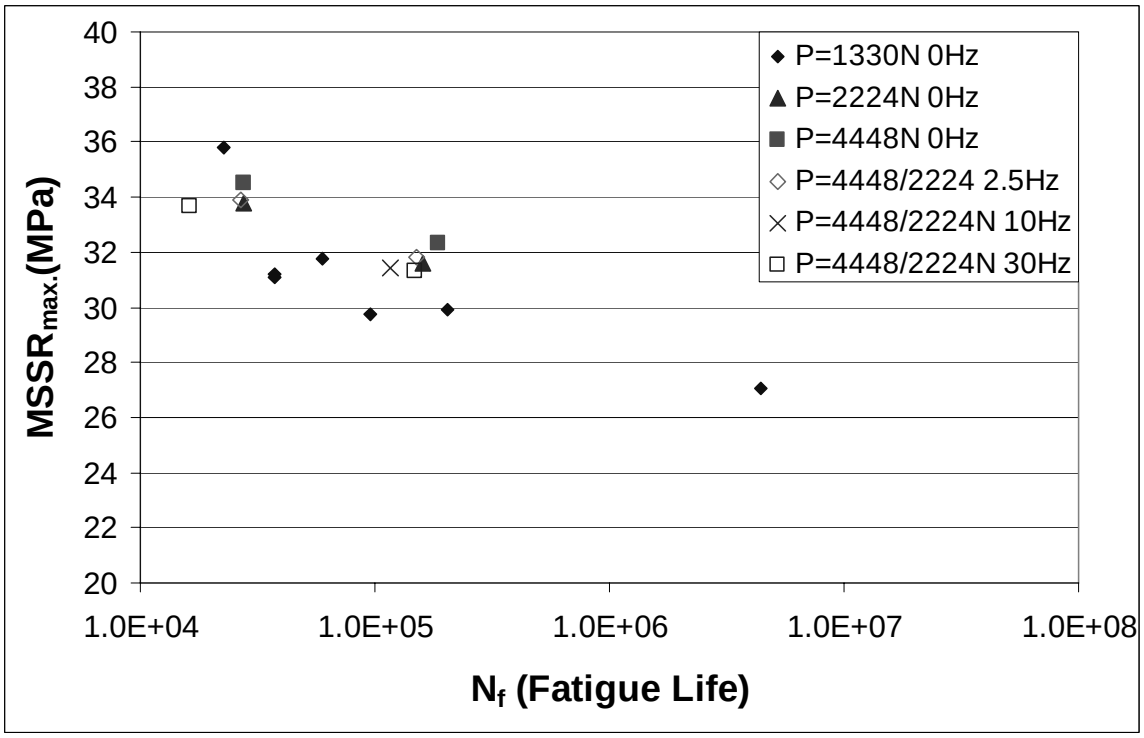

(a) $MSSR_{max}$-N_f for Shot-peened Specimen with Different Stress Relaxation

Figure 52. $MSSR_{max}$-N_f with Average MSSR for 2.5 Hz Contact Load Tests

Table 14. Summary of Stress Range and Effective Stress for Shot-peened Specimens with Surface Crack Initiation (Data from Lee's Study [3])

Test #	Shot peen	σ_{max} (MPa)	$\Delta\sigma$ (MPa)	σ_{eff} (Mpa) Relaxation Rate						P_{max} (N)	P_{min} (N)	P_{Freq} (Hz)	N_f (cycle)
				0%	20%	30%	40%	50%	100%				
1	y	333	300	434	413	402	391	380	318	1335	1335	0	1,189,508
2	y	422	380	521	499	488	477	465	403	1335	1335	0	3,562,668
3	y	444	400	543	521	510	498	487	424	1335	1335	0	2,415,267
4	y	500	450	597	575	563	552	540	477	1335	1335	0	155,545
5	y	500	450	597	575	563	552	540	477	1335	1335	0	30,839
6	y	556	500	651	628	617	605	593	530	1335	1335	0	124,222
7	y	667	600	759	735	724	712	700	636	1335	1335	0	62,501

Note:

The Values of σ_{eff} listed in this table is calculated by applying Equation (33) defined in Section 2.5.2.

Table 15. Summary of $MSSR_{max}$ for Shot-peened Specimens with Surface Crack Initiation (Data from Lee's Study [3])

Test #	Shot peened	σ_{max} (MPa)	σ_{min} (MPa)	P_{max} (N)	P_{min} (N)	P_{Freq} (Hz)	N_s	$MSSR_{max}$ under Stress Relaxation					
								100%	50%	40%	30%	20%	0%
1	y	333	33	1335	-	-	1,189,508	31.2	30.1	28.7	27.3	-	22.9
2	y	422	42	1335	-	-	3,562,668	33.8	32.3	30.9	29.6	-	25.5
3	y	444	44	1335	-	-	2,415,267	33.2	32.0	30.6	29.2	-	25.2
4	y	500	50	1335	-	-	30,839	36.1	34.5	-	32.0	30.7	28.2
5	y	500	50	1335	-	-	155,545	38.1	35.1	-	32.6	-	28.8
6	y	556	56	1335	-	-	124,222	41.1	36.1	-	34.1	-	31.2
7	y	667	67	1335	-	-	62,501	38.1	36.7	-	34.3	33.1	30.7

Note:

$MSSR_{max}$ tabulated above is computed on the contact surface where cracks initiated from experimental observations.

Table 16. Stress States among Different Steps near Trailing Edge along Contact Surface

(a) Stress States for Test 1

Step	$x/a_{Ruiz,max}$	S11 (MPa)	S22 (MPa)	S12 (Mpa)
2	0.942	928	-16	2
3	0.942	-247	-146	78
4	0.942	924	-17	2
5	0.942	-248	-146	78
6	0.942	923	-17	2
7	0.942	-248	-146	78
8	0.942	923	-17	2

Load Condition: σ_{max} =600 MPa, σ_{min} =60 MPa, P_{max} =2224 N, P_{min} =2224 N, P_{Freq} =0 Hz
Un-peened Specimen

(b) Stress States for Test 3

Step	$x/a_{Ruiz,max}$	S11 (MPa)	S22 (MPa)	S12 (Mpa)
10	0.952	1,005	-12	3
11	0.952	-168	-60	50
12	0.952	853	-2	2
13	0.952	40	-1	1
14	0.952	769	-1	1
15	0.952	39	-1	1
16	0.952	852	-2	2
17	0.952	-171	-61	51
18	0.952	1,003	-12	4

Load Condition: σ_{max}=600 MPa, σ_{min}=60 MPa, P_{max}=4448 N, P_{min} =2224 N, P_{Freq} =2.5 Hz
Un-peened Specimen

(c) Stress States for Test 4

Step	$x/a_{Ruiz,max}$	S11 (MPa)	S22 (MPa)	S12 (Mpa)
8	0.944	1,031	-13	5
9	0.944	626	-1	1
10	0.944	367	-151	-59
11	0.944	56	-1	1
12	0.944	367	-151	-59
13	0.944	624	-1	1
14	0.944	1,031	-14	5

Load Condition: σ_{max}=600 MPa, σ_{min}=60 MPa, P_{max}=4448 N, P_{min} =2224 N, P_{Freq} =30 Hz
Un-peened Specimen

Bibliography

1. H.I. Yuksel. “Effects of Shot-peening on High Cycle Fretting Fatigue Behavior of Ti-6Al-4V,” MS Thesis AFIT/GAE/ENY/02-12. Air Force Institute of Technology (AU), Wright-Patterson AFB OH, December 2002.
2. S.A. Martinez. “Quantitative Characterization of Fretting Fatigue Damage in Shot-peened Ti-6Al-4V,” Thesis, University of Dayton, Dayton, Ohio (August 2004).
3. H. Lee, O. Jin, and S. Mall. “Fretting Fatigue Behaviour of Shot-peened Ti-6Al-4V at Room and Elevated Temperature,” *Fatigue Fract Engng Master Struct*, 26: 1-12 (2003).
4. D. Hills and D. Nowell. *Mechanics of Fretting Fatigue*, Kluwer Academic Publishers, Netherlands, 1994.
5. L. Fellows, D. Nowell, and D. Hills. “Contact Stresses in a Moderately Thin Strip,” *Wear*, 185: 235-238 (1995).
6. K. Chan and Y. Lee. *Ruiz Program*, South West Research Institute, Personal Communication, 1998.
7. R.B. Waterhouse. “Fretting Fatigue,” *International Materials review*, 37: 77-97 (1992).
8. R.L. Mattson. “Fatigue: Residual Stress and Cold Working,” International Conference on Fatigue of Metals, *Institude of Mechanical Engineers*, 593-603 (1956).
9. S. Namjoshi, V.K. Jain, S. Mall. “Effects of Shot-peening on Fretting Fatigue Behavior of Ti-6Al-4V,” *Transactions of the ASME*, 124: 222-228 (April 2002).
10. R.B. Waterhouse and M.K. Dutta. “The Fretting Fatigue of Titanium and Some Titanium Alloys in a Corrosive Environment,” *Wear*, 25: 171-175 (1973).
11. M.H. Wharton and R.B. Waterhouse. “Environmental Effects in the Fretting Fatigue of Ti-6Al-4V,” *Wear*, 62:287-297 (1980).
12. D.W. Hoeppner, A.M. Taylor, and V. Chandrasekaran. “Fretting Fatigue Behavior of Titanium Alloys,” In: Fretting Fatigue: Advances in Basic Understanding and Applications. Eds. Y. Mutoh, S.E. Kinyon, and D.W. Hoeppner. West Conshohocken PA: ASTM International (2003).
13. S.A. Martinez, S. Sathish, M.P. Blodgett, S. Namjoshi, and S. Mall. “Residual Stress Relaxation due to Fretting Fatigue in Shot-peened Surfaces of Ti-6Al-4V,” *American Institute of Physics*, 1531-1537 (2003).
14. V.M. Hauk and E. Macherauch. “A Useful Guide for X-ray Stress Evaluation (XSE),” *Advances in X-ray Analysis*, 27: 81-99 (1984).
15. H. Lee, S. Mall. “Stress Relaxation Behavior of Shot-peened Ti-6Al-4V under Fretting Fatigue at Elevated Temperature,” *Materials Science and Engineering* A366: 412-420 (2004).

16. V. Sabelkin, S.A. Martinez, S. Mall, S. Sathish, and M.P. Blodgett. “Effects of Shot peening Intensity on Fretting Fatigue Crack Initiation Behavior of Ti-6Al-4V,” Department of Aeronautics and Astronautics, Air Force Institute of Technology, Wright_Pattern Air Force Base, Ohio, in press.

17. W.Y. Allen. “Fretting Fatigue Behavior of Shot-peened Titanium Alloy Ti-6Al-4V under Seawater Conditions,” Master’s thesis, AFIT/GAE/ENY/04-J01, Air Force Institute of Technology, Wright-Patterson Air Force Base, Ohio.

18. K. Iyer and S. Mall. “Effects of Cyclic Frequency and Contact Pressure on Fretting Fatigue under Two-level Block Loading,” *Fatigue Fract. Engng. Mater. Struct*., 23: 335-346 (2000).

19. D. Hills, D. Nowell, and A. Sackelfield. “Surface Fatigue Considerations in Fretting Interface Dynamic, Proceedings of the 14th Leeds-Lyon Symposium on Tribiology, D. Dawson, C. M. Taylor, M. Godet, D. Berthe Eds. Elsevier, Amsterdam, 1988.

20. C.D. Lykins, S. Mall, and Douglas. “An Investigation of Fretting Fatigue Crack Initiation Behavior of the Titanium Alloy Ti-6Al-4V,” PhD. dissertation, University of Dayton, December 1999.

21. K. Iyer and S. Mall. “Analysis of Contact Pressure and Stress Amplitude Effects on Fretting Fatigue Life,” *Journal of Engineering Materials and Technology*, 123:85-93 (January 2001).

22. S.A. Namjoshi, S. Mall, V.K. Jain, and O. Jain. “Effects of Process Variables on Fretting Fatigue Crack Initiation in Ti-6Al-4V,” *Journal of Strain Analysis*, 37, No.6: 535-542 (2002).

23. C.D Lykins, S. Mall, and V.K Jain. “A Shear Stress Based Parameter for Fretting Fatigue Crack Initiation,” *Fatigue and Fracture of Engineering Materials and Structures*, 24: 461-473 (2001).

24. S. Namjoshi, S. Mall, V.K. Jain, O. Jin. “Fretting Fatigue Crack Initiation Mechanism in Ti-6Al-4V,” *Fatigue Fract Eng master Struct*, 25: 955-64 (2002).

25. A.J. Jutte. ”Effect of a Variable Contact Load on Fretting Fatigue Behavior of Ti-6Al-4V,” Thesis, Air Force Institute of Technology, Wright-Patterson Air Force Base, Ohio, 2004.

26. R.B. Waterhouse and M.K. Dutta. “The Fretting Fatigue of Titanium and Some Titanium Alloys in a Corrosive Environment,” *Wear*, 25: 171-175 (1973).

27. M.H. Wharton and R.B. Waterhouse. “Environmental Effects in the Fretting Fatigue of Ti-6Al-4V,” *Wear*, 62: 287-297 (1980).

28. D.W. Hoeppner, A.M.H. Taylor, and V. Chandrasekaran. “Fretting Fatigue Behavior of Titanium Alloys,” in Fretting Fatigue: Advances in Basic Understanding and Applications. Eds.Y. Mutoh, S.E.Kinyon, and D.W.Hoeppner. West Conshohocken PA: ASTM International, 2003.

29. L.C. Lietch. ”Fretting Fatigue Behavior of the Titanium Alloy Ti-6Al-4V under Seawater Conditions,” Master’s thesis, AFIT/GMS/ENY/04-M02, Air Force Institute of Technology, Wright-Patterson Air Force Base, Ohio, 2004.

30. L. Coffin, Jr. “A Study of the Effects of Cyclic Thermal Stresses on a Ductile Metal,” Trans. ASME, 76: 931-950 (1954).

31. S. Manson. “Behavior of Materials under Conditions of Thermal Stress,” *NACA Technical Report* TN 2933 (1953).

32. O. Basquin. “The Exponential Law of Endurance Tests,” *Am. Soc. Test. Mater Proc.*, 10: 625-630 (1910).

33. K. Walker. “The Effect of Stress Relation during Crack Propagation and Fatigue for 2024-T3 and 7075-T6 Aluminum,” Presented to subcommittee E-9V Winter Meeting (Feb 1969).

34. D. Socie. “Multiaxial fatigue Damage Models,” *Journal of Engineering Materials and Technology*, 109: 293-298 (Oct 1987).

35. K. Nishioka and K. Hirakawa. “Fundamental Investigations into Fretting Fatigue,” Part 3, *Bulletin of JSME*, 12, No.51: 397-407 (1969).

36. K. Nishioka and K. Hirakawa. “Fundamental Investigations into Fretting Fatigue,” Part 2, *Bulletin of JSME*, 12, No.50: 180-187 (1969).

37. K. Iyer. “Peak Contact Pressure, Cyclic Stress Amplitudes, Contact Semi-width and Slip Amplitude: Relative Effects on Fretting Fatigue Life,” *International Journal of Fatigue*, 23:193-206 (2001).

38. K. Smith, P. Watson, and T. Toper. “A Stress Strain Function for the Fatigue of Metals,” *Journal of Materials*, JMLSA, 5, No. 4: 767-778 (1970).

39. M. Szolwinski, and T. Farris. “Mechanics of Fretting Fatigue Crack Formation”, *Wear*, 93-107 (1996).

40. R. Neu, J. Pape, and D. Swalla-Michaud. “Methodologies for Linking Nucleation and Propagation Approaches for Predicting Life under Fretting Fatigue”, Fretting Fatigue: Current Technology and Practices, ASTM 1367, D. Hoeppner, V. Chandrasekaran and C. Elliot, Eds. American Society for Testing and Materials.

41. S. Mall, V.K. Jain, S. Namjoshi, and C.D. Lykins. ”Fretting Fatigue Crack Initiation Behavior of Ti-6Al-4V,” *Standard Technical publication 1425*, ASTM International (2003).

42. K. Walker. “The Effective Stress Ratio during Crack Propagation and Fatigue for 2024-T3 and 7075-T6 Aluminum,” In: Effects on Environment and Complex Load History on Fatigue Life. Philadelphia (PA): *American Society for Testing and Materials*, 1-14 (1970).

43. C.D. Lykins, S. Mall, and V.K. Jain. “An Evaluation of Parameters for Predicting Fretting Fatigue Initiation,” *Int J fatigue*, 22: 703-16 (2000).

44. W.N. Findley. ”Fatigue of Metals under Combination of Stresses,” *Trans ASME*, 79: 1337-48 (1975).

45. D.W. Hoeppner, V. Chandrasekaran, and C.B. Elliot. “Fretting-Fatigue: Current Technology and Practices,” ASTM STP 1367, American Society for Testing and Materials, West Conshohocken, PA (2000).

46. D. Rayaproula, and R. Cook. “A Critical Review of Fretting fatigue Investigations at the Royal Aerospace Establishment,” In: Standardization of Fretting-fatigue Test Methods and Equipment, ASTM STP 1159, American Society for Testing and Materials, Philadelphia, PA, USA, 129-152 (1992).

47. T. Lindley and K. Nix. “Fretting Fatigue in the Power Generation Industry: Experiments, Analysis and Integrity assessment,” In: Standardization of Fretting Fatigue Test Methods and Equipment, ASTM STP 1159, American Society for Testing and Materials, Philadelphia, PA, USA, 153-169 (1992).

48. L.J. Fellows, D. Nowell, D.A. Hills. *Wear* 185: 235-8 (1995).

49. D.A. Hills and D. Nowell. “A Discussion of: Peak Contact Pressure, Cyclic Stress Amplitude, Contact Semi-width and Slip Amplitude: Relative Effects on Fatigue Life”, *International Journal of Fatigue*, 23: 747-748 (2001).

50. S. A. Namjoshi, S. Mall, V. K. Jain, and O. Jin. “Fretting Fatigue Crack Initiation Mechanism in Ti-6Al-4V,” *Fatigue Fract Engng Master Struct*, 25: 955-964 (2002).

51. Norman E. Dowling, *Mechanical Behavior of Materials*, Prentice Hall, 2nd Edition, (1999).

Vita

Captain Chia-hwa Lee graduated from Chia-yi High School in Chia-yi City, Taiwan, ROC. He attended National Defense University in Tao-yuan County, Taiwan, for undergraduate studies where he graduated with a Bachelor of Science degree in Aeronautical Engineering in 1995.

His first assignment was at Army Headquarters, Tao-yuan County, as a dispatcher of military land-based transportation vehicles. In 1998, he became an Integrated Logistics Analyst for army's advanced attack helicopters. Before being selected to attend the Air Force Institute of Technology, he served as technical assistant specializing in missile and rocket design and fabrication in Zhong-Shan Institute of Technology. Upon graduating with a Master of Science degree in Material Engineering and Science, he will be assigned back to Zhong-Shan Institute of Technology as an advanced project and budget manager.

REPORT DOCUMENTATION PAGE

Form Approved
OMB No. 074-0188

1. REPORT DATE *(DD-MM-YYYY)*	**2. REPORT TYPE**	**3. DATES COVERED** *(From – To)*
15-12-2004	**Master's Thesis**	December 2002 – December 2004

4. TITLE AND SUBTITLE

Effects of Variable Contact Load on Fretting Fatigue Behavior of Shot-peened and Un-peened Titanium Alloy

5a. CONTRACT NUMBER

5b. GRANT NUMBER

5c. PROGRAM ELEMENT NUMBER

6. AUTHOR(S)

Chia-hwa Lee, Captain, Taiwan Army

5d. PROJECT NUMBER

5e. TASK NUMBER

5f. WORK UNIT NUMBER

7. PERFORMING ORGANIZATION NAMES(S) AND ADDRESS(S)
Air Force Institute of Technology
Graduate School of Engineering and Management (AFIT/EN)
2950 Hobson Way, Building 641
WPAFB OH 45433-7765

8. PERFORMING ORGANIZATION REPORT NUMBER

AFIT/GAE/ENY/04-D01

9. SPONSORING/MONITORING AGENCY NAME(S) AND ADDRESS(ES)
AFRL/MLLP
Attn: Dr. M. P. Blodgett
2230 10th Street Suite 1
WPAFB OH 45433 DSN: 255-9799

10. SPONSOR/MONITOR'S ACRONYM(S)

11. SPONSOR/MONITOR'S REPORT NUMBER(S)

12. DISTRIBUTION/AVAILABILITY STATEMENT
APPROVED FOR PUBLIC RELEASE; DISTRIBUTION UNLIMITED.

13. SUPPLEMENTARY NOTES

14. ABSTRACT

Fretting fatigue occurs between two components in contact under relative motion and reduces fatigue life when compared with plain fatigue. Shot-peening, on th other hand, is the most commonly used cold working process to improve material fatigue resistance in aeronautical industries. Nearly all work accomplished to date has assumed a constant contact load while investigating fretting fatigue. The primary goal of this study was to explore fretting fatigue behavior under constant and variable contact load configurations using both shot-peened and un-peened specimens made up of Ti-6Al-4V alloy. Contact loads were applied with four frequencies, and they were 0 Hz, 2.5 Hz, 10 Hz, and 30 Hz. Applied axial loads were also manipulated to produce tension-tension and tension-compression test conditions on the specimens at the frequency of 10 Hz. Cracks were always found to initiate near the trailing edge for all tests. The crack initiated on the contact surface of un-peened specimens and within the interior of shot-peened specimens. Finite element analysis was performed by a commercially available software, ABAQUS, to obtain contact region state variables such as stress, strain, and displacement which were computed for the development of fretting fatigue parameters. Fatigue parameters, such as the stress range, effective stress, and modified shear stress range (MSSR), were analyzed for their applicability on fretting fatigue life prediction. No strong correlation between contact load conditions and fretting fatigue mechanisms was found, and shot-peening improved fretting fatigue life despite contact load conditions. Also, the MSSR parameter was effective in fretting fatigue predictions under constant and variable contact load conditions in terms of fatigue life, crack initiation location and orientation.

15. SUBJECT TERMS
Fretting, Fatigue, Titanium Alloys, Contact Load, Shot-peening

16. SECURITY CLASSIFICATION OF:			**17. LIMITATION OF ABSTRACT**	**18. NUMBER OF PAGES**	**19a. NAME OF RESPONSIBLE PERSON**
REPORT	**ABSTRACT**	**c. THIS PAGE**			Dr. Shankar Mall, AFIT/ENY
U	**U**	**U**	**UU**	230	**19b. TELEPHONE NUMBER** *(Include area code)* (937) 255-3636X4587; e-mail: shankar.mall @afit.edu

Standard Form 298 (Rev: 8-98)
Prescribed by ANSI Std. Z39-18